Exploring Magnetotail Structure and Dynamics with Magnetohydrodynamic Simulations

by

John D. Haiducek

A dissertation submitted in partial fulfillment
of the requirements for the degree of
Doctor of Philosophy
(Atmospheric, Oceanic and Space Sciences)
in The University of Michigan
2018

Doctoral Committee:

Dr. Natalia Ganushkina, Co-Chair
Prof. Tamas Gombosi, Co-Chair
Prof. Edward Ionides
Prof. Daniel Welling
Prof. Shasha Zou

John D. Haiducek

jhaiducе@umich.edu

ORCID iD: 0000-0002-4027-8475

ACKNOWLEDGEMENTS

I would like to thank my advisers, Dr. Daniel Welling, Dr. Natalia Ganushkina, and Dr. Tamas Gombosi for their support, encouragement, and wisdom. I would like to thank Prof. Gombosi for his role in admitting me to Michigan, and for providing part of my funding during the first few years. I would like to thank Dr. Welling for encouraging me to come to Michigan, and advising me through the initial stages of my research, particularly through the work in Chapters III and VI of this dissertation. I would also like to thank him for his sense of humor and for enjoyable conversations about Counter-Strike and internet memes. I would like to thank Dr. Ganushkina for advising me through the later stages of my research, particularly the work in Chapters IV and V of this dissertation. Her advice on the style and content of papers has been very helpful. I would also like to thank Prof. Shasha Zou and Prof. Edward Ionides for serving on my committee, and for their feedback on the dissertation.

In addition to my advisers, I received extensive feedback from Dr. Steven Morley on the work in Chapters III and VI. Dr. Stepan Dubyagin provided observational data and empirical model output for Chapters IV and V, and assisted in preparing the manuscript. Dr. Xiangning Chu provided the output from his implementation of the MPB (midlatitude positive bay) index, as well as advice on its use. I am very grateful for their help and advice along the way.

I would like to thank Dr. Dogacan Su Ozturk for providing some of the SWMF (Space Weather Modeling Framework) simulation output presented in Chapter III, and Dr. Ruth Skoug for providing solar wind observations from ACE (Advanced

Composition Explorer) to fill data gaps in the publicly available OMNI dataset, and Dr. Howard Singer for providing GOES (Geostationary Operational Environmental Satellite) data for V. In addition, I would like to thank the maintainers of the SuperMag and OMNI datasets, the THEMIS (Time History of Events and Macroscale Interactions during Substorms) and GOES magnetometer teams for making their data publicly available, and the maintainers of the CDAWeb interface through which I obtained much of the data used in this dissertation.

I would also like to thank the funding agencies that supported the research in this dissertation, including the Department of Veterans Affairs through the Post 9/11 GI Bill, the U.S. Department of Energy Laboratory Directed Research and Development (LDRD) project award 20170047DR, the International Space Science Institute (ISSI) in Bern, Switzerland, the European Unions Horizon 2020 research and innovation program under grant agreement 637302 PROGRESS, NASA research grants NNX14AF34G, NNX17AI48G, NNX17AB87G, and 80NSS17K0015 through the ROSES-2013 and ROSES-2016 programs, and the National Science Foundation under grant agreement 1663770.

I would also like to thank Dr. Gabor Tóth for advising me during my first year at Michigan, and Dr. Kenneth Hansen, and Dr. Greg Cunningham for advising me briefly during the following summer.

Dr. Delores Knipp, Dr. Odile de L Beaujardiere, and Dr. John Retterer all played an instrumental role in developing my interest in space weather. I am grateful for the education they provided me and for their encouragement as I followed in their footsteps.

A number of instructors and collaborators were instrumental in developing my background in computational fluid dynamics, a skillset which has been invaluable to me in working with magnetohydrodynamic codes. These include Dr. Andrew Lofthouse, Dr. Philip Roe, Dr. Reece Neel, and Dr. Bill McGrory. I would also like

to thank Dr. Gabriel Font-Rodriguez, Dr. Kyle Novak, Dr. Victor Putz, Dr. Alan Paxton, and Dr. Sam Butler for helping me to develop computational and numerical modeling skills generally. I am especially grateful to Dr. Timothy Madden, who in addition to building my skills as a computational modeler also served as my primary supervisor and mentor during the latter half of my Air Force career, giving me just what I needed to grow at that stage in my development as a scientist.

I would like to thank my flight instructors Mel, Amy, Kathryn, and Chris, and my safety pilot Ryan for helping me improve my flying skills when I wasn't doing science. I would like to thank my friends Thomas, Evan, and Taikara for wonderful conversation and fellowship during conferences, and my neighbors Sophia and Maggie for being a frequent source of joy (and welcome distraction). My officemate Dr. Judit Szente has cheered me on many times along the way, and I am grateful to have her as a friend.

I would like to thank my wife, Dr. Sarah Cannon, for her support through both the dissertation and the simultaneous job hunting process (not to mention wedding planning). Her perspective and advice was immensely helpful, and she provided much-needed encouragement at many of the more difficult stages.

Finally, I would like to thank my parents for traveling down from Midland to attend my defense, and for giving me the encouragement and ability to pursue my dreams.

TABLE OF CONTENTS

LIST OF FIGURES

Figure

LIST OF TABLES

Table

LIST OF APPENDICES

Appendix

LIST OF ABBREVIATIONS

ACE (Advanced Composition Explorer) ii, 49

AL (auroral lower) Geomagnetic index computed from the minimum northward component of auroral magnetometers vi, ix, xi, xv, xxi, 19, 23, 29, 32, 49, 52, 54–56, 71–73, 77, 79, 80, 82, 124, 125, 204

AMPERE (Active Magnetosphere and Planetary Electrodynamics Response Experiment) 46

AMR (adaptive mesh refinement) 38, 39, 212

BATS-R-US (Block Adaptive Tree Solar-Wind, Roe-type Upwind Scheme) 35–43, 46, 50, 52, 77, 129, 152, 167, 200, 212

CIR (corotating interaction region) 20

CME (coronal mass ejection) 20, 46, 51, 52

CPCP (cross-polar cap potential) vi, ix, x, xv, 15, 32, 40, 47–49, 52, 54, 55, 57, 73–79, 81, 82, 203, 204, 208

CSS (current sheet scattering) xxi, xxii, 9–11, 31–33, 83–85, 91, 106, 111, 114, 117–119, 121–123, 137, 138, 147, 151, 153–155, 157, 203, 204

Dst (disturbance storm time) Geomagnetic index computed hourly from the northward component of equatorial magnetometers 18, 19

EMIC (electromagnetic ion-cyclotron) 9, 10, 33, 83, 84, 114, 117, 119, 121, 123, 148, 153–155, 206, 207

ABSTRACT

The magnetotail, the region of stretched magnetic field lines on the night side of the Earth, is important in a number of space weather processes, in particular geomagnetic storms and substorms. These processes can cause effects such as geomagnetically induced currents on the ground, spacecraft charging, and communications outages, which cause damage to infrastructure and disruption to human activities. Better understanding of the magnetotail and its properties can help to understand and perhaps predict these phenomena. The vast size of the magnetotail, and combined with a limited number of satellites traversing it, mean that models and simulations play an important role in providing insights into the magnetotail's structure and its involvement in geospace processes.

This dissertation consists of four studies aimed at improving understanding of the magnetotail using MHD simulations performed using the SWMF. The first of these is a validation study which showed that SWMF was able to reproduce important characteristics of the observed distributions of the Kp, Sym-H, and AL indices, as well as cross-polar cap potential. The model's ability to reproduce these quantities indicates that it accurately represents many aspects of the magnetospheric current system. However, a tendency to under-predict the strength of the most negative diversions of AL was also noted.

The second study explores the ion IB, a feature within the ionosphere as a result of pitch angle scattering in the magnetosphere. One of the processes that can cause this is called CSS (current sheet scattering), the strength of which is controlled by the paramter $K = \frac{R_c}{r_g}$, the ratio of the field line radius of curvature to the particle

gyroradius. The study estimates K using SWMF and using several empirical models for quiet conditions on 13 February 2009, when CSS was expected to be the operative mechanism for IB formation. After applying correction factors based on in situ satellite observations from the magnetotail, K was shown to be less than 10 in a majority of cases, supporting the hypothesis that the IB's were formed by CSS.

The third study extends the second into storm conditions on 4-6 April, 2010, in which wave-particle interaction as well as CSS is expected to play a role in IB formation. K estimates from SWMF and from empirical models were used to estimate the fraction of IB observations that might have been associated with CSS during this interval. Based on the assumption that the threshold for CSS could fall between $K = 8$ and $K = 12$, we found that between 20% and 69% of the IB observations might have been associated with CSS. We also found that K did not vary with local time, suggesting that CSS played a significant role in a majority of the IB's observed.

The fourth study explores the ability of MHD to predict magnetospheric substorms. A new procedure is introduced for combining lists of substorms identified using several different techniques, and this procedure is applied to both MHD output and observational data. It is shown that the procedure reduces false positive identifications and helps to address gaps in observational data, and that the resulting substorm list is consistent with certain known characteristics of substorms. The MHD output is shown to reproduce the observed distribution of substorm waiting times, and is shown to have statistically significant skill in predicting substorm onset times.

CHAPTER I

Introduction

The space environment is populated with a highly dynamic mix of charged particles referred to collectively as plasma. The term "plasma" may refer to charged particles of any energy, although the work in this dissertation focuses mainly on plasma populations with energies below 200 keV. Visible to the human eye only near the solar surface, during solar eclipses, and during interactions with the Earth's atmosphere such as auroral displays, this plasma nonetheless has significant effects on society through its impact on radio communications, electric power transmission, satellite operations, and in some instances human health. The term "space weather" is now used to describe plasma processes that affect, or have the potential to affect, human activities and infrastructure. The need to better understand, predict, and mitigate hazards associated with space weather has led to the development of various technologies and techniques to observe and simulate plasma processes. This dissertation seeks to advance the understanding of some of these processes, while providing new tools that can be used for future efforts to understand and forecast space weather.

1.1 The Solar Wind

Most space weather in our solar system begins at the sun. In addition to its intense emission of infrared, visible, and ultraviolet light, the sun is also the source

Parameter	Value
Flow speed (km/s)	450
Proton density (cm^{-3})	6.6
Proton temperature (K)	1.2×10^5
Magnetic field magnitude (nT)	7

Table 1.1: Typical values of solar wind parameters at Earth orbit, from *Gombosi* (1998).

of a stream of particles known as the solar wind, which flows at supersonic speeds, in an approximately radially outward direction (*Parker*, 1958). Average values of solar wind parameters are shown in Table 1.1. These can vary considerably depending on solar activity; some important examples of dynamical solar wind processes that can affect the Earth are discussed in Section 1.2.3.3.

Within any plasma, the bulk velocity of the plasma $\mathbf{u}$ and the time evolution of the magnetic field B are related through the induction equation,

$$\frac{\partial \mathbf{B}}{\partial t} = \nabla \times (u \times \mathbf{B}) + \eta \nabla^2 \mathbf{B}, \tag{1.1}$$

where η is the resistivity. Because of the high velocity and low density (and hence low resistivity) of the solar wind, the second term can be ignored, and in this approximation the evolution of the magnetic field depends only on the flow velocity, and magnetic fields move with the flow of the plasma. This is known as the "frozen-in" or "frozen flux" approximation. As a result, the sun's magnetic field, commonly referred to as the IMF (interplanetary magnetic field), is transported with the plasma from the sun out into the solar system.

1.2 The Magnetosphere

The magnetosphere is a region of space around the Earth in which the Earth's presence influences the motion of the plasma. The Earth affects plasma motion

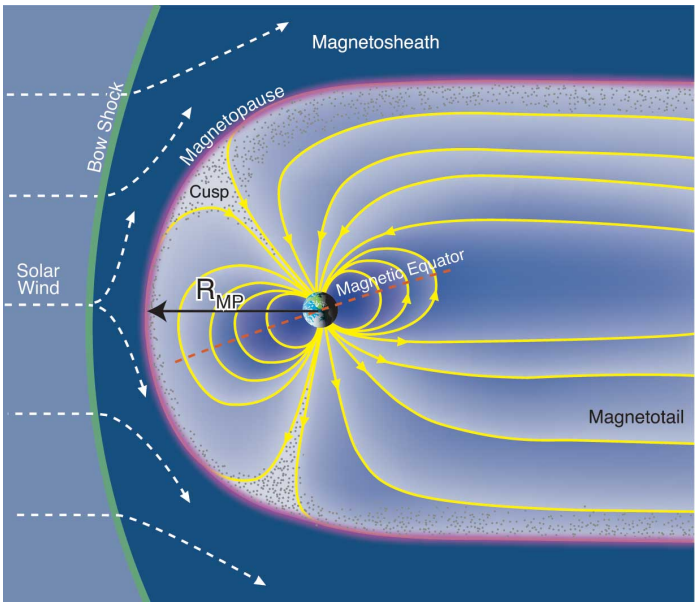

Figure 1.1: The Earth's magnetosphere, showing the solar wind, bow shock, magnetopause, magnetosheath, and magnetotail. From `http://lasp.colorado.edu/home/mop/resources/graphics/graphics/`, created by Fran Bagenal and Steve Bartlett.

primarily through its intrinsic field, and secondarily through the interaction of the Earth's atmosphere with the plasma. The magnetosphere and its regions are illustrated in Figure 1.1. The incident solar wind is shaded light blue on the left side of Figure 1.1. Unlike the solar wind, the plasma within the magnetosphere flows at subsonic speeds, and the outer extent of the magnetosphere is marked by a standing shock wave, known as the bow shock, where the solar wind slows abruptly. This is denoted by a green line in Figure 1.1. Behind the bow shock is the magnetosheath, consisting of solar wind plasma that has been decelerated and diverted around the Earth. This region is colored dark blue in Figure 1.1.

Behind the magnetosheath is the magnetopause, denoted with a pink line in Figure 1.1. At subsolar point of the magnetopause, the dynamic pressure of the solar wind equals that of the magnetic pressure from the Earth's intrinsic magnetic field.

That is,

$$\rho_{sw}\mathbf{u}_{sw}^2 = \frac{\mathbf{B}_{earth}^2}{\mu_0}, \tag{1.2}$$

where ρ_{sw} is the mass density of the solar wind.

The opposing magnetic pressure arrests the Earthward motion of the magnetosheath plasma. The magnetic field undergoes a discontinuity at the magnetopause, sharply transitioning from the magnetosheath field, whose orientation varies widely with the IMF direction, to the inner magnetosphere field, which tends to be aligned with the Earth's dipole axis. This discontinuity results in the formation of a current at the magnetopause, called the magnetopause current or the Chapman-Ferraro current after *Chapman and Ferraro* (1929) in which it was first described. The region behind the magnetopause is known as the inner magnetosphere, where plasma moves under the direct influence of the Earth's magnetic and electric fields.

While on the day side of the Earth the magnetosphere is compressed by the incident solar wind, on the night side the opposite occurs, and the magnetosphere extends far in the anti-sunward direction to form the magnetotail. Magnetic field lines in the magnetotail tend to be stretched in the anti-sunward direction, as shown in the right side of Figure 1.1. The stretched magnetic fields result in oppositely-directed magnetic fields in fairly close proximity to one another at the center of the magnetotail. This results in the formation of a current in the plasma, in much the same way that the magnetic field discontinuity at the magnetopause creates the magnetopause current. This current forms in a broad and relatively thin layer called the current sheet or central plasma sheet, and the current in this region is called the cross-tail current. The amount of stretching in the magnetotail and the position, thickness, and structure of the current sheet can vary dramatically depending on solar wind conditions and other factors, and such processes play an important role in a number of space weather processes.

At times, a portion of the cross-tail current can be redirected toward the Earth through field-aligned currents, closing through the ionosphere to contribute to a westward current known as the electrojet. This process is particularly important during substorms, which will be discussed in detail in Section 1.2.3.4.

1.2.1 Particle Motion Within the Magnetosphere

The motion of a charged particle within a magnetic field $\mathbf{B}$ is governed by the Lorentz force law, which expresses the force $\mathbf{F}$ on the particle as

$$\mathbf{F} = q\mathbf{E} + q\mathbf{v} \times \mathbf{B}, \tag{1.3}$$

where q is the particle's charge and $\mathbf{E}$ is the local electric field, and $\mathbf{v}$ is the particle's velocity. The second term exerts a force perpendicular to the particle's velocity, resulting in circular or toroidal motion relative to the local magnetic field. The frequency with which the particle gyrates under the influence of a magnetic field known as the gyrofrequency, given by

$$\Omega_g = \frac{|q||\mathbf{B}|}{m}, \tag{1.4}$$

where m is the particle's mass. The radius of the particle's orbits, called the gyroradius or Larmour radius, is given by

$$r_g = \frac{mv_\perp}{|q||\mathbf{B}|}, \tag{1.5}$$

where $v_\perp$ is the component of the particle's velocity in the direction perpendicular to $\mathbf{B}$. During successive particle orbits the quantity

$$I_1 = \int_0^{2\pi} mv_\perp r_g d\phi = \frac{2\pi m^2 v_\perp^2}{|q||\mathbf{B}|}, \tag{1.6}$$

is conserved. I_1 is known as the "first adiabatic invariant," referring to the fact that it remains constant in the case of adiabatic (i.e., slowly changing) magnetic field conditions.

The gyro motion resulting from Equation 1.3 causes each particle to remain bound to a particular magnetic field line. As long as the field strength is constant, the particle moves freely along the length of the field line. However, as the particle enters a region with stronger magnetic field, it experiences a force pushing it back in the direction it came from, with the magnitude of the force proportional to the gradient of the field magnitude in the direction parallel to the field line. In the magnetosphere, the particles experience stronger magnetic fields as they move toward the Earth. Eventually, the force can become strong enough to reverse the particle's direction, causing Earthward-moving particles to be pushed away. If the particle is on a closed magnetic field line, that is, one that is connected to the Earth in both the Northern and Southern Hemispheres, this results in a "bounce" motion in which the particle repeatedly approaches the Earth in each hemisphere in turn, only to be pushed away again. The points at which the particle reverses direction are known as mirror points. Throughout this bounce motion, the quantity

$$I_2 = \int mv_{||} ds = 2mv \int_{m_1}^{m_2} \sqrt{1 - \frac{|\mathbf{B}|}{|\mathbf{B}_0|} \sin^2 \Theta_0} ds, \tag{1.7}$$

is conserved, where $v_{||}$ is the component of the particle's velocity in the direction parallel to $\mathbf{B}$. Θ is the particle's pitch angle, that is, the angle between the particle's velocity vector and the local magnetic field. Θ_0 and the magnetic field vector $\mathbf{B}_0$ are obtained at a reference location, typically the equatorial plane. The integration path s extends along the magnetic field line to which the particle is bound, with endpoints at the mirror points m_1 and m_2.

The particle motion described so far keeps a particle confined to a single magnetic

field line, but additional forces cause the particle to drift from one field line to another. Any additional (non-magnetic) force F causes the particle to drift at the velocity

$$\mathbf{v} = \frac{\mathbf{F} \times \mathbf{B}}{q\mathbf{B}^2}. \tag{1.8}$$

In general, the drift velocity depends on the particle charge q, resulting in the formation of a current since ions and electrons drift in opposite directions. However, in the case of an electric field the force is proportional to q (see the $q\mathbf{E}$ term in the Lorentz force law), cancelling out the $\frac{1}{q}$ term in Equation 1.8. This results in a drift velocity in the direction $\mathbf{E} \times \mathbf{B}$ for both ions and electrons, and does not produce a current.

Additional drift motion results from nonuniformity in the magnetic field. If a gradient is present in the magnetic field, this results in a drift of the form

$$\mathbf{v}_G = \frac{mv_\perp^2 \mathbf{B} \times \nabla \mathbf{B}}{2q|\mathbf{B}|^3}, \tag{1.9}$$

where m is the particle mass and $v_\perp$ is the component of the particle's velocity that is perpendicular to the local magnetic field. Any curvature in the magnetic field results in an additional drift, known as curvature drift:

$$\mathbf{v}_C = \frac{mv_{||}^2 \mathbf{B} \times \nabla \mathbf{B}}{q|\mathbf{B}|^3}, \tag{1.10}$$

where $v_{||}$ is the component of the particle's velocity in the direction parallel to the magnetic field. Note that direction of motion resulting from gradient and curvature drifts is dependent on the particle charge. Because of this, electrons and ions in the inner magnetosphere drift in opposite directions, resulting in a current known as the ring current which is present throughout much of the inner magnetosphere.

1.2.2 The Isotropic Boundary

Particles undergoing bounce motion reverse direction at a point referred to as the mirror point. The location of the mirror point depends on the particle's pitch angle Θ, which as discussed earlier is typically referenced at the equatorial plane. If the pitch angle is above a certain threshold, called the loss cone angle, then the particle reverses direction at the mirror point and continues bouncing; in this case the particle is said to be trapped in the magnetic field. If a particle's pitch angle is less than the loss cone angle, the particle encounters the atmosphere before reaching the mirror point. Such particles are said to have precipitated out of the magnetosphere.

Low-altitude spacecraft provide direct observations of the precipitating particles. Such observations have shown that, at low latitudes, the vast majority of particles that are observed to be on trapped trajectories. Over the polar cap, on the other hand, the flux of precipitating particles is comparable to that of trapped particles. In addition, a sharp delineation is observed between the two domains, which is termed the isotropic boundary (IB). Normally this boundary occurs somewhere in the auroral zone. Observations equatorward of the IB find dramatically reduced fluxes parallel to the magnetic field (corresponding to precipitating trajectories), while observations poleward of the IB find comparable amounts of flux in directions perpendicular and parallel to the local magnetic field. This was first noted by *Søraas* (1972) in observations by the ESRO IA and IB spacecraft, and has since been observed by a number of other spacecraft (e.g. *Imhof et al.*, 1977, *Sergeev et al.*, 1983, *Newell et al.*, 1998).

Figure 1.2 shows an example of satellite observations obtained while crossing the IB. The x-axis shows universal time, and is additionally labeled with the satellite's magnetic latitude (CGLat) and MLT (magnetic local time). The y-axis shows the rate at which ions entered the satellite's two particle detectors. The upper curve, labeled j_T, shows the rate at which particles entered a detector oriented approximately perpendicular to the local magnetic field. This count consists mainly of trapped

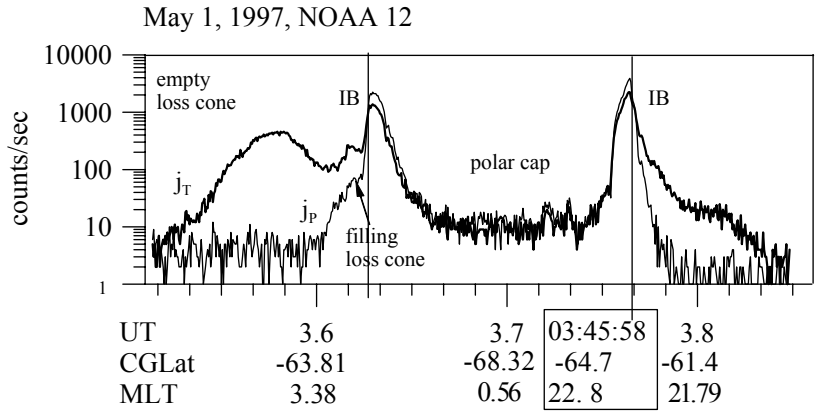

Figure 1.2: Example of satellite observations obtained while crossing the isotropic boundary. From *Ganushkina et al.* (2005).

particles (hence the subscript "T"). The lower curve, labeled j_P, shows the rate at which particles entered a detector oriented approximately perpendicular to the local magnetic field. This count consists mainly of precipitating particles (hence the subscript "P"). On the left side of the plot, the satellite is equatorward of the IB, and mainly detects trapped particles ($j_T > j_P$). j_P increases as the satellite approaches the IB, and increases very sharply in the immediate vicinity of the IB. Both j_P and j_T decrease together as the spacecraft traverses the polar cap, rising again as the spacecraft approaches the IB again on the opposite side of the polar cap. As the spacecraft crosses the IB again from the poleward side, j_P decreases sharply, so that once again $j_T > j_P$ on the equatorward side of the IB.

The sharp increase in particle precipitation at the IB indicates that some process acts to scatter particles into the loss cone, that is, to alter their pitch angles so that their equatorial pitch angles fall into the loss cone. The process responsible for the pitch angle scattering must occur along field lines whose foot points are at or above the IB latitude. The main processes responsible for this are CSS (current sheet scattering) and wave-particle interactions involving EMIC (electromagnetic ion-cyclotron) waves.

EMIC waves are formed when a population of energetic ions passes through a cold plasma (*Cornwall*, 1965). When an EMIC wave interacts with a particle whose

gyrofrequency is near the frequency of the wave, a violation of the first adiabatic invariant results. This can cause the particle's pitch angle to change dramatically, potentially placing the particle's new pitch angle into the loss cone (*Kennel and Petschek*, 1966).

CSS occurs when the radius of curvature of the local magnetic field line becomes comparable to the gyroradius of a particle (*West et al.*, 1978, *Büchner and Zelenyi*, 1987, *Sergeev et al.*, 1993). This occurs mainly in the current sheet, where the field line radius of curvature typically reaches its minimum. Like EMIC waves, the CSS process results in a violation of the first adiabatic invariant, potentially altering the particle's pitch angle and scattering it into the loss cone.

A number of papers (e.g. *Sergeev and Tsyganenko*, 1982, *Sergeev et al.*, 1993, *Ganushkina et al.*, 2005) have identified CSS as the main mechanism for IB formation during quiet conditions. Part of the reason for this is that EMIC waves are less common during quiet times (e.g. *Bräysy et al.*, 1998, *Halford et al.*, 2010, *Usanova et al.*, 2012). During storms and substorms, however, EMIC waves become an important IB formation mechanism (*Søraas et al.*, 1980, *Gvozdevsky et al.*, 1997, *Yahnin and Yahnina*, 2007, *Sergeev et al.*, 2010, *Dubyagin et al.*, 2018). Storms and substorms are described in Section 1.2.3.

Because the CSS mechanism depends strongly on magnetic field geometry, it has been proposed as a proxy for the amount of field line stretching in the magnetotail (*Sergeev et al.*, 1993, *Sergeev and Gvozdevsky*, 1995, *Meurant et al.*, 2007). When the magnetotail becomes more stretched, the IB moves to a lower latitude, and when the magnetotail becomes more dipolar, the IB moves to a higher latitude. However, this is only true when CSS is the mechanism controlling the IB latitude. When EMIC scattering occurs, the IB may form at a higher latitude independently of tail stretching. Thus, to infer magnetic field geometry from the IB latitude requires a means of determining whether or not CSS is the controlling mechanism. Chapters IV

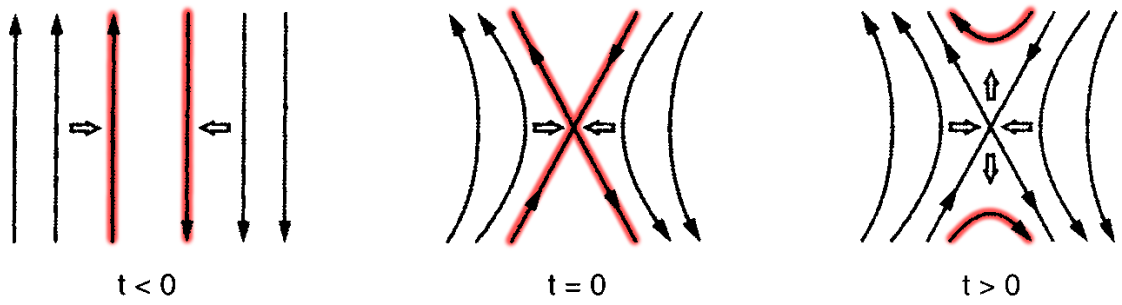

Figure 1.3: Illustration of the reconnection process. Left: Field lines converging prior to reconnection, Middle: Field lines reconnecting, Right: Field lines exit the reconnection region as reconnection process continues for new pairs of field lines. (adapted from *Gombosi*, 1998)

and V use magnetospheric models to explore the threshold conditions for CSS and test how often those threshold conditions are exceeded during storm conditions.

1.2.3 Dynamics of the Magnetosphere

Much of the energy and plasma in the magnetosphere has its origin in the solar wind. Because of this, the behavior of the solar wind can have profound effects on processes occurring within the magnetosphere. One of the main processes responsible for the entry of solar wind plasma into the magnetosphere is magnetic reconnection.

Magnetic reconnection occurs when oppositely-directed magnetic field lines converge. The process is illustrated in Figure 1.3. The figure shows three illustrations of magnetic fields. In the first, a pair of field lines, highlighted in red, is shown moving toward each other. In the second, the field lines meet, forming a structure known as an X-line. In the third, the reconnected field lines exit the reconnection region, as the process continues for new sets of field lines.

The rate at which reconnection occurs, usually measured by the velocity v_{in} at which plasma flows into the reconnection region, depends on several factors. *Sweet* (1958) and *Parker* (1957) obtained the first theoretical expression for the reconnection

rate, given by

$$v_{in} = \frac{v_A}{S^{1/2}}, \tag{1.11}$$

where v_A is the Alfvén speed, given by

$$v_A = \frac{|\mathbf{B}|}{\sqrt{\mu_0 \rho}} \tag{1.12}$$

and S is the Lundquist number, given by

$$S = \frac{\mu_0 L v_A}{\eta}, \tag{1.13}$$

in which L is the length of reconnection zone and η is the resistivity. In typical space plasmas, the resistivity η is quite low, resulting in large S and small v_{in}. *Petschek* (1964) noted that the reconnection rates obtained by Equation 1.11 are not fast enough to explain the observed rate of energy release from solar flares (where reconnection is also an important means of energy transfer), but showed that the the energy release from solar flares could be explained by a new formula for the reconnection rate

$$v_{in} = \frac{\pi v_A}{8 \log S}, \tag{1.14}$$

which he derived by accounting for additional diffusion and wave propagation mechanisms. It happens that these mechanisms are also significant for reconnection in the magnetosphere.

Research into reconnection rates has continued to the present. *Sonnerup* (1974) obtained theoretical upper limits for reconnection in a magnetospheric context. *Borovsky and Hesse* (2007) and *Cassak and Shay* (2007) obtained scaling laws for the reconnection rate and related parameters using numerical simulations.

Reconnection occurs at the magnetopause when the IMF is oriented southward

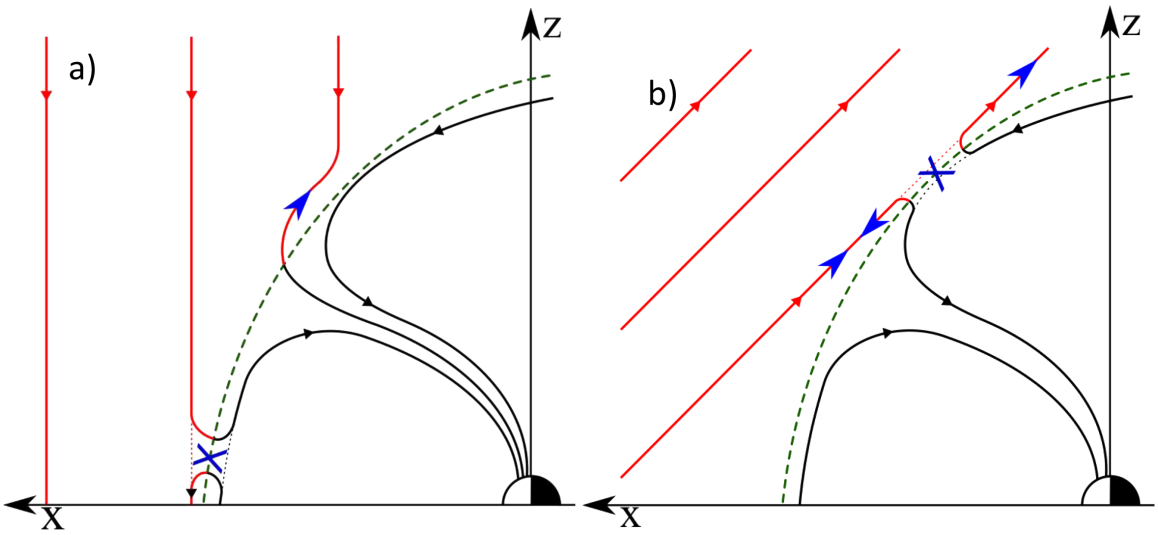

Figure 1.4: Illustrations of reconnection during (a) southward and (b) northward IMF. Adapted from *Slapak et al.* (2015).

(opposite the Earth's magnetic field). The process is illustrated in Figure 1.4a. Solar wind magnetic field lines are shown in red, and magnetosphere field lines are shown in black. The magnetopause is shown as a dashed green line, and the X-line is denoted with a blue X. Each IMF field line that arrives at the magnetopause is split in two and joined with a magnetospheric field line, forming a new pair of open field lines, each of which connect to the Earth at one end and to the solar wind at the other. Solar wind plasma along these new field lines is then able to enter the magnetosphere.

During northward IMF, rapid reconnection does not occur at the magnetopause, but can occur at high latitudes where the solar wind encounters the night-side magnetic field. This is illustrated in Figure 1.4b, which depicts northward IMF with a reconnection point connected to the northern hemisphere.

Dayside reconnection plays an important role in magnetospheric dynamics, including those at the magnetotail, because reconnection at the dayside is one of the main mechanisms through which energy and plasma from the solar wind enter the magnetosphere. As a result, the rate of reconnection at the dayside strongly influences dynamics throughout the magnetosphere, including in the magnetotail.

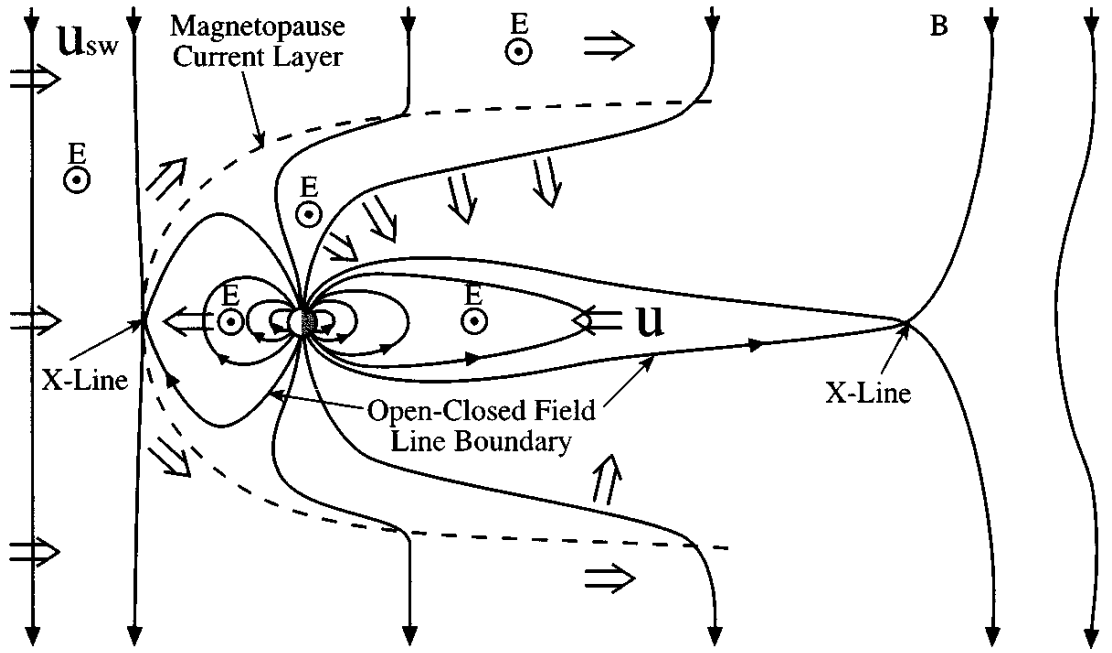

Figure 1.5: Simultaneous day side and night side reconnection during southward IMF. Incident solar wind approaches from the left, and north is at the top of the figure. The solar wind induced electric fields are directed out of the page. (From *Schunk and Nagy*, 2000.)

1.2.3.1 Magnetospheric Convection

Because the reconnected field lines are connected to the solar wind, they are transported toward the night side of the Earth. This is the beginning of a process called the Dungey cycle after *Dungey* (1961) who first described it in detail. The Dungey cycle is illustrated in Figure 1.5. The solar wind enters from the left, and imposes an electric field $\mathbf{E} = \mathbf{u} \times \mathbf{B}$, which is out of the page in the figure. Due to the high conductivity along the field lines, this electric field maps down to the ionosphere, the region of plasma located closest to the Earth. This results in a tailward $\mathbf{E} \times \mathbf{B}$ drift over the polar cap at all altitudes, and eventually causes the field lines to meet and reconnect in the current sheet.

The $\mathbf{u} \times \mathbf{B}$ electric field across the polar cap results in a charge build-up at the boundary between open and closed field lines in the magnetosphere, with a positive

charge on the dawn side of the Earth and a negative charge on the dusk side. The potential difference between the points of maximum positive and negative charge is called the CPCP (cross-polar cap potential), and is used as a measure of the rate at which solar wind energy is fed into the magnetosphere. The charge build-up at the open-closed boundary results in an oppositely directed field in the region of closed field lines, which causes the closed field lines to drift sunward, where they can once again reconnect with IMF field lines at the magnetopause, thus completing the Dungey cycle. The overall motion bears some resemblance to convection patterns that form due to localized heating in a neutral fluid, and as a result the term "magnetospheric convection" is commonly used to refer to the Dungey cycle and other processes that produce similar motion in the magnetosphere.

An additional mechanism for solar wind energy to enter the magnetosphere was described by *Axford and Hines* (1961). In this process, solar wind energy is fed into the magnetosphere through viscous interactions across the entire magnetopause. *Axford and Hines* (1961) did not describe the mechanism of these interactions, but only their consequences. In the *Axford and Hines* (1961) model, the viscous interactions behave like frictive viscosity in a collisional fluid, in which strong velocity gradients are dispersed through collisions between molecules. The plasma at the magnetopause is rarified such that such collisions are often considered insignificant, but *Axford and Hines* (1961) proposed that solar wind momentum might nonetheless be transferred across the magnetopause boundary by some viscous-like process. According to *Axford and Hines* (1961), momentum transfer from the solar wind pulls the magnetospheric plasma near the magnetosheath in an antisunward direction, much like the reconnection-driven flow of the Dungey cycle. Like the Dungey cycle, the plasma is transported Earthward at lower latitudes. Given the low density of plasma at the magnetopause, the primary mechanism by which viscous momentum transfer occurs is likely to be some other process besides collisions. A number of papers have provided

evidence that waves in the plasma could enable such a momentum transfer to occur without collisional interaction.*Sonett* (1960) presented observational evidence for the transport of solar wind momentum across the magnetopause boundary through the action of plasma waves, and *Axford* (1964) presented evidence that turbulent longitudinal waves at the magnetopause could transfer enough momentum to account for typical geomagnetic storm dynamics. *Rajaram et al.* (1973) performed a more detailed theoretical analysis plasma waves at the magnetopause and their role in providing the viscous interaction required by the *Axford and Hines* (1961) model. A number of papers (e.g. *Miura and Pritchett*, 1982, *Pu and Kivelson*, 1983, *Fairfield et al.*, 2000) have presented evidence that Kelvin-Helmholtz waves, which are known to form on the magnetopause boundary due to the velocity shear present there, may play an important role in transporting momentum across the magnetopause boundary.

The *Axford and Hines* (1961) and *Dungey* (1961) models should be regarded as complementary, rather than mutually exclusive. Both are supported by considerable observational evidence; for instance, a large body of research beginning with *Fairfield and Cahill* (1966) has shown southward IMF is associated with increased geomagnetic activity, a result that is explained by the *Dungey* (1961) model but not the *Axford and Hines* (1961) model. On the other hand, considerable observational evidence has been presented (see the previous paragraph) that momentum transfer across the magnetopause can occur through the action of plasma waves, and *Reiff et al.* (1981) found a persistent 35 kV background value in cross-polar cap potential, which could not be explained by reconnection-driven convection and which they attributed to viscous-like interactions in the *Axford and Hines* (1961) fashion.

1.2.3.2 Geomagnetic Indices

Although much of the action involved in magnetospheric convection and other magnetospheric processes occurs tens of thousands of kilometers from Earth, convec-

tion and other processes can be observed on the ground using magnetometers. The Earth's intrinsic magnetic field constitutes the bulk of the magnetic field observed on the ground. However, currents in the space environment such as the ring current, the magnetopause current, the cross-tail current, and field-aligned currents produce magnetic fields as well, and changes in these are routinely observed using ground-based magnetometers. Such changes in magnetic fields provided some of the first observations of space weather processes, long before the availability of in situ observations from spacecraft. For instance, early magnetometer studies found variability in the geomagnetic field (e.g. *Sidgreaves and Stewart*, 1868), and a correspondence between sun-spots and geomagnetic activity (e.g. *Cortie*, 1912). Today, ground-based magnetic field observations continue to play an important role in helping to ascertain the behavior of the magnetosphere. For instance, several recent spacecraft missions aiming to study the ionosphere and magnetosphere have been accompanied by deployments of ground-based magnetometers (e.g. *Mann et al.*, 2008, *Russell et al.*, 2008, *Tanskanen*, 2009).

Fluctuations in a single magnetometer reveal relatively little about the magnetosphere as a whole, since with only one magnetometer it is difficult or impossible to distinguish contributions from relatively distant currents in the magnetosphere from those in the ionosphere directly above the detector. Geological features near each magnetometer can also influence the magnetometer's response, further complicating interpretation. However, strength and direction of currents, as well as other properties such as drift velocities can be estimated by analyzing data from multiple magnetometers together (e.g. *Clauer and Kamide*, 1985, *Friis-Christensen et al.*, 1985, *Richmond and Kamide*, 1988, *Anderson et al.*, 2004, *Gjerloev*, 2009). The need to efficiently and consistently analyze data from many magnetometers has led to the development of geomagnetic indices, which combine observations from multiple ground-based magnetometers (ranging in number from single digits to hundreds of

magnetometers, depending on the index) in order to produce a single number designed to measure a particular aspect of magnetospheric activity.

Kp (planetarische Kenziffer) is the oldest geomagnetic index in current use, having been originally introduced by *Bartels* (1949) based on the local K index (*Bartels et al.*, 1939). The local K index is computed from the range R, representing the greatest difference between maximum and minimum value reached by any single component (north, east, or vertical) measured at each of 13 magnetometer stations over a 3-hour period (*Bartels et al.*, 1939). R is converted to K using pseudo-logarithmic scales which were developed individually for each station and given in *Bartels et al.* (1939), and Kp is computed as the mean of the K values from the individual stations (*Lincoln*, 1967). The 13 magnetometer stations used have geomagnetic latitudes ranging from 54 to 63 degrees (*Rostoker*, 1972, *Mayaud*, 1980). Because it is obtained from the magnitude of variations at multiple magnetometer stations, Kp is typically interpreted as a measure of overall geomagnetic activity. However, because the stations used within or just equatorward of the auroral zone, Kp is particularly sensitive to magnetospheric convection and to the latitude of auroral currents (*Thomsen*, 2004). Kp has historically been reported with fractional values denoted with "+" and "−" symbols, with e.g. 4+ indicating $4\frac{1}{3}$ and 4− indicating $3\frac{2}{3}$. Since the "+" and "−" notation would complicate presentation and analysis, Kp values in this dissertation are presented as purely numerical values, where the "+" and "−" components are represented as decimals rounded to the nearest tenth, i.e., "4−"=3.7, "4+"=4.3, etc. The Kp index takes values from 0 to 9, with 0 representing minimal activity, and 9 representing exceptionally strong activity.

The Sym-H index was described by *Iyemori* (1990) and is designed to measure the strength of currents circulating azimuthally around the Earth's dipole axis. It is an improvement on the earlier Dst index (e.g. *Kertz*, 1958, *Hendricks and Sugiura*, 1967, *Sugiura and Poros*, 1972), using a larger number of magnetometers and a higher

time resolution. *Wanliss and Showalter* (2006) showed that despite the differences in how Sym-H and Dst are calculated, Sym-H can effectively be used as a high-resolution substitute for Dst. Sym-H and Dst are widely interpreted as measures of ring current strength, but have been shown to be sensitive to other currents as well (see e.g. *Maltsev*, 2004, and references therein), and the contributions from these other currents can be significant or even dominant during disturbed conditions (e.g. *Ohtani et al.*, 2001, *Liemohn et al.*, 2001, *Ganushkina et al.*, 2004, *Kalegaev et al.*, 2005, *Dubyagin et al.*, 2014). Both are computed from the north-south components of the fields measured by low-latitude magnetometers. During quiet time, the Sym-H index typically takes values near zero (either positive or negative, with magnitudes less than about 20 nT). During geomagnetic storms the Sym-H index becomes more negative in response to an intensification of the ring current, reaching a minimum of -50 to -200 nT or more depending on the strength of the storm.

The AL (auroral lower) index was introduced in *Davis and Sugiura* (1966), and is designed to measure the strength of the westward electrojet, a current that forms in the ionosphere when field-aligned currents from the magnetosphere enter and exit the ionosphere. This occurs primariliy during substorms, which are discussed in detail in Section 1.2.3.4. The AL index represents the minimum of the deviations from background conditions (i.e., time variation in the field after quiet-time diurnal variations are removed) observed in the north-south component at any of 10 magnetometer stations in the auroral zone (though alternative versions exist that use a larger number of magnetometers). As a result of their location in the auroral zone, these magnetometers respond strongly to the electrojet current produced by substorms, which produces a southward deviation at magnetometer stations located beneath the current. The AL index usually takes negative values, with a relatively small magnitude during quiet conditions and with magnitudes of up to thousands of nT during active periods.

1.2.3.3 Geomagnetic Storms

A geomagnetic storm is the magnetospheric response to strong solar wind driving. Periods of elevated driving typically begin with the arrival of a shock front in the solar wind, followed by a sustained period of elevated wind speeds, and this is accompanied by changes in solar wind density or temperature, as well as changes in the strength or direction of the IMF. Strong solar wind driving can take a variety of forms including that of a coronal mass ejection (CME) or a corotating interaction region.

CMEs occur when closed field line regions in the solar atmosphere reconnect with themselves, resulting in an explosive release of plasma into the solar wind. The CME propagates as a single, large mass, contained by its own magnetic field structure (e.g. *Gosling et al.*, 1991). Within the CME, the plasma is characterized by typically lower densities and stronger magnetic fields compared with the surrounding solar wind (e.g. *Burlaga et al.*, 1981).

Corotating interaction regions (often abbreviated CIR) are formed when high speed streams from the sun overtake slower plasma, resulting in the formation of intense (up to 30 nT) magnetic fields (*Gonzalez et al.*, 1999). They were originally identified and named by *Smith and Wolfe* (1976) using observations from Pioneer 10 and 11. Because the high speed streams originate from relatively long-lived features on the solar surface, they exhibit a periodicity corresponding to the sun's 27-day rotation period (*Mursula and Zieger*, 1996).

Whether caused by a CME, CIR, or some other phenomenon, the arrival of a solar wind disturbance at the magnetopause signals the start of the storm. The amount of energy entering the magnetosphere increases as a result of stronger solar wind driving due strong southward IMF, higher solar wind speed, or both. As was discussed at the beginning of Section 1.2.3, southward IMF enables rapid reconnection to occur at the magnetopause, increasing the amount of energy and plasma entering the magnetosphere from the solar wind. At the same time, increased flow velocities transport

magnetic flux to the magnetopause at a higher rate, increasing the reconnection rate further.

In many geomagnetic storms, the initial effect of the increased solar wind driving (that is, the southward IMF and/or higher flow velocity) is a sudden compression of the bow shock and magnetopause, accompanied by an intensification of the Chapman-Ferraro current (e.g. *Chapman and Ferraro*, 1931, 1940, *Ferraro*, 1952). These responses are collectively called the storm sudden commencement (SSC), and result in abrupt changes in magnetic fields at the surface of the Earth, including a northward shift in magnetic fields near the magnetic equator (e.g. *Dessler et al.*, 1960, *Burlaga and Ogilvie*, 1969). The Sym-H index becomes abruptly more positive during the storm sudden commencement. Although the sudden commencement is a common feature at the beginning of storms, storms can occur without a sudden commencement, and sudden commencements can occur without being followed by a geomagnetic storm (e.g. *Burlaga and Ogilvie*, 1969, *Burton et al.*, 1975).

After the storm sudden commencement, the increased solar wind driving (either more strongly southward IMF, higher speed, or both) causes an increase in magnetospheric convection in the manner described by *Dungey* (1961). This increased convection causes an intensification of night-side reconnection, which in turn increases the rate at which particles are injected into the inner magnetosphere, and intensifies the ring current (e.g. *Burton et al.*, 1975). The initial phase, during which the ring current intensifies, can take anywhere from 10 minutes to 8 hours (*Akasofu and Chapman*, 1963). This is followed by the main phase of the storm, during which the ring current strength continues to be elevated (*Akasofu and Chapman*, 1963). The main phase typically lasts about 8-9 hours, but may range from very brief (under an hour) to longer than a day (*Yokoyama and Kamide*, 1997). The increased ring current strength causes a southward shift (i.e. weakening) of magnetic fields at the surface of the Earth, and causes the Sym-H index to become strongly negative.

Eventually the solar wind returns to something closer to average conditions, and the period of increased convection stops, causing the storm to transition into the recovery phase. The magnetopause expands outward, and the rate at which new particles are injected into the ring current also decreases (*Perreault and Akasofu*, 1978). With particles lost from the ring current no longer being replenished, the ring current gradually decays, causing the surface magnetic field to return to normal and the Sym-H index to increase toward zero (e.g. *Williams and Lyons*, 1974, *Liemohn et al.*, 1999). This process can take between a few hours to several days (*Yokoyama and Kamide*, 1997).

1.2.3.4 Magnetospheric substorms

Another major form of activity within the magnetosphere is the magnetospheric substorm, first described in detail in *Akasofu* (1964). A substorm occurs when solar wind energy is stored in the magnetotail in the form of an unstable stretched magnetic field configuration, and then released explosively. As in the Dungey cycle, dayside reconnection during southward IMF causes magnetic flux to enter the magnetotail. However, rather than dissipating immediately due to reconnection, the flux builds up and then is released in a rapid burst of reconnection.

Substorms occur in three phases, termed growth, expansion, and recovery (e.g. *Voronkov et al.*, 2003, *Akasofu*, 2015).[1] During the growth phase, magnetic energy and flux accumulates in the magnetotail. During the expansion phase, this energy is released abruptly, and the energy release is observed in the form of a sudden Earthward flow of energetic particles from the tail, and the development of field-aligned currents leading to the intensification of the auroral electrojet current. During the recovery phase, the magnetosphere returns to its pre-substorm configuration.

The field-aligned currents formed by a substorm connect the magnetotail to the

[1] *Akasofu* (1964) and other early papers describe the process as having two phases, expansion and recovery. The growth phase was first mentioned in *McPherron* (1970).

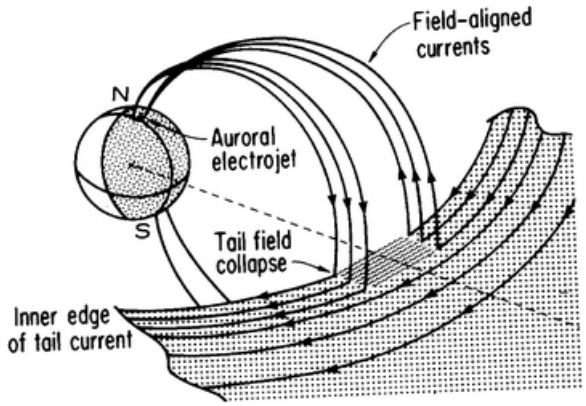

Figure 1.6: The substorm current wedge. (From *McPherron*, 2015.)

auroral-zone ionosphere, forming the substorm current wedge (e.g. *McPherron*, 1972, *McPherron et al.*, 1973, *Kepko et al.*, 2015). A schematic of these currents is shown in Figure 1.6. The figure shows a portion of the cross-tail current being diverted toward the Earth in a pair of field-aligned currents, one Earthward from the post-midnight sector and the other tailward in the pre-midnight sector. The field-aligned currents close through the auroral-zone ionosphere, contributing to the auroral electrojet.

Field-aligned currents produce magnetic signatures that can be detected from the ground. The integrated effect of the field-aligned currents can be seen in midlatitude magnetometers, where a northward shift in the magnetic fields, called a "midlatitude positive bay" is detected (e.g *Akasofu and Meng*, 1969, *Meng and Akasofu*, 1969, *McPherron*, 1972). The auroral electrojet produces a southward shift in the magnetic field on the ground directly below where the current forms, which can be seen in the AL index as a sharp negative diversion called a "negative bay" (e.g. *Akasofu and Meng*, 1969, *Meng and Akasofu*, 1969, *Kamide et al.*, 1974).

The Earthward injection of particles produced by a substorm can be observed at geosynchronous orbit (e.g. *Lezniak et al.*, 1968, *DeForest and McIlwain*, 1971, *Kamide et al.*, 1974, *Cayton et al.*, 1989). Some of these particles enter the ionosphere in the auroral zone, where they cause a brightening and expansion (in latitude) of the aurora

which is observed during the expansion phase (e.g. *Akasofu*, 1960, *Liou et al.*, 1997, *Voronkov et al.*, 2003, *Frey et al.*, 2004).

The rapid release of energy from the magnetotail during a substorm can be explained by several models. Among the most important are the near-Earth neutral line model, in which the energy is released through a sudden increase in reconnection in the magnetotail, and the current disruption model, in which a plasma instability in the magnetotail causes a portion of the cross-tail current to be redirected into field-aligned currents to form the substorm current wedge.

The near-Earth neutral line model is illustrated in Figure 1.7. The top half of Figure 1.7 shows the magnetosphere near the end of the growth phase. There is a significant accumulation of magnetic flux in the magnetotail, but no reconnection occurs to dissipate this flux. The bottom half of Figure 1.7 shows the magnetosphere at the onset of the expansion phase, in which flux is released through reconnection in the tail. The reconnection results in the formation of a plasmoid, that is, a mass of plasma and magnetic field, tailward of the reconnection region. Outflow from the reconnection region causes the plasmoid to move tailward. At the same time, plasma and magnetic field lines are injected Earthward from the reconnection site. This causes several effects, including dipolarization (a reduction in the stretching of nightside magnetic field lines), and the injection of energetic particles along high-latitude magnetic field lines toward the auroral zone.

The current disruption model was originally described in *Chao et al.* (1977). In this model, ions flowing across the current sheet develop an instability, causing an increase in resistivity within the current sheet. This causes a disruption of the cross-tail current, resulting in the redirection of a portion of the current along field lines. The plasma instability explains the Earthward injection of particles, while the resulting increase in resistivity and disruption of current explains the formation of the substorm current wedge. Proponents of the current disruption model have suggested that sub-

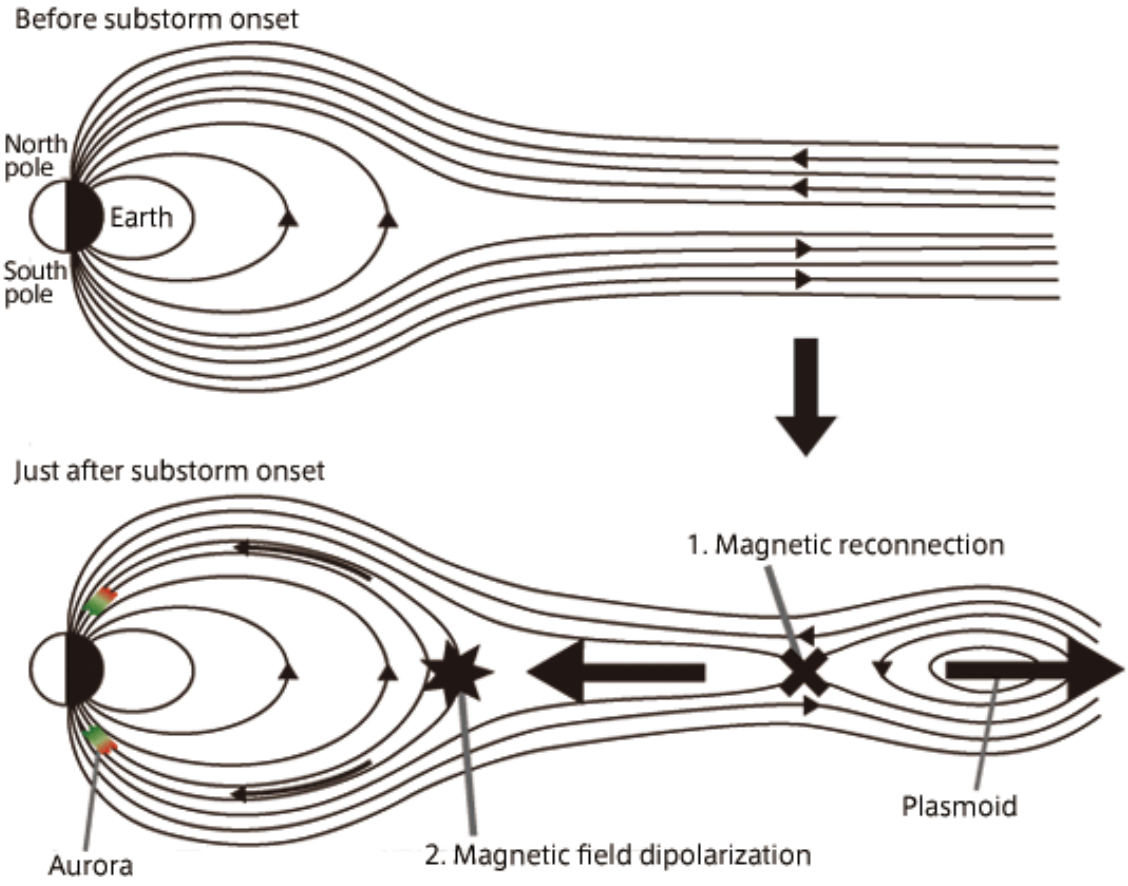

Figure 1.7: An illustration of plasmoid formation and release. (From `http://www.isas.jaxa.jp/e/forefront/2010/miyashita/02.shtml`.)

storms are not initiated by reconnection but rather that reconnection develops later as a result of the effects initiated by the substorm.

1.3 Motivation

Geomagnetic storms and substorms can have profound effects on infrastructure. Spacecraft may be affected by surface charging, single-event upsets, total dose effects, and increased drag, all of which can be exacerbated by storms and substorms (e.g. *Wilkinson*, 1994, *Koons and Fennell*, 2006). Storms and substorms cause fluctuations in magnetic fields on the ground, which can result in geomagnetically induced currents in long-distance conductors such as power transmission lines and oil pipelines (e.g. *Campbell*, 1980, *Ngwira et al.*, 2008, *Pulkkinen et al.*, 2017). In some cases such currents can become strong enough to damage or destroy transformers or other components of the power grid. A notable example is the 1989 failure of the Hydro-Quebec power network due to a geomagnetic storm (*Boteler*, 2001, *Bolduc*, 2002). In the case of oil pipelines, geomagnetically induced currents can increase corrosion and reduce the lifetime of the pipes (e.g. *Campbell*, 1980). Geomagnetic storms are also associated with radiation hazards for astronauts and for air crews and passengers in arctic regions. For instance, *Mertens et al.* (2010) showed that the penetration of solar energetic particles to the atmosphere can increase by up to a factor of 2 during storm conditions due to changes in the magnetic fields in the magnetosphere. Storms and substorms can also substantially alter the structure and composition of the ionosphere, degrading or disrupting radio communications between spacecraft and the ground, causing outages for activities relying on satellites for communication and navigation (e.g. *Skone and de Jong*, 2000, *Ledvina et al.*, 2002). Finally, air-to-ground and ground-to-ground radio communications in the HF (high frequency) and sometimes the VHF (very high frequency) bands can be disrupted by geomagnetic storms and substorms (e.g. *Allen et al.*, 1989, *Blagoveshchensky and Borisova*, 2000).

Numerical models currently exist that are capable of predicting many of the dynamics of geomagnetic storms. Much like terrestrial weather forecast models, such models are used to produce forecast products that enable operators of spacecraft, aircraft, and power grids to anticipate and respond to space weather hazards. For instance, the SWMF (Space Weather Modeling Framework) (*Tóth et al.*, 2005, 2012) is currently used operationally at the NOAA (National Oceanographic and Atmospheric Administration) SWPC (Space Weather Prediction Center). (See for instance `https://www.swpc.noaa.gov/news/announcing-geospace-model-version-15`.) A major difference between these models and those used for terrestrial weather forecasts is that the lead times of SWMF simulations are dramatically shorter, sometimes as little as a few tens of minutes, compared with terrestrial weather models which can predict up to 10 days in the future. This is because of the need for solar wind observations to provide input to space weather models.

Besides the short lead times, the SWMF forecasts are lacking in several important respects. While the SWMF predicts the large-scale effects of storms such as changes to the ring current fairly accurately, it is not currently used to predict specific effects such geomagnetically induced currents or the fluxes of particles that cause single-event upsets and surface charging.[2] SWPC currently provides products using empirical models for this purpose, such as the *Baker et al.* (1990) model which predicts the fluxes of relativistic electrons that can contribute to spacecraft anomalies, and the *O'Brien* (2009) model which predicts spacecraft anomalies themselves (See `https://www.swpc.noaa.gov/products/relativistic-electron-forecast-model` and `https://www.swpc.noaa.gov/products/seaesrt`). However, both models are limited to providing predictions at geosynchronous orbit, based on a single input (solar wind speed in the case of *Baker et al.* (1990) and Kp index in the case

[2]While the MHD (magnetohydrodynamic) model of SWMF lacks the ability to track individual particle fluxes directly, the MHD solution could be used in combination with other models to provide predictions of particle fluxes and their effects.

of *O'Brien* (2009)). The simplicity of these models contributes to their practicality, but it also implies that many important physical processes are not included.

One of the obstacles for more widespread adoption of physics-based models in space weather forecasting is that efforts to validate such models have been somewhat limited in scope. The selection of SWMF for operational use at SWPC was the result of a validation effort involving six storm events, described in *Pulkkinen et al.* (2013). Relatively little testing was done for quiet conditions. More extensive validation efforts, incorporating a wider variety of conditions, would increase confidence in the model and provide more information on its strengths and limitations. The operational use of SWMF at SWPC will provide a large volume of data that can be used for this purpose, but further testing using different settings of the model and different combinations of model components is necessary if improvements are to be made.

One area for improvement in magnetospheric models is to develop better capabilities for predicting subtler phenomena than the major large-scale effects of large geomagnetic storms. Magnetospheric substorms present a particular challenge in this regard. In contrast to geomagnetic storms, which consist of a reasonably prompt response to a fairly large disturbance in the solar wind, with the recovery phase beginning when the disturbance subsides, the relationship between solar wind driving and substorm onset and recovery is more subtle and complex. Attempts have been made to identify specific triggers in the solar wind that are responsible for substorm onset (e.g. *Caan et al.*, 1977, *Rostoker*, 1983, *Lyons et al.*, 1997). However, more recent research has cast doubt on the idea of substorm triggering. Some authors have concluded that a fraction of substorm onsets are triggered (e.g. *Hsu and McPherron*, 2003, 2004), while others have found evidence that substorm onset is normally independent of any specific solar wind trigger (e.g. *Morley*, 2007, *Freeman and Morley*, 2009, *Johnson and Wing*, 2014).

While the indirect relationship between solar wind driving and substorm onset

makes it challenging to develop a predictive model for substorms, the benefits of doing so are significant. Like geomagnetic storms, substorms produce magnetic perturbations that can lead to geomagnetically induced currents (e.g. *Campbell*, 1980, *Pirjola et al.*, 2000), can influence spacecraft surface charging (e.g. *DeForest*, 1972, *Leach and Alexander*, 1995), as well as affect radio communications and navigation (e.g. *Blagoveshchensky and Borisova*, 2000, *Skone and de Jong*, 2000). They can also contribute to damage associated with storm events: For instance, the 1989 Hydro-Quebec event was associated with a substorm that occurred in conjunction with a geomagnetic storm (*Boteler*, 2001). As a result, the development of a practical forecast capability for substorms could provide significant utility in terms of helping to prevent damage and disruption to infrastructure caused by substorm-associated particle injections and current systems.

The objective of validating a model for substorm prediction is complicated by the lack of a community consensus around how to properly identify a substorm. This problem has been discussed in the literature, for instance *McPherron and Chu* (2017) noted the lack of a universally agreed upon definition for a substorm, nor a definitive list of substorm onsets to compare with. One of the factors contributing to this is that substorms may be identified by numerous methods, using different types of observations, each of which carries its own risks of missed identifications and false positive identifications. For instance, the auroral electrojet current can be highly localized and may produce little or no response in the AL index if the current closes in a region without magnetometers to detect it (*Newell and Gjerloev*, 2011a). On the other hand, negative bays can occur in the AL index due to storm sudden commencements and pseudobreakups (e.g. *Heppner*, 1955, *Sugiura et al.*, 1968, *Koskinen et al.*, 1993, *Ohtani et al.*, 1993, *Aikio et al.*, 1999). Thus, a prerequisite for validating a model for substorm prediction is the development of a robust procedure for substorm identification.

Substorms have additional utility as a test case for magnetospheric models. Substorms represent one of the more complex dynamical processes that occur within the magnetosphere, depending not only on magnetospheric driving conditions but also on the past history of the system. To accurately predict substorm dynamics requires an accurate representation of the magnetospheric state prior to and during substorm onset. Depending on the class of model, this may include the magnetic field geometry, plasma populations, and current systems. The amount of resistivity in the magnetotail, which controls the reconnection rate and formation of field-aligned currents, must also be incorporated in some way, and must be reasonably close to reality. Depending on the class of model, the ability to model substorms requires incorporating several (or perhaps all) of these factors. Since many of these same factors influence other processes such as geomagnetic storms and even the quiet-time behavior of the magnetosphere, efforts to model substorms may lead to capturing the dynamics of other magnetospheric processes with higher fidelity.

An important aspect of the magnetospheric state, particularly prior to substorm onset, is the degree of field line stretching in the magnetotail. It is believed that the magnetotail becomes more stretched than usual just prior to substorm onset and plasmoid formation, and the details of this stretching likely play an influential role in the onset and development of the substorm. In addition, the interaction between the magnetosphere and the auroral-zone ionosphere plays a key role in the evolution of substorms, and to properly model this interaction requires an accurate representation of the magnetic field lines along which the interaction occurs. As a result, the degree to which a model can reproduce the magnetotail field may have a substantial affect on its ability to reproduce substorm dynamics.

Unfortunately, direct in situ observations of the magnetotail field are not always available, and when such observations are available they come from at most 8-10 spacecraft, each of which provides a single point observation at any given time. This

seriously limits the ability to determine magnetic field stretching and other aspects of the magnetotail field geometry. An alternative is to use IB (isotropic boundary) observations to estimate the amount of magnetotail stretching, as was originally proposed in *Sergeev et al.* (1993). These can serve as an additional test of the accuracy of the magnetotail field in a model. The complexity of substorm dynamics may preclude the use of the IB to probe magnetic field geometry during the substorm expansive phase, but it can be used to determine the amount of stretching during quiet intervals or during the substorm growth phase. Even for quiet periods, the use of the IB as a probe of magnetic field geometry suffers from significant limitations. First, it has been shown that the IB latitude is related to the parameter $K = \frac{R_c}{r_g}$, the ratio of the local field line radius of curvature to the particle's effective gyroradius. This is because when R_c is close to the r_g or smaller, the affected particles experience substantially different magnetic fields as they moves through their gyro motion. When this occurs condition for adiabaticity, (slowly varying magnetic field) is no longer satisfied, and the first adiabatic invariant (Equation 1.6) is no longer conserved. When this occurs, the particles' pitch angles Θ may change, possibly resulting in an equatorial pitch angle that falls within the loss cone, i.e., pitch angle scattering. So, CSS can occur if K falls below some threshold. However, the threshold condition for K has significant uncertainties which have not been fully quantified, with published estimates ranging from $K = 1$ (*Delcourt et al.*, 1996) to $K = 33$ (*Ilie et al.*, 2015). Second, the IB is only an indicator of field line stretching when it is formed by the CSS mechanism. An accounting for uncertainty in the K threshold condition and a means to determine when CSS is the responsible IB formation process are both required before the IB method can be used reliably for testing the accuracy of a model's field geometry.

1.4 Objectives

The overarching objective of this work is to better understand the dynamics of the magnetotail during all conditions, and to identify paths toward improved predictive capabilities for those dynamics. This will be accomplished by simulating quiet, substorm, and storm conditions using the SWMF, with the model output compared with observational data both to validate the model and to study magnetospheric dynamics. IB observations will be used in conjunction with SWMF simulations and empirical magnetic field models to further constrain the range of K associated with CSS, and the conditions under which CSS is responsible for IB formation.

Specific objectives contributing to this main goal include:

1. **Further the validation of SWMF by testing a realistic mix of storm and quiet conditions with a variety of model configurations.** This is addressed primarily in in Chapter III, which presents simulations of a one-month period using SWMF using three different configurations testing different grid geometries and model couplings. The model output is compared with observed values of Kp, Sym-H, AL, and CPCP from the same time period. Additional validation efforts are presented in Chapters IV, V, and VI.

2. **Provide better constraints on the possible range of K associated with IB formation by CSS.** This is addressed in Chapter IV, which describes efforts to estimate K using the SWMF and using empirical models during quiet conditions when CSS is expected to be the operative mechanism. A new correction procedure was developed to remove the major effects of model errors on the K estimates.

3. **Test the accuracy of magnetotail stretching in SWMF.** This is addressed for quiet-time conditions in Chapter IV and for storm-time conditions in Chapter V. In both cases, the magnetotail stretching is tested by comparison to in

situ satellite observations and by estimating K associated with IB observations.

4. **Test what fraction of storm-time IB's are associated with CSS.** This is addressed in Chapter V, which presents results of categorizing model-derived K values, corrected using satellite observations, as being the result of CSS or EMIC based.

5. **Develop improved procedures for substorm identification.** This is addressed in Chapter VI, which presents a framework for substorm identification that aims to reduce false positive and missed identifications by combining onset times identified using multiple datasets. The procedure is applied to both observational data and simulation output.

6. **Determine whether consistent substorm prediction is possible with MHD, and test the accuracy of such predictions.** This is addressed in Chapter VI, which applies the framework for substorm identification mentioned above to produce lists of substorm onset times. The onset times are then used to compute skill scores evaluating the model's ability to predict whether substorms occur within given time intervals. Confidence intervals are computed to test whether these skill scores are statistically significant.

Throughout the work, multiple configurations of the SWMF are used, varying grid geometries, couplings between components, and other settings. This makes it possible to determine how the SWMF's output varies with such settings, and will help to identify paths for improvement in SWMF's ability to predict phenomena such as substorms and magnetotail stretching. Chapter VII provides a summary of the findings, and identifies paths for further research, both to gain new insights into magnetospheric dynamics and to develop better forecasting capabilities for magnetospheric processes and phenomena that depend on them.

CHAPTER II

The Space Weather Modeling Framework

For decades, computational models have been essential tools for understanding plasma processes (e.g. *Jaggi and Wolf*, 1973, *Kamide and Matsushita*, 1979, *Richmond et al.*, 1980, *Lyon et al.*, 1981, *Spiro et al.*, 1982, *Foster*, 1983). When applied to the space environment, specialized models are often created for simulating specific environments or plasma populations. For instance, a number of models have been created specifically for the inner magnetosphere (e.g. *Jordanova et al.*, 1996, *Fok et al.*, 2001, *Toffoletto et al.*, 2003, *Liemohn et al.*, 2004, *Zaharia et al.*, 2006, *Ilie et al.*, 2012), and similarly for the ionosphere (e.g. *Dickinson et al.*, 1981, *Hajj et al.*, 2004), with further divisions between the low-latitude (e.g. *Huba et al.*, 2000) and high-latitude ionosphere (e.g. *Spiro et al.*, 1982, *Weimer*, 1995).

In region-specific or population-specific models, the contributions from other regions or plasma populations may be ignored, or modeled using simplistic models. In the last two decades it has been recognized that specific regional models such as those mentioned in the previous paragraph often fail to account for important interactions between disparate regions, plasma populations, and length scales. This has led to the development of coupled systems of models which incorporate two or more regional models (e.g. *Janhunen*, 1996, *Raeder et al.*, 1998a, *Wiltberger et al.*, 2004).

One of these coupled systems of models is the Space Weather Modeling Framework

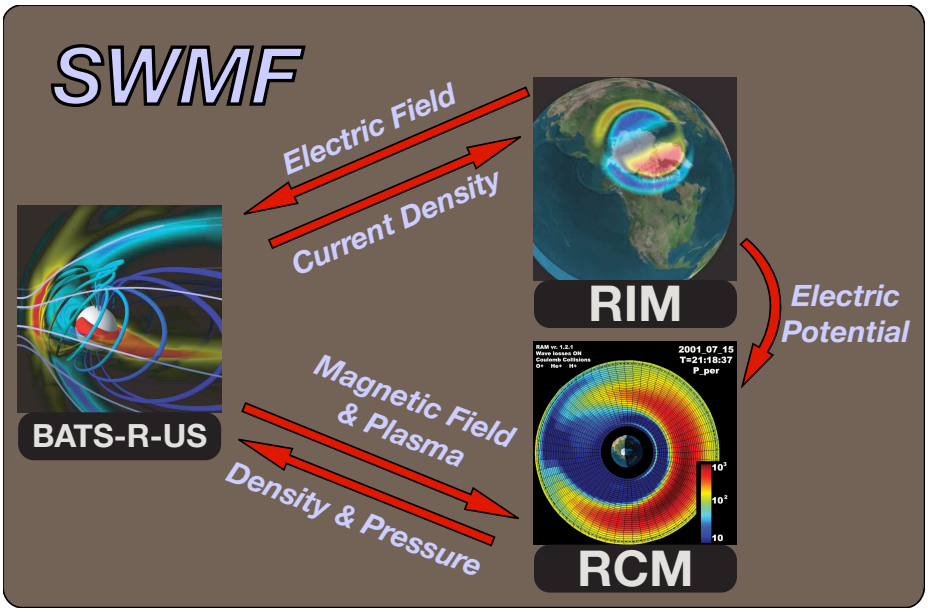

Figure 2.1: Illustration of the models (components within SWMF) and couplings in use. Arrows denote the information that is passed between the components.

(SWMF, *Tóth et al.*, 2005), which was used to produce most of the results in this dissertation. SWMF incorporates multiple regional models, providing capabilities to simulate the solar corona and heliosphere, and magnetospheres throughout the solar system. For simulating the magnetosphere, SWMF provides the Block Adaptive Tree Solar-wind Roe-type Upwind Scheme (BATS-R-US, *Powell et al.*, 1999, *De Zeeuw et al.*, 2000) magnetohydrodynamic (MHD) code. In typical usage, BATS-R-US is coupled with the Ridley Ionosphere Model (RIM, *Ridley and Liemohn*, 2002, *Ridley et al.*, 2004). BATS-R-US and RIM can be optionally coupled with one of several inner magnetosphere models, of which the Rice Convection Model (RCM, *Wolf et al.*, 1982, *Sazykin*, 2000, *Toffoletto et al.*, 2003) is used in this dissertation.

Figure 2.1 illustrates the coupling between the BATS-R-US, RCM, and RIM. The couplings are as follows:

- BATS-R-US MHD delivers magnetic field and plasma moments to RCM
- RCM provides plasma density and pressure to BATS-R-US

- BATS-R-US sends current density to RIM
- RIM delivers electric field to BATS-R-US
- RIM delivers electric potential to RCM

The remainder of this section describes the individual models in more detail along with the manner in which information is shared between them.

2.1 BATS-R-US MHD Solver

BATS-R-US is used to solve for plasma motion in the solar corona and heliosphere, as well as the magnetosphere. It solves the ideal MHD equations, which are an idealized representation of the plasma which assumes charge neutrality and thermal equilibrium, and neglects diffusion, viscosity, and resistivity.[1] This enables the plasma motion to be described using the Euler equations of fluid dynamics, consisting of conservation laws for mass, energy, and momentum, along with a subset of Maxwell's equations. The theory of ideal MHD is described only briefly here; more detailed discussions can be found in a number of books including (*Gombosi*, 1998). The ideal MHD equations as they are implemented in BATS-R-US are

$$\frac{\partial \rho}{\partial t} + \nabla \cdot (\rho \mathbf{u}) = 0 \tag{2.1}$$

$$\frac{\partial \rho \mathbf{u}}{\partial t} + \nabla \cdot \left(\rho \mathbf{u}\mathbf{u} + p_{tot}\mathbf{I} - \frac{\mathbf{B}\mathbf{B}}{\mu_0} \right) = -\frac{1}{\mu_0}\mathbf{B}\nabla \cdot \mathbf{B} \tag{2.2}$$

$$\frac{\partial E}{\partial t} + \nabla \cdot \left((E + p_{tot})\,\mathbf{u} - \frac{1}{\mu_0}\mathbf{B}\mathbf{B} \cdot \mathbf{u} \right) = -\frac{1}{\mu_0}(\mathbf{u} \cdot \mathbf{B})\nabla \cdot \mathbf{B} \tag{2.3}$$

$$\frac{\partial \mathbf{B}}{\partial t} + \nabla \cdot (\mathbf{u}\mathbf{B} - \mathbf{B}\mathbf{u}) = -\mathbf{u}\nabla \cdot \mathbf{B} \tag{2.4}$$

[1] BATS-R-US is also capable of solving several forms of non-ideal MHD equations, which relax some of these assumptions, but these are not used in the work presented in this dissertation.

In these equations ρ is the mass density, $\mathbf{u}$ the bulk velocity, E the internal energy, and $\mathbf{B}$ is the magnetic field. p_{tot} is the thermal plus magnetic pressure, given by

$$p_{tot} = p + \frac{B^2}{\mu_0}. \tag{2.5}$$

Equation 2.1 is the continuity equation, representing mass conservation. Equations 2.2 and 2.3 are the conservation equations for energy and momentum, respectively. Equation 2.4 is obtained from the induction equation (Equation 1.1) under the assumption of low resistivity.

Note that the right hand sides of Equations 2.2-2.4 all contain $\nabla \cdot \mathbf{B}$ source terms. According to the Maxwell equations, these terms should equal zero. However, in the numerical approximation this is not guaranteed. Moreover, retaining the $\nabla \cdot \mathbf{B}$ terms makes the system symmetrizable, which is useful in constructing a numerical approximation because it causes entropy to be conserved and also makes the system Gallilean invariant (*Powell et al.*, 1999). One of the consequences of this is that $\nabla \cdot \mathbf{B}$ is passively convected through the system, which means that $\nabla \cdot \mathbf{B}$ will remain small as long as the initial and boundary conditions are divergenceless in $\mathbf{B}$.

Equations 2.1-2.4 are given in the conservative form, that is, each is in the form of a time rate of change of a conserved quantity, which because it is conserved, must equal the divergence of the flux of that same quantity. This formulation is the basis for the finite volume method, which is a common method for solving fluid equations and is used in BATS-R-US to solve the MHD equations. The finite volume method was originally introduced in *Tikhonov and Samarskii* (1962), and was first applied to MHD by *Brio and Wu* (1988). The approach involves estimating fluxes on the faces of each grid cell, which are used to compute the amount of each conserved quantity transported across each cell face within the computational domain. At each face, the same value is subtracted from the losing cell and added to the gaining cell. This approach has the advantage of ensuring that conservation is maintained to within the

numerical precision of the addition/subtraction operations. Fluxes at each cell face are estimated using the MHD equations using schemes based on Roe's approximate Riemann solver (*Roe and Balsara*, 1996). Details of the specific schemes used in BATS-R-US are described in *Powell et al.* (1999) and *Sokolov et al.* (2002).

The space environments that BATS-R-US is typically used to simulate are characterized by vast spatial domains, within which processes interact with each other at highly disparate spatial scales. Simulating the entire magnetosphere or heliosphere at the finest possible spatial scale is extremely costly in terms of computational resources. However, for many problems the finest spatial scales are only important in certain regions. For instance, in studies of the magnetotail such as are presented in this dissertation, the magnetotail itself must be well resolved, as well as the auroral zone near the Earth since it interacts strongly with the magnetotail. However, other regions of the magnetosphere do not need to be resolved in detail.

To reduce the computational cost of simulations, BATS-R-US employs an adaptive mesh refinement (AMR) grid. This approach involves the use of multiple grids with varying resolution, similar to multigrid methods (e.g. *Fedorenko*, 1962) but without the use of calculation on courser grids to correct finer ones (instead the solution is computed on the fine grid directly). The AMR implementation in BATS-R-US is described in *Stout et al.* (1997) and *Powell et al.* (1999), and is based on earlier work by *Berger and Jameson* (1985), *Berger* (1987), and *Berger and Colella* (1989). The spatial domain is represented as a Cartesian grid.[2] When additional resolution is needed in a given region, regions of the grid may be subdivided to produce double the resolution within a section of the grid, and these regions may be further subdivided as required. This subdivision provides high grid resolution where it is required, while retaining a lower resolution elsewhere. Because the number of computations required per time step is directly proportional to the number of grid cells, the adaptive

[2]Spherical grids can also be used, but Cartesian is typical for magnetospheric applications.

mesh scheme greatly reduces the computational cost compared with a high-resolution uniform grid.

Within the code, the AMR grid is divided into blocks with a uniform number of cells (but with varying linear dimensions), and these are stored in a tree structure as described in *Stout et al.* (1997). These blocks also serve as the organizational structure for parallelism within the code: Each processor is assigned a particular subset of all the blocks within the computational grid, and between iterations data is passed between processors to populate ghost cells along the boundaries of each block.

Most magnetospheric simulations using BATS-R-US, and all the simulations used in this dissertation, use the GSM (geocentric solar magnetospheric) coordinate system. The x axis of this coordinate system lies along the Sun-Earth line, with the positive x direction pointed toward the sun. The z axis is the projection of the Earth's dipole axis into the plane perpendicular to the x axis. This places the dipole axis in the x-z plane. The y axis completes the right-handed system, pointing approximately duskward. Because the dipole axis is tilted approximately 11° relative to the Earth's rotation axis, the GSM coordinate system is non-inertial; relative to an inertial coordinate system it rotates in an oscillatory manner about the Sun-Earth line to stay aligned with the dipole.

All BATS-R-US simulations in this dissertation use a Cartesian grid whose outer boundaries form a cube 256 Earth radii (R_e) in width. The grids are offset in the x direction so that they extends 32 R_e sunward of the Earth and 224 R_e tailward. In the y and z directions the grids are centered around the Earth, extending 128 R_e from the Earth along each of those axes. An inflow boundary condition populated with time-dependent solar wind data is used on the boundary located at x=32 R_e, while the opposite face (at x=-224 R_e) uses an outflow boundary condition. The remaining outer boundaries use a zero-gradient boundary condition. The inner boundary of BATS-R-US is a sphere of radius 2.5 R_E, which is populated by setting a density and

temperature indended to represent typical ionospheric outflow conditions, with the density optionally varied proportional to CPCP (cross-polar cap potential). The flow velocity at the inner boundary is determined by the electric fields computed by the Ridley Ionosphere Model (RIM), which is described in Section 2.3.

The placement of the inner boundary at 2.5 R_E is due to stability limits for the MHD solution. At closer distances to the Earth, the Alfvén speed

$$v_A = \frac{|\mathbf{B}|}{\sqrt{\mu_0 \rho}} \tag{2.6}$$

increases rapidly because of the strong magnetic field imposed by the Earth. At this point the high speed of Alfvén waves becomes the limiting factor for stability of the numerical scheme. As a result, placing the inner boundary closer to the Earth would require a large reduction in the time step in order to maintain stability, greatly increasing the computational cost of the simulation.

In addition to the inner boundary information provided by RIM, BATS-R-US is also coupled with an inner magnetosphere model which solves for particle kinetics on closed field lines. Coupling with these models, as well as some analysis tasks such as isotropic boundary studies presented in Chapters IV and V, requires tracing magnetic field lines through the BATS-R-US grid. The field line tracing is accomplished using parallel algorithms described in *De Zeeuw et al.* (2004) and *Glocer et al.* (2009a).

2.2 Rice Convection Model

The ideal MHD equations solved by BATS-R-US are incapable of representing the gradient and curvature drift described in Section 1.2.1. These processes are of particular importance in the inner magnetosphere, where they are responsible for the formation of the ring current which strongly influences the overall magnetic field as well as playing a crucial role in magnetospheric convection. In addition, since the

drift velocities depend on the particle charge and energy, the use of a single fluid with a single bulk velocity in the ideal MHD equations means that these processes cannot be added simply by adding terms to the momentum equation. Instead, BATS-R-US is coupled with any of several inner magnetosphere models, which solve equations describing the the drift motion of particles on closed field lines.

For most of the simulations in this dissertation, BATS-R-US was coupled to the Rice Convection Model (RCM, *Wolf et al.*, 1982, *Sazykin*, 2000, *Toffoletto et al.*, 2003). RCM represents the particle energy distribution by a finite number of energy and charge states, and the spatial distribution by a set of flux tubes on an ionospheric grid. The particle energy state is represented by

$$\lambda_s = W_s V^{2/3}, \tag{2.7}$$

where W_s is the particle's kinetic energy and $V = \int ds/B$ is the flux tube volume, which is provided by BATS-R-US using the field line tracing routines described in the previous section. The density of particles in a given flux tube and energy state is given by $\eta = n_s V$, where n_s is the number density of particles in a given energy state s. RCM evolves the particle distribution by solving the equation

$$\frac{\partial \eta_s}{\partial t} + \frac{\mathbf{B} \times \nabla \left(\Phi + \Phi_c + \frac{\lambda_s}{q_s} V^{-2/3} \right)}{\mathbf{B}^2} \cdot \nabla \eta_s = -L, \tag{2.8}$$

where Φ is the electric potential in the ionosphere and Φ_c is the corotation potential, and L represents a rate of particle loss (primarily due to charge exchange and precipitation). When used within SWMF, RCM receives Φ through coupling to RIM, and L is set to produce an exponential decay of ring current ions, typically with a decay time constant of 10 hours, a value which was determined by experimentation to produce realistic ring current decay rates within the coupled BATS-R-US/RCM/RIM system.

The method of coupling between BATS-R-US and RCM is described in *De Zeeuw et al.* (2004). Coupling between BATS-R-US and RCM involves integrating along field lines within BATS-R-US to obtain a total volume and mass for each flux tube in the RCM grid, and extracting the temperature and pressure from the BATS-R-US grid at the points where each flux tube crosses the plasma sheet. These values are used to construct a distribution of η_s throughout the RCM domain for initializing RCM, and at the RCM outer boundary for the rest of the simulation. BATS-R-US is also used to determine the boundary between open and closed magnetic field lines, which serves as the outer boundary for RCM. Pressures in the inner magnetosphere are computed as

$$P = \frac{2}{3} V^{-5/3} \sum_s \lambda_s \eta_s, \tag{2.9}$$

and these values are used to correct the pressure in the MHD solution. This process is repeated as the simulation progresses.

2.3 Ridley Ionosphere Model

Certain magnetospheric dynamics depend strongly on the ionosphere. Outflow from the ionosphere contributes to the plasma populations in the magnetosphere, and the magnitude and distribution of ionospheric conductance strongly influences the behavior of field-aligned currents. The latter is addressed, in SWMF, using the Ridley Ionosphere Model (RIM, *Ridley and Liemohn*, 2002, *Ridley et al.*, 2004). RIM provides height-integrated ionospheric conductance and electric potential, given a distribution of field-aligned currents and F10.7 solar radio flux.

RIM obtains the ionospheric potential by solving the equation

$$J_{||} = \left(\nabla_\perp \cdot \left(\Sigma \cdot \nabla \psi \right)_\perp \right), \tag{2.10}$$

where $J_{||}$ is the field-aligned current, Σ is the height-integrated conductivity, and ψ is the ionospheric potential.

The conductivity Σ includes contributions from solar EUV, starlight and galactic sources, auroral precipitation, and polar cap precipitation. Solar EUV flux increases conductance by ionizing neutral particles. EUV flux is estimated using F10.7 radio flux, and the resulting conductances are obtained using empirical formulas from *Moen and Brekke* (1993). Incident radiation from starlight and galactic sources increases conductivity in the same manner as solar EUV, and is added as a constant component.

BATS-R-US does not simulate the energetic particles whose precipitation contributes to the auroral oval, so their fluxes cannot be used to directly compute the conductance. Instead, the conductance is estimated using an empirical relationship between field-aligned current and conductivity. The field-aligned current values are obtained from the inner boundary of BATS-R-US.

Similar to the auroral oval, the polar cap experiences particle precipitation which cannot be directly estimated using BATS-R-US. This precipitation, called "polar rain," is approximately uniform over the polar cap (*Newell and Meng*, 1992). A constant value is added to the conductance over the polar cap to model this effect.

2.4 Summary

The SWMF can be configured in many other ways besides what is described here. In addition to simulating Earth's magnetosphere, BATS-R-US can be used to model the magnetospheres of other planets, or the solar corona and heliosphere. For modeling Earth's magnetosphere, BATS-R-US provides multi-fluid and Hall MHD capabilities, which relax some of the assumptions of ideal MHD. Several other inner magnetosphere models can be used in place of RCM, and additional components can be used to provide more realistic ionospheric outflow or to better model reconnection regions. However, the combination of models described in this chapter is the most

widely used and most well tested for the magnetosphere, and this serves as the baseline for the SWMF simulations used in the remainder of this dissertation.

CHAPTER III

Validation of the model with near-Earth observations

3.1 Introduction

SWMF (Space Weather Modeling Framework) provides a potent combination of models that provides a detailed representation of magnetospheric dynamics that is applicable under a wide variety of conditions. These capabilities naturally make the coupled global MHD (magnetohydrodynamic) and ring current approach attractive for forecasting applications. As discussed in Chapter I, SWMF and its components underwent validation tests prior to SWMF's selection by NOAA (National Oceanographic and Atmospheric Administration) SWPC (Space Weather Prediction Center) for use as an operational forecast model. This was the result of a community validation effort focusing on six storm events, in which three MHD models and two empirical models were evaluated with respect to their ability to predict $\frac{dB}{dt}$ at several ground-based magnetometer stations. The validation effort is described in *Pulkkinen et al.* (2013), and builds from *Pulkkinen et al.* (2010) and *Rastätter et al.* (2011). *Pulkkinen et al.* (2013) found that the SWMF achieved the best predictive skill of the models evaluated, but with the caveat that the predictions delivered by SWMF may not be adequate for some operational uses. A number of follow-up papers have

examined the results of this effort further. *Glocer et al.* (2016) evaluated the models' ability to reproduce the local K index, finding that the SWMF performed especially well in predicting local K. *Welling et al.* (2017) showed that the SWPC events exceeded the range of validity for the empirical ionospheric conductance models used in the participating MHD codes, and that all of the models tended to under-predict surface $\frac{dB}{dt}$, though SWMF less so than the others. *Anderson et al.* (2017) compared the field-aligned currents from the models with those obtained using AMPERE (Active Magnetosphere and Planetary Electrodynamics Response Experiment).

Though unique in its rigorous comparison of multiple models, the scope of *Pulkkinen et al.* (2013) was limited to a small number of storm events. This has been common practice within the MHD modeling community in recent years. Simulations of single storm events constitute a majority of existing MHD papers. Some representative examples include *Raeder et al.* (2001a), which simulated the 14-16 July 2001 "Bastille Day" storm using the OpenGGCM (Open Geospace Global Circulation Model), *Palmroth et al.* (2003), which simulated a major storm from April 6-7 2000 using the the GUMICS-4 (Grand Unified Magnetosphere Ionosphere Coupled Simulation, version 4), *Lopez et al.* (2001) which simulated a March 1995 substorm and a January 1997 storm using the LFM (Lyon-Fedder-Mobarry) MHD solver, and *Kress et al.* (2007) which shows LFM and particle tracing results for the 29 October 2003 storm. MHD models have also been used to study hypothetical extreme events to better understand the possible effects of such events. For instance, *Groth et al.* (2000) simulated a CME (coronal mass ejection) from the sun and the resulting effects on Earth using an early version of BATS-R-US (Block Adaptive Tree Solar-Wind, Roe-type Upwind Scheme), *Ngwira et al.* (2014) simulated the effects of a hypothetical "Carrington-type" space weather event using SWMF, and *Ngwira et al.* (2013) presented SWMF simulations aimed at predicting the effects of the 23 July 2012 CME if it had been directed Earthward.

MHD models have been used to study quiet-time conditions as well. Early work such as *Wu et al.* (1981) and *Ogino et al.* (1992) simulated steady solar wind conditions, while *Raeder et al.* (1998b) modeled time-dependent quiet-time conditions. Some more recent work such as *Welling and Ridley* (2010) has included quiet time periods, although that paper focused primarily on storms. However, these constitute a minority of papers in recent years, and like the storm papers, they tend to cover short periods of time.

Only a few papers to date describe MHD simulations more than a few days in duration. *Guild et al.* (2008) compared in situ plasma sheet observations with MHD output from a 2-month simulation, finding the model generally able to reproduce the gross features of the plasma sheet in a statistical sense. *Zhang et al.* (2011) analyzed the field-aligned current structures and polar cap potentials from the *Guild et al.* (2008) simulations, finding a significant under-prediction of current strength and over-prediction of CPCP (cross-polar cap potential). *Huang et al.* (2010) found an MHD code to be capable of reproducing the statistics of ULF waves in geosynchronous orbit over a 27-day simulation. *Juusola et al.* (2014) compared MHD derived CPCP and auroral index predictions with observations for a 1-year period using *Facskó et al.* (2016)'s 1-year global MHD simulation. That work was accomplished using a large number of short simulations run independently of each other, because the Grand Unified Magnetosphere-Ionosphere Coupling Simulation (GUMICS-4) developed by *Janhunen et al.* (2012) is a single core code. This way the simulation state was effectively re-initialized approximately every 5 hours. *Facskó et al.* (2016)'s simulations were unsuccessful at reproducing a number of aspects of the auroral oval structures, and obtained ground magnetic field perturbations that were weaker than observed by at least a factor of 5 (*Juusola et al.*, 2014). *Facskó et al.* (2016) derived the magnetic footprints by magnetic field mapping from the Cluster SC3 spacecraft using the GUMICS simulation from *Juusola et al.* (2014) and also using the Tsyga-

nenko (T96) model in order to compare two methods. The study showed that the footprints determined using the GUMICS simulation agreed relatively well with the T96 empirical model, however the footprints agreed better in the northern hemisphere than the southern one during quiet conditions. *Wiltberger et al.* (2017) covers a period of nearly a month (March 20 to April 16, 2008), which was chosen because it contains a wide variety of solar wind conditions but no major geomagnetic storms. The results presented in *Wiltberger et al.* (2017) focused on field-aligned currents and CPCP, finding that the simulations reproduced the statistical features of the observed field-aligned current patterns but tended to produce weaker field-aligned currents and higher potentials than the Weimer05 empirical model.

Some focus on storms is no doubt appropriate due to the hazards posed by such events. However, the approach of manually selecting storm events to validate a model can be problematic. Manual selection of storm events can introduce biases since the particular storms chosen may not be representative examples. Furthermore, undue focus of validation efforts on strong storm events could result in a model that is optimized for such events at the expense of moderately disturbed or quiet conditions. This can potentially undermine the model's usefulness as a forecasting tool, since a model designed only to model storms could over-predict or under-predict activity in weakly or moderately disturbed conditions. In the case of over-prediction, this could lead to an elevated false alarm rate for storm conditions. In the case of under-prediction, it could lead to potentially significant activity being missed. In either case, it could erode confidence in the model on the part of forecasters and customers if the model appears to be useful only during times of strong activity.

If a model performs poorly during quiet time conditions, this could be symptomatic of problems that persist during disturbed periods as well. Small deficiencies in a model may in some cases be apparent during quiet time but be difficult to notice during storm time. In addition, quiet-time conditions just prior to a storm may subtly

affect the dynamics of the storm itself. Therefore, improvements to a model's representation of the quiet-time magnetosphere are likely to improve its representation of storm-time dynamics as well.

In the present work, we investigate the capability of the SWMF to deliver accurate predictions of geomagnetic indices and cross-polar cap potential. We include a realistic mix of quiet and disturbed conditions by studying the entire one-month period of January, 2005, rather than a set of selected events. In addition, the use of a single continuous time period for validation reduces any errors caused by a poor initial condition (provided those errors dissipate over time). Finally, use of a single continuous run is more representative of operational forecasting usage, in which a continuous stream of real-time data is fed into the model.

We drive three different configurations of the SWMF (the details of which are described in Section 3.2.1) with solar wind data observed by the ACE (Advanced Composition Explorer) spacecraft. The model's input data is described in more detail in Section 3.2.2. The model provides magnetic field values at a number of ground stations. From these we calculate values of the geomagnetic indices Sym-H, Kp, and AL, as well as CPCP. These quantities were introduced in Chapter I, but they will be described again briefly here. Sym-H is the longitudinally symmetric northward component of six low-latitude magnetometers, typically regarded as a measure of ring current and other current systems. Kp (planetarische Kenziffer) is an index computed from a number of mostly mid-latitude magnetometers and is typically regarded as a general measure of global geomagnetic activity. AL (auroral lower) is computed from the most negative northward component of a set of auroral magnetometers, and is regarded as a measure of auroral zone currents, primarily the westward electrojet. CPCP is the difference between the minimum and maximum electrostatic potential over the polar cap, and provides an indication of the coupling strength between the solar wind and the magnetosphere. The method by which these quantities are com-

puted in the model is described in Section 3.2.3.

After obtaining observed values for the indices and calculating equivalent values from the model, we calculate metrics to measure each model configuration's ability to predict each geomagnetic index, and from these identify strengths and weaknesses of each model configuration. The specific metrics are described in Section 3.2.4. Results for each geomagnetic index are presented and discussed in Section 3.3, and conclusions given in Section 3.5.

3.2 Methodology

3.2.1 Model description

We run the model in three different configurations, summarized in Table 3.1. The SWPC configuration is nearly identical to that used operationally by SWPC (the main differences, besides the input data being historical rather than real-time, being in what output files are written during the run). The other configurations are similar, but use a higher resolution grid and other modifications. The two grids that are used are described in detail in Section A.1.0.1. The switch to the higher resolution grid necessitated other modifications in order to maintain the model's performance with respect to Sym-H. First, the plasma sheet O/H mass density ratio (used in coupling between BATS-R-US and RCM (Rice Convection Model)) is determined adaptively based on the current values of F10.7 flux and Kp index using the empirical model from *Young et al.* (1982), rather than using a fixed ratio as is used in the SWPC configuration. Second, a boundary condition parameter that controls how much the inner boundary density increases as cross-polar cap potential increases (described in *Pulkkinen et al.*, 2013) was reduced from 0.1 to 0.08. These changes result in Sym-H predictions that are similar to the SWPC configuration, and have minimal effect on the other quantities analyzed in this work. Details of the model configuration,

Name	Grid	RCM	Composition model
SWPC	SWPC	Y	Fixed
Hi-res w/ RCM	Hi-res	Y	*Young et al.* (1982)
Hi-res w/o RCM	Hi-res	N	Fixed

Table 3.1: Summary of the model configurations used.

including settings for each component, are described in Appendix A.

3.2.2 Model execution

In order to create a dataset for statistical evaluation of the model, we ran the model for the entire month of January, 2005. Since January occurs during northern hemisphere winter (and relatively near the winter solstice), the Earth's dipole axis was oriented so that the north pole was tilted toward the night side, shifting the magnetotail southward and placing the current sheet below the equatorial plane on average. We repeated this for each of the three configurations described in Section 2 of this chapter. This time period was selected to support a project currently in progress to evaluate the model's capability to predict magnetospheric substorms. Sequences of substorms in January, 2005 were previously studied in *Morley* (2007) and *Morley et al.* (2009), and the period was identified as having a sufficiently large number of substorms to allow statistical analysis with regard to substorm predictions. The month was in the late declining phase of solar cycle 23. Minima, maxima, and medians of observed quantities characterizing the month are shown in Table 3.2. The month includes three geomagnetic storms. The first, on January 7, was the result of a CME (coronal mass ejection) indicated by a small velocity change but a large spike in proton density. The January 7 storm reached a minimum Sym-H of -112 nT. The second storm, on January 16, was the result of a CME indicated by a solar wind velocity increase from 600 to 800 km/s and a large density spike. An additional CME arrived on January 18th, before the completion of recovery from the January 16

	Min	25th percentile	Median	75th percentile	Max
IMF B_z (nT)	-27.97	-1.7	0.28	2.83	30.92
SW u_x (km/s)	318	468	570	672	1055
SW p_{dyn} (nPa)	0.0859	1.53	2.07	3.03	80.62
Kp	0.0	2.0	3.0	4.0	8.0
Sym-H (nT)	-112	-29	-17	-7	57
AL (nT)	-4418	-279	-123	-40	10
CPCP (kV)	6.67	27.0	63.2	77.5	1460

Table 3.2: Minimum, 25th percentile, median, 75th percentile, and maximum for a number of observed quantities characterizing the solar wind conditions and (observed) geomagnetic conditions during the month of January, 2005. These include interplanetary magnetic field (IMF), the x component of solar wind velocity (u_x), the solar wind dynamic pressure (p_{dyn}), the Kp, Sym-H, and AL indices, and CPCP. Components of IMF and solar wind velocity are given in GSM coordinates.

storm. The January 16 storm reached a minimum Sym-H of -107 nT. The third storm was on January 21. The January 21 storm was the result of a CME which resulted in a solar wind speed increase from 600 to 900 km/s and a large density spike. The January 21 storm reached a minimum Sym-H of -101 nT. A final CME arrived on 31 January but did not result in a geomagnetic storm.

To simulate this month, we drive the model using solar wind velocity, magnetic field, density, and temperature, which are used to construct the upstream boundary condition of BATS-R-US. The only other input parameter is F10.7 flux, which is used by RIM in computing ionospheric conductivity (*Ridley et al.*, 2004, *Moen and Brekke*, 1993). In the high-resolution configuration with RCM, F10.7 is also used to compute the oxygen to hydrogen ratio via the *Young et al.* (1982) empirical model.

Solar wind parameters are obtained from the 1-minute OMNI dataset provided by the NASA Goddard Spaceflight Center (GSFC). This is a combined dataset which includes data from multiple spacecraft, although during the time period in question the data came primarily from the ACE spacecraft. The OMNI date is provided "time shifted" to the bow shock nose using the techniques described in *Weimer and King*

(2008). We obtain F10.7 observations from `http://lasp.colorado.edu/lisird/tss/noaa_radio_flux.html`, which combines the historical archive available through the National Centers for Environmental Information (NCEI) with modern measurements managed by NOAA SWPC. The flux values are the 1 AU adjusted flux observed at Penticton, BC (*Tapping*, 2013).

The solar wind data receives some additional processing before being input to the model. In addition to the OMNI data, we use temperatures from the ACE spacecraft, time-shifted by 45 minutes. To simplify some of the post-processing and analysis, only the x component of velocity was used and the y and z components were set to zero. This reduces the motion of the magnetotail so that it remains near the x axis of the grid. Although the y and z components can significantly affect the orientation of the magnetotail, we expect they would have relatively little impact on the geomagnetic indices that are the focus of the present work (see e.g. *Borovsky*, 2012). The x component of the interplanetary magnetic field (IMF) was also set to zero in order to reduce the divergence of the magnetic field in the simulation.

Gaps of less than 1 hour in the OMNI data are filled by linear interpolation. Three gaps of longer duration had to be filled in from other sources. The first of these was on 18 January from 06:11 to 13:52 UT, the second was from 7:14 UT on 20 January to 21:44 on 21 January, and the third was from 01:04 to 09:13 UT on 22 January. These were due to instrument problems that occurred with the Solar Wind Electron, Proton, and Alpha Monitor (SWEPAM) instrument on the ACE satellite in its default mode, which attempts to track the solar wind peak in energy. SWEPAM operates in a second mode approximately once every 1/2 hour, which samples most of the instrument's energy range rather than just the peak (*McComas et al.*, 1998). The data from this secondary mode was used for solar wind density, temperature, and velocity during the gaps in the OMNI dataset. Magnetic fields for the gap periods were available at a 1-minute cadence from the ACE Level 2 data.

Since the ACE spacecraft is located well beyond the upstream boundary of the model, it must be propagated to the upstream boundary in some way. The data obtained from OMNI are provided already time-shifted to the bow shock nose and were used as-is (see `https://omniweb.gsfc.nasa.gov/html/HROdocum.html` for a description of the time shifting algorithm). The ACE SWEPAM data used to fill the gaps on 18-22 January were propagated to the upstream boundary by solving a system of 1-D advection equations:

$$\frac{\partial q_i}{\partial t} = u_x \frac{\partial q_i}{\partial x}. \tag{3.1}$$

Here, q_i denotes one of the solar parameters, and u_x denotes the solar wind velocity in the x direction. The "time shifting" method used to create the OMNI dataset (similar techniques are described in a number of papers such as *Weimer et al.*, 2003, *Weimer*, 2004, *Cash et al.*, 2016) is equivalent to solving Equation 3.1 using the method of characteristics.

In the present work we solve the advection equation using a second-order finite volume method with a minmod limiter and explicit Euler time integration on an evenly spaced 1000-point grid. The time step is adjusted dynamically to maintain a maximum Courant-Friedrichs-Lewy (CFL) number of 0.5. The particulars of this class of numerical schemes are described in a number of references such as *Hirsch* (2007).

Once the runs are completed, we evaluate the model configurations with regard to their ability to predict Kp, Sym-H, AL, and CPCP. Observational data for the Kp index provided by the NOAA National Geophysical Data Center (NGDC) and was obtained through the NASA/GSFC 1-hour OMNI dataset. Observational data for the Sym-H index provided by World Data Center Kyoto was obtained through the NASA/GSFC 1-minute OMNI dataset. Magnetic fields at ground-based magnetometer stations were obtained from SuperMAG (`http://supermag.jhuapl.edu/`

Gjerloev, 2012) and used to calculate the AL index as described in Section 3.2.3. Since no direct observation of CPCP is available, we instead use the Assimilative Mapping of Ionospheric Electrodynamics (AMIE) model, which estimates CPCP based on a number of observational datasets (*Richmond and Kamide*, 1988, *Richmond*, 1992). The Spacepy python library (*Morley et al.*, 2011, *Morley et al.*, 2014) was used for a number of tasks including reading the MHD output and some of the observational datasets.

3.2.3 Predicted quantities assessed

In order to reproduce the geomagnetic indices with the MHD model, the magnetic fields resulting from magnetospheric and ionospheric currents are calculated at various points on the Earth's surface. This is accomplished using a Biot-Savart integral over the entire MHD domain, as well as the height-integrated Hall and Pedersen currents computed by RIM (*Yu and Ridley*, 2008, *Yu et al.*, 2010). From these magnetic fields we obtain equivalents to the geomagnetic indices Kp, Sym-H, and AL.

Although the model Kp could be computed using the model output for the 13 stations used observationally, we instead use a different set of locations. These consist of an evenly spaced ring of 24 points having a constant latitude of 60 degrees. For each of the 24 points, the local K value is calculated using the procedure described in *Bartels et al.* (1939). The K-scale mapping for the magnetometer station Niemegk (also given in *Bartels et al.*, 1939) is applied to all stations. This choice of mapping was found by trial and error to produce the best Kp predictions. Having obtained the local K values for each of the 24 points, the Kp index is then computed as the mean of these local K values, rounded to the nearest one-third. Rather than calculating the model Kp every 3 hours as is done in the observations, the model Kp is calculated using a rolling 3-hour window, and values are output every minute. This rolling 3-hour window ends at the time of each output, so that at the time of the observations

the model's rolling window coincides with the period used to calculate the observed Kp.

Davis and Sugiura (1966), in which AL was first introduced, used a set of 10 magnetometer stations. We instead calculate the AL index from an alternate set of magnetometers, the complete list of which is provided in the supplemental data of *Haiducek et al.* (2017). An identical set of magnetometer locations is used in both the model and observations. Since the Biot-Savart integrals used in the model explicitly exclude the intrinsic field of the Earth, the baseline removal step described in *Davis and Sugiura* (1966) is not necessary for the model output. For the observational data, we use data from SuperMAG which has the baseline signal removed according to the procedures described in *Gjerloev* (2012). The remainder of the AL calculation procedure (following baseline removal) is the same for both model and observations and is implemented as described in *Davis and Sugiura* (1966).

The observed Sym-H index is calculated from a set of near-equatorial magnetometers according to procedures described *Iyemori* (1990) and `http://wdc.kugi.kyoto-u.ac.jp/aeasy/asy.pdf`. The difference between Sym-H and similar indices such as Dst can be used to estimate their uncertainty. *Katus and Liemohn* (2013) found that the difference (measured in RMSE (root mean squared error)) between Sym-H and Dst was 9.1 nT during the period 1985-2005. During the same interval, the RMSE difference between Sym-H and USGS Dst (a 1-minute cadence Dst implementation provided by the U.S. Geological Survey, described in *Gannon and Love*, 2011) was 11.0 nT. Since these very similar indices differ from each other on the scale of 9-11 nT, one could consider model predictions of Sym-H with errors less than 9-11 nT to be indistinguishable from observations.

As with Kp, SWMF provides output for Sym-H. Rather than calculating Sym-H using the set of surface magnetometers used in the observations, SWMF calculates the magnetic perturbation in the direction of the magnetic pole via a Biot-Savart

integration of all currents within the MHD domain about a point at the center of the Earth. Since the magnetic field is calculated at the center of the Earth, the step of averaging in longitude described in *Iyemori* (1990) is not needed. This methodology was validated against storm-time observations in *Rastätter et al.* (2011).

The last quantity we assess is CPCP. CPCP is dependent on the solar wind electric field, the size of the open flux region connecting the polar cap to the magnetopause, and the magnetospheric dynamics that determine the strength of the coupling between those two regions (*Bristow et al.*, 2004, *Lockwood and Morley*, 2004, *Milan*, 2004). Observationally, CPCP must be obtained indirectly, and for the present work we used output from the AMIE model (*Richmond and Kamide*, 1988, *Richmond*, 1992), which computes a potential pattern through an expansion of basis functions chosen by fitting to observations from magnetometers, radar, and spacecraft. CPCP in the model is obtained from the potentials computed by the RIM ionosphere model.

3.2.4 Assessing prediction quality

To give an overall picture of the model's agreement with the observations we calculate accuracy and bias metrics for the entire month, as well as probability distributions, for each predicted quantity. Given a set of observations x_i and corresponding predictions y_i, the error is given by

$$\epsilon_i = y_i - x_i. \tag{3.2}$$

Mean error is defined as

$$\bar{\epsilon} = \frac{1}{n}\sum_{i=1}^{n} \epsilon_i. \tag{3.3}$$

$\bar{\epsilon}$ is a measure of bias; a positive value indicates that the model over-predicts on average, while a negative value indicates that the model under-predicts on average.

An unbiased prediction will be indicated by $\bar{\epsilon}$ at or near zero.

The root mean squared error (RMSE),

$$RMSE = \sqrt{\frac{1}{n}\sum_{i=1}^{n}\epsilon_i^2}, \tag{3.4}$$

provides a measure of the average discrepancy between predictions and observations, independent of the sign of the error. RMSE is always positive and, like $\bar{\epsilon}$, has the same units as the input data. A smaller value for RMSE indicates a more accurate prediction.

Both mean error and RMSE are computed from a mean, and hence their uncertainty can be computed using the formula for computing the uncertainty of a mean:

$$\sigma_{mean} = \frac{\sigma}{\sqrt{n}}, \tag{3.5}$$

where n is the number of points, and σ is sample standard deviation of the points from which the mean is computed (*Taylor*, 1997). Taking σ as the standard deviation of all the points ($std(x)$), the uncertainty of RMSE is estimated by

$$\sigma_{RMSE} = \sqrt{\frac{std(\epsilon^2)}{\sqrt{n}}} \tag{3.6}$$

and the uncertainty of mean error is estimated by

$$\sigma_{\bar{\epsilon}} = \frac{std(\epsilon)}{\sqrt{n}}. \tag{3.7}$$

All of the above metrics require a set of observations x_i and corresponding predictions y_i. Since the model is configured to produce output at specific times that may or may not coincide with the observations, linear interpolation of the model output is used to obtain values that correspond to the exact time of the observations. In the case of Kp, the model produces output at a much higher time resolution than

the available observations, and this process results in a set of Kp predictions which correspond with the observations in terms of the number of values and in terms of the time range of the magnetometer data from which those values are derived.

Summarizing bias or accuracy with a single number provides a useful summary of a model's capabilities, but this single number can be misleading, particularly if the quantity being predicted has an asymmetric distribution. In the case of Kp, the pseudo-logarithmic scale complicates interpretation further. To get a more detailed picture of the model's predictive ability than is possible using mean error and RMSE, we compute probability density functions (PDFs) or distribution functions for each predicted quantity and its error. A PDF (or distribution function) of a quantity is a function that gives the relative likelihood that the variable will have a given value. Ideally, the distribution of the model values for a predicted quantity should be identical to the distribution of the observations for that quantity. Systematically biased predictions will result in a curve that is shifted right or left relative to the observations. When the shape of the PDF differs, this may indicate a tendency to over-predict or under-predict under a specific set of conditions. For the distribution of an error, the ideal case is a narrow, symmetric peak centered at zero. Bias in the model results in an off-center or asymmetric peak in the error distribution. An inaccurate prediction is indicated by a broad peak.

For this work we approximate PDFs using kernel density estimation (*Parzen*, 1962). This approximates the underlying PDF from a finite set of observations by smoothing with a kernel function, in this case a Gaussian. The bandwidth (the width of the Gaussian kernels) is determined for each PDF using Scott's Rule (*Scott*, 2015). The specific implementation for the kernel density estimates is that of the Scipy software library (*Jones et al.*, 2001, updated frequently).

3.3 Results

The mean error and RMSE of several predicted quantities were calculated for the entire month for each model configuration; these and their associated uncertainties are shown in Table 3.3. In addition to mean error and RMSE, we also give a normalized RMSE for each predicted quantity, which is computed by dividing the RMSE by the standard deviation of the observed values. By normalizing the RMSE values by the spread of the observational data, we obtain a unitless accuracy metric. This provides a means to compare between RMSE values for disparate quantities. The normalized RMSE values seem to suggest that the model predicts Kp better than any other quantity. However, this is likely due to the fact that Kp is based on a 3-hour maximum of magnetic field variations, and is therefore insensitive to variations of shorter duration or magnitude. The other predicted quantities have 1-minute time resolutions, so the prediction quality metrics for those quantities reflect errors in predicting high-frequency oscillations that are removed in the calculation of Kp. Note all of the metrics in Table 3.3 are calculated for the entire month, and as a result are likely dominated by the quiet-time tendencies for each quantity.

The results are discussed in detail for each predicted quantity in sections 3.3.1-3.3.4, and differences between quiet and active periods are addressed where appropriate. The figures in the following sections use a common color scheme to identify results from the different model configurations. The SWPC configuration is shown in red, the high-resolution grid with RCM is shown in orange, and the high-resolution grid without RCM is shown in blue. Observations, where applicable, are shown as a thick, light blue curve.

3.3.1 Kp

The mean error and RMSE metrics for Kp are shown in Table 3.3. These values represent deviations on the pseudo-logarithmic Kp scale, and hence are dimensionless.

Metric	Model configuration SWPC	Hi-res w/ RCM	Hi-res w/o RCM
		Kp metrics	
Mean error	0.68 ± 0.05	0.84 ± 0.06	-0.17 ± 0.07
RMSE	1.1 ± 0.3	1.3 ± 0.3	1.1 ± 0.4
Normalized RMSE	0.6 ± 0.2	0.8 ± 0.2	0.6 ± 0.2
		Sym-H metrics	
Mean error (nT)	-7.36 ± 0.07	-3.99 ± 0.08	21.54 ± 0.09
RMSE (nT)	17 ± 2	18 ± 2	29 ± 3
Normalized RMSE	0.77 ± 0.09	0.86 ± 0.09	1.4 ± 0.1
		AL metrics	
Mean error (nT)	71 ± 1	15 ± 1	123 ± 1
RMSE (nT)	250 ± 40	230 ± 40	270 ± 40
Normalized RMSE	0.9 ± 0.1	0.8 ± 0.1	1.0 ± 0.1
		CPCP metrics	
Mean error (kV)	2.5 ± 0.2	14.9 ± 0.2	14.5 ± 0.2
RMSE (kV)	46 ± 10	47 ± 9	48 ± 9
Normalized RMSE	0.8 ± 0.2	0.8 ± 0.1	0.8 ± 0.1

Table 3.3: Metrics for all quantities and all model configurations, given as the value $\pm$ one standard error.

Kp predictions from the high-resolution configuration without RCM have the smallest RMSE (1.1), which indicates that these predictions have on average the best accuracy of the three model configurations, but the uncertainties in these RMSE values are large enough that the difference may not be significant. The high-resolution configuration without RCM also has the lowest bias with respect to Kp prediction, with a mean error of -0.20, indicating a slight under-prediction. Both configurations with RCM have positive biases, indicating over-prediction, and the biases are of greater magnitude than those for the configuration without RCM. Although the metrics seem to suggest that the configuration without RCM performs the best, they are misleading in this case as will be discussed later in this section when the distributions of Kp are examined in detail.

Figure 3.1a shows the probability distribution of Kp error for the three model configurations. The Kp error curve for the configuration without RCM is nearly

centered about zero, indicating that the errors are relatively unbiased. The half width at half max of that curve is about 1, also consistent with the RMSE of 1.1 from Table 3.3. The Kp error curves for the SWPC configuration and the high resolution with RCM configuration are both centered to the right of zero. This indicates that these configurations tend to over-predict Kp, consistent with the positive mean errors shown in Table 3.3 for those configurations.

The probability distributions of the actual Kp values are shown in Figure 3.1b. In addition to distributions obtained from the three model configurations, the observed distribution is shown as a thick, light blue curve. The observations have a mode at Kp = 3.3. The two models that incorporate RCM (SWPC and high-resolution with RCM) reproduce the observed distribution fairly closely, having peaks between 3 and 4 (reasonably close to the observed peak at Kp = 3.3). However, they under-predict how often Kp values less than 2 will occur compared to the observations. The model configuration without RCM reproduces the observed distribution more closely in the Kp = 0 − 2 range than do the configurations with RCM. However, the Kp distribution from the without-RCM configuration also has its peak to the left of the observations, and indeed the entire distribution seems to be shifted to the left. The fact that the configuration without RCM agrees with the observations more closely in the low Kp range seems to be merely a side-effect of this leftward shift. This means that the configuration without RCM produces more realistic quiet-time Kp values, but does so at the expense of accuracy during disturbed conditions.

Figure 3.2 shows distributions of Kp similar to the one in Figure 3.1b, but broken down into bins covering specific ranges of observed Kp. The range of observed Kp values in each bin is labeled using the notation $[\mathrm{Kp}_{min}, \mathrm{Kp}_{max})$, indicating that the observed values in the bin start with Kp_{min} and go up to but do not include Kp_{max}. For each bin, the model output is shown for the points in time corresponding to the observational data in that bin. The number of data points per bin range from 40 (in

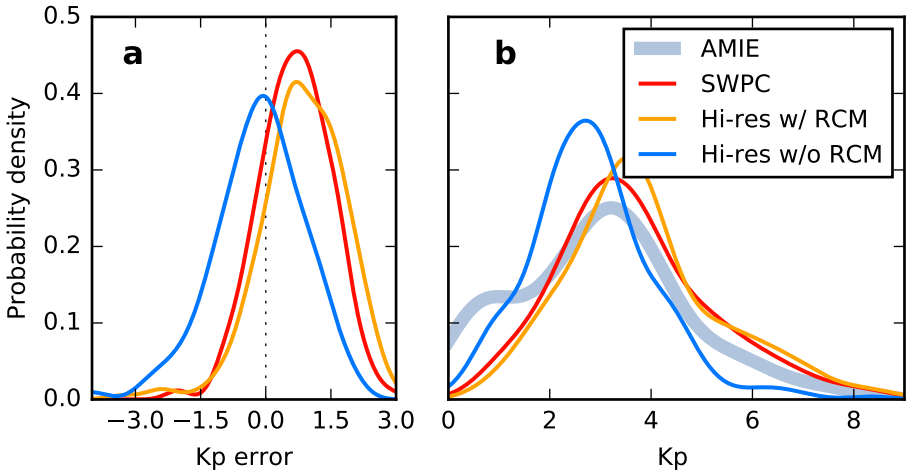

Figure 3.1: Probability density of Kp error (**a**) and Kp itself (**b**) for all model configurations during 1-31 January 2005. Distributions for the three model configurations are plotted as colored curves: SWPC in red, high-resolution with RCM in orange, and high-resolution without RCM in blue. Observations are shown as a thick, light blue curve.

the Kp $\in [6, 9)$ bin) to 200 (in the Kp $\in [3, 4)$ bin). Note that the Kp $\in [6, 9)$ bin covers a greater Kp range than the others; this was done to ensure the bin contains a sufficient number of points for analysis.

The binned distributions of Figure 3.2 provide a sense for how the model performance varies with the amount of geomagnetic activity. For the lowest Kp bins ($[0, 1)$ and $[1, 2)$), all of the models produce distributions shifted to the right compared with the observations, indicating a tendency to over-predict Kp during times of low activity. The over-prediction appears to be least severe for the no-RCM configuration, and most severe for the high-resolution grid with RCM. The high-resolution grid without RCM matches the observations fairly closely in the Kp $\in [2, 3)$ bin, but tends to under-predict for all higher Kp bins. The SWPC and Hi-res with RCM configurations continue to over-predict Kp up to the Kp $\in [3, 4)$ bin. For the higher Kp values these configurations seem to produce relatively unbiased predictions.

Figure 3.3 shows the mean error for each of the Kp bins. The x axis shows the Kp bins using the same notation as Figure 3.2. The no-RCM configuration has positive

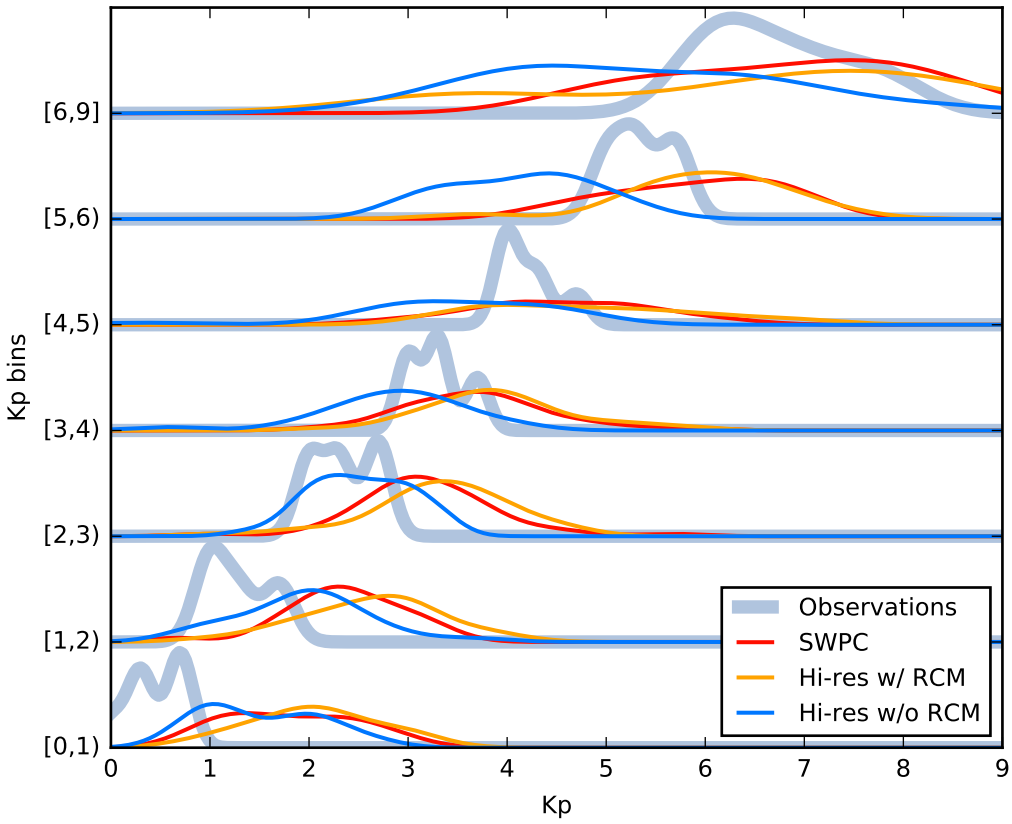

Figure 3.2: Probability density of Kp for observations and for all model configurations, binned by observed Kp. Tick labels on the y axis show the range of observed Kp values contained in each bin in the form $[\mathrm{Kp}_{min}, \mathrm{Kp}_{max})$. The light blue curve within each bin shows the probability density of Kp for the observations within that bin, while the colored curves show the distribution of predictions for each model corresponding to the times of the observations falling in the bin using the same color scheme as Figure 3.1.

mean error (indicating over-prediction) for low Kp, but the mean error decreases with increasing Kp, reaching zero around Kp = 2, and having negative values thereafter (indicating under-prediction). The two configurations with RCM (red and orange curves) also have a positive mean error for low Kp, with similar values to each other but greater magnitude (stronger bias) than that of the no-RCM configuration. The mean errors for these also decrease as Kp increases, but at a slower rate than the no-RCM configuration. For the configurations with RCM the mean error remains positive up to Kp = 5, but turns negative for Kp > 6.

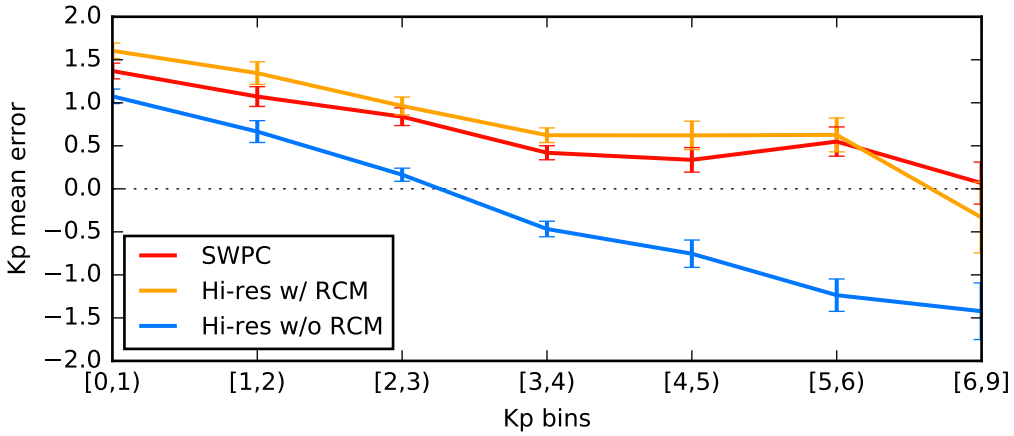

Figure 3.3: Mean error for each Kp bin. The ranges for each bin are denoted in the x axis labels in the form $[\mathrm{Kp}_{min}, \mathrm{Kp}_{max})$. The color scheme follows the previous figures. All the configurations over-predict low values of Kp, and the without-RCM configuration under-predicts the higher Kp values.

These results are similar to those of *Glocer et al.* (2016), which evaluated SWMF and several other models based on their predictions of local K. *Glocer et al.* (2016) did not include bias or accuracy metrics in their results, but in their supplemental data they provided distributions of predicted K for several values of observed K. From these, an unbiased prediction is apparent for observed K = 4, a under-prediction occurs for observed K = 6, and even greater under-prediction for observed K = 8. Thus the downward trend in bias is apparent as K increases in the *Glocer et al.* (2016) results, similar to the present work. The *Glocer et al.* (2016) results do not seem to

show the positive bias that we see at lower values of Kp; this difference may be due to the *Glocer et al.* (2016) results being based on a study of storm events while our results include a considerable amount of quiet periods, as well as the difference in using individual magnetometer stations in that study versus the global Kp index in the present work.

The model's ability to predict Kp during disturbed periods is notably improved with the addition of RCM, primarily during disturbed periods. This suggests that the differences between the model without RCM and those with (SWPC and Hi-res with RCM) are due primarily to differences in those current systems that are affected by the coupling with RCM, specifically the azimuthal currents that are modeled directly by RCM, and the Region 2 field-aligned currents which are driven by inner magnetosphere pressure gradients affected by the coupling.

3.3.2 Sym-H

From the Sym-H results in Table 3.3, it is apparent that the two configurations using RCM (SWPC and Hi-res with RCM) predict Sym-H more accurately than the configuration without RCM. This is indicated by the comparatively low error (measured by RMSE) and bias (mean error closer to zero) relative to the configuration without RCM. The SWPC configuration predicts Sym-H with a slightly lower RMSE but a higher mean error than the high-resolution configuration with RCM. The configuration without RCM tends to over-predict Sym-H by 21.54 nT. The two configurations with RCM under-predict, but do so with a much lower magnitude (by a factor of 3-5) than the configuration with RCM.

Comparing these values of mean error and RMSE to the difference between Sym-H and similar indices gives a sense for whether the metrics indicate a good quality prediction. As mentioned earlier, *Katus and Liemohn* (2013) found discrepancies on the order of 9-11 nT between Sym-H and two similar indices. Therefore, Sym-H

predictions with an RMSE of less than about 9-11 nT might be considered to be of good quality. The predictions from all three of our model configurations exceed 11 nT, but the two configurations with RCM exceed this threshold by only 55-65%, while the configuration without RCM exceeds it by 160%.

The probability distribution of Sym-H error (Figure 3.4a) shows a similar tendency as the metrics with regard to bias. The two runs with RCM appear largely similar to each other. Both are centered around zero (indicating an unbiased prediction), and have a half width at half maximum of about 15 nT. The run without RCM is centered around 15 nT, indicating a clear positive bias.

The distribution of Sym-H itself is shown the Figure 3.4b. The underlying cause for the positive bias of Sym-H from the no-RCM configuration is clearly apparent: It tends to produce Sym-H values near zero (as indicated by the high probability density at that point), while the observed distribution peaks around -20 nT and a long tail extending to -120 nT. The two configurations with RCM, on the other hand, produce a distribution that is largely similar to the observations.

A notable exception is the part of the distribution corresponding to Sym-H greater than 10 nT, where the configuration without RCM seems to produce a more realistic Sym-H distribution than the configurations with RCM. The observed distribution shows a small but significant probability for positive values of Sym-H going as high as 15 nT on Figure 3.4. The configuration without RCM appears to capture the outer part of this area (5-15 nT) fairly accurately. The two configurations with RCM, on the other hand, predict positive Sym-H values at a much lower rate than occurs in the observations, as evidenced by the near-zero Sym-H probabilities between 5 and 15 nT for those configurations.

Figure 3.5 shows time series of Sym-H during the storms on 7 and 21 January. For both of these storms, the configurations with RCM make reasonably good predictions of Sym-H, while the configuration without RCM produces very little Sym-H response

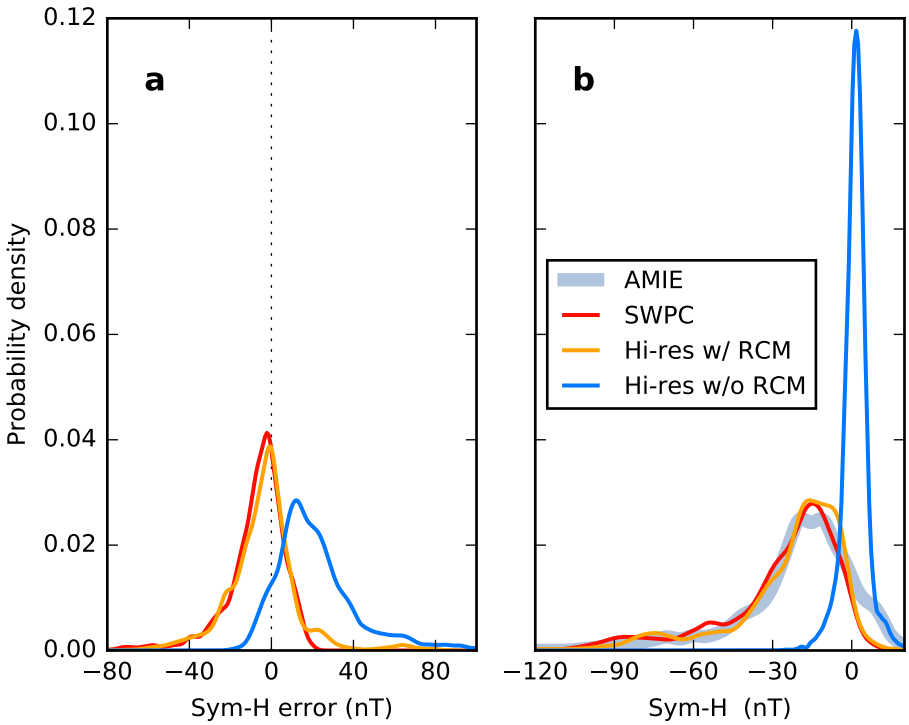

Figure 3.4: Probability density of Sym-H error (**a**) and Sym-H itself (**b**) for all model configurations. The color scheme follows the previous figures. The two configurations with RCM reproduce the observed Sym-H fairly well, while the one without RCM tends to produce Sym-H values near zero regardless of conditions.

except for some oscillations immediately following the initial disturbances. The two configurations with RCM, on the other hand, produce reasonably good approximations of the observed Sym-H response. These warrant further examination.

For the 7 January storm, the two configurations with RCM produce a minimum Sym-H of around -160 nT, while the observed Sym-H reached a minimum of -100 nT. Thus the model Sym-H deviates from the observations by about 50% at the time of greatest disturbance. The models recover gradually over the course of about a day, at which point they are again close to the observed Sym-H. For the 21 January storm, the configurations with RCM produce a Sym-H curve that descends more sharply than the observations and rapidly reaches a minimum of -120 nT, again stronger than the observed minimum. In this case, however, the Sym-H from the configurations with RCM recovers rapidly, with the high-resolution configuration briefly becoming less negative than the observed Sym-H (from about 22:00 UT on 21 January to about 03:00 UT on 22 January) before descending again to match the observations. For the 21 January storm it took about 2 days (until 00:00 UT on 24 January) to recover, but in this case the model output (for the configurations with RCM) followed the observations closely throughout the recovery.

The tendency of the configurations with RCM (SWPC and Hi-Res w/ RCM) to miss positive Sym-H values previously noted in Figure 3.4 is apparent in both time series shown in Figure 3.5. In the case of the 21 January storm, a storm sudden commencement (SSC) is apparent. The configuration without RCM reproduces the observed Sym-H signature resulting from the SSC quite well, but the two configurations with RCM severely under-predict the magnitude of the SSC oscillations. A possible explanation for this is that the inner magnetosphere currents produced by RCM counteract the effects of magnetopause currents to a greater degree than occurs in reality. This reduces the influence of such currents on the surface magnetic fields and in turn the frequency and magnitude of positive Sym-H values as seen in Figure

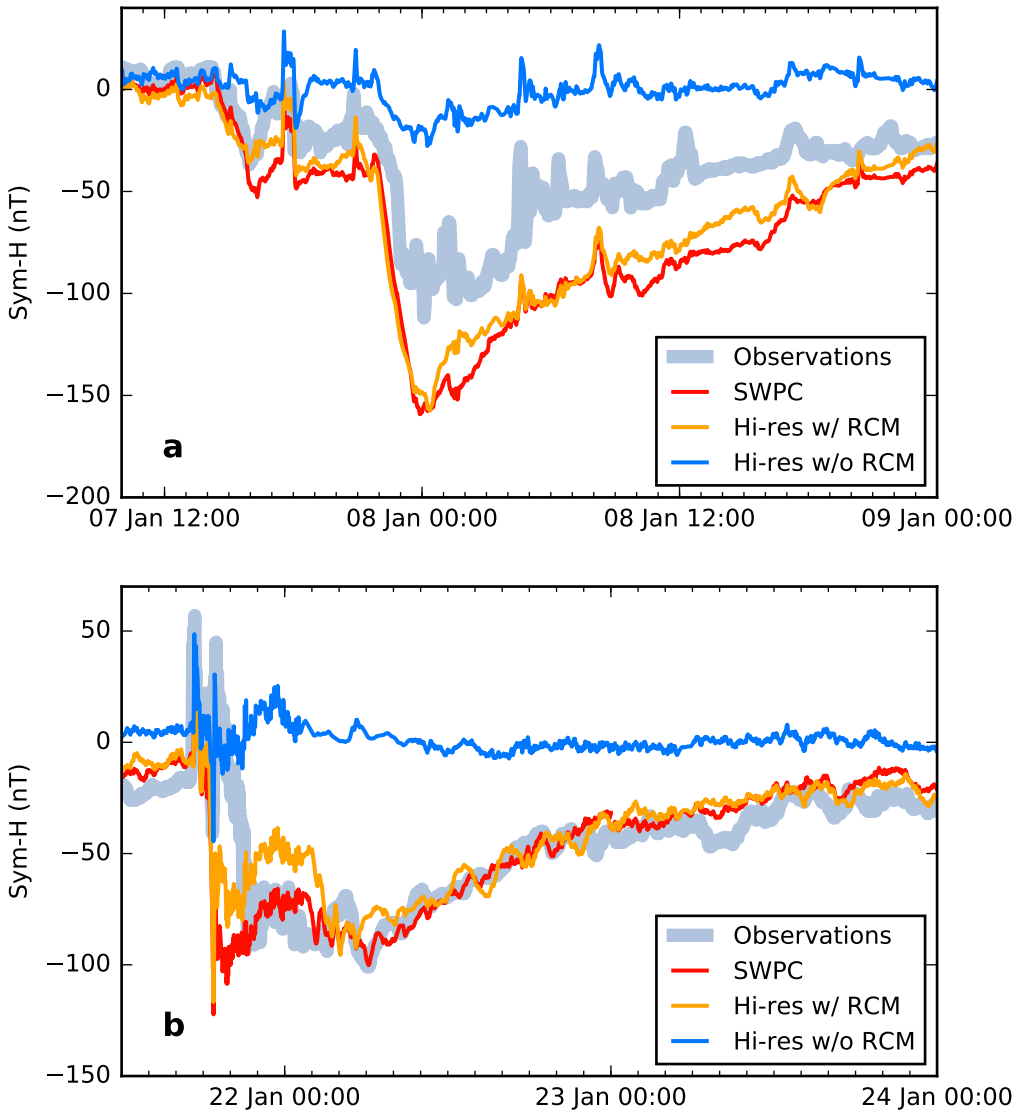

Figure 3.5: Sym-H time series for the storms on 7 Jan (panel a) and 21 Jan (panel b). The color scheme is the same as the previous figures. The model configurations with RCM produce stronger (by 20-50%) Sym-H responses than the observations, while the configuration without RCM produces little response to the storms.

3.4.

The time series plots of Sym-H show considerable improvement in Sym-H predictions over some earlier results such as *Ganushkina et al.* (2010) in which SWMF predicted Sym-H with approximately correct magnitudes but with an approximately 6-hour delay compared to the observed Sym-H. A similar improvement can be seen in other work such as *Liemohn et al.* (2013) and in some (though arguably not all) of the Dst time series plots in *Rastätter et al.* (2013).

The stark difference in Sym-H predictions with and without the RCM component highlights the importance of the inner magnetosphere model in producing realistic ring current dynamics. The inner magnetosphere model can also, through coupling with the MHD solver, affect mid-tail currents to which Sym-H is sensitive, as evidenced by increased tail stretching in MHD models when coupling to an inner magnetosphere model is used (e.g. *Welling et al.*, 2015, *Pembroke et al.*, 2012). That SWMF predicts Dst (similar to Sym-H) better when a ring current model is used has been shown previously in *Rastätter et al.* (2013). Changing the MHD grid resolution, on the other hand, seems to have relatively little effect on Sym-H.

3.3.3 AL

Table 3.3 shows that the mean error in AL is positive for all configurations, indicating a tendency to over-predict AL. Note that AL has negative values during times of high activity, so over-prediction of AL implies under-prediction of geomagnetic activity. Of all the model configurations, the high-resolution grid with RCM exhibits the lowest mean error for AL. The RMSE values are comparable for all three model configurations, falling within the uncertainty bounds of each other. The RMSE values for all of the models are much larger than the mean error, suggesting that random errors rather than bias are the main contributor to the RMSE values.

The distribution of error in AL is shown in the Figure 3.6a. Because the distri-

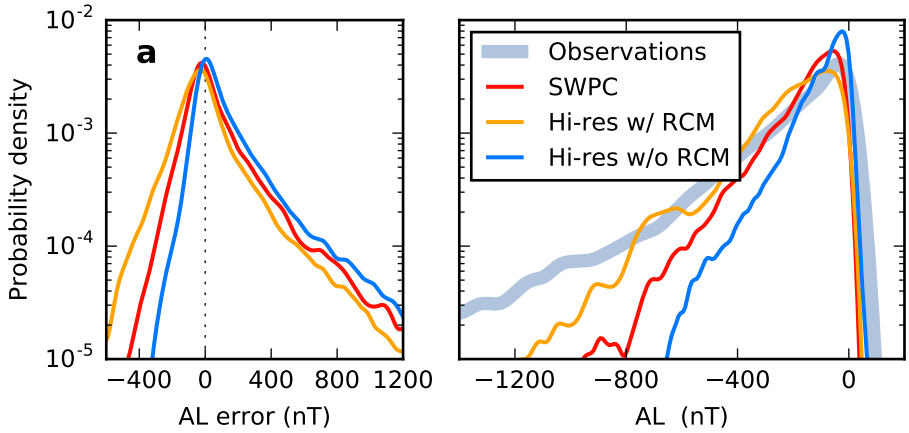

Figure 3.6: Probability density of AL error (**a**) and AL itself (**b**) for observations and for all model configurations. The color scheme follows the previous figures. The distribution is shown on a logarithmic scale due to the importance of the wings of the distribution. All three model configurations capture the overall shape of the distribution, but under-predict the probability of large negative values.

bution is characterized by a long tail, it is plotted on a logarithmic scale. All three configurations peak around zero, but the wings of the distributions are asymmetric, with higher probabilities in the positive direction than the negative. This asymmetry is apparently responsible for the positive biases shown in the AL section of Table 3.3. The asymmetry is most severe for the high-resolution configuration with RCM, and least severe for the high-resolution configuration with RCM. The fact that the curves peak near zero suggests that the model produces fairly unbiased AL predictions most of the time, but the asymmetry indicates an occasional tendency toward over-prediction.

The distribution of the AL values themselves is shown in Figure 3.6b. All of the model configurations peak just to the left of zero, similar to the observations. At the same time, they under-predict the probabilities of the more negative AL values. The high-resolution grid with RCM under-predicts less severely than the other configurations. As a result, the high-resolution grid with RCM comes somewhat closer to reproducing the observed distribution. The under-prediction of the frequency of

strongly negative values is probably the main cause of the biases apparent in the AL section of Table 3.3 and Figure 3.6a. It's worth noting that positive AL values are under-predicted by all of the models, and less severely by the configuration without RCM. This may be related to the results for Kp, where the no-RCM configuration performed better than the others during times of low activity.

The fact that the error curves peak near zero (Figure 3.6a) suggests that the model configurations all tend to produce realistic quiet-time conditions. The wings in the error distributions suggest less accurate predictions during times of higher activity. At the same time, all the model configurations under-predict how often the strongest negative AL values will occur (Figure 3.6b). This implies that the model produces a weaker westward electrojet current during disturbed periods than occurs in the observations. Since the westward electrojet is often associated with substorms (*Akasofu and Yoshida*, 1966), this suggests that the model under-predicts the magnitude of substorm-related field aligned currents.

3.3.4 CPCP

The errors for CPCP are calculated relative to the AMIE model (*Richmond and Kamide*, 1988, *Richmond*, 1992). In the CPCP section of Table 3.3, all three SWMF configurations show positive mean error for CPCP compared to AMIE, indicating over-prediction. The SWPC configuration over-predicts only slightly, while the two high-resolution configurations over-predict more significantly. All three configurations have an RMSE that well exceeds the mean error, indicating that the errors in CPCP are not dominated by a systematic bias in one particular direction.

Probability distributions of CPCP error are shown in Figure 3.7a. All of the error distributions have peaks to the right of zero (around 20-30 kV), consistent with the positive mean errors reported for CPCP in Table 3.3. The peaks are centered 5-15 kV higher than the mean errors shown in Table 3.3, perhaps due to the long, thin

tail of negative errors found in all three distributions.

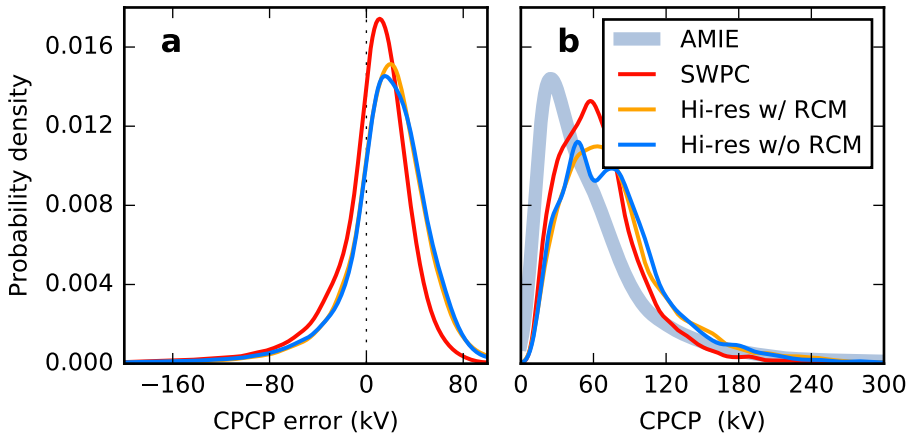

Figure 3.7: Probability densities of CPCP error relative to the AMIE model (**a**) and of CPCP itself (**b**) for all model configurations. The color scheme is the same as the previous figures. These plots show that all of the model configurations over-predict CPCP.

The distribution of CPCP itself is shown in Figure 3.7b. The probability density of AMIE outputs (thick, light blue curve) peaks around 25 kV, while the model configurations all peak around 50-60 kV. This results in the models overestimating CPCP on average, as was seen in Table 3.3. The CPCP distributions obtained from all three models have half widths at half max of around 45 kV, slightly greater than the width of the observed distribution.

Figure 3.8 shows distributions of CPCP, binned by observed CPCP. The range of observed CPCP values in each bin is labeled using the notation $[CPCP_{min}, CPCP_{max})$, much like Figure 3.2. From these it is immediately clear that all three models over-predict CPCP during quiet times, but under-predict during active times. This pattern is similar to what occurred for Kp, except that the configuration without RCM no longer stands out from the others.

Discrepancies between modeled and observed CPCP could be attributed to a number of possible underlying causes, including strength and location of field-aligned currents, ionospheric conductivity, and ionospheric outflow. The field-aligned current

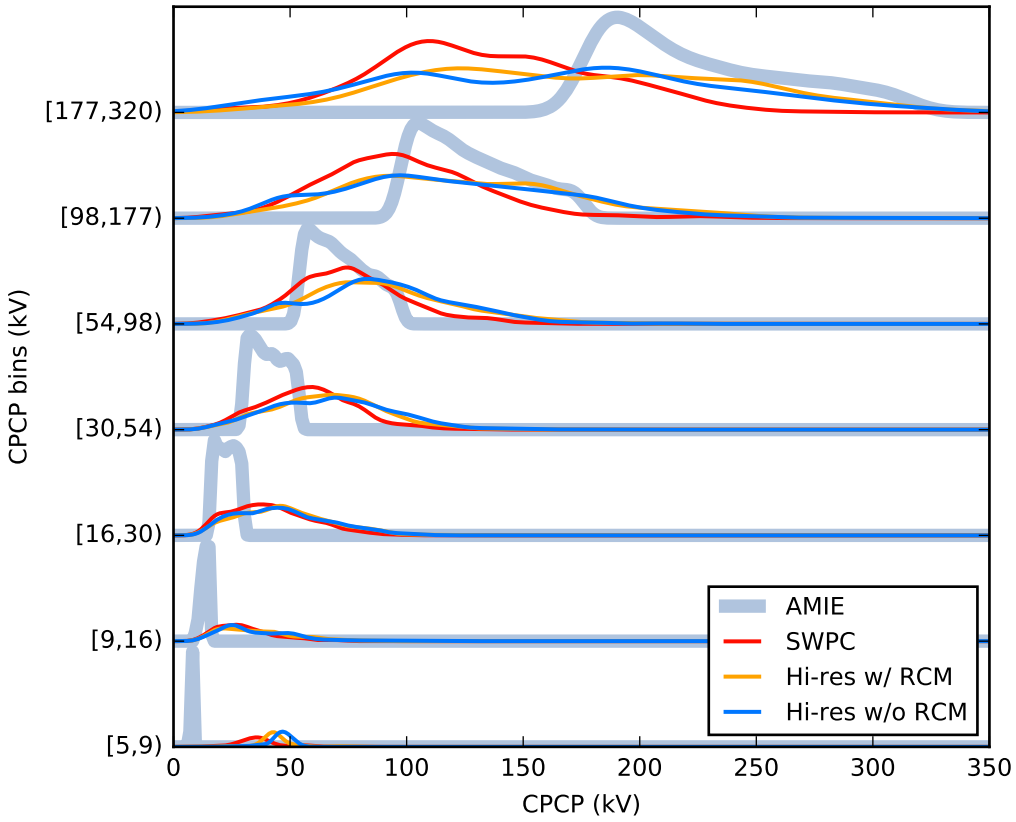

Figure 3.8: Probability density of CPCP for observations and for all model configurations, binned by observed CPCP. Tick labels on the y axis shown the range of observed CPCP values contained in each bin in the form $[CPCP_{min}, CPCP_{max})$. Probability distributions corresponding to each bin are plotted following the same color scheme used in previous figures. The model tends to over-predict CPCP during quiet times, but under-predict during the most active times.

structure and conductivity both affect the potential through Ohm's Law, $\mathbf{J} = \sigma\mathbf{E}$, where the potential is proportional to the current and inversely proportional to conductivity. Thus, over-prediction of the potential (which occurs primarily during quiet time) indicates either over-prediction of field-aligned current strength, or under-prediction of the conductivity. Conversely, under-prediction of the potential (which occurs primarily during active times) indicates either under-prediction of the field-aligned current strengths or over-prediction of the conductivity.

The conductivity connection may also indicate a discrepancy in rate of outflow from the ionospheric boundary. CPCP has been shown to decrease as heavy ion outflow from the ionosphere increases (*Winglee et al.*, 2002b, *Welling and Zaharia*, 2012), so the fact that the models over-predict CPCP could be an indication that the model is under-predicting such outflow. This could be addressed through tuning of the inner boundary condition parameters, but such tuning is complicated by the fact that the outflow is itself dependent on CPCP (*Winglee*, 2000, *Welling and Liemohn*, 2014) and is likely to affect other aspects of the model such as tail dynamics, ring current, and the Sym-H values that are predicted (*Kronberg et al.*, 2014, *Welling and Liemohn*, 2016). First-principles models of ionospheric outflow provide an alternative, but at present they are too computationally expensive for long-period runs such as those described in the present work.

3.4 Discussion

The relatively good accuracy achieved by the model implies a reasonably good model of the magnetospheric currents that affect the various observed quantities, including the dependency of those currents on solar wind driving and other aspects of the dynamics. Furthermore, the similarities between the results for the two highest resolution runs suggests that the model configuration is near grid convergence with regard to the predicted quantities examined in this chapter. A notable exception

is the AL index, where a larger difference can be seen. This could be due to the high-latitude current structures to which AL is sensitive, which may require a higher resolution in order to be fully resolved.

It's worth noting that the high-resolution configuration with RCM differs from the SWPC configuration not only in the grid but also its use of the *Young et al.* (1982) empirical composition model in the coupling between BATS-R-US and RCM. This means that we cannot definitively attribute differences in predictions from those two configurations to the difference in grid resolution. Another limitation of these results is that the data come from a single one-month period, so any dependence of the results on season, such as those found by *Juusola et al.* (2014), or solar cycle will not be apparent.

The fact that Sym-H is predicted more accurately when RCM is used is expected because RCM simulates current systems to which Sym-H sensitive. These same current systems are likely responsible for improving the Kp distribution as well. Kp can be directly influenced by the current systems that affect Sym-H, particularly during times when the strength of the currents are rapidly changing. At the same time, the Region 2 field-aligned currents, to which Kp is also sensitive, are driven mainly by azimuthal pressure gradients in the region modeled by RCM. This was first shown theoretically by *Vasyliunas* (1970). *Zheng et al.* (2006) and *Zheng et al.* (2008) demonstrated that the currents modeled by an inner magnetosphere model (specifically, the Comprehensive Ring Current Model) can affect the Region 2 field-aligned currents. The mean error and RMSE metrics for Kp seem to suggest a detrimental effect of RCM, but this is due to the quiet-time overprediction Kp being masked by an overall reduction in the magnitude of Kp due to the lack of a ring current.

Since the model over-predicts both Kp and CPCP during quiet times, it seems that there may be a common cause (or causes) behind the discrepancies in those quantities. Both Kp and CPCP are sensitive to middle and high latitude ionospheric state and

dynamics (particle precipitation, conductivity, and currents). One possible underlying cause of these discrepancies is the model of ionospheric conductivity, which directly affects CPCP and affects Kp through the current structure. In the present model, the ionospheric conductivity is obtained from a number of empirical relationships. The range of validity for these empirical relationships can easily be exceeded during execution of an MHD model under realistic conditions, and in fact were exceeded during the month in question. *Welling et al.* (2017) identifies the range of validity for these models in terms of solar wind electric field to be from -1.84 mV/m to 2.30 mV/m. Solar wind electric field is defined in that paper as $u_x B_z$, where u_x is the solar wind velocity in GSM coordinates and B_z is the IMF magnetic field in the GSM z direction. $u_x B_z$ for January, 2005 ranged from -28.6 mV/m to 25.2 mV/m, roughly an order of magnitude greater than the valid range listed in *Welling et al.* (2017). The observational data used to construct the empirical conductivity model used in RIM came from solar flux observations from 1985-1990 and magnetometer data from a one-month period of January, 1997 (*Ridley et al.*, 2004, *Moen and Brekke*, 1993). Construction of a more comprehensive empirical model by including more recent data would certainly be possible. Such an improved conductance model might result in better representation of auroral current systems and, in turn, indices and other observable quantities that are sensitive to them.

Like the present work, *Wiltberger et al.* (2017) found $\frac{1}{4}$ R_e to be sufficient resolution for resolving certain aspects of magnetospheric dynamics. They compared field aligned currents for a one-month run of the Lyon-Fedder-Mobarry (LFM) MHD model, and compared the results with the *Weimer* (2005) empirical model. They presented results using three different grid resolutions, the finest of which had cell sizes between $\frac{1}{4}$ and $\frac{1}{2}$ R_e in the inner magnetosphere, similar to the SWPC grid used in the present work. They found that the relationship between field-aligned currents and CPCP was very similar between the two highest resolution grids, and

concluded that the model was approaching a common solution at those resolutions. However, the results they reported were based on time averages for the entire run, so under-resolved transient features might not affect the results significantly. The indications in the present work are that the greatest magnitudes of the AL index are under-predicted, and these correspond with transient phenomena.

Wiltberger et al. (2017) also found that LFM under-predicted field-aligned current strength and over-predicted CPCP compared to the *Weimer* (2005) model. This could be explained by an under-prediction of ionospheric conductivity in that model. Analyzing field-aligned current strength in SWMF might shed some light on the problem of ionospheric conductivity, but such an analysis is beyond the scope of the present work. Nonetheless, the results of the present work, like *Wiltberger et al.* (2017), suggest that ionospheric conductivity is an area for improvement.

3.5 Conclusions

This work shows the strengths and limitations of the SWMF with regard to prediction of geomagnetic indices and CPCP. By testing a one-month period with three different model configurations, we have accumulated a sufficient quantity of data to make statistical comparisons with observations under a variety of conditions.

We find that the model does an excellent job of predicting the Sym-H index. With RCM turned on, the model predicts Sym-H with RMSE values of 17-18 nT, only 50-60% larger than the observational uncertainty for that index. The model predicts the Kp index well during storm conditions, with absolute mean errors of less than one for Kp values above 3. During quiet time though, it consistently over-predicts Kp, with all configurations over-predicting by at least 1 Kp unit on average. An over-prediction of quiet-time activity is also apparent in the model's prediction of CPCP, with mean errors between 2.5 and 14.9 kV. The model tends to under-predict the magnitude of the AL index, with mean errors between 15 and 230 nT.

Of the quantities assessed in this work, the model performs best at predicting Sym-H, and least well at predicting AL. That the model predicts Sym-H poorly without RCM is an expected exception to this. The model's relatively poor performance in predicting AL indicates problems in capturing the structure of auroral-zone currents. A better model of ionospheric conductivity would probably be the most effective way to improve these in the near term, although better predictions of dynamics affecting the field-aligned current structure are needed if the auroral-zone observations are to be predicted to a high degree of accuracy. Depending on what changes are made, such improvements may also reduce the problem of over-predicting Kp during quiet time as well, since Kp is also sensitive to auroral-zone dynamics.

Increasing the grid resolution compared with the SWPC grid had relatively little effect on prediction quality. For all four predicted quantities, the model's predictive accuracy, measured by RMSE, changed by insignificant amounts, as indicated by the error bounds of each RMSE value. There are some indications that the increased grid resolution may have improved the model's prediction of the more extreme values attained by the AL index, however. This implies that the auroral currents during disturbed periods are improved by the increased grid resolution.

Unlike the grid resolution, the presence or absence of an inner magnetosphere model has a dramatic effect on the Sym-H results, with the distribution of Sym-H taking a notably different shape and width when RCM was turned off, and a resulting change in RMSE that far exceeded the uncertainty bound (29 nT without RCM versus 18 nT with). The Kp and AL indices are also affected by the use of RCM, though to a lesser degree than the Sym-H index. Like the Sym-H index, the predictive skill for the AL index was improved by the use of RCM, with RMSE increasing from 230 nT to 270 nT when RCM was turned off. RMSE proved to be somewhat misleading as a measure of accuracy for Kp. RMSE decreased notably when RCM was turned off, which ordinarily would indicate better accuracy. However, a careful examination of

the dataset reveals that the accuracy only improved during relatively quiet periods (Kp $\leq$ 2), while the accuracy during the most disturbed intervals was noticeably worse. CPCP was the only quantity not affected significantly by the use of the inner magnetosphere model, with only a very small change in RMSE when RCM was turned off.

It may be useful to conduct additional work like this covering other time periods. This would make it possible to assess variations depending on season or solar cycle. The resulting datasets could also be analyzed in combination, which would produce results with increased statistical significance and enable more detailed statistical analysis.

The datasets produced in this work can be utilized for a number of possible follow-on projects. The MHD solution can be used to reproduce spacecraft observations, which will enable an assessment of the model's ability to predict magnetic fields in the inner magnetosphere, and locations of the bow shock and magnetopause. As mentioned in the previous section, the field-aligned current structure can be analyzed in detail in order to determine what aspects of the field-aligned currents the model is able to capture. Finally, the model output can be analyzed to identify signatures of substorms, in order to assess how well the model reproduces their timing and dynamics. An initial demonstration of substorm identification in MHD using the Hi-res simulation from this work is presented in Chapter VI.

CHAPTER IV

Investigation of quiet-time isotropic boundaries

4.1 Introduction

All of the quantities evaluated in Chapter III depend on coupling processes between the magnetosphere and ionosphere. Closure of currents through the magnetosphere enable magnetospheric convection to occur (e.g. *Dungey*, 1961, *Ridley et al.*, 2004), and increased convection causes Kp to increase and Sym-H to decrease. The AL index responds to convection, but is particularly responsive to substorms, which involve closure of field-aligned currents from the magnetosphere through the ionosphere. CPCP (cross-polar cap potential) is also affected by magnetospheric convection through the influence of the $\mathbf{u} \times \mathbf{B}$ electric field imposed on the ionosphere by the solar wind, and is also influenced by the ionospheric conductance which in turn depends on particle precipitation from the magnetosphere.

Understanding the nature of interaction between the magnetosphere and ionosphere requires determining the structure of the Earth's magnetic field under varying solar wind conditions, in order to obtain mappings between the ionosphere and locations within the magnetosphere. This requires having magnetic field vectors throughout the relevant parts of the magnetosphere, so that field lines can be traced connecting the ionosphere to the magnetosphere. At present, the available spacecraft observations are sparsely distributed, and magnetospheric models play a crucial role

by providing estimations of the magnetic field throughout the geospace environment.

One way to gain insight into field line mappings is by studying the isotropic boundary (IB), a distinct feature that can be used to probe connections between the ionosphere and magnetosphere. The IB refers to a latitude in the auroral zone at which a substantial change occurs in the flux of downwelling particles into the ionosphere. Equatorward of the IB, the flux in directions perpendicular to the local magnetic field well exceeds the downwelling flux parallel to the local magnetic field. Poleward of the IB, comparable fluxes are detected in the directions parallel and perpendicular to the field. This has been observed by many satellites, including Injun 1 and 3, ESRO IA and IB, NOAA, and DMSP (*Søraas*, 1972, *Imhof et al.*, 1977, *Sergeev et al.*, 1983, *Newell et al.*, 1998). For protons, the IB is observed in all MLT (magnetic local time) sectors and at all activity levels (*Sergeev et al.*, 1993).

The difference in loss-cone filling poleward and equatorward of the IB indicates that the particles observed at the IB originate from a transitional region within the magnetosphere, in which the rate of pitch angle scattering changes significantly. On the night side, one mechanism for this is a transition from adiabatic to chaotic particle motion as particles cross the current sheet, a process termed current sheet scattering (CSS) (*West et al.*, 1978, *Büchner and Zelenyi*, 1987, *Sergeev et al.*, 1993). This occurs when the radius of curvature of the local magnetic field line, R_c, becomes comparable to the effective particle gyroradius r_g (*Alfvén and Fälthammar*, 1963, *Tsyganenko*, 1982, *Büchner and Zelenyi*, 1987, *Delcourt et al.*, 1996), and the strength of this scattering process is parameterized by the ratio $K = R_c/r_g$. That the CSS mechanism results in isotropic precipitation from the plasma sheet is undisputed, because for $K < 1$ the particle motion in the plasma sheet is chaotic (see e.g. *Coroniti*, 1980, *Chen and Palmadesso*, 1986, *Büchner and Zelenyi*, 1987). In general the IB may be formed by other processes, most importantly the interaction of particles with electromagnetic ion-cyclotron (EMIC) waves (*Kennel and Petschek*, 1966, *Liang et al.*, 2014, *Sergeev*

et al., 2015b,a). The role of such interactions in particle precipitation has long been recognized (see e.g. the review paper by *Hultqvist*, 1979). However, EMIC waves cannot always be responsible for IB formation, because the intensity of EMIC waves varies strongly with activity and MLT (e.g. *Bräysy et al.*, 1998, *Halford et al.*, 2010, *Usanova et al.*, 2012). A number of efforts have identified pitch-angle scattering due to CSS as the main source for particle precipitation from the magnetotail during quiet conditions (*Sergeev and Tsyganenko*, 1982, *Sergeev et al.*, 1993, *Ganushkina et al.*, 2005). CSS does not require the presence of waves and can explain the fact that the IB is observed in all activity levels and all MLTs on the night side. However, scattering by waves can sometimes cause the IB to form at a different latitude than would occur for CSS, particularly during storms and substorms (*Søraas et al.*, 1980, *Gvozdevsky et al.*, 1997, *Yahnin and Yahnina*, 2007, *Sergeev et al.*, 2010, *Dubyagin et al.*, 2018), and there is evidence for IB formation by waves during quiet periods as well (*Sergeev et al.*, 2015a).

When the CSS mechanism is responsible for IB formation, the IB location is determined by the field geometry. This enables the IB latitude to be used to estimate the degree of magnetotail field stretching (*Sergeev et al.*, 1993, *Sergeev and Gvozdevsky*, 1995, *Meurant et al.*, 2007). This motivates further study of the role of CSS in IB formation, in order to better determine the conditions under which CSS (as opposed to scattering by EMIC waves or some other process) is the controlling mechanism responsible for IB formation. One means to do so is by estimating the value of K associated with observed IB locations. Numerical tracing of particle trajectories from the current sheet (e.g. *Delcourt et al.*, 1996, 2000, 2006) has shown that CSS acts when $K \lesssim 1 - 10$ (a range spanning an order of magnitude). *Delcourt et al.* (1996) noted significant dependence on the incident particle population. However, in analysis it is often useful to use a specific critical value (rather than a range) as the threshold for CSS, and for this purpose many researchers have used $K_{crit} = 8$ as

originally proposed by *Sergeev et al.* (1983).

To determine whether the IB is associated with CSS requires mapping IB observations to the current sheet, and estimating K there. Both steps require a magnetic field model of some kind. A number of previous efforts, including *Sergeev et al.* (1993), *Ganushkina et al.* (2005), *Sergeev et al.* (2015a), and *Dubyagin et al.* (2018), have accomplished this using empirical models such as the Tsyganenko models. Such models have good traceability to observational data since they are constructed by fitting to available satellite measurements. However, such models tend to be limited to representing features that are resolved by the observational data used in their construction or represented in the form of the equations that are fit to that data. Global first-principles models such as magnetohydrodynamic (MHD) and hybrid simulation codes offer an alternative. Such models have the potential to produce features that are governed by the physics incorporated in the models, without necessarily requiring observational data that resolves those features directly. This makes first-principles models potentially useful in understanding the IB, which depends on the magnetic configuration in the magnetotail, a region that is highly dynamic and only sparsely covered by observational data.

To date, only *Gilson et al.* (2012) and *Ilie et al.* (2015) have used MHD models to explore the IB and its properties. Of these, *Ilie et al.* (2015) is of particular interest to us because they mapped the locations of in situ IB observations through the MHD fields to estimate K in much the same way as was previously done with empirical models. That effort focused on a one-day quiet interval on February 13, 2009, using IB observations obtained from the Medium Energy Proton and Electron Detector (MEPED) instruments (*Evans and Greer*, 2000) on the NOAA (National Oceanographic and Atmospheric Administration) POES (Polar Orbiting Environmental Satellites) and METOP spacecraft. A quiet interval was chosen in order to reduce the chance of particle scattering due to wave-particle interactions. Nonethe-

less, the estimates of K derived from MHD ranged from 27 to 44, unexpectedly high values for K associated with quiet-time IB.

Many of the above studies produced K values covering a fairly wide range. Moreover, since most use only a single model to map the IB to the magnetotail and to compute K, it is generally not possible to tell what part of this wide variation is due to differences in the actual state of the magnetosphere (either in the field geometry or the action of other scattering mechanisms such as waves) and what part is due to differences between models and observational methodologies. Using multiple models to study the same event in combination with in situ magnetic field observations will provide a means to distinguish variation in K due to model error from variation due to physical causes.

The goals of this chapter are twofold: 1) Determine whether MHD is capable of estimating K correctly for quiet-time IB observations 2) Provide better constraints on the range of K values associated with night-side IB formation during quiet time. The chapter is organized as follows: Section 4.2 describes the event and the observations used to identify the IB locations from the observations. Section 4.3 gives the methodology used, including details of the three MHD simulations used in this chapter, and the procedures used for field tracing and for computing K. Section 4.4 presents comparisons of the MHD simulations to magnetic field observations. Section 4.5 gives the results of the field line tracing from the IB locations using MHD, and gives the computed K values for all the IB crossings. Section 4.6 presents results of field line tracing and resulting K values obtained using the empirical models. Section 4.7 compares the two classes of models and shows results of the K correction procedures. Section 4.8 discusses the implications of these results in the context of previous studies.

4.2 Event and observations

We analyze the IB observations and their associated K values for the 24 hour interval beginning at midnight UTC on 13 February, 2009. Since the interval shown in this chapter is the same one that was used in *Ilie et al.* (2015), we refer the reader to Figure 1 of that paper for an illustration of the solar wind driving conditions. The solar wind velocity remained between 300 and 350 km/s with no noticeable discontinuities, and the B_z component of the IMF (interplanetary magnetic field) remained within $\pm$2.5 nT. The solar wind temperature remained below 10^5 K and the density below 30 cm^{-3}. This interval was selected because it is a quiet period in terms of geomagnetic activity (AE $<$ 150 nT, Sym-H $>$ -10, Kp $<$ 2), and because of the availability of magnetic field observations in the night-side magnetosphere from the five THEMIS (Time History of Events and Macroscale Interactions during Substorms) spacecraft. THEMIS A, D, and E had apogee at distances of 11.6-11.7 R_E, near the region that is expected to map to the IB, while THEMIS B and C had apogee at distances of 28.6 and 19.4 R_E, respectively.

Isotropic boundaries were identified using proton flux data from the MEPED instruments on board several NOAA POES and METOP spacecraft. The MEPED instrument, which is described in *Evans and Greer* (2000), includes two telescopes, which measure proton fluxes in four energy bands ranging from 30 to 6900 keV. The first telescope, called the 0° telescope, is within 10° of the spacecraft's zenith direction (i.e. away from Earth). At high latitudes this direction places the 0° telescope close to the direction of the local magnetic field, so that it primarily detects precipitating particles. The second telescope, termed the 90° telescope, is oriented nearly orthogonal to the 0° telescope. The 90° telescope primarily detects locally trapped particles.

The IB locations used in this work are the same as those from *Ilie et al.* (2015). These were determined from the MEPED P1 energy channel (30-80 keV). Although

the nominal low energy limit of the P1 channel is 30 keV, it is actually somewhat higher and varies among the satellites due to detector degradation. In addition, the 90°- telescopes degrades more strongly than 0°-telescope. Table 4.1 shows the low energy limits for 0°- telescope as given by *Asikainen et al.* (2012). To recalibrate 90°-telescope data to the 0°- telescope energy limit, we use procedure described in the Appendix of *Dubyagin et al.* (2018). After this correction, we found IB crossings using the procedure in *Dubyagin et al.* (2013) which identifies a poleward and equatorward limit for the IB location. Identifying a poleward and equatorward limit for the IB gives an uncertainty range of latitudes for each IB crossing, which was less than 0.3° for the selected events (*Ilie et al.*, 2015). The criteria for determining the equatorward limit of the IB were chosen to avoid identifying brief periods of isotropic or nearly isotropic fluxes near the low-latitude limit of the auroral oval, which may be the result of wave-particle interactions (*Gvozdevsky et al.*, 1997, *Yahnin and Yahnina*, 2007). In total, 94 IB crossings were identified from five ionospheric satellites (NOAA 15-18 and METOP-02) using this procedure, of which 27 were within three hours MLT of local midnight. As an additional measure to reduce the chances that the selected IB observations could be influenced by wave-particle interactions, only those IB observations that were of typical appearance were used. Typical appearance means a sharp transition from an empty loss cone on the low-latitude side of the IB to a filled loss cone on the high-latitude side, with both the 0° and 90° fluxes reaching a maximum on the high-latitude side of the IB, followed by a monotonic decrease in fluxes going toward the polar cap. Rather than using all suitable IB observations, we include only those for which the THEMIS A, D, or E spacecraft was conjugate with the IB location. For the purpose of this work we define "conjugate" as being within ± 1 hour MLT and within the radial distance range of $r = 7 - 10\ R_E$ from the Earth. This enables us to verify the accuracy of the model magnetic fields in the vicinity of locations in the magnetotail that map to the location of each IB observation, and to

Satellite	Time	Detector energy (keV)	Mag. Lat.	MLT
METOP-02	2009-02-13/01:41:16	36	-68.06	22.77
METOP-02	2009-02-13/03:22:00	36	-67.97	0.04
NOAA-16	2009-02-13/02:23:16	45	-67.98	23.97
NOAA-16	2009-02-13/02:25:23	45	-68.11	22.82
NOAA-17	2009-02-13/02:41:34	45	-68.01	23.50
NOAA-17	2009-02-13/04:22:02	45	-68.34	0.91
NOAA-18	2009-02-13/16:54:17	30	67.83	2.53

Table 4.1: Times and locations of the IB observations, as well as detector cutoff energies for each spacecraft.

correct for errors in those fields. After eliminating the IB observations that were of atypical appearance and those without suitable THEMIS observations, the final list consisted of 7 IB observations, which are shown in Table 4.1.

An illustration of the locations of the THEMIS A, D, and E spacecraft is shown in Figure 4.1. Figure 4.1a shows the positions of THEMIS A (represented by blue squares) in the GSM (geocentric solar magnetospheric) $z = 0$ plane at the time of selected IB observations. The spacecraft was located near midnight for six of the seven IB observations. For the seventh, it was located closer to dawn, though still more than 5 R_E down-tail. Figures 4.1b and 4.1c show the relative locations of THEMIS A, D, and E at 4:22 UT. THEMIS D is represented by a purple upward-pointing triangle, while THEMIS E is represented by a red downward-pointing triangle. It is apparent that THEMIS A and E are separated significantly in the z direction (more than 1 R_E apart), but are more closely spaced in the x and y directions. This enables us to estimate gradients in the z direction by comparing values at THEMIS A and E, which we will use in Section 4.7 to estimate the influence of errors in R_c on the K values computed by the models.

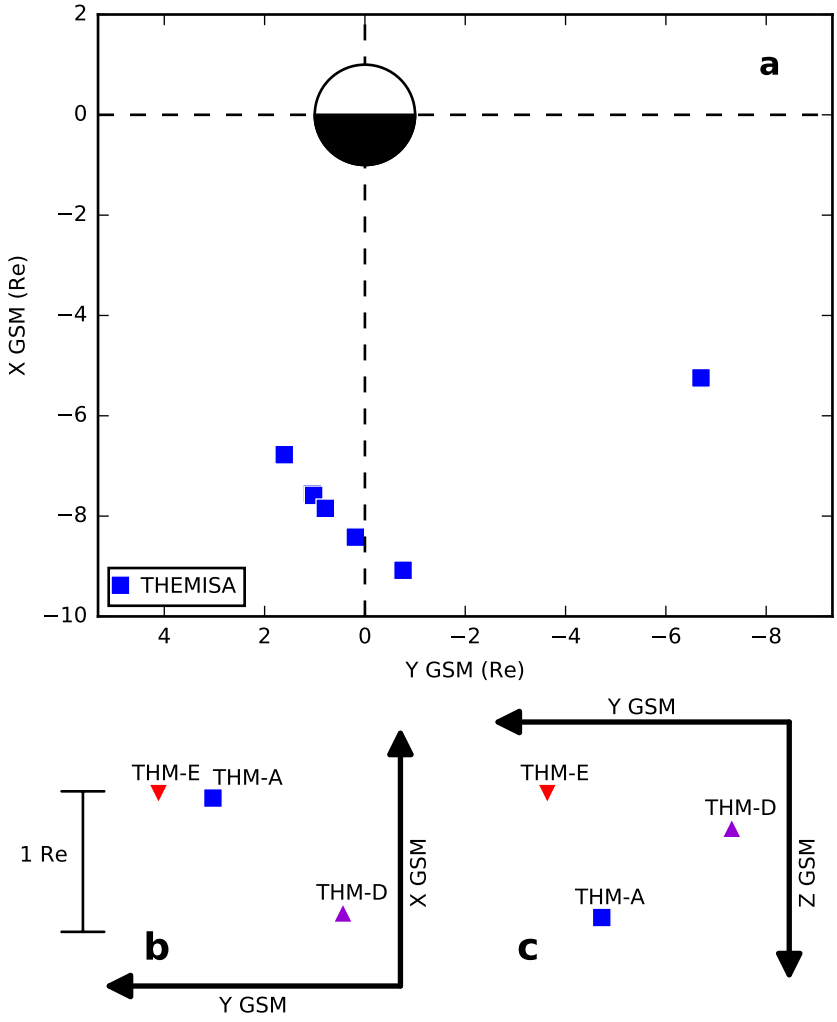

Figure 4.1: (a) THEMIS A location for the times of the IB observations. (b) and (c) Relative locations of THEMIS A, D, and E at 4:22 UT.

4.3 Methodology

Having obtained the list of IB observations in Table 4.1 which are conjugate with the THEMIS A, D, or E spacecraft, we next proceed to computing K at a magnetotail location corresponding with each IB observation. This will provide an indication of whether the estimated field geometry is consistent with CSS for the observed IB crossings. Neither the mapping nor the computation of K can be accomplished directly from the available observational data due to the small number of satellites operating in the magnetotail. Therefore we require models to estimate the magnetic fields in order to do both the mapping and the K calculation. We begin by tracing a field line from each IB observation using the model-derived magnetic fields. Along this field line we find the location were $|B|$ reaches its minimum, and there compute $K = R_c/r_g$ from the model-derived magnetic fields. The tracing and the K calculation are accomplished using magnetic fields obtained from several models, including three MHD simulations performed using the Space Weather Modeling Framework (SWMF) and six empirical models (T96, T01, TS05, TA15B, TA15N, and TA16RBF). The SWMF simulations are described in detail later in this section, and the Tsyganenko models are described in Section 4.6.

For each field line traced, we search for the point where $|B|$ reaches its minimum. At the location of $|B|_{min}$, the field line radius of curvature is computed as

$$R_c = \frac{1}{|(\mathbf{b} \cdot \nabla)\mathbf{b}|}, \tag{4.1}$$

where b is the unit vector along the magnetic field direction, and $\nabla\mathbf{b}$ is computed using a two-point centered difference. We then compute the effective particle gyroradius r_g. When computing r_g, we take the low energy limit of the detector as the particle energy. As mentioned earlier, the detector energy limit varies among the different satellites due to the degradation of the detectors over time (*Asikainen et al.*,

2012), and the values used for each spacecraft are shown in Table 4.1.

Our SWMF simulations consist of the Block Adaptive Tree Solar-Wind, Roe-Type Upwind Scheme (BATS-R-US) MHD model (*Powell et al.*, 1999, *De Zeeuw et al.*, 2000), coupled with the Rice Convection Model (RCM) (*Wolf et al.*, 1982, *Sazykin*, 2000, *Toffoletto et al.*, 2003) and the Ridley Ionosphere Model (RIM) (*Ridley and Liemohn*, 2002, *Ridley et al.*, 2004). The inputs to the model were solar wind parameters obtained from the 1-minute OMNI dataset provided by the NASA Goddard Spaceflight Center (GSFC), and the F10.7 radio flux observed at Penticton, BC (*Tapping*, 2013).

We ran three SWMF simulations, with the same inputs but with differences in grid resolution, numerical scheme, and coupling parameters. By testing different settings of SWMF we are able to determine in a general sense how sensitive the results are to various SWMF settings. The first SWMF simulation, henceforth referred to as "SWMFa," used settings based on those in *Ilie et al.* (2015). The settings of SWMF differ from those used in *Ilie et al.* (2015) in the following ways:

- The simulation in *Ilie et al.* (2015) used a dipole moment of 31.1 μT oriented at 289.1° geographic longitude and 79.0° latitude, which was the default in SWMF at the time. The simulations for the present work used the IGRF dipole parameters for February 13, 2009, which were 287.86° geographic longitude and 79.96° latitude, and a dipole moment of 29.97 μT.

- Minimum values for pressure and density were set to improve numerical stability

- The numerical scheme was changed from an implicit-explicit scheme to a fully explicit one in order to improve stability. The switch to fully explicit in turn required a reduction in the time step.

The grid of SWMFa is the same as was used in *Ilie et al.* (2015), and contains about 4 million cells. The minimum cell size is 1/8 R_E near the Earth, and the

maximum cell size is 2 R_E at the outflow boundaries.

The other two SWMF simulations used settings described in Chapter III, and previously published in *Haiducek et al.* (2017). The first of these, termed "Hi-res" in *Haiducek et al.* (2017), is identified as "SWMFb" in this chapter. SWMFb used a grid with about 2 million cells. The grid for SWMFb was the same as that used in SWMFa within the near-Earth region (out to about 60 R_E in each direction). Beyond 60 R_E, SWMFa used a 2 R_E resolution everywhere. SWMFb, on the other hand, used a 1 R_E cell size in the current sheet region out to 120 R_E, and beyond 120 R_E the cell size increases until reaching 8 R_E near the outflow boundaries. As a result, SWMFb had a higher resolution in the current sheet region but a smaller total number of cells due to coarser resolution in the deep tail (120 R_E and beyond). Besides the grid refinement, SWMFb differed from SWMFa in terms of the RCM settings. In the coupling between BATS-R-US and RCM, SWMFb used the *Young et al.* (1982) composition model to determine the ratio of oxygen to hydrogen in the coupling with RCM, where SWMFa used a fixed ratio. Finally, an ad hoc decay was applied to the RCM ring current in SWMFb, which is designed to improve agreement with observations during storm recovery but is not expected to affect the quiet-time results substantially.

The final simulation, termed "SWMFc," was also described in detail in *Haiducek et al.* (2017), and in that paper was referred to as the "SWPC" simulation due to the settings being largely the same as those used operationally at NOAA Space Weather Prediction Center (SWPC). SWMFc used a coarser grid than either SWMFa or SWMFb, with a minimum cell size of 1/4 R_E near the Earth, a maximum cell size of 8 R_E at the outflow boundaries, and no additional refinement in the tail or current sheet. The RCM coupling settings were the same as SWMFb except that a fixed oxygen to hydrogen ratio was used.

For all of the SWMF simulations, field lines were traced through the MHD domain

from the location of each IB crossing identified using the MEPED data. This was done once every minute of simulation time. The inner boundary of the MHD domain lies at 2.5 R_E from the center of the Earth (rather than at the surface). Since the altitudes of the NOAA and METOP spacecraft were lower than this, the IB locations were mapped to 2.5 R_E prior to tracing through the MHD domain. In order to minimize the influence of non-dipole harmonics on the mapping, we implemented the mapping by first transforming the IB locations into altitude adjusted corrected geomagnetic coordinates (AACGM, *Baker and Wing*, 1989), with the reference height set to 0 km. After conversion to AACGM coordinates, each IB location was mapped to 2.5 R_E using a dipole field. Within the MHD domain, the field lines were traced using a third order Runge-Kutta scheme with a second-order error estimator and adaptive step size.

4.4 Validation of magnetic fields with magnetospheric satellite observations

In order to verify the accuracy of the SWMF in estimating the magnetic field geometry, we compared the magnetic fields estimated by SWMF along the orbits of the GOES and THEMIS satellites with observations from the fluxgate magnetometers onboard the spacecraft (*Singer et al.*, 1996, *Auster et al.*, 2008) during the time from 0000 to 1800 UT on February 13, 2009. This time period includes all of the IB observation times listed in Table 4.1. For the THEMIS spacecraft, we additionally restrict the analysis to points in time for which the spacecraft was at least 7 R_E from the Earth, since this was the minimum distance used for including a THEMIS spacecraft in analysis of an IB event. As an example, Figure 4.2 shows fields at THEMIS A. In Figure 4.2, time series plots of the magnetic fields estimated by each SWMF simulation are overlaid on top of a plot of the observed magnetic field. The

observational data is shown in light blue, SWMFa in medium blue, SWMFb in orange, and SWMFc in green. The left hand column (Figures 4.2a, 4.2c, and 4.2e) shows the B_x, B_y and B_z (GSM) components of the total magnetic field. The right hand column (Figures 4.2b, 4.2d, and 4.2f) shows the same components for the external magnetic field. We obtain the external field by subtracting a dipole field from the total field, with the parameters of the dipole being the IGRF parameters given in Section 4.3 that were used within the SWMF simulations. The same dipole field was subtracted from both from the model and from the observed total fields to obtain the respective external fields. Throughout Figure 4.2, the times of the IB observations listed in Table 4.1 are denoted with vertical dotted lines. Note that the IB observations at 02:23 and 02:25 UT were very close together in time, and while individual lines are drawn for those two events, they are difficult to distinguish in the plot.

The B_x component of the total field (Figure 4.2a) is consistently negative throughout the time period shown. This indicates that the spacecraft was located south of the current sheet. The largest discrepancy between the modeled and observed B_x is an overestimation of the magnitude of B_x by SWMFb and SWMFc between 0800 and 1600, visible in both Figures 4.2a and 4.2b, with the greatest overestimation being 12.0 nT by SWMFb at 10:44 UT. Since the difference is present in the external field, it must be due to differences in magnetospheric currents. The underestimation of the magnitude of B_x indicates that the the current sheet in the simulation was farther north than actual, or that the model current sheet was thinner or contained stronger currents than the actual one, resulting in a stronger gradient in B_x across the current sheet. The data in Figure 4.2a cannot distinguish between these two explanations, but given the finite grid resolution of the model it is more likely that the current sheet would be thicker than observed rather than thinner, in which case the underestimation of the B_x magnitude indicates an error in the current sheet location.

The estimation of the B_y component (Figure 4.2d) is somewhat more accurate

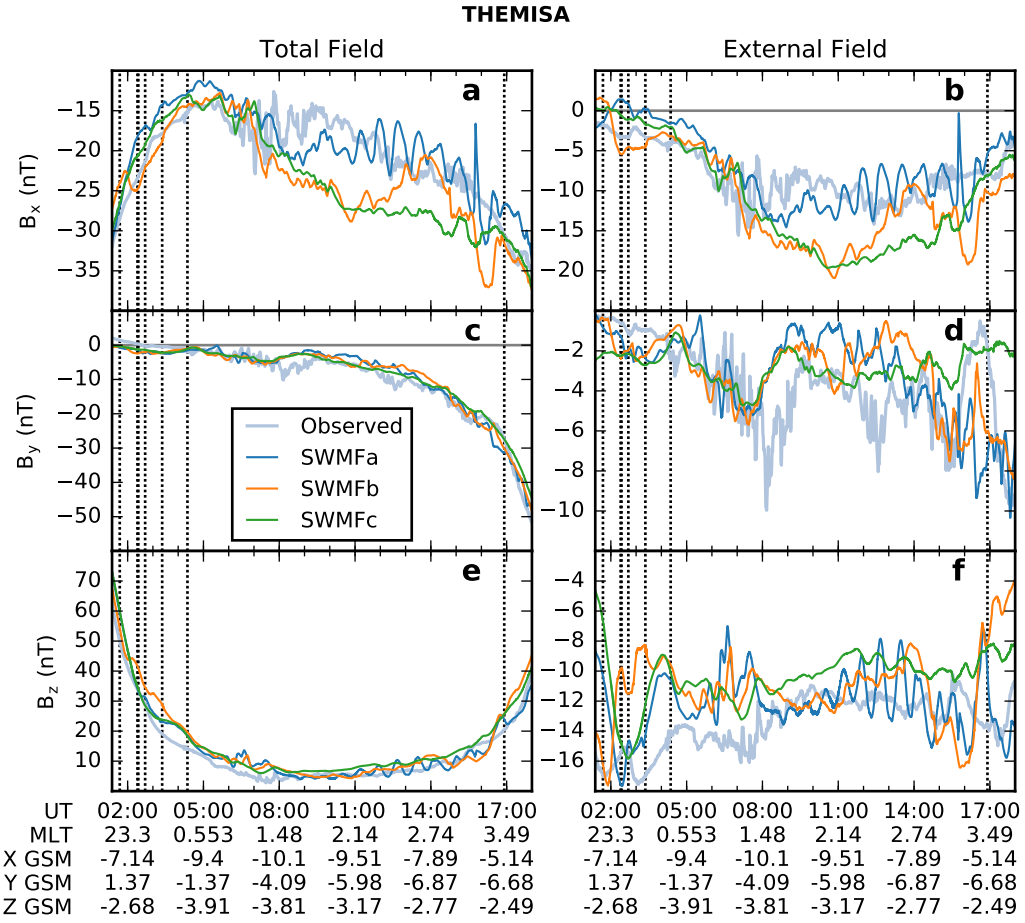

Figure 4.2: Magnetic field components in GSM coordinates at the THEMIS A satellite, observed and predicted, for February 13, 2009. Left column shows the total field, while the right column shows the external field (intrinsic field of the Earth removed). Spacecraft locations in MLT and GSM coordinates are displayed below the time scale.

than that of B_x. All three models miss two negative diversions of the observed B_y that occur at 0800 and 1230 UT. The largest discrepancy is an underestimation (in magnitude) of 7.6 nT by SWMFc at 17:45 UT, at which time the external B_y in SWMFc is -2.1 nT while the observations and the estimations by SWMFa and SWMFb are all around -10 nT. At 17:45 UT the spacecraft was moving toward the Earth, and the B_y component of the total field was around -50 nT (Figure 4.2c).

From the external B_z plot (Figure 4.2f) it is apparent that all three model configurations tend to overestimation B_z throughout the time period of the plot, though there are a few brief periods of underestimation by SWMFa and SWMFb. The largest discrepancy is an overestimation of 11.2 nT by SWMFc at 0131 UT. This occurs at a time when the B_z component of the total field was around 70 nT (Figure 4.2e). An overestimation of B_z was previously reported for SWMF in *Ganushkina et al.* (2010).

Similar results were obtained for THEMIS D and E as for THEMIS A. For THEMIS B and C the behavior of the observed magnetic field was substantially different from THEMIS A, D, and E due to the THEMIS B and C spacecraft having apogee farther down-tail. The model delivered similarly close estimations for the GOES 11 and 12 magnetic fields: The greatest diversion from observations by any single component was 13.3 nT, and most SWMF estimations were within 5 nT of observations. A persistent overestimation of B_z (like that seen at THEMIS A) was found at GOES 12 but not at GOES 11.

The SWMF simulations estimated the fields with reasonably good accuracy overall. Many differences are present in the behavior of transient features, but typically the differences between the model and observations even during these transients are of a magnitude of only a few nT, and the differences only occasionally exceed 10 nT. The general behavior of the fields is captured well by the simulation, and we find the estimations to be of sufficient quality to warrant their use in studying the IB.

4.5 Mapping locations of isotropic boundaries with MHD

Having verified that the SWMF simulations give reasonably good estimations of the magnetic fields in the magnetotail, we proceed to tracing magnetic fields from the locations of the IB observations. This will enable us to use the SWMF output to obtain information about the conditions leading to IB formation. Figure 4.3 shows the results of tracing field lines from two of the IB observations through the magnetic fields computed by the SWMFb MHD simulation. These two events were selected as representative examples from the total of 21 traces (7 IB observations and 3 model runs). The left column (panels a-e) show the IB crossing at 0225 UT, while the right column (panels f-j) shows the IB crossing at 0422 UT. Panels a and f show the location of the IB observation, the field line traced from the IB location, and satellite locations in the GSM x-y plane. Panels b and g show the same in the x-z plane. The Earth is denoted by a black circle, and surrounded by a grey circle representing the inner boundary of the MHD domain. The location of the observed IB, mapped to the inner boundary of the MHD domain, is denoted with a small circle. The locations of the THEMIS A and E spacecraft are also shown. The field line traced from the IB location is shown as a dashed line, and the minimum $|B|$ point along this field line is denoted by an "X."

By tracing the field lines within each SWMF simulation, we computed a surface defined by $|B| = |B|_{min}$ along each field line. The solid line extending outward from the Earth in Figures 4.3a, 4.3b, 4.3f, and 4.3g denotes a radial line in this surface from the center of the Earth through the point where the IB field line intersects the minimum $|B|$ surface. Figures 4.3c-4.3e and 4.3h-4.3j show simulation output along this minimum $|B|$ line as a function of x in GSM coordinates. The location where the IB field line intersects this surface is denoted with an "X."

Figures 4.3c and 4.3h show $|B|$ along the minimum $|B|$ line described above. Figures 4.3d and 4.3i show R_c, the field line radius of curvature, along the minimum

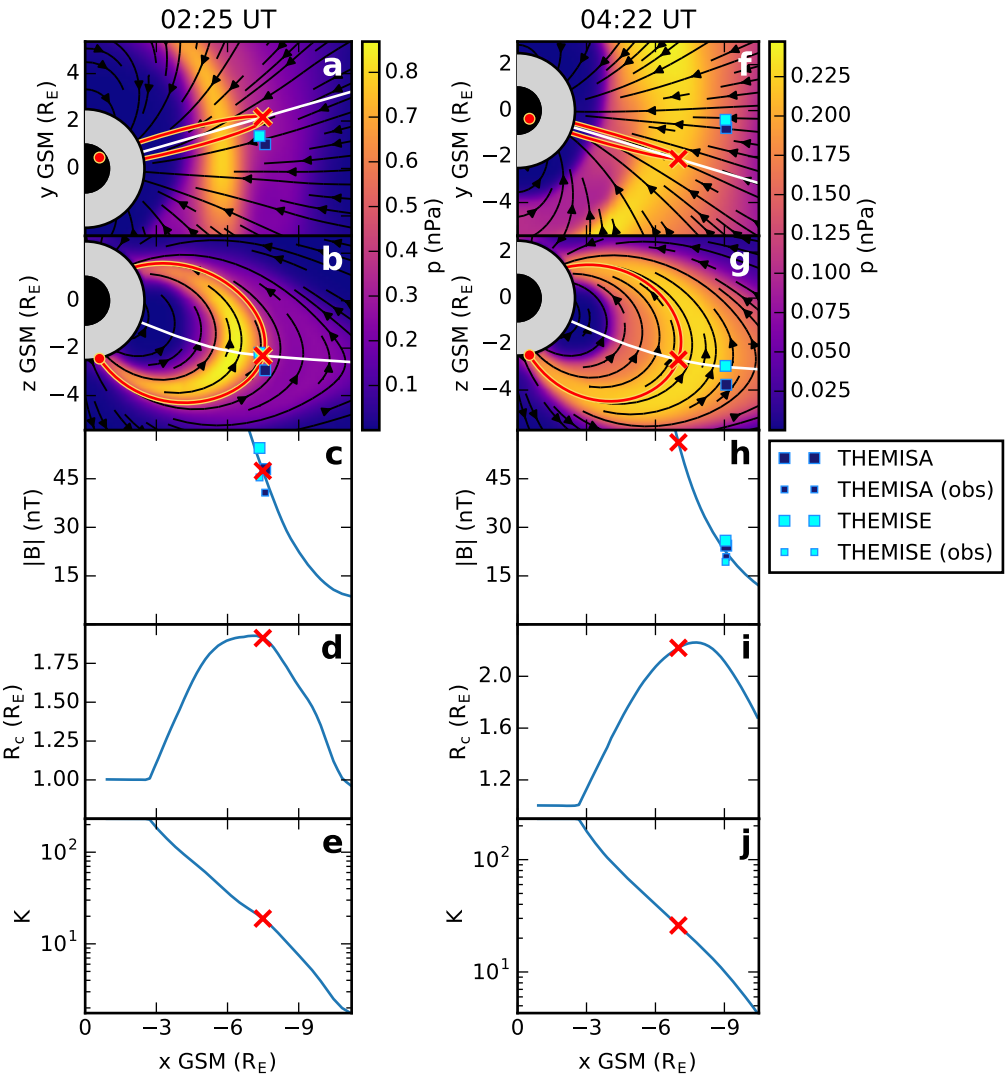

Figure 4.3: Example of tracing field lines for two IB crossings, using the MHD solution from the SWMFb simulation. Left column: IB crossing of the NOAA-16 spacecraft at 02:25 UT; right column: IB crossing of the NOAA-17 spacecraft at 04:22 UT. (a), (b), (f), and (g) show the IB location, field line traced from the IB location, and satellite positions in the GSM x-y and y-z planes. The IB location (mapped to 2.5 Re) is shown as a small circle. A dashed line denotes the field line traced from this location, projected into the plane of the figure. The minimum B point along this line is denoted with an "X." Locations of THEMIS A and E spacecraft are shown using the same symbols as in Figure 4.1. A solid line denotes a radial line through the minimum B point, projected into the minimum B surface and subsequently into the the plane of the figure. This line crosses the field line at the X. The remaining plots show quantities computed along this line, as a function of GSM x. (c) and (h) show $|B|$, (d) and (i) show magnetic field line radius of curvature R_c, and (e) and (j) show K.

$|B|$ line. In both cases, the point that maps to the IB location (denoted with an "X") occurs near the maximum of R_c. This local maximum indicates a transition from a dipolar to a stretched field configuration. Within a dipolar field, the radius of curvature increases linearly with distance, so the presence of a local maximum indicates that the field has diverged significantly from dipolar. At the same time, $|B|$ is continuing to decrease rapidly, resulting in an increase in the gyroradius r_g and making it increasingly likely that the conditions for adiabatic motion will be violated. Similar plots of R_c as a function of x can be found in *Sergeev and Tsyganenko* (1982) and *Yue et al.* (2014), in both cases produced using empirical magnetic field models, and these exhibit generally similar behavior. The R_c plots in both *Sergeev and Tsyganenko* (1982) and *Yue et al.* (2014) reaches a maximum at a somewhat closer distance to the Earth and drops off more rapidly compared to the plots in Figures 4.3c and 4.3h of the present work. However, the behavior of R_c in the magnetotail is quite volatile and depends strongly on local conditions in the plasma sheet and on the general disturbance level of the magnetosphere.

The plots in Figures 4.3c and 4.3h show larger R_c than either *Sergeev and Tsyganenko* (1982) or *Yue et al.* (2014). The position at which the maximum R_c occurs is also slightly farther from the Earth than in *Yue et al.* (2014). This indicates that the MHD fields shown in this figure are less stretched than those shown in the similar figures of *Sergeev and Tsyganenko* (1982) and *Yue et al.* (2014).

A local maximum of R_c combined with a rapidly falling $|B|$ implies a move toward conditions favorable for pitch angle scattering. However, the point where pitch angle scattering occurs is controlled more directly by K. Figures 4.3e and 4.3j show K as a function of x. For both of these, K decreases monotonically as a function of x. The K values at the points mapped from the IB locations (the points marked with an "X") in Figure 4.3e and 4.3j are 18.9 and 26.0, respectively.

From Figures 4.2 and 4.3 we see that the SWMF simulations are tending to pro-

duce magnetic fields that are more dipolar (less stretched) than actual, resulting in larger B_z, and likely causing an overestimate of K. We can quantify the discrepancy in the field stretching by directly comparing with available in situ magnetic field measurements for each IB observation. For this purpose, we use in situ B observations from the THEMIS satellites that are conjugate with each IB observation under the criteria specified in Section 4.2. We define $\overline{\Delta B_z} = \overline{(B_{z_{model}} - B_{z_{observations}})}$ as the average of error in B_z at the spacecraft that are conjugate with each IB observation. Figure 5.5 shows K as a function of $\overline{\Delta B_z}$ for all simulations and all the IB observations shown in Table 4.1. The y-axis of Figure 4.4 is shown on a logarithmic scale. It is apparent from the figure that the K values obtained from SWMFa and SWMFc show a common dependence on $\overline{\Delta B_z}$. A least squares fit to the combined K estimates from SWMFa and SWMFc is plotted on top of the points. K estimates from SWMFb have been omitted from the fit because they exhibited a substantially different dependence on K: Fitting to the SWMFb points produces a lower slope and higher intercept, while the SWMFa and SWMFc data had similar slopes and intercepts to each other. To assess the quality of the fits, we use coefficient of determination (R^2), defined as

$$R^2 = 1 - \frac{\sum_i (K_i - \overline{K})^2}{\sum_i (K_i - f(\overline{\Delta B_z}))^2}, \tag{4.2}$$

where $f(\overline{\Delta B_z})$ is the regression curve. R^2 represents the fraction of the variation in K that is explained by $f(\overline{\Delta B_z})$, and for a perfect fit we would get $R^2 = 1$. For SWMFb, R^2 was only 0.02, while SWMFa and SWMFc had R^2 values of 0.65 and 0.60, respectively. The poor fit for SWMFb seems to be due in part to the influence of outlier points and in part to the points being clustered in a fairly narrow range of $\overline{\Delta B_z}$.

The common dependence of K on $\overline{\Delta B_z}$, and the fact that it is similar for both SWMFa and SWMFc, can be explained by first noting that K can be approximated

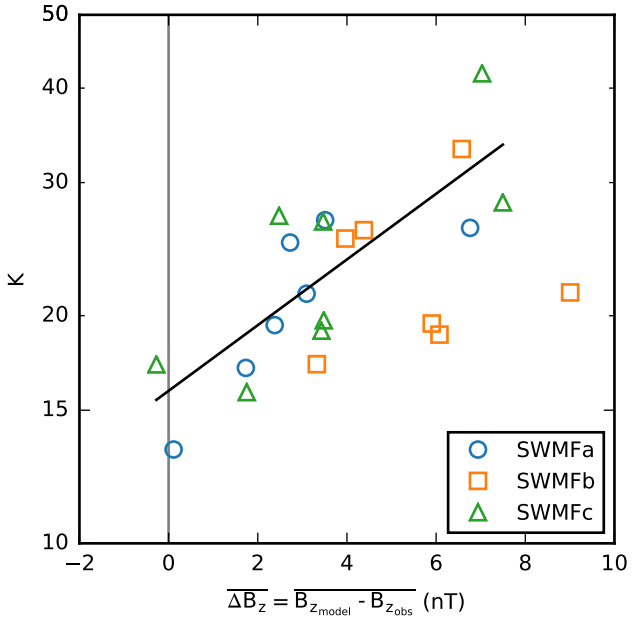

Figure 4.4: K as a function of the error $\overline{\Delta B_z}$ averaged over the THEMIS spacecraft that were conjugate with each IB. Black line denotes a fit to the SWMFa and SWMFc points.

by

$$K = \frac{R_c}{r_g} \approx \frac{qB_z^2}{\sqrt{2m\bar{E}}dB_r/dz}, \tag{4.3}$$

where q denotes the particle charge, m the particle mass, and E the particle energy. B_r is the radial component of magnetic field in GSM coordinates, defined as

$$B_r = \frac{xB_x + yB_y}{\sqrt{x^2 + y^2}}. \tag{4.4}$$

Since we are working with protons, q and m are the elementary charge and the proton mass. B_z and B_r denote the magnetic field z and radial components in GSM coordinates. This expression indicates a quadratic relationship between B_z and K. We take the logarithm of both sides to obtain $\log K \propto \log B_z$, and then linearize the

right hand side of the equation to obtain

$$\log K = A_1 + A_2\overline{\Delta B_z}, \tag{4.5}$$

which is the expression for the fit curve shown in Figure 4.4. A_2 represents the linear dependence of K on B_z, which is the result of both the expression for K and the characteristics of the model and the physical system it represents. By setting $\overline{\Delta B_z} = 0$ we obtain $K_0 = \exp(A_1) = 16$, an estimate of the average K in the absence of B_z error. In order to determine the uncertainty associated with A_1, we estimate the 95% confidence interval for the intercept A_1 as described in e.g. *Montgomery et al.* (2012). The 95% confidence interval for $\exp(A_1)$ is [13, 19], indicating that the intercept value of $K_0 = 16$ is significantly lower than the value of $K = 33$ reported in *Ilie et al.* (2015), but also significantly higher than the commonly used threshold value $K_{crit} = 8$.

4.6 Estimation of K using empirical models

In this study we use the following empirical magnetospheric models: *Tsyganenko* (1995) (T96), *Tsyganenko* (2002) (T01), *Tsyganenko and Sitnov* (2005) (TS05), *Tsyganenko and Andreeva* (2015) (TA15N and TA15B), *Tsyganenko and Andreeva* (2016) (TA16RBF). For all these models, the magnetic field is built as a sum of analytical functions of the model's driving parameters. These functions can represent separate current systems (T96–TA15), or just be basis functions which have no counterpart among conventional current systems in the magnetosphere. Below we briefly summarize the model's features which can be critical for K-parameter estimation. Since we analyze a quiet event, the ring current is very weak and the magnetic field at the region of expected IB formation as well as ionosphere-magnetosphere mapping are mostly controlled by the tail current system.

The distinctive feature of the T96 model is its optimization for an accurate ionosphere magnetosphere mapping: the angular difference between the modeled and observed magnetic field vectors was minimized when T96 was fitted to observed magnetic field vectors. For all other models, the squared difference of magnetic field components was minimized. On the other hand, since T96 is the earliest model, its structure is rather simple. The T96 tail current thickness and position with respect to the Earth is fixed and only its intensity changes with activity which is parameterized by Akasofu epsilon parameter.

The T01 model represents a further development of the concept used for T96. The T01 tail model thickness does not vary with activity but the tail current inner edge moves towards the Earth when activity grows. In addition, the tail module includes two independent sub-modules which add a flexibility to the tail current radial profile.

The TS05 model was specially designed to describe the magnetosphere during storm-time disturbances. The model was fit to the measurements made during storm intervals and likely should not be used for modeling a quiet event. Its tail current thickness and position vary with activity which is parameterized by complex integral functions of the solar wind plasma and IMF parameters taking into account the prehistory of the conditions in the solar wind. TS05 has the most advanced parameterization of geomagnetic activity among all empirical models.

The TA15 model is a forecasting model which is parameterized entirely by external parameters (no ground-based indices are used). The tail current thickness and position vary with activity and the current intensity is assumed to fall off with distance as a power law. There are two versions of the model referred to as TA15N and TA15B, which are parameterized by external driving functions described in *Newell et al.* (2007) and *Boynton et al.* (2011), respectively.

It should be noted, that for T96–TA15 models, to a large extent, the current system geometries are determined in an ad hoc manner. For example: although the

tail current thickness in TS05 and TA15 models can vary with activity, its variance with activity is parameterized for the current sheet as a whole, and its variance with X and Y is defined by a realistic but arbitrary function. This drawback was corrected in TA16RBF model where the field is represented as a sum of elementary functions, each depending on activity parameters (*Newell et al.*, 2007). This approach minimizes the role of the authors in the current geometry definition. However, the amount of the existing spacecraft measurements does not allow the model to resolve fine spatial structures.

Using these models and geomagnetic dipole to represent the Earth's inner field, we traced the field lines from IB locations (in AACGM coordinates). The standard field line tracing subroutine from Geopack FORTRAN package was used. The package as well as the model input driving parameters can be found at `http://geo.phys.spbu.ru/~tsyganenko/modeling.html`. $K = \frac{R_c}{r_g}$ was estimated at the minimum magnetic field point (in the equatorial part of the field line), using Equation 4.1 to estimate R_c and the cutoff energies from Table 4.1 to estimate r_g. The output from the models was also computed at the locations of the THEMIS probes and was compared with THEMIS observations.

Figure 4.5 shows the computed K values versus $\overline{\Delta B_Z}$ for all aforementioned models in the same format as in Figure 4.4 for MHD. It is apparent that all models except for TS05 exhibit a common K vs. $\overline{\Delta B_z}$ dependence. It can be seen that T96 and T01 show the best agreement with observations, based on their comparatively low values of $\overline{\Delta B_z}$. TA16RBF shows the worst agreement, with observations systematically underestimating the B_Z values. The TS05 model produced unrealistically low K-values for 6 of 7 IBs. It can be speculated that the deviation of TS05 from the common dependence is a result of its narrow specification. Since it was fitted to storm-time observations, quiet periods perhaps comprised a negligible part of the data. For this reason, the TS05 model output is an extrapolation in the region of

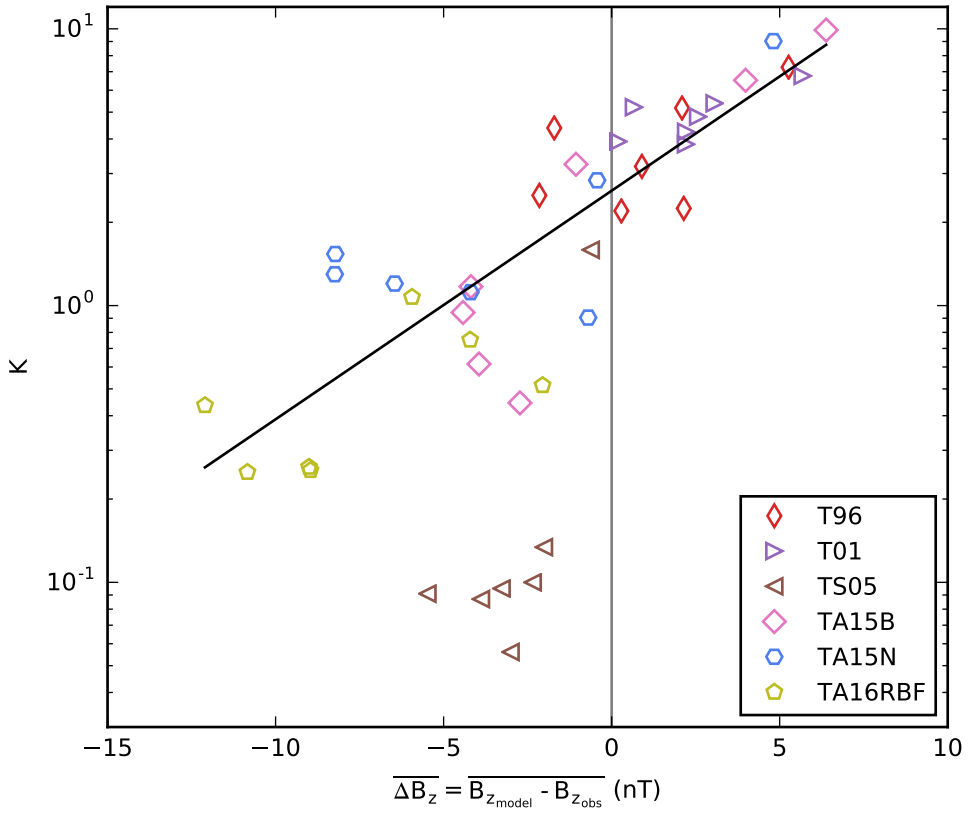

Figure 4.5: Results of K estimation for the four empirical models. Black line denotes a least-squares fit to all points except those produced by TS05.

quiet external conditions. Equation 4.5 has been fit to the points of the plot, excluding TS05 due to the substantial number of outliers present, and the resulting fit curve is plotted in black. The y-axis intercept of this fit occurs at $K = K_0 = 2.6$, with a 95% confidence interval of [2.1, 3.2]. This is significantly lower than the $K_0 = 16$ obtained with SWMF. $K_0 = 2.6$ falls within the range expected for CSS, but is appreciably below $K_{crit} = 8$.

4.7 Comparison of empirical and MHD results

Comparing between Figures 4.4 and 4.5, large differences are apparent between the SWMF simulations and the empirical models. In a preliminary effort to account for the influence of magnetic field errors $\overline{\Delta B_z}$, we fitted Equation 4.5 to each dataset

and noted the y-axis intercepts, which provide an estimate for the average K in the absence of these errors. Even these values differed by nearly an order of magnitude between the SWMF simulations and the empirical models. This indicates a significant difference in the dependency between K and B_z between the different models. One possible reason for this is a systematic difference in R_c within the current sheet, which depends on the model current sheet thickness. Given the sparsity of the available observational data, we have no means to determine the true value of R_c. However, the THEMIS configuration allows a rough estimation of $G = \frac{dB_r}{dz}$, which appears in the denominator of Equation 4.3, and is a major contributor to the value of R_c. As was mentioned in Section 4.2, it is evident from Figures 4.1c and 4.1d that THEMIS A and E are closely spaced in the x and y directions but are significantly displaced in the z direction. This enables us to estimate G as

$$G \approx \frac{B_{r_{THE}} - B_{r_{THA}}}{z_{THE} - z_{THA}}, \tag{4.6}$$

where the subscripts THA and THE refer to the spacecraft THEMIS A and E, and the values z_{THA} and z_{THE} refer to the GSM z coordinates of the spacecraft.

To test the validity of this estimate, we define

$$\Delta r_{xy_{E-A}} = \sqrt{(x_{THE} - x_{THA})^2 + (y_{THE} - y_{THA})^2} \tag{4.7}$$

and

$$\Delta z_{E-A} = z_{THE} - z_{THA}, \tag{4.8}$$

where again the positions are given in GSM coordinates and the subscripts THA and THE refer to the spacecraft THEMIS A and E. By taking the satellite positions at the seven selected IB observations shown in Table 4.1, we find that the ratio $\frac{\Delta z_{E-A}}{\Delta r_{xy_{E-A}}}$ ranges from 1.44 and 2.3, indicating that the displacement in z is consistently

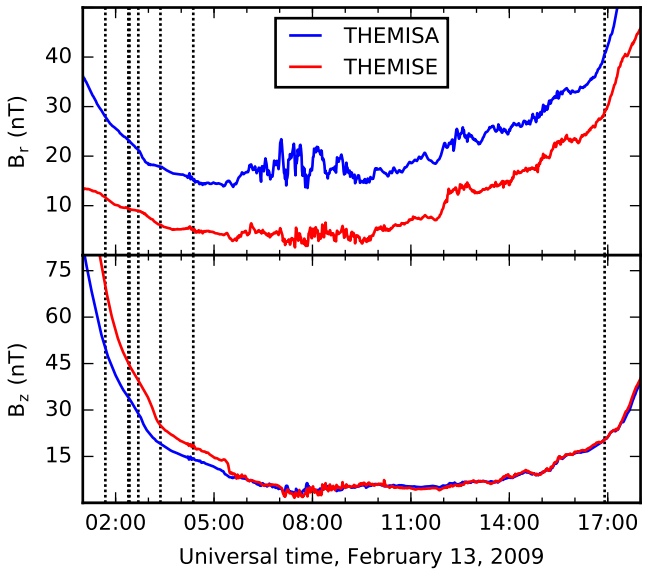

Figure 4.6: Observed B_r and B_z (GSM) for THEMIS A and E. IB crossing times are denoted with vertical dashed lines. Both spacecraft had an elliptical orbit with apogee around 11 R_E from the Earth, but the THEMIS A spacecraft was located approximately 1 R_E southward at apogee relative to THEMIS E.

greater than the horizontal displacement $\Delta r_{xy_{E-A}}$. The ratio 1.44 not ideal since it indicates the horizontal distance between the spacecraft is significant compared with their displacement in z. This may contribute to the uncertainty in estimates of G, since any horizontal (x or y) gradient in B_r will influence the estimate of G. Another source of uncertainty is the distance of the spacecraft from the center of the current sheet, since we will apply this G estimation to correct K estimations computed in the current sheet.

To obtain reasonable estimates for G, we need B_r to differ appreciably between the THEMIS A and E spacecraft. Figure 4.6 shows the observed B_r and B_z magnetic field components at THEMIS A and E. Both spacecraft observed positive B_r, indicating that they are south of the current sheet. However, the B_r component is comparatively weak (¡10 nT around apogee) at THEMIS E, while it is 15-20 nT greater at THEMIS A. This indicates that THEMIS E was located fairly close to the current sheet (for

most of the day), while THEMIS A was farther below it. For the last IB crossing (16:54 UT), the B_r component at THEMIS E is 30.0 nT, significantly stronger than for the earlier IB crossings, indicating a more significant displacement from the current sheet. However, even for the 16:54 UT IB crossing the field at THEMIS E is still significantly weaker (by 11.6 nT) than that observed by THEMIS A at that time. It is worth noting that B_z also differs significantly between the two spacecraft. This means that the configuration is not 1-D. In a 1-D magnetic field (one in which $\frac{d\mathbf{B}}{dx} = \frac{d\mathbf{B}}{dy} = 0$), B_z cannot vary with z without violating $\nabla \cdot \mathbf{B} = 0$. While the current sheet can sometimes be approximately 1-D, the fact that B_z varies with z in the THEMIS observations implies that gradients in x and y are present, which will contribute to errors in estimating G.

The SWMF and empirical model results are shown together in Figure 4.7. Like Figures 4.4 and 4.5, Figure 4.7 shows K plotted as a function of $\overline{\Delta B_z}$. However, the points are now colored according to $\Delta G = G_{model} - G_{obs}$. For both the observations and the models, we estimate G using the difference between the THEMIS A and THEMIS E locations according to Equation 4.6. As shown in Figure 4.1, the two spacecraft were located relatively close in GSM x, but were displaced in z, and this resulted in significantly different B_r components as shown in Figure 4.6.

Fits to the SWMF points and the empirical model points (the same fits shown in Figures 4.4 and 4.5) are drawn in black in Figure 4.7. It is apparent that the simulations and empirical models are producing distinctly different results, with the SWMF consistently producing higher K values. At the same time, the empirical models tend to overestimate G, while the SWMF simulations tend to underestimate G. From Equation 4.3 we expect that overestimations of G will lead to smaller K values, and vice versa. Thus, the systematic underestimation of G by SWMF contributes to its comparatively large K estimates, and the systematic overestimation of G by the empirical models contributes to their smaller K estimates.

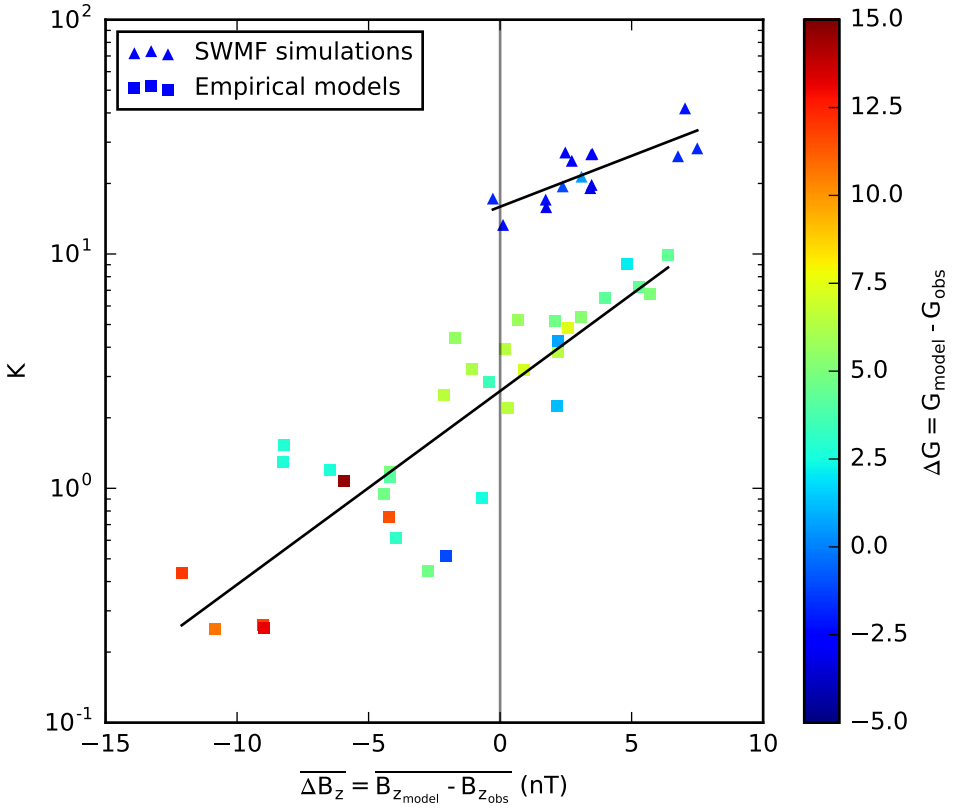

Figure 4.7: Estimated K as a function of $\overline{\Delta B_z}$ for the SWMF simulations (except SWMFb) and the empirical models (except TS05). Colors denote ΔG, the estimation error in the derivative $G = \frac{dB_r}{dz}$. Black lines denote least-squares fits to the SWMF simulations and empirical models.

We now attempt to correct the K estimates based on the available observations. We first apply a correction for $\overline{\Delta B_z}$ using the same procedure used in *Dubyagin et al.* (2018). Equation 4.5 provides an average relationship between K and $\overline{\Delta B_z}$ for each of the two classes of models (MHD and empirical). We use this relationship to correct particular K values by replacing the fitted y-axis intercept A_1 with a value $\log K^*$, where K^* is the value for a particular K that would be computed in the absence of B_z error, assuming the linear relationship of Equation 4.5 holds. This produces the relationship

$$\log K = \log K^* + A_2\overline{\Delta B_z}, \tag{4.9}$$

from which we compute K^* as

$$K^* = K \exp(-A_2\overline{\Delta B_z}). \tag{4.10}$$

Furthermore, motivated by the trends in G noted in Figure 4.7, we construct a new linearization of Equation 4.3, incorporating both $\overline{\Delta B_z}$ and ΔG:

$$\log K = C_1 + C_2\overline{\Delta B_z} + C_3\Delta G. \tag{4.11}$$

C_1, C_2, and C_3 are obtained using least squares minimization using all of the points shown in Figure 4.7 (that is, the output from SWMFa, SWMFc, and all the empirical models except TS05). Solving this equation for K in the case of $\overline{\Delta B_z} = \Delta G = 0$ gives $K_0 = \exp(C_1) = 6.0$ with a 95% confidence interval of [4.7, 7.8]. This can be regarded as an average corrected K for the case of zero magnetic field error. It falls within the expected range for CSS, but somewhat below the $K_{crit} = 8$ threshold.

For the general case (non-zero field error), we obtain a new correction K^{**}, which

we derive from Equation 4.11 by substituting K^{**} for C_1 giving

$$\log K = \log K^{**} + C_2\overline{\Delta B_z} + C_3\Delta G, \tag{4.12}$$

which we can solve for K^{**} to obtain

$$K^{**} = K\exp(-C_2\overline{\Delta B_z} - C_3\Delta G). \tag{4.13}$$

Figure 4.8 shows the overall effect of applying these two correction schemes. The figure shows probability density functions (PDFs) of K, K^*, and K^{**}, obtained through kernel density estimation (*Parzen*, 1962). Kernel density estimation approximates a PDF as a sum of Gaussian kernel functions centered at each data point. The resulting plot can be interpreted as a normalized histogram. The mean, median, and interquartile range (IQR) of the distributions shown in Figure 4.8 can be found in Table 4.2, along with the y-axis intercepts (with 95% confidence intervals) of the fits used to compute K^* and K^{**}. Figure 4.8a shows PDFs of K for SWMFa and SWMFc, and for all empirical models except TS05. The two distributions overlap negligibly, with the SWMF K values uniformly greater than those of the empirical models. Figure 4.8b shows PDFs of K^*, with the fit to Equation 4.5 having been performed separately for the empirical models and for SWMF. This correction leads to both distributions becoming more narrow. The many small K values of the empirical models are shifted higher, while many of the larger SWMF values are shifted down. There is still no overlap between the two distributions, however. Figure 4.8c shows PDFs of K^{**}. The two classes of models did not individually have a clear linear relationship between K and G, so to compute K^{**} a single fit was performed for all models together, once again omitting TS05 and SWMFb. Some overlap can be seen in the distributions of K^{**} in Figure 4.8c, although the corresponding interquartile ranges shown in Table 4.2 for K^{**} do not overlap.

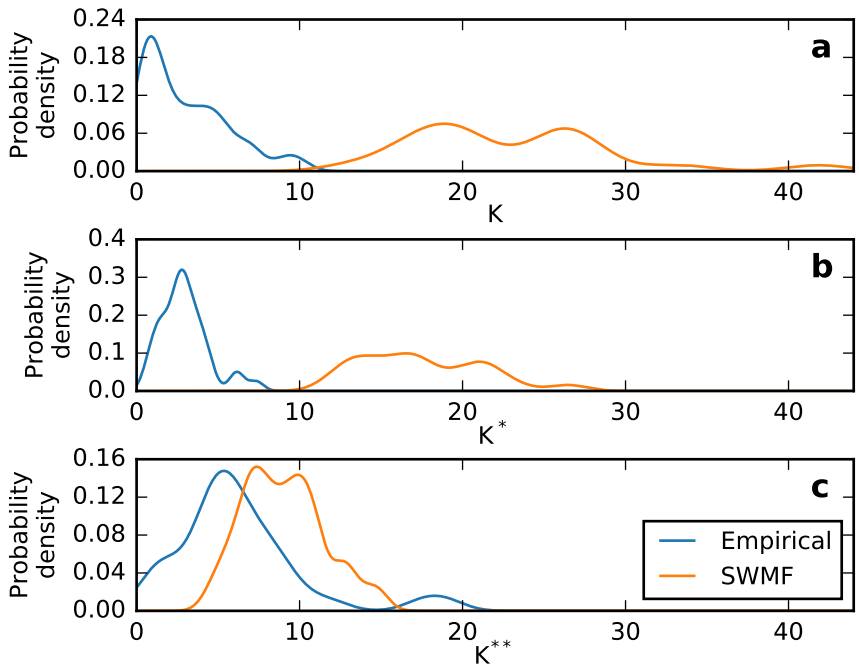

Figure 4.8: Kernel density plots of (a) K, (b) K^*, and (c) K^{**} for SWMFa, SWMFb, and for all empirical models except TS05.

Model type	25th percentile	Median	75th percentile	y-axis intercept	Intercept 95% CI
			Uncorrected K		
SWMF	18	21	27	–	–
Empirical	0.93	2.3	4.6	–	–
Both	1.2	4.3	17	–	–
			K^* *correction*		
SWMF	14	15	19	16	[13, 19]
Empirical	2.0	2.8	3.7	2.6	[2.1, 3.2]
Both	2.5	3.5	13	–	–
			K^{**} *correction*		
SWMF	7.6	9.9	11	6.0	[4.7, 7.8]
Empirical	4.4	5.4	7.6	6.0	[4.7, 7.8]
Both	4.7	6.2	9.5	6.0	[4.7, 7.8]

Table 4.2: Summary of the results of the correction schemes. The 25th percentile, median, and 75th percentile are shown for K, K^*, and K^{**}. For K^* and K^{**} the y-axis intercept (i.e., the correction value for the special case of $\overline{\Delta B_z} = \Delta G = 0$) and its 95% confidence interval are shown. Note that in the case of K^{**} the y-axis intercept is the same for both SWMF and empirical models since a fit is obtained by fitting to both types of models simultaneously and the same fit is used to correct both types of models.

4.8 Discussion and conclusions

The goal of this study is to test the viability of using MHD for estimating K values associated with IB observations, and to provide better constraints on the range of K associated with the IB during quiet time. To accomplish this, we used multiple models, both physics-based and empirical, to compute K values corresponding to IB observations. We ran three SWMF simulations using different simulation parameters, as well as six different empirical models. We used the same time interval and the same IB observations that were used by *Ilie et al.* (2015). A quiet interval was chosen in order to reduce the chance of particle scattering due to wave-particle interactions, which occur primarily during active periods (*Bräysy et al.*, 1998, *Halford et al.*, 2010, *Usanova et al.*, 2012), and to reduce possible inaccuracies in the model mapping. In addition, *Ilie et al.* (2015) noted an absence of observational evidence for EMIC waves during the interval chosen. We first traced fields from the locations where the IB was observed through the magnetic fields of each model. We computed K at the point of minimum $|B|$ along each of these field lines. However, this computed K is still subject to errors in the model field relative to reality. To address this, we corrected each K value based on the error in B relative to observations by nearby THEMIS spacecraft. By computing K with multiple models, and correcting for the errors in those models, we are able to better constrain the possible range of K associated with CSS driven IB formation, and to test the hypothesis that these quiet-time IB observations are associated with CSS.

Comparison between the SWMF simulations and in situ observations indicates a tendency toward an under-stretched night side magnetic field geometry in the simulations. This same tendency was reported in *Ilie et al.* (2015) for the same event with SWMF, and other previous papers have also reported under-stretched fields with MHD (e.g. *Welling and Ridley*, 2010, *Ganushkina et al.*, 2010), though this can be reduced through the use of non-ideal MHD (e.g. *Meng et al.*, 2013). The empirical

models exhibited a range of behaviors in terms of magnetotail stretching: The T01 fields tend to be under-stretched and the TS05, TA16RBF, and TA15N fields are consistently over-stretched, while the T96 and TA15B fields are sometimes over-stretched and sometimes under-stretched. This reflects a variety of observational datasets used to construct the models, as well as different strategies used for fitting. There has been some evolution in terms of field stretching in empirical models. The T96 model has been previously reported as producing over-stretched fields, but the over-stretching was most pronounced during disturbed periods (*Tsyganenko*, 2001, *Ganushkina et al.*, 2002, *Huang et al.*, 2008). *Huang et al.* (2008) reported TS05 as producing less field stretching than T96, but this was for a storm interval and at closer distances than our THEMIS observations. The fact that our results do not show this tendency in T96 may be due in part to the use of a quiet period for this study. The TA16RBF model was previously reported as having similar tail stretching as the older T89 model in the 10-12 R_E region (*Tsyganenko and Andreeva*, 2016), and T89 in turn has been reported as producing over-stretched fields in the magnetotail (*Tsyganenko*, 1989, *Peredo et al.*, 1993).

At the same time, the SWMF consistently produces negative values for ΔG, implying a thicker and/or weaker than actual current sheet. The empirical models, on the other hand, uniformly overestimate G, which implies a current sheet that is thinner and/or stronger than actual. The combined effect of the discrepancies in B_z and G is that the SWMF consistently produces large K values, while the empirical models generally produce smaller K.

The large range of K values we obtain, and their association with magnetic field errors, highlights the importance of quantifying the influence of magnetic field errors on the K estimates, as we did in computing K^* and K^{**}. However, it should be noted that K^* and K^{**} should be regarded as rough estimates of the true value of K. The corrections are subject to a number of sources of uncertainty. These include

errors due to linearization of the nonlinear K formula, the position of the satellites relative to the $|B|_{min}$ point, and the fact that we perform linear fits of multiple models and multiple IB observations, effectively averaging them together. Estimations of the dependence of K on G are especially sensitive to the satellite positions, because G has a larger gradient in z (compared to B_z), and because the errors due to the positions of the spacecraft relative to the $|B|_{min}$ point are compounded by the errors contributed by the positions of the spacecraft relative to each other (on which the estimation of G depends). A more complex K correction that accounts for the position of the satellites relative to the $|B|_{min}$ point might be possible, but this could be error prone as it would require introducing new assumptions about the variation of B_r and B_z with position. It is possible that some effects of the relative distances and directions to spacecraft are somehow corrected for as a result of the fitting process used to obtain the correction factors, but this is by no means certain. A final source of uncertainty is the fact that we include only the G and B_z contributions in the correction of K. Including additional field components would likely result in over-fitting given the small number of points used in our analysis, but might be appropriate for a larger scale study.

Despite the aforementioned sources of uncertainty, the narrow range of values obtained for K^{**} (compared with the range of the uncorrected K), and the overlap between the two classes of models, indicate that the procedure is largely successful in accounting for the influence of magnetic field errors on K estimates in the models. This means that both B_z and $G = \frac{dB_r}{dz}$ contribute significantly to errors in estimating K, and that the two corrections in combination account for a large fraction of the variation in model K estimations.

The relatively narrow ranges we obtained for K^{**} also suggests that the IB events we analyzed were formed by a common mechanism which depends primarily on field geometry. A majority of the K^{**} values (53% for SWMF, and 91% for the empirical

models) are below $K = 10$, which implies that CSS is the likely mechanism forming the IB in these cases. The fact that we obtain this using two classes of models, with very different underlying assumptions, lends additional confidence to this result. By comparing the IQR we obtained for K with the results of *Ilie et al.* (2015), we find that our results and systematically smaller, and slightly more tightly distributed, than those obtained by *Ilie et al.* (2015) for the same event. The IQR of K was 30-42 in the data reported by *Ilie et al.* (2015); the fact that this range does not overlap with the IQR of our data indicates that the difference between their results and ours is larger than the degree of variation within each dataset. That we obtain smaller values of K over a narrower range compared with *Ilie et al.* (2015) indicates that more accurate dipole parameters and other changes to the simulation settings had a substantial effect. We obtain a much narrower IQR for K^{**}, indicating that a large part of the variation in SWMF-derived K can be attributed to correctable errors in the model's magnetic field estimation, rather than to differences in the IB formation process over time. The range of K^{**} is also narrower than the range of K values obtained by *Sergeev et al.* (2015a). In the present work we aimed to only study IB's that were likely to have been formed by CSS. To that end we chose a quiet-time interval, checked for the absence of EMIC wave observations, and only used events that had typical appearance. *Sergeev et al.* (2015a) studied a longer time period which was mostly, but not exclusively, quiet time. Since they do not describe any special efforts to restrict their analysis to "typical" IB observations, it is likely they used all available events that were conjugate with THEMIS spacecraft. Since *Sergeev et al.* (2015a) used adaptive models that attempted to minimize the magnetic field error relative to the THEMIS observations, the fact that we obtain a narrower range for K^{**} is likely due to the use of a longer time period, more IB observations, and a wider range of conditions in *Sergeev et al.* (2015a) compared to the present work.

The $K = 6.0$ value we obtained is marginally lower than the commonly used

$K_{crit} = 8$ threshold. Since the $K_{crit} = 8$ is outside the 95% confidence interval for K, our result is significantly lower in a statistical sense. However, the 95% confidence interval accounts only for the scatter in the data used in the fit, and does not account for the other sources of uncertainty mentioned above. The confidence interval would be somewhat larger were these taken into account.

Our work shows that even after restricting the analysis to a few quiet-time IB observations with ideal spatial distribution of fluxes across the IB, and after correcting the results for errors in the magnetic field models, a substantial uncertainty remains in the range of K. The remaining uncertainty is consistent with the dependency on the incident particle population reported by *Delcourt et al.* (1996), so there is no need to invoke an additional scattering mechanism to explain it. Therefore, obtaining a more precise threshold condition than the range we obtained will likely require not only an improved magnetic field model but also an accounting for the phase space distribution of particles prior to scattering.

The conclusions of the chapter can be summarized as follows:

1. Prior to correction, the MHD simulations often (though not always) produce K values above the expected range for CSS, while the empirical models produce K values at the low end of the expected range for CSS.

2. The corrected K^* and K^{**} values have much narrower spread than the uncorrected K values. This implies that much of the spread in K was due to errors in the estimated magnetic field, but also shows that these errors can be corrected.

3. The distributions of K^{**} overlap substantially for the MHD and for the empirical models.

4. A majority of the corrected K^{**} values (53% for SWMF, and 91% for the empirical models) fall within the expected range for CSS, which supports the hypothesis that the IB was formed by CSS in those cases.

5. We estimate K_0, the average value of K in the absence of magnetic field error, to be 6.0 with a 90% confidence interval of [4.7, 7.8]. This is within the expected range for CSS, and somewhat lower than $K_{crit} = 8$.

The results of this chapter demonstrate that, with appropriate corrections, both SWMF and the empirical models produce values of K that are consistent with CSS during conditions for which CSS is expected. Chapter V will apply these techniques to storm conditions, when the magnetosphere is much more dynamic and EMIC scattering is expected to play a more significant role.

CHAPTER V

Investigation of storm-time isotropic boundaries

5.1 Introduction

During geomagnetic storms, the shape and structure of the magnetotail can change rapidly and dramatically. This includes changes in the orientation of the current sheet, as well as rapid stretchings and dipolarizations. Although storms are driven by the solar wind, the ionosphere plays an important role in regulating the geomagnetic response to these solar wind inputs (e.g. *Daglis*, 1997, *Glocer et al.*, 2009b, *Brambles et al.*, 2011, 2013, *Welling and Liemohn*, 2016). As such, characterizing the connections and interaction between the ionosphere and the magnetotail during storms is necessary in order to fully understand the behavior of the magnetosphere during storm conditions.

Most interaction between the magnetosphere and the ionosphere occurs through the flow of particles and currents along magnetic field lines. Characterizing the structure of these field lines can help us to determine the origins and destinations of plasma flows between the magnetosphere and ionosphere, and thus to better understand how the two regions interact with each other. Unfortunately, our ability to determine field line structure is limited by the very sparse distribution of satellite observations throughout much of the magnetosphere. As a result, models of field line structure are often poorly constrained, particularly during storm conditions when rapid changes in

field line shape pose an added challenge in determining the global system state at any given time.

To supplement the sparse magnetospheric observations, ionospheric observations can be used to help better determine the state of the magnetotail. Ionospheric observations have the advantage of being at a low altitude where relatively large numbers of satellites with fairly short orbital periods provide much better data coverage than is available in most of the magnetosphere. For instance, at present three NOAA (National Oceanographic and Atmospheric Administration) POES (Polar Orbiting Environmental Satellites) satellites are in operation at altitudes of 800-900 km and with orbital periods around 100 minutes (`https://www.ospo.noaa.gov/Operations/POES/status.html`). Similarly, two METOP satellites are in orbit at an 817 km altitude (`https://www.eumetsat.int/website/home/Satellites/CurrentSatellites/Metop/index.html`), and several Defense Meteorological Satellite Program (DMSP) spacecraft orbit at a nominal 850 km orbit (`http://www.au.af.mil/au/awc/space/factsheets/dmsp.htm`).

In order to leverage ionospheric observations to help determine magnetotail structure, we must identify a feature in the ionosphere that maps to a known location in the magnetosphere (or at least, to a location with known characteristics). This is the case for the isotropic boundary (IB). Chapter IV presented evidence supporting the hypothesis that current sheet scattering (CSS) plays a dominant role in forming the IB during quiet conditions. This enables the IB to be used as a proxy for field line stretching in the tail. However, it was mentioned that the IB can also be formed through scattering by electromagnetic ion cyclotron (EMIC) waves. EMIC waves were not observed during the time period studied in Chapter IV. However, EMIC waves are more common during disturbed conditions.

Determining which mechanism is responsible for IB formation at a given time and longitude requires estimating the value $K = \frac{R_c}{r_g}$ (which parameterizes the effectiveness

of the CSS process) associated with a given IB observation. This was done in Chapter IV for quiet conditions. Smaller values of K indicate greater CSS effectiveness. *Sergeev et al.* (1983) proposed $K < 8$ as a threshold condition for CSS scattering, while *Delcourt et al.* (1996, 2000, 2006) showed that CSS operates when $K \lesssim 1-10$, and *Sergeev et al.* (2015a) suggested that CSS could be responsible for IB formation with K as high as 12. In the present work, recognizing that no single value of K can be regarded as the definitive threshold, we adopt the range $K = 8-12$ as a nominal uncertainty range for the CSS scattering threshold.

As was discussed in Chapter IV, the process of estimating K requires a magnetic field model which can be used both for tracing magnetic field lines and for computing the value of K. In Chapter IV this was accomplished using a magnetohydrodynamic (MHD) model, with additional K estimates obtained from several empirical models for comparison. The work of Chapter IV showed that MHD can be used to produce accurate estimates of K during quiet conditions. However, where MHD is likely to be most advantageous for studying the IB is during storm conditions, when the physics incorporated into the model can be used to shed light on the causes of storm-time dynamics. Several previous papers have presented K estimates during storm conditions, but all have used empirical models which were constructed from fits to historical satellite observations (e.g. *Sergeev et al.*, 1993, *Ganushkina et al.*, 2005, *Dubyagin et al.*, 2018). Since MHD models simulate the physics of the magnetosphere rather than presenting a fit to historical observations, it has the potential to reproduce features and dynamics of storm events that may be missed by empirical models, as well as provide additional information that can shed light on the causes of any dynamics that are reproduced by the model. The use of MHD to explore IB properties during disturbed conditions (specifically, during a substorm) was previously demonstrated by *Gilson et al.* (2012), but no estimates of K were provided. To date, no published work has used MHD to explore IB properties during a geomagnetic storm.

The goal of the present work is to estimate what fraction of IB observations might be the result of CSS during storm conditions, and to test whether MHD and empirical models produce consistent values of K during storm conditions. We estimate K using multiple MHD simulations and multiple empirical models, in order to obtain a better representation of the range of variability for K than would be possible using any single model alone. We compare our K values with the $K = 8$ and $K = 12$ threshold conditions to estimate what fraction of the IB observations may have been the result of CSS (as opposed to EMIC wave scattering). We estimate errors in the model output by comparing with in situ magnetic field observations, and apply procedures from *Dubyagin et al.* (2018) and Chapter IV of this dissertation to correct for these errors. The present work is the first to use MHD to explore IB properties during a geomagnetic storm, and the first to estimate K using MHD during disturbed conditions.

This chapter is organized as follows. Section 5.2 provides a description of the time period chosen and the observational data used. Section 5.3 describes the procedures used to estimate K, and the details of the MHD simulations. Sections 5.4 and 5.5 present results from the MHD and empirical models, respectively. Section 5.6 outlines the procedure for correcting the K values and presents the overall results for K and the corrections, and the chapter concludes with Section 3.4.

5.2 Event and observations

We chose the time period 4-6 April, 2010 for our analysis. The major feature of this time period is a moderate storm with a minimum Sym-H of -90 a maximum Kp of 7.7. Solar wind parameters are shown in Figures 5.1a-5.1d. The observational data shown in Figure 5.1 come from the 1-minute OMNI dataset provided by the NASA Goddard Spaceflight Center (GSFC), with data gaps in OMNI filled with observations from the Cluster spacecraft (*Rème et al.*, 2001, *Daly*, 2002). For this

time period the OMNI data were obtained from from the ACE spacecraft. The storm onset is marked by a sudden increase in solar wind speed between 0800 and 0900 UT on 5 April (Figure 5.1a), accompanied by sharp increases in density (Figure 5.1b) and temperature (Figure 5.1c). The B_z component of the interplanetary magnetic field (IMF, Figure 5.1d) abruptly became more negative at the same time, and oscillated rapidly for the next few hours.

To quantify the magnetospheric response to the storm, we use the Sym-H, Kp, and AL indices. Sym-H is designed to measure the strength of azimuthal currents circulating around the Earth. Kp is commonly used as a measure of overall magnetospheric activity. Its usefulness as a measure of activity derives in part from its sensitivity to the latitude of auroral current systems (*Thomsen*, 2004). AL is designed to measure the strength of the westward electrojet current. The latitude of the IB has been found to be sensitive to all three of the indices Sym-H (e.g. *Søraas*, 1972, *Hauge and Söraas*, 1975, *Søraas et al.*, 2002, *Asikainen et al.*, 2010, *Ganushkina et al.*, 2005, *Lvova et al.*, 2005, *Dubyagin et al.*, 2013, 2018), Kp (e.g. *Søraas*, 1972, *Sergeev et al.*, 1993, *Yue et al.*, 2014), and AL (e.g. *Søraas*, 1972, *Lvova et al.*, 2005, *Dubyagin et al.*, 2013).

The Sym-H, Kp, and AL indices during 4-6 April 2010 are shown in Figures 5.1e, 5.1f, and 5.1g. From the Sym-H index (Figure 5.1e), a storm sudden commencement can be seen just after 0800 UT on 5 April, followed by a sharp decrease in Sym-H. The minimum Sym-H of -90 does not occur until almost 24 hours later. The maximum Kp of 7.7 occurred around 0900 UT on 5 April (Figure 5.1f), simultaneous with the jump in solar wind speed and density noted in Figures 5.1a and 5.1b, and Kp remained at or above 3 throughout the event. The AL index (Figure 5.1g) dropped rapidly after the storm commencement, reaching a minimum of -2152 nT. AL quickly recovered to less strongly negative values, approaching quiet-time values from 1130 to 1330 on 5 April, and for the remainder of the interval exhibited moderately negative values

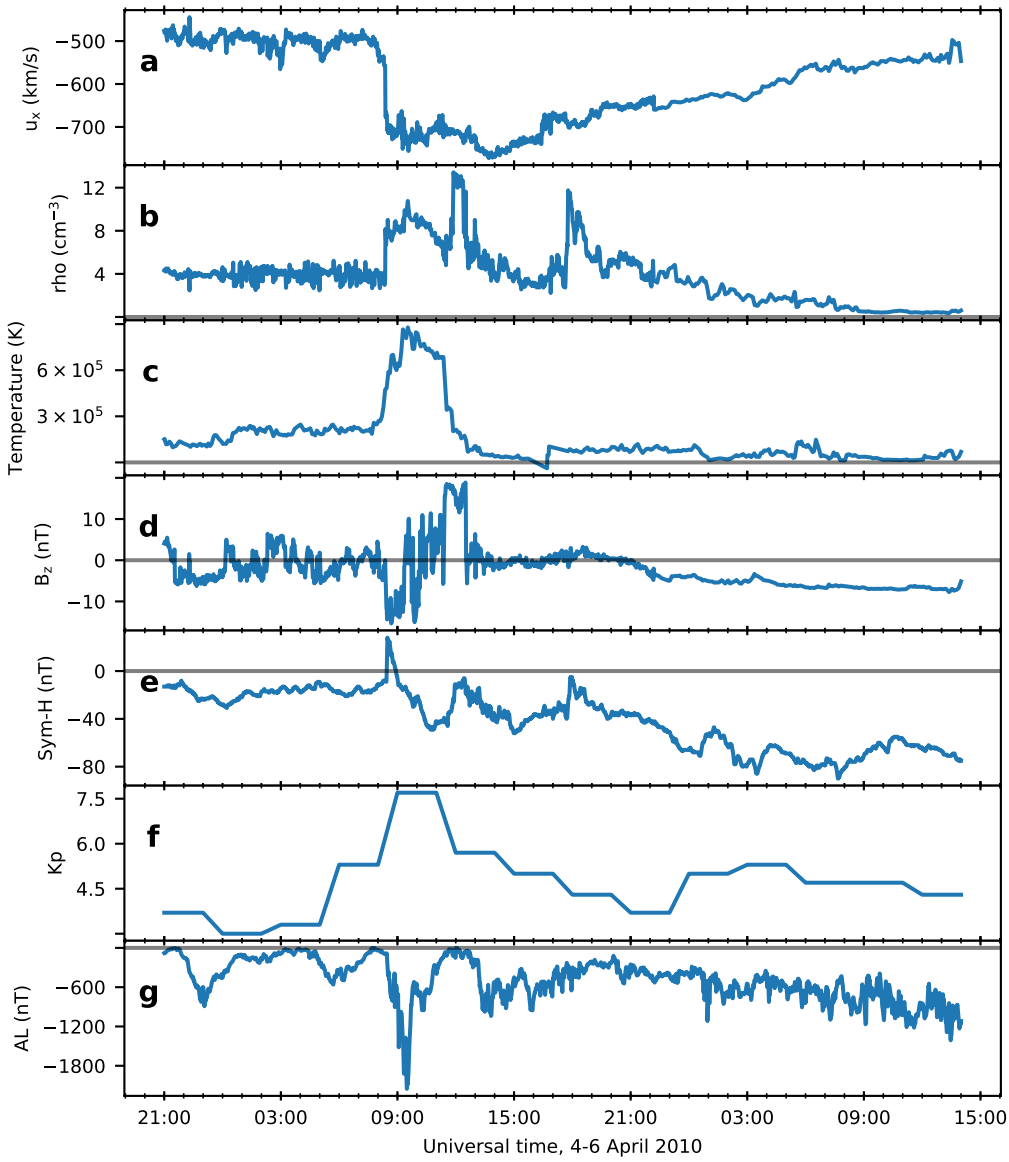

Figure 5.1: Solar wind driving parameters from the 1-minute OMNI dataset with gaps filled using CLUSTER observations, along with geomagnetic indices parameterizing the magnetospheric response. (a) x velocity in GSM coordinates, (b) proton density, (c) temperature, (d) IMF B_z, (e) Sym-H, (f) Kp, (g) AL.

(-200 to -1200 nT) along with rapid oscillations.

As with the work shown in Chapter IV, observations of isotropic boundaries were obtained using the Medium Energy Proton and Electron Detector (MEPED) instruments (*Evans and Greer*, 2000) on the NOAA POES (Polar Orbiting Environmental Satellites) and METOP spacecraft. The instrument consists of two telscopes, referred to the 0° and 90° telescope after their approximate directions relative to the spacecraft's zenith. IB locations were identified from the MEPED P1 energy channel. Nominally, this energy channel spans 30-80 keV, but as was discussed in Chapter IV the actual energy limit increases over time as the detectors degrade. Table 5.1 shows the low energy limits used in this analysis, as given by *Asikainen et al.* (2012) (note that some of the values from the equivalent values in Table 4.1 owing to the data having been taken from just over one year later). Also like the work in Chapter IV, the difference in cutoff energy between the 0° and 90° telescopes was corrected for using the procedure given in the Appendix of *Dubyagin et al.* (2018). IB crossings were identified using the procedure described in *Dubyagin et al.* (2013) and summarized in Chapter IV. This procedure identifies a latitudinal confidence interval for the IB based on the ratio F^0/F^{90} of the flux observed at the 0° and 90° telescope, where the equatorward boundary of the IB is defined as the polewardmost point where $F^0/F^{90} < 0.5$ for four consecutive points, and the poleward boundary is defined as the most equatorward point at which $F^0/F^{90} > 0.75$ for four consecutive points. We denote these boundaries HL ("high latitude") and LL ("low latitude"). Only IB observations from the night side were used. In total, 127 HL and 127 LL IB observations were identified.

To enable correction of the model-derived K values, we used only those spacecraft for which in situ magnetic field observations were available at a location near the equatorial plane between 4 and 12 R_E from the Earth and conjugate with the IB observation. We define a spacecraft as being conjugate when it is within 1 hour

Spacecraft	Energy (keV)
METOP-02	36.0
NOAA-15	64.8
NOAA-16	45.9
NOAA-17	45.6
NOAA-18	30.3
NOAA-19	30.0

Table 5.1: Lower energy limits for the P1 energy channels

MLT (magnetic local time) of the IB observation. The spacecraft meeting these criteria were Time History of Events and Macroscale Interactions during Substorms (THEMIS, *Auster et al.*, 2008, *McFadden et al.*, 2008b,a) A, D, and E, and Geostationary Operational Environmental Satellite (GOES *Singer et al.*, 1996) 11-15. Representative locations for these spacecraft are shown in Figure 5.2. Figure 5.2a shows the positions of THEMIS A and GOES 11 in the x-y GSM (geocentric solar magnetospheric) plane at the times of all the IB observations, using orbital data from the Satellite Situation Center Web (https://sscweb.gsfc.nasa.gov). THEMIS A is shown as aqua pentagons, and GOES 11 is depicted as purple rightward pointing triangles. Note that the satellite positions shown in Figure 5.2a correspond to the times of all the IB observations, not only those for which the respective satellite was conjugate with an IB. As a result, some points show GOES 11 on the day side in Figure 5.2a, although no IB observations from the day side were included in the analysis.

Figures 5.2b and 5.2c show the relative positions of THEMIS A, D, and E at 0700 UT on 5 April, when all three were near apogee. Figure 5.2b shows the x-y (GSM) plane, while Figure 5.2c shows the y-z plane. THEMIS E is depicted as a purple hexagon, and THEMIS D as an orange diamond. Note that the spacecraft are spaced relatively closely in x and y, but THEMIS A is separated significantly in the z direction from THEMIS D and E. This configuration allows the estimation of gradients in the z direction by computing a difference between THEMIS A and E.

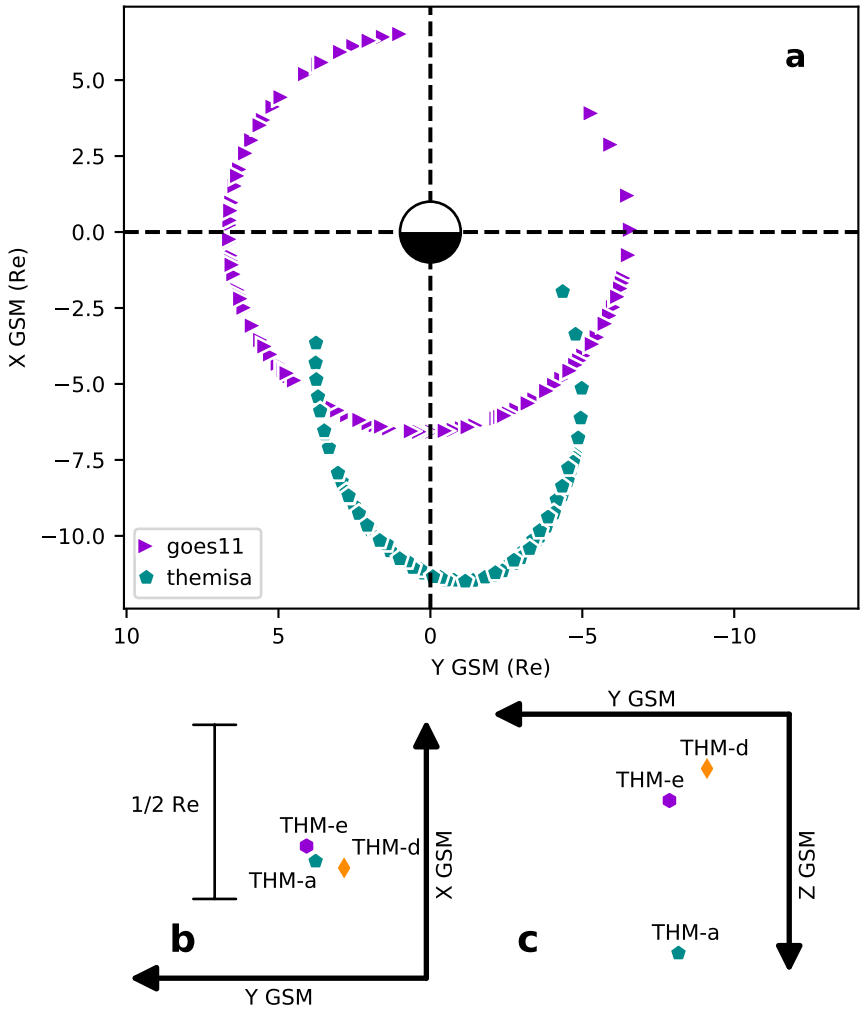

Figure 5.2: (a) Locations of THEMIS A and GOES 11 at the times of all the IB observations. (b) and (c) Relative positions of THEMIS A, D, and E at 0700 UT on 5 April.

Configurations like this occurred numerous times throughout the time interval under study, and we use such satellite configurations to estimate R_c and its influence on K.

5.3 Methodology

For each of the night-side IB crossings identified from the MEPED data for which a conjugate spacecraft was identified satisfying the criteria described in the previous section, we trace a magnetic field line from the location of the IB observation, and

compute $K = \frac{R_c}{r_g}$ at the point along the field line that is farthest from the Earth. Both the field line tracing and the computation of K require a model to estimate the magnetic fields. For this purpose we use MHD simulations executed using the Space Weather Modeling Framework (SWMF) and using the T01, TS05, and TA16 empirical magnetic field models. The set-up for the SWMF simulations is described in detail later in this section, and the empirical models are described in Section 5.5.

For each field line traced, we search for the point that is farthest from the Earth. At this location, we compute R_c, the field line radius of curvature using Equation 4.1. The effective gyroradius r_g is computed for protons whose energy is equal to the low energy limit of the respective detector, as given in Table 5.1. We then use these estimates of R_c and r_g to compute K.

Our SWMF simulations use the BATS-R-US (Block Adaptive Tree Solar-Wind, Roe-type Upwind Scheme) MHD code (*Powell et al.*, 1999, *De Zeeuw et al.*, 2000). This is coupled with the RCM (Rice Convection Model) (*Wolf et al.*, 1982, *Sazykin*, 2000, *Toffoletto et al.*, 2003) and the RIM (Ridley Ionosphere Model) (*Ridley and Liemohn*, 2002, *Ridley et al.*, 2004). The inputs to the model are solar wind parameters (velocity, density, temperature, and magnetic field) and F10.7 solar radio flux. Solar wind parameters were obtained from the 1-minute OMNI dataset, and data gaps in OMNI were filled with observations from the CLUSTER spacecraft. F10.7 flux was obtained from observations at Penticton, BC (*Tapping*, 2013).

We ran three SWMF simulations, with the same inputs but with different grid resolutions and differences in numerical schemes and coupling parameters. By comparing the results obtained with the three simulations we are able to assess qualitatively how sensitive the model-derived K values are to the model settings. The simulations used the same three model set-ups described in Chapter IV, and like in Chapter IV they are labeled SWMFa, SWMFb, and SWMFc. Also like in Chapter IV, magnetic field lines were traced from the locations of the IB observations every one minute of sim-

ulation time, with the coordinates first transformed into altitude adjusted corrected geomagnetic (AACGM) coordinates, then mapped to 2.5 R_E using a dipole field and traced through the MHD domain using a third order Runge-Kutta scheme.

5.4 MHD results

To verify that the simulation accurately reproduces the magnetic field in the magnetotail, we plot simulated and observed magnetic field values along the orbit of the THEMIS A satellite. The result is shown in Figure 5.3. Figures 5.3a, 5.3c, and 5.3e show the x, y, and z (GSM) components of the total magnetic field, while Figures 5.3b, 5.3d, and 5.3f show the same for the external field, which was obtained by removing dipole component of the Earth's intrinsic field, evaluated using Geopack (`http://geo.phys.spbu.ru/~tsyganenko/modeling.html`). We remove only the dipole component because that is how the intrinsic field is represented within SWMF. As mentioned in the previous section, the influence of non-dipole harmonics on the K estimations is minimized by converting the IB locations to AACGM coordinates prior to tracing the fields in SWMF. Points where the spacecraft is closer than 4 R_E to the Earth have been excluded from the plot, since such points do not meet the criteria for selection of conjugate points with IB observations. In all of these plots, the observed field is depicted as a light blue curve, and the SWMFa, SWMFb, and SWMFc simulations are shown as thinner curves colored in medium blue, orange, and green, respectively. THEMIS data were downloaded and calibrated using the THEMIS Data Analysis Software (TDAS, `http://themis.ssl.berkeley.edu/software.shtml`).

Multiple sign changes in B_x can be seen in Figure 5.3a, which are indicative of current sheet crossings. This occurs most noticeably between 0900 and 1600 UT on 5 April during the initial phases of the storm, and a few additional current sheet crossings occur between 2100 and 0200 UT on 5-6 April and around 1200 on 6 April.

From Figure 5.3, it can be seen that the SWMF simulations reproduce many of

the major variations in the observed field. During the quiet period before the storm, the error generally remains within 25 nT in all three components (Figures 5.3b, 5.3d, and 5.3f).

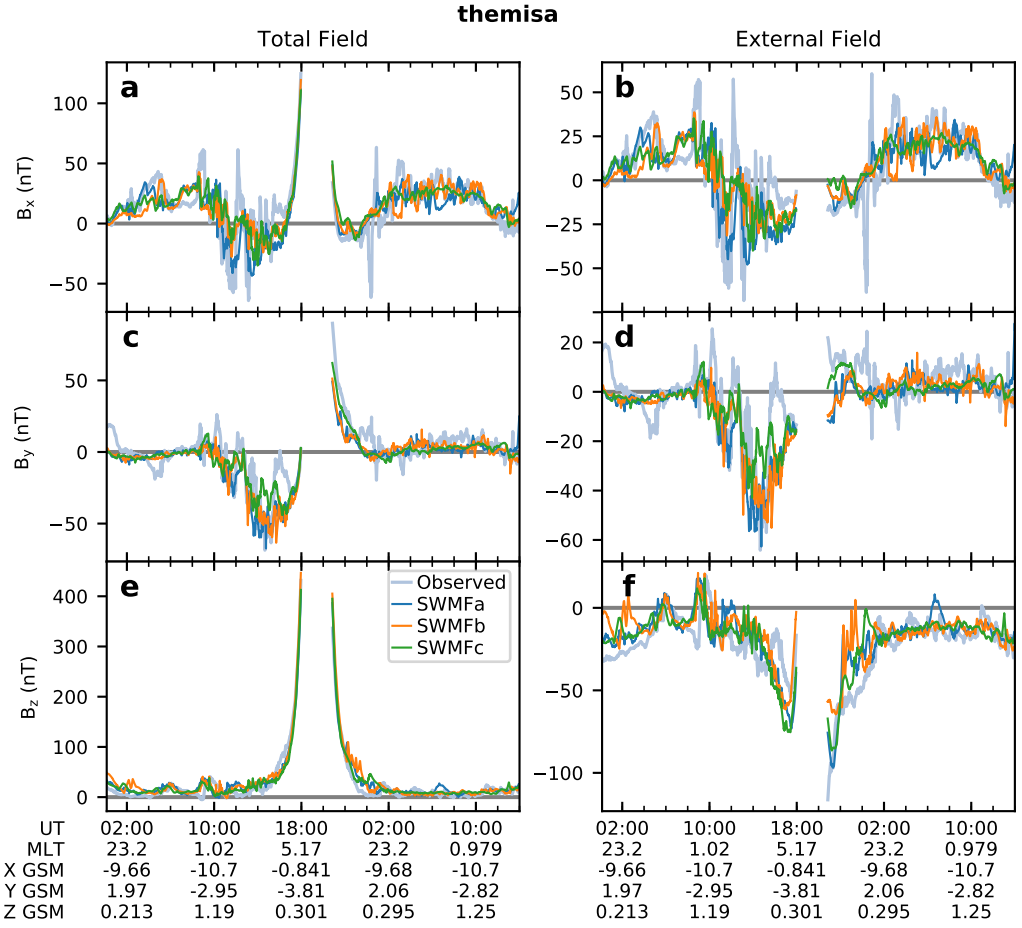

Figure 5.3: Magnetic field components of the total field in GSM coordinates at the THEMIS A satellite, observed and simulated, for April 4-6, 2010.

At the storm sudden commencement around 0900 UT on 5 April, a sharp increase in observed B_z occurs, and is accompanied by an increase in B_x and oscillations in B_y. Similar behavior occurs in the simulations, but the timing is slightly different and the variation in B_x and B_y is weaker than observed. After the storm sudden commencement, all three simulations reproduce the general trend in the observations, in which B_x and B_y become more negative, and B_z increases sharply and then decreases.

Like the observations, rapid fluctuations in B_x and B_y are apparent, though the magnitude of these fluctuations is weaker and the timing is not exactly the same as the observations. In some cases this results in particularly large magnetic field errors such as the spike in B_x around 1200 UT on 5 April which was not reproduced by any of the simulations. The somewhat weaker magnitude of oscillations in the model output may indicate a thicker or weaker current sheet compared with reality. From about 1300 to 1800 UT on 5 April the simulations produce more negative B_x than observed, which suggests that the model current sheet is more northerly than actual during that time, or that the current in the model is stronger than actual. During the next orbit of the spacecraft (2100 UT on 5 April to 1400 UT on 6 April) the conditions are somewhat quieter, with the largest disturbance being a brief but substantial ($\approx$ 60 nT) oscillation in B_x and B_y around 2400 UT and a weaker one around 0300 UT, neither of which is reproduced by the simulations. Some fairly large ($\approx$ 50 nT) errors occur in SWMFb between 2200 and 2400. Aside from the aforementioned periods, the simulation fields during the second orbit remained generally within 20 nT of the observations.

Figure 5.4 shows the behavior of the Kp and Sym-H indices and the IB mapping parameters over the course of the storm. Figures 5.4a and 5.4b show Kp and Sym-H*, respectively, with the observations drawn with thick light-blue lines and the SWMF simulations with thinner lines (SWMFa in blue, SWMFb in orange, and SWMFc in green). Sym-H* was introduced by *Burton et al.* (1975) and is computed from the Sym-H index by applying a correction for solar wind dynamic pressure p_{dyn}. The correction removes the solar wind contribution to the dayside magnetopause current, which influences the ground-based measurements used to construct Sym-H but has a much weaker effect in the region of IB formation. Figure 5.4c shows the absolute value of the magnetic latitude at which each IB was observed. Observations from the equatorward boundary of the IB (labeled LL for low latitude) are shown as circles,

while observations from the poleward boundary of the IB (identified as HL for high latitude) are shown as crosses. The two boundaries are identified according to the procedure from *Dubyagin et al.* (2013), which was summarized briefly in the previous section. Colors denote the hemisphere of the observations, with northern hemisphere observations in red and southern hemisphere in blue. Figure 5.4d shows the MLT of each IB observation, with the marker shapes again denoting the HL and LL IB boundaries and colors denoting the hemisphere as in Figure 5.4c. Figure 5.4e shows the maximum distance from the Earth along the field line traced from each of these IB observations. This was chosen as an estimate of where the field line crosses the current sheet. Although intuitively the point of minimum $|\mathbf{B}|$ would indicate the current sheet, we found that in some cases the field line approached the current sheet without crossing it, only to cross again later, and as a result the maximum distance proved to be a more robust indicator of where the field line crossed the current sheet. The points in Figures 5.4e include both the HL and the LL sets, as well as both hemispheres. The results for each SWMF simulation are shown, with SWMFa depicted as blue circles, SWMFb as orange squares, and SWMFc as green triangles. Figure 5.4f shows the values of K obtained from the MHD solution at the locations depicted in Figure 5.4e.

From Figure 5.4a it is apparent that the simulated Kp is generally within 1 Kp unit of the observations, except for a Kp of zero computed at the beginning of the simulations, an early increase in Kp three hours before the storm onset and a decrease in Kp reported by SWMFc near the end of the storm. Figure 5.4b shows that the simulated Sym-H* values are generally within 20 nT of the observed Sym-H*, with exceptions being an overestimation (in magnitude) of Sym-H* during some of the stronger periods of the storm, and an underestimation (in magnitude) of Sym-H* by SWMFc near the end of the storm.

From Figure 5.4c it is apparent that the IB latitude varies over time during the

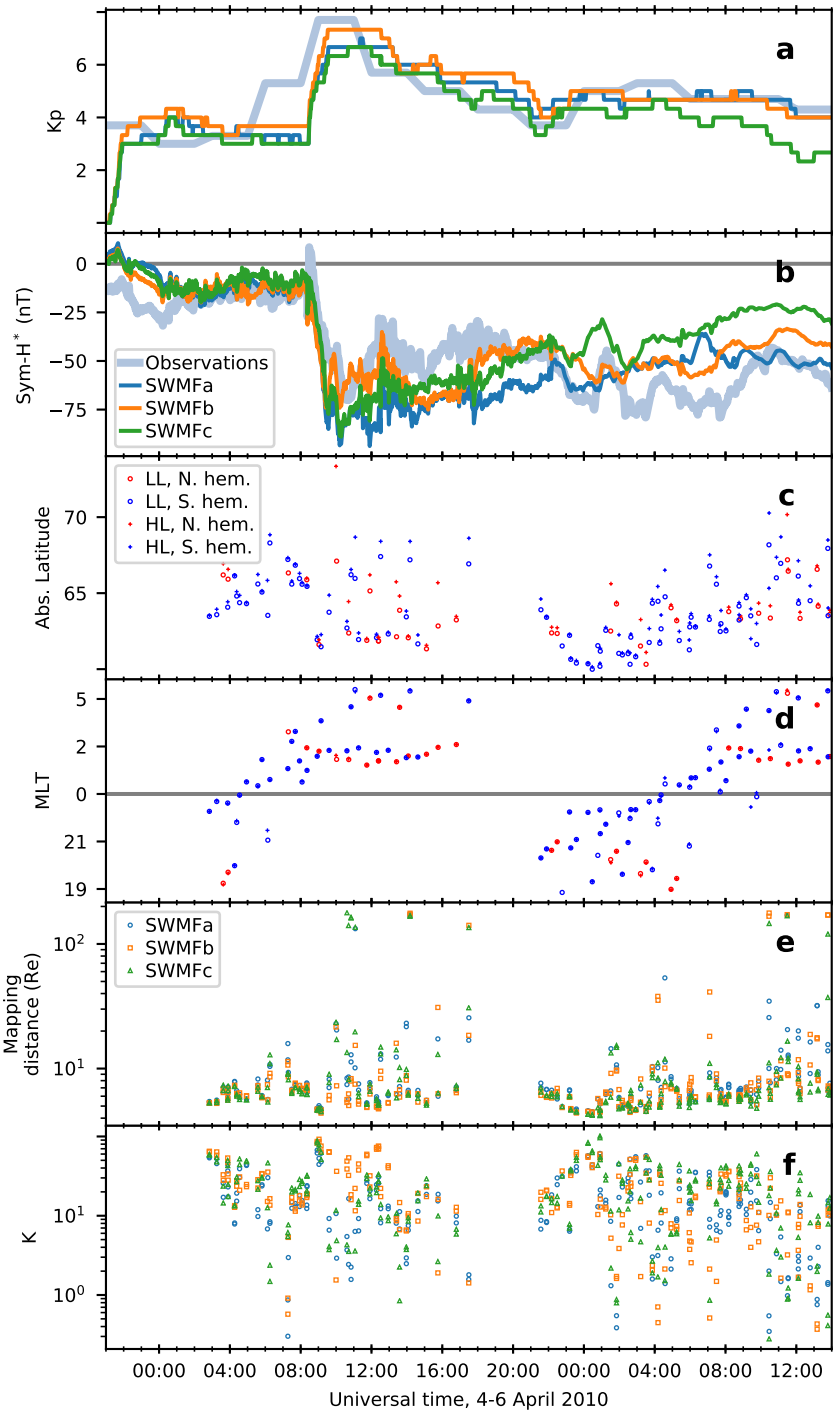

Figure 5.4: IB parameters and geomagnetic indices as a function of time. (a) Kp index, observed and simulated, (b) Sym-H* index, observed and simulated, (c) Absolute value of magnetic latitude of the IB observations, (d) MLT of the IB observations, (e) Maximum down-tail distance of the field lines mapped from the IB locations, for each of the three MHD simulations, (f) K computed from the MHD solution at the farthest point of each field line,

storm. The few quiet-time IB observations are spaced fairly close together in latitude, and their latitude gradually increases from around 63 to 66 degrees between 0300 and 0800 UT. When the storm commences around 0900 UT, the IB latitude sharply decreases to around 62 degrees. 62 degrees remains the most common latitude for the next several hours, but outlier IB observations occur as high as 73 degrees. After 2000 UT, the number and severity of high-latitude outliers decreases somewhat, and the lower latitude limit of IB observations initially decreases to 60 degrees around 2400 UT on 5 April, then increases gradually until reaching 64 degrees around 1200 UT on 6 April.

Figure 5.4d shows distinct trends in MLT over time as well. The initial observations between 0300 and 0500 UT on 5 April are mainly in the dusk to pre-midnight sector, and the IB observations gradually move toward dawn from 0400 to 1200 UT. From 1200 to 1700 UT on 5 April the IB observations are in the post-midnight to pre-dawn sectors. The trend repeats starting at 2000 UT on 5 April with IB observations again coming from the dusk to pre-midnight sector and moving again toward dawn from 2000 UT on 5 April to 1200 UT on 6 April. These trends in MLT are the result of the orbits of the conjugate THEMIS and GOES spacecraft. Since we only use IB observations that were conjugate with at least one of these spacecraft, the IB observations used in our analysis move counterclockwise over time, following the counterclockwise motion of the GOES and THEMIS orbits. Since the POES and METOP satellites use sun-synchronous orbits, their orbital trajectory does not cause trends in MLT in this manner. Since IB latitude is known to vary with MLT (e.g. *Ganushkina et al.*, 2005, *Lvova et al.*, 2005, *Asikainen et al.*, 2010, *Dubyagin et al.*, 2018), these variations in MLT are probably responsible for some of the variations in IB latitude seen in Figure 5.4c, particularly the upward trend in latitude from 0000 UT to 1200 UT on 6 April, as well as for some of the spread in IB latitude.

The distances in Figure 5.4e reflect the latitudes shown in Figure 5.4c. Prior to

the onset of the storm (from 0300 to 0900 UT on 5 April), a slight upward trend is apparent in the mapping distances, which mirrors the upward trend previously noted in the IB latitudes. After the storm onset, clusters of points are found closer to the Earth, from 0800 to 1600 UT on 5 April a majority of the IB observations map to distances between 4 and 8 R_E, mirroring the clustering of IB observations between 61 and 64 degrees latitude during the same time. The increase in outliers observed in the IB latitudes after the onset of the storm at 0900 is also reflected in the mapping distances. Prior to storm onset, the farthest mapping distance is less than 20 R_E, while after the storm onset outlier points can be found as far as 100 R_E. The mapping distances are seen to decrease along with the latitudes between 2000 and 2400 UT on 5 April, increasing gradually until 1200 on 6 April, again following the same general trend as the IB latitudes during the same time. This correspondence between latitude and mapping distance is expected. For a dipole field, distance increases monotonically with increasing latitude of field line foot-points, and the stretched geometry of the nightside magnetosphere results in an even faster increase.

A similar correspondence with latitude can be seen in Figure 5.4c, but the behavior is reversed, with K apparently decreasing with increasing latitude. K values begin around 50-70 at 0300 UT, and trend downward as the IB latitudes increase. The storm onset at 0900 sees a large spread in K, with a few values approaching 100 but outliers occurring as low as 0.8. Some clusters of K values can be seen in the upper end of the K range, though the clustering tendency is not as pronounced as for the mapping distances. From 2000 to 2400 UT on 5 April the downward trend in IB latitude is mirrored by an upward trend in K, with values initially ranging from 7 to 20, and gradually increasing so that K at 2400 UT ranges from 40 to 100. K decreases from 0000 to 1200 UT on 6 April, ranging from 1 to 40 at 1200 UT.

The overall range of K from the SWMF simulations is shown in the first two rows of Table 5.2, which shows the total number of points, 25th percentile, median,

and 75th percentile of K for all the simulations together. The percentiles for $K = 8$ and $K = 12$ (i.e., the percentage of K values falling below $K = 8$ and $K = 12$) are also shown. The number of K estimates falling below these thresholds provides an estimate for what percentage of the IB's might have been formed by CSS. By using two different thresholds we are able to provide a rough estimate of the uncertainty range for this percentage. The $K_{Crit} = 8$ threshold, as discussed in the Introduction, was originally introduced by *Sergeev et al.* (1983) as a rough estimate of the threshold condition for CSS, and has been widely adopted by other researchers. In the present work, we adopt $K = 8$ as a probable low end of the uncertainty range for K_{crit}. For the upper end, we note that *Sergeev et al.* (2015a) found differences in the properties of IB's above and below $K = 12$, while *Dubyagin et al.* (2018) noted that 90% of points with $4.5 < K < 13$ fell within 1 R_E of where $K = 8$ in the TS05 model, and in Chapter IV we obtained corrected K values falling mostly below $K = 11$ for carefully chosen IB observations in quiet conditions. Considering that $K = 12$ is the median of these, we adopt it as a probable upper end of the uncertainty range for K_{crit}. Note that the results in Table 5.2 exclude points for which the mapping distance exceeded 15 R_E. The results in Table 5.2 are separated according to whether they were obtained from observations of the high-latitude (HL) or low-latitude (LL) boundary of the IB. The interquartile range extends from 8.18 to 30.9 for the HL set, and from 9.69 to 33.1 for the LL set, indicating that the K values less than one or approaching 100 are indeed outliers. Both the medians and the interquartile ranges of K are somewhat higher for the LL set, consistent with the tendency noted in the previous paragraph that increases in IB latitude are associated with decreases in K and vice versa.

The negative correlation between K and IB latitude can be explained by noting from Equation 4.3 that $K \propto B_z^2$. B_z near the equatorial plane decreases as $\frac{1}{r^3}$ in a dipole field, and faster than that in the nightside magnetosphere. This can result in

Model type	IB set	n	25th percentile	Median	75th percentile	K=8 percentile	K=12 percentile
			Uncorrected K				
SWMF	HL	254	8.18	16.7	30.9	23.6	35.0
SWMF	LL	339	9.69	18.9	33.1	20.1	32.7
Empirical	HL	254	3.93	10.3	15.9	40.2	57.9
Empirical	LL	273	6.01	12.3	20.0	31.5	48.0
Both	HL	508	6.32	13.0	22.4	31.9	46.5
Both	LL	612	7.98	15.4	27.9	25.2	39.5

Table 5.2: Values summarizing the distribution of K estimates.

an inverse relationship where K to decreases with increasing distance, resulting in the approximately inverse profile of K and distance seen in Figures 5.4b and 5.4c. However, for CSS-driven IB observations, K is directly related to the IB formation, so this relationship should be much weaker when CSS is the operative scattering mechanism *Dubyagin et al.* (2018).

Noting the quadratic dependence of K on B_z in Equation 4.3, we estimate the error in B_z at the locations were K was estimated by computing the B_z errors at each of the conjugate spacecraft for each IB observation, and averaging these estimated errors together. We denote the averaged error as $\overline{\Delta B_z}$. Figure 5.5 shows K as a function of $\overline{\Delta B_z}$ for the points from Figure 5.4 (including both hemispheres and both the HL and LL datasets) for all three MHD simulations. Results from each model run are depicted using the same color and marker scheme as Figure 5.4. A fit line is drawn in black on top of the points. Points that mapped farther than 15 R_E from the Earth have been excluded. As one would expect from Equation 4.3, K increases with increasing $\overline{\Delta B_z}$.

The second and third lines of Table 5.2 summarize the range of K obtained from the empirical models. K values from the HL IB boundary have a median of 10.3, while the LL values have a median of 12.3. Like the SWMF estimates of K, with

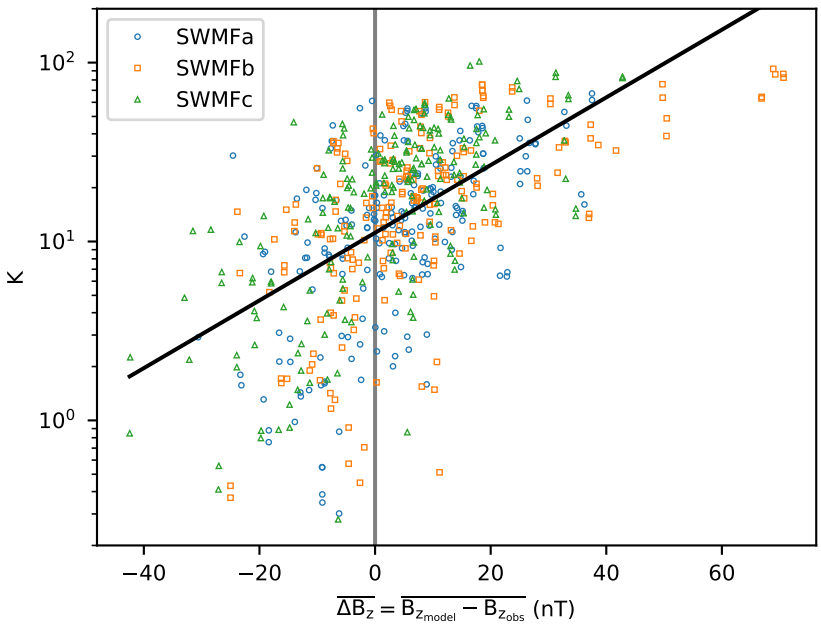

Figure 5.5: K as a function of $\overline{\Delta B_z}$ for all three MHD simulations. The black line shows a linear fit (in log space) to the data.

the median, 25th, and 75th percentiles are all higher for the LL boundary than for the HL boundary. K values at all three quartiles are lower than they are for SWMF, indicating a systematic tendency toward lower K values with the empirical models. On the other hand, the interquartile ranges overlap substantially between the two classes of models.

From Figure 5.5 it appears that the SWMF has a tendency to over-predict B_z, with a substantial fraction of the ΔB_z values falling between 0 and 20 nT. Most of the K values corresponding to this range of ΔB_z fall within the interquartile ranges shown in the first two rows of Table 5.2. Anomalously low K values ($K \lesssim 4$) appear only when $\Delta B_z \lesssim 12$. Despite the correlation between K and ΔB_z, K values seem to be constrained to $K \lesssim 100$, with K remaining below that threshold even for the largest overestimations of B_z.

Table 5.3 shows metrics for $\overline{\Delta B_z} = 0$, including the total number of points, the

Model	n	25th percentile (nT)	Median (nT)	75th percentile (nT)	$\overline{\Delta B_z} = 0$ percentile
SWMFa	199	-2.11	5.17	12.6	30.7
SWMFb	196	-3.89	5.38	14.3	31.1
SWMFc	198	-5.60	4.13	11.0	36.9
All SWMF	593	-4.57	5.15	12.7	32.9
T01	159	-11.8	-4.50	4.12	67.9
TS05	187	-4.07	1.99	7.78	42.8
TA16	181	-4.66	2.03	8.10	39.2
All empirical	527	-6.62	0.150	7.29	49.1

Table 5.3: Median, interquartile range, and percentage less than zero for $\overline{\Delta B_z}$.

25th percentile, median, 75th percentile, and the percentile at which $\overline{\Delta B_z} = 0$ (i.e., the percentage of points for which $\overline{\Delta B_z} \leq 0$). The median values are between 4 and 6 nT. This indicates that on average the SWMF simulations tend to overestimate ΔB_z, as noted earlier. The last column shows that the simulations overestimated B_z about 65-70% of the time. Given the correlation between K and ΔB_z, these overestimations of B_z probably reflect an overestimation of K as well.

In addition to the dependence on B_z, Equation 4.3 shows that K should depend on $G = \frac{\partial dB_r}{dz}$. Using the THEMIS magnetic field measurements we can estimate the gradient of B_r in the z direction, which depends on current sheet strength and thickness. Larger values of this gradient indicate either a thinner current sheet or stronger current. Using THEMIS spacecraft that are conjugate with an IB observation as, we estimate $G = \frac{dBr}{dz}$

$$G = \frac{B_{r_1} - B_{r_2}}{z_1 - z_2}, \tag{5.1}$$

where the subscripts 1 and 2 denote members of a pair of THEMIS spacecraft.

Figure 5.6 shows a time-series of observed magnetic fields at THEMIS A, D, and

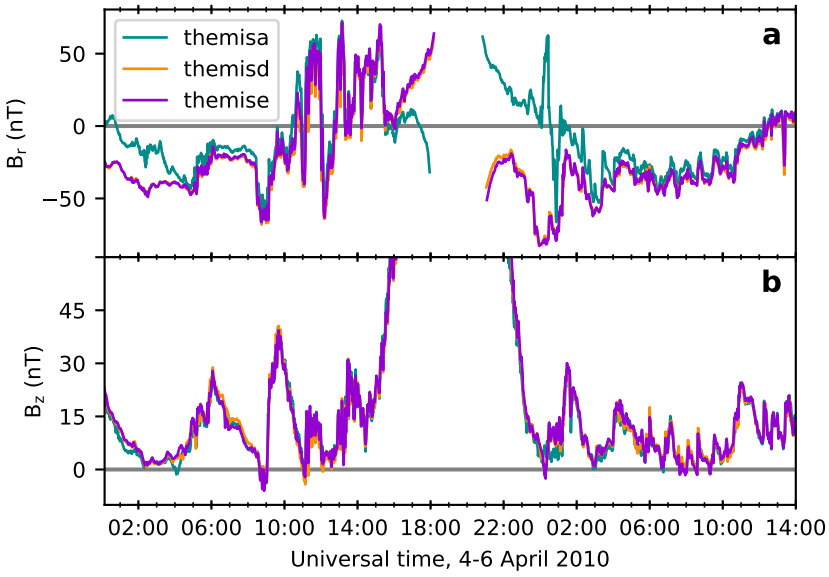

Figure 5.6: Observed magnetic fields at all THEMIS A, D, and E. Spacecraft are identified by color following the scheme of Figure 5.2. (a) B_r component (b) B_z component.

E, with B_r shown in Figure 5.6a and B_z shown in Figure 5.6b. The spacecraft are identified by color in the same manner as Figure 5.2. B_r was often quite different at THEMIS A than at THEMIS D or E, while values of B_z remained very close between all three spacecraft. On the other hand, it is not clear that the difference in B_r is always sufficient for accurate estimation of gradients in z. We therefore developed a procedure to determine whether the spacecraft are suitably positioned for accurate estimation of G. To this end, we define

$$\phi = \tan^{-1}\left(\frac{|z_1 - z_2|}{\sqrt{(x_1 - x_2)^2 + (y_1 - y_2)^2}}\right) \tag{5.2}$$

as an angle parameterizing the z-alignment of the two spacecraft, where x, y, and z are components of the spacecraft location in GSM coordinates. In addition, we define

$$\theta = \tan^{-1}\left(\frac{B_z}{\sqrt{B_x^2 + B_y^2}}\right), \tag{5.3}$$

which roughly corresponds to the distance from the neutral sheet.

To select pairs of spacecraft for G estimation we apply the following rules to the THEMIS spacecraft that are conjugate with each observed IB location:

1. If more than two spacecraft are conjugate with the IB, the pair with the smallest ϕ is selected.

2. Pairs for which $\phi > 45^\circ$ are rejected.

3. Pairs for which $\theta > 45^\circ$ at either satellite are rejected.

4. Pairs for which $\Delta z = |z_1 - z_2| < 0.2$ are rejected.

Table 5.4 shows metrics summarizing the distribution of $\Delta G = |G_{model}| - |G_{obs}|$, where $|G_{model}|$ is the estimate of $|G|$ obtained from one of the models and $|G_{obs}|$ is the estimate of $|G|$ obtained from observations (note that absolute values are used here because G is negative in the current sheet). The metrics shown are the same as those in Table 5.3. It is apparent that SWMFa tends to overestimate $|G|$, SWMFb has a slight tendency to underestimate, and SWMFc overestimates and underestimates with roughly equal frequency. When all three simulations are put together, we find that SWMF overestimates $|G|$ slightly more often than than it underestimates $|G|$, which suggests that the current sheet in the simulations is thinner and/or stronger than the real current sheet. Greater magnitude of G also implies a smaller R_c compared to reality, which would result in an underestimation of K.

5.5 Empirical results

In this work we use the following empirical magnetic field models: *Tsyganenko* (2002) (T01), *Tsyganenko and Sitnov* (2005) (TS05), and *Tsyganenko and Andreeva* (2016) (TA16). All three are available at `http://geo.phys.spbu.ru/~tsyganenko/modeling.html`. These models operate by computing a sum of analytical functions of a set of solar wind and geomagnetic activity parameters. In the case of T01

Model	n	25th percentile (nT/R_e)	Median (nT/R_e)	75th percentile (nT/R_e)	$\Delta G =$ 0 percentile
SWMFa	18	-0.961	7.82	16.4	27.8
SWMFb	20	-7.30	-1.42	1.25	60.0
SWMFc	18	-3.50	-0.00164	6.94	50.0
All SWMF	56	-5.78	0.300	10.9	46.4
T01	13	-13.1	-1.26	-0.305	76.9
TS05	12	-14.1	-6.60	0.600	66.7
TA16	12	7.21	9.39	19.1	16.7
All empirical	37	-13.1	-1.18	7.21	54.1

Table 5.4: Median, interquartile range, and percentage less than zero for $\Delta|G|$.

and TS05 these functions represent specific current systems, while in TA16 they are radial basis functions with no correspondence among the known current systems in the magnetosphere.

We now describe some of the features of these models that are relevant to estimating K. In the T01 model, the current sheet thickness is constant, but the inner edge of the tail current moves Earthward with increasing activity, and the tail current radial profile is controlled by two independent sub-modules.

The TS05 model was designed specifically to model storm-time conditions, and it was constructed by fitting to data from storm periods. The position and thickness of the TS05 tail current vary with activity, and are parameterized by a complex integral functions of the time history of solar wind parameters.

While the T01 and TS05 models used pre-determined functions to define the magnetospheric current systems, the TA16 model replaces these ad hoc functions with a sum of radial basis functions controlled by driving parameters (*Newell et al.*, 2007). This avoids imposing assumptions about the form of the current systems through the choice of fitting functions. However, the limited number of observations available for fitting precludes resolving fine spatial structures by this method.

We traced field lines from the IB locations (in AACGM coordinates) using each of these models, and with a dipole representation for intrinsic field of the Earth. Geopack was used to perform the actual tracing of the field lines. As with the SWMF simulations, $K = \frac{R_c}{r_g}$ was estimated at the point of maximum distance from the Earth along each field line, using the cutoff energies from Table 5.1 to estimate r_g and Equation 4.1 to estimate R_c. The output from the models was also computed at the locations of the THEMIS spacecraft for comparison with observations.

Figure 5.7 shows the K values obtained from the empirical models as a function of $\overline{\Delta B_z}$, which as with the SWMF simulations represents the model error in B_z, averaged over the THEMIS spacecraft that were conjugate with each IB observation. Points from T01 are shown as red diamonds, TS05 as purple right-pointing triangles, and TA16 as brown left-pointing triangles. As with Figure 5.5, the plot includes both the HL and LL datasets, and points that mapped farther than 15 R_E have been excluded. A least-squares fit (in log-space) through all the points is shown in black. It appears that the three models performed similarly, and a general similarity with the SWMF simulations is also apparent, although the K values are somewhat lower and the tendency to overestimate B_z is less pronounced.

Table 5.3 shows that the TS05 and TA16 models tend to overestimate B_z more often than not (about 57-60% of the time), while the T01 model underestimates B_z about 70% of the time. The medians mirror this tendency. This suggests that the T01 fields may be over-stretched, while the TS05 and TA16 fields are likely under-stretched. Over-stretching leads to IB observations mapping farther down-tail, resulting in smaller values of K because B_z becomes weaker $|G| = |\frac{dB_r}{dz}|$ becomes larger at greater distances down-tail.

Table 5.4 shows that the T01 and TS05 models tends to underestimate $|G|$, while the TA16 model tends to overestimate $|G|$. This suggests that the TA16 model produces a thinner or stronger current sheet compared with reality, while the current

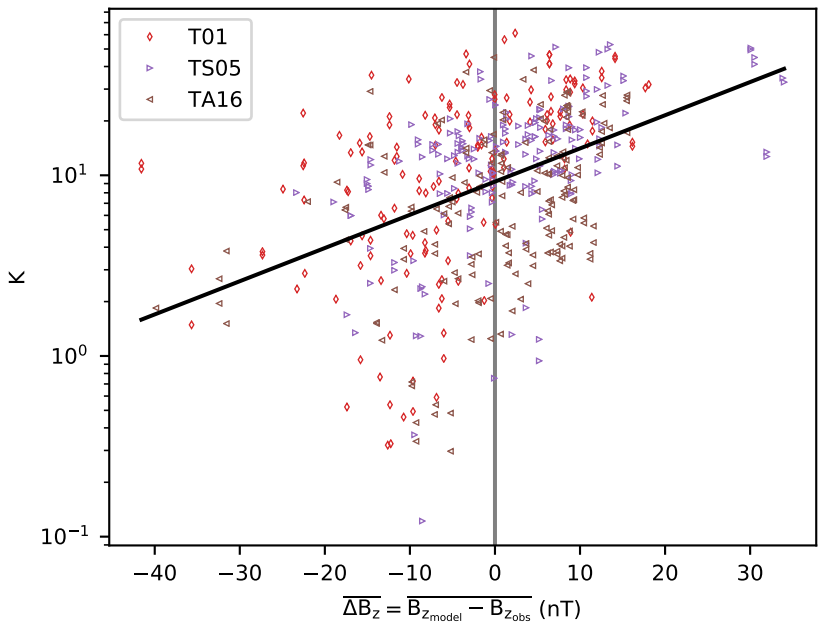

Figure 5.7: K as a function of $\overline{\Delta B_z}$ for the empirical models. The black line shows a linear fit (in log space) to the data.

sheets in the T01 and TS05 models are thicker and/or weaker than actual. When the results for all three empirical models are combined together, we find slightly (8.2%) more underestimations than overestimations of $|G|$, consistent with a thicker and/or weaker current sheet compared with reality. It is expected that these underestimations of $|G|$ lead to overestimation of K, since larger $|G|$ implies greater R_c.

5.6 K correction

We have seen that both the SWMF simulations and the empirical models have appreciable inaccuracies with respect to the observed magnetic fields. However, both the SWMF simulations and the empirical models exhibit a positive correlation between K and $\overline{\Delta B_z}$, which is consistent with the quadratic relationship between K and B_z seen in Equation 4.3. This relationship enables us to correct the model-derived K values for the known errors in B_z, using the correction procedures to obtain a cor-

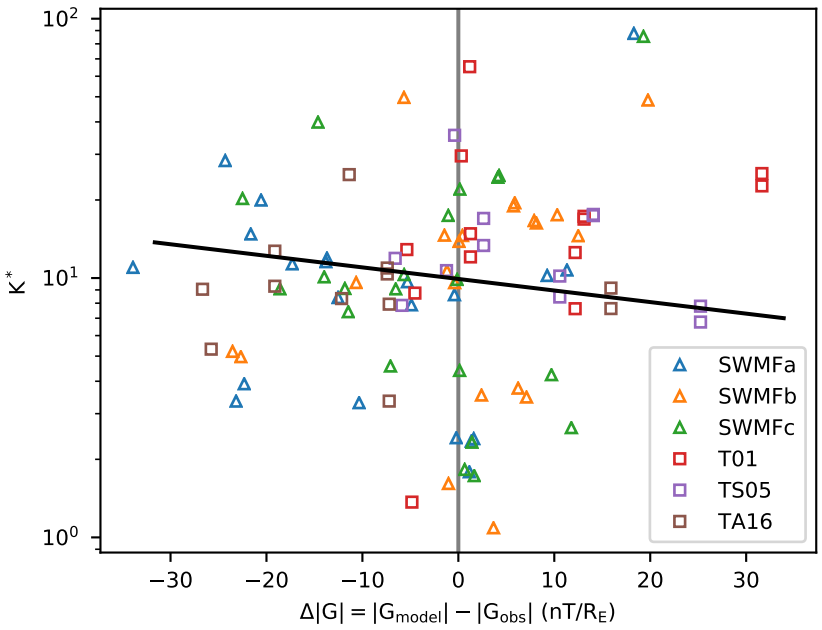

Figure 5.8: K^* as a function of $\Delta|G|$, the estimation error in the derivative $|G| = |\frac{dB_r}{dz}|$. Both the SWMF simulations and the empirical models are shown. Black line denotes a least-squares fit to the data in log space.

rected value K^* as described in Section 4.7. The $G = \frac{dB_x}{dz}$ estimates obtained using the THEMIS spacecraft enable an additional correction, K^{**}, the derivation of which is also described in Section 4.7.

Figure 5.8 shows K^* as a function of $\Delta|G| = |G|_{model} - |G|_{obs}$. Both G_{model} and G_{obs} are obtained using Equation 5.1. MHD simulations are plotted using triangles, and empirical models using squares, with their colors identifying individual simulations or models following the color schemes from Figures 5.5 and 5.7. A log-linear fit through all the data points is drawn in black.

From Figure 5.8 it is apparent that higher K^* values are associated with lower $\Delta|G|$, as expected from Equation 4.3. This correlation indicates that correcting for $\Delta|G|$ is likely to have an affect on the K estimates (though the correlation is weak so the effect may not be large). This enables us to correct simultaneously for $\overline{\Delta B_z}$ and ΔG by fitting Equation 4.11 and computing K^{**} from Equation 4.13.

Model type	IB set	n	25th percentile	Median	75th percentile	K=8 percentile	K=12 percentile	y-axis intercept	Intercept 95% CI
				Uncorrected K					
SWMF	HL	254	8.18	16.7	30.9	23.6	35.0	–	–
SWMF	LL	339	9.69	18.9	33.1	20.1	32.7	–	–
Empirical	HL	254	3.93	10.3	15.9	40.2	57.9	–	–
Empirical	LL	273	6.01	12.3	20.0	31.5	48.0	–	–
Both	HL	508	6.32	13.0	22.4	31.9	46.5	–	–
Both	LL	612	7.98	15.4	27.9	25.2	39.5	–	–
				K^* *correction*					
SWMF	HL	254	7.21	12.8	20.3	29.1	43.3	11.5	[10.3, 12.8]
SWMF	LL	339	8.26	14.9	24.6	23.3	39.2	13.6	[12.4, 14.9]
Empirical	HL	254	4.99	9.61	15.7	42.5	62.6	7.87	[7.01, 8.83]
Empirical	LL	273	6.95	12.7	19.3	31.1	46.9	10.7	[9.54, 11.9]
Both	HL	508	5.61	10.8	17.1	36.4	54.3	9.35	[8.62, 10.1]
Both	LL	612	7.54	13.8	21.5	27.3	43.3	12.1	[11.3, 13.0]

Table 5.5: Values summarizing the distribution of K and K^*.

Table 5.5 shows statistics for K and K^*. Data are shown for the SWMF simulations, empirical models, and both together. Each is further broken down into results for the HL and LL IB observations. The total number of points, 25th percentile, median, and 75th percentiles are given for each. These are followed by the percentile corresponding to $K = 8$ and $K = 12$, i.e., the percentage of IB observations for which $K \leq 8$ and $K \leq 12$. As discussed earlier, using this pair of thresholds provides a means to roughly estimate how uncertainty in the K threshold impacts uncertainty in the estimate of how many of the IB observations could have been formed by CSS. For K^* and K^{**}, the y-axis intercept from the fit of Equation 4.5 or 4.11, as appropriate, is also given, along with its 95% confidence interval. The intercepts provide an estimation of what the average value of K would be in the case of zero magnetic field error.

From the values in Table 5.5, it is apparent that the SWMF tends to produce higher values of K (as indicated by the higher median and interquartile ranges) com-

pared with the empirical models. The K^* correction tends to produce smaller values compared with the uncorrected K values, while also reducing the amount of difference between the SWMF and the empirical model results compared with K.

The values in Table 5.5 also show that the LL IB observations tended to be associated with larger values of K and K^* compared with the HL observations. Each of the rows of the table showing data from the LL set has a higher median than the corresponding row from the HL set. For instance, the SWMF K estimations for the HL set have a median of 16.7, while those from the LL set have a median of 18.9. Similarly, the empirical model estimations for the HL set have a median of 10.3, while those for the LL set have a median of 12.3. This is consistent with the expected relationship between K and latitude discussed earlier.

The $K = 8$ and $K = 12$ percentiles in Table 5.5 provide an estimate of what fraction of the IB observations might have been produced by current sheet scattering (for which $K \lesssim 8 - 12$ is expected). The remaining IB observations (those for which $K \gtrsim 8 - 12$) could potentially be the result of EMIC wave interactions. For SWMF, 23.6% of the uncorrected HL K values fall below $K = 8$, and 35.0% fall below $K = 12$; for the LL set it is 20.1% and 32.7%. For the empirical models 40.2% of the values from the HL set are below $K = 8$ and 52.8% are below $K = 12$, while for the LL set it is 31.5 and 48.0. The K^* correction increases the number of SWMF estimates that fall below the $K = 8$ and $K = 12$ thresholds, to 29.1% and 43.3%, respectively, for the HL set, and 23.3% and 39.2%, respectively, for the LL set. The K^* correction has a less significant effect on the empirical model results, with the percentages below the $K = 8$ and $K = 12$ thresholds changing by no more than 3% compared with the uncorrected K.

Table 5.6 shows the effect of the K^{**} correction, in the same format as Table 5.5. Values for K and K^* are shown as well, now restricted to only those IB's for which G estimation was performed to enable comparison with K^{**}. It can be seen that the

Model type	IB set	n	25th percentile	Median	75th percentile	K=8 percentile	K=12 percentile	y-axis intercept	Intercept 95% CI
				Uncorrected K					
SWMF	HL	24	3.98	10.6	15.0	37.5	58.3	–	–
SWMF	LL	32	6.60	13.1	18.7	28.1	46.9	–	–
Empirical	HL	18	7.21	10.8	14.2	38.9	55.6	–	–
Empirical	LL	19	9.27	14.3	19.1	15.8	36.8	–	–
Both	HL	42	6.53	10.6	14.6	38.1	57.1	–	–
Both	LL	51	8.03	13.6	19.1	23.5	43.1	–	–
				K^* correction					
SWMF	HL	24	4.71	9.19	10.9	41.7	79.2	7.44	[5.49, 10.1]
SWMF	LL	32	7.17	11.9	16.1	31.3	50.0	10.6	[7.46, 15.1]
Empirical	HL	18	7.56	10.2	13.6	44.4	61.1	9.83	[7.64, 12.6]
Empirical	LL	19	9.55	12.5	16.5	15.8	42.1	13.1	[8.75, 19.5]
Both	HL	42	7.13	9.33	11.9	38.1	76.2	8.45	[6.93, 10.3]
Both	LL	51	8.35	12.5	16.2	23.5	47.1	11.4	[8.80, 14.7]
				K^{**} correction					
SWMF	HL	24	4.99	9.37	11.3	37.5	79.2	7.54	[5.38, 10.6]
SWMF	LL	32	7.67	13.4	16.5	28.1	40.6	10.8	[7.65, 15.3]
Empirical	HL	18	8.04	10.5	12.6	27.8	61.1	9.46	[7.45, 12.0]
Empirical	LL	19	10.3	13.7	15.5	15.8	42.1	12.8	[8.41, 19.4]
Both	HL	42	6.87	9.84	12.4	31.0	69.0	8.60	[7.07, 10.5]
Both	LL	51	8.62	13.4	15.7	19.6	39.2	11.3	[8.81, 14.6]

Table 5.6: Summary of the properties of K

K^{**} values tend to be marginally greater than the K^* values, and this results in a reduction in the fraction of points falling below the $K = 8$ and $K = 12$ thresholds. The median values for SWMF increase from $K^* = 9.19$ to $K^{**} = 9.37$ (HL) and from $K^* = 11.9$ to $K^{**} = 13.4$ (LL), while the median value for the empirical models increases from $K^* = 10.2$ to $K^* = 10.5$ (HL) and from $K^* = 12.5$ to $K^* = 13.7$ (LL).

Figure 5.9 shows the distributions of K before and after correction, represented using kernel density estimation (KDE, *Parzen*, 1962). A KDE approximates a PDF by convolving a set of discrete points with a Gaussian kernel. The resulting plot can be interpreted in much the same way as a normalized histogram. The high-latitude (HL) IB data is shown in blue, and low-latitude (LL) IB data is shown in orange.

Only IB observations for which G estimations were available are included. Figure 5.9a shows the distribution of K values estimated by SWMF, while Figure 5.9b shows the corresponding distribution of K^*, and Figure 5.9c shows the distribution of K^{**}. Figures 5.9d, 5.9e, and 5.9f show K, K^*, and K^{**} for the empirical models, while Figures 5.9g, 5.9h, and 5.9i show the results of combining the SWMF and empirical results into a single dataset and computing K^* and K^{**} for the combined dataset.

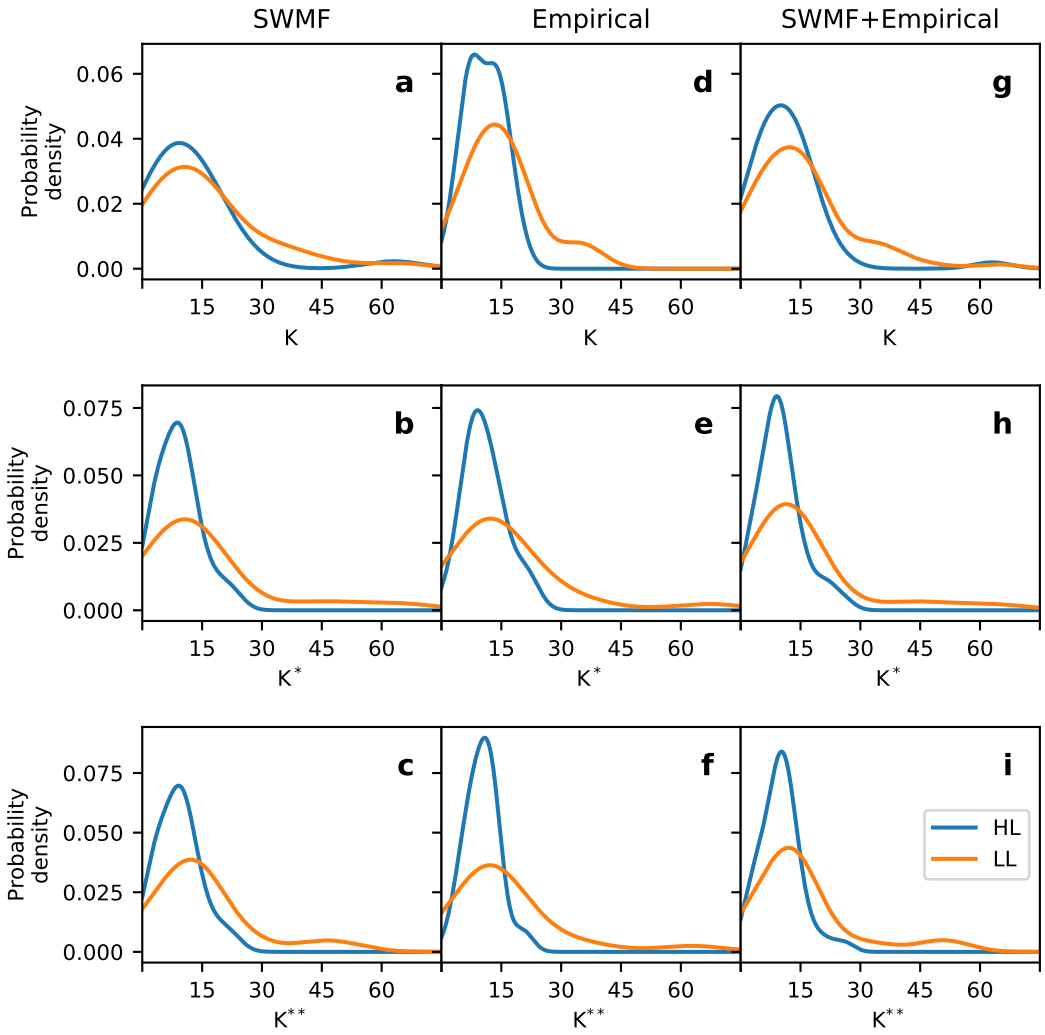

Figure 5.9: Distributions of (a) K and (b) K^* for all three MHD simulations. The distributions have been separated according to whether the observations came from the high-latitude or the low-latitude edge of the IB.

The empirical models (Figures 5.9d, 5.9e, and 5.9f) produce smaller values nar-

rower distributions of K compared with SWMF (Figures 5.9a, 5.9b, and 5.9c). For both classes of models, the K^* correction (Figures 5.9b, 5.9e, and 5.9h) produces a narrower distribution for the HL set compared with the uncorrected K values (Figures 5.9a, 5.9d, and 5.9g). However, for the LL set the opposite is true, with the SWMF distribution being relatively unaffected and the empirical distribution being widened appreciably. The K^{**} correction (Figures 5.9c, 5.9f, and 5.9i) seems to have relatively little effect, with the empirical HL distribution being narrowed slightly and the others largely unaffected. In all the distributions of Figure 5.9, a subtle but perceptible difference can be seen between the LL and HL data. For values of K, K^*, and K^{**} greater than about 20, the probability density is higher for the LL set than for the HL set, while for values less than this, the probability density is higher for the HL set than for the LL set. This means that the LL points tend to be associated (to a slight degree) with higher values of K. This is consistent with the tendency previously noted in Table 5.5. When the K^* correction (Figures 5.9b, 5.9e, and 5.9h) or K^{**} correction (Figures 5.9c, 5.9f, and 5.9i) is applied, the same pattern is seen that LL observations are associated with higher values, and the effect is more pronounced for the corrected values.

5.7 Discussion

The goal of this study is to test what fraction of observed IB's during the storm on 4-6 April 2010 may have been the result of CSS. To accomplish this, we estimated $K = \frac{R_c}{r_g}$ associated with ion isotropic boundary observations. K provides a measure of the effectiveness of the CSS process at a particular location. We used MHD and empirical models to trace field lines from the IB observation locations to the magnetotail, and to estimate K where those field lines cross the current sheet. We then corrected our K estimations for errors in the model magnetic fields that could be quantified with in situ observations from spacecraft in the magnetotail. By correcting for these errors,

and by using of multiple models to estimate K, we are able to constrain the possible range of K. This is the first study to explore IB properties using an MHD model during storm conditions.

A number of previous studies have noted a tendency for SWMF to produce under-stretched magnetic fields on the night side. As discussed in Section 5.4, this is expected to result in overestimation of K. *Glocer et al.* (2009b) found that SWMF overestimated B_z at GOES spacecraft during a storms on 4 May 1998 and 31 March 2001, though they also found that this could be improved by coupling a wind model to BATS-R-US. *Ganushkina et al.* (2010) showed that SWMF overestimated B_z at GOES spacecraft during storms on 6-7 November, 1997 and 21-23 October, 1998. *Ilie et al.* (2015) reported over-prediction at GOES, Geotail, and THEMIS spacecraft during a quiet interval on 13 February, 2009, Chapter IV showed this for different simulations of the same event. In the present study we find this tendency as well, with all three simulations overestimating $\overline{\Delta B_z}$ for about 65-70% of the IB observations.

The amount of tail stretching in TA16 was previously reported to be similar to the older T89 model (*Tsyganenko and Andreeva*, 2016), which in turn has been reported as producing over-stretched fields in the magnetotail (*Tsyganenko*, 1989, *Peredo et al.*, 1993). In Chapter IV we found under-stretched fields for T01 and over-stretched fields in TS05 and TA16. Results in the present work show a slight tendency toward over-stretching in T01, but a slight tendency toward under-stretching in TS05 and TA16, based on errors in B_z relative to in situ observations.

Compared with SWMF, the empirical models tend to produce smaller values of K, consistent with the tendency noted above of under-stretched fields in SWMF and over-stretched fields in the empirical models. However, the distributions of K overlap significantly between the two classes of models even before correction. This is different from the quiet-time results of Chapter IV, which included non-overlapping distributions of uncorrected K, with the empirical models tending toward quite small

values of K and the SWMF K values uniformly above 10. The overlapping distributions reflect the presence of much higher K estimates (on average) coming from the empirical models compared with Chapter IV, along with marginally lower K estimates from SWMF and broader distributions for both classes of models. The broader distributions are probably the result of using less restrictive selection criteria for the IB observations, as well as storm-time variability. Storm conditions likely increase the range of K estimates both by causing the true value of K to vary more broadly (due to EMIC scattering, as well as producing CSS under a wider variety of conditions). Storm conditions also create rapidly varying dynamics which the models are not always able to reproduce, contributing to errors in magnetic field configuration and causing randomly varying errors in K.

The results in Chapter IV made it clear that errors in the magnetic field models can affect K values significantly, but also that such errors, if quantified, can be corrected for effectively. However, it should be noted that the corrections provide only a rough estimate of the true value of K. These corrections are subject to a number of sources of uncertainty, including errors due to the linearization of the expression for K, the position of satellites relative to where K is actually estimated, and the fact that our correction procedure involves a fit to numerous K estimates from numerous IB observations, each of which came from a different time, with a different magnetospheric state and different satellite positions for each. By fitting all of these points together we find the average relationship between the magnetic field errors and K estimates. The true relationship between the two probably varies with the magnetospheric state and the satellite positions, which our correction procedure does not account for. With the ΔB_z estimates there is a potential issue with the GOES magnetometer data in that it may contain offsets of unknown magnitude. In addition, the estimation of G is subject to additional errors since the spacecraft used to compute the gradient in z are generally not positioned exactly in the z direction

relative to each other. The amount of separation between them in the z direction can also affect the accuracy of the gradient estimates, since separation that is too close may result in a gradient that effectively measures local structure within the current sheet rather than the overall behavior of the current sheet, while separation that is too large results in an average gradient over a long distance, which might not be representative of the gradient across the current sheet if one or both spacecraft is located too far away from the current sheet. We attempt to maximize the accuracy of our gradient estimates by selecting spacecraft pairs according to the criteria in Section 5.4, but the amount of accuracy provided using these criteria depends on local conditions that are not fully known.

Despite these sources of uncertainty, there are indications that the correction procedure is successful in removing much of the difference between the two classes of models. The distributions of K become narrower and substantially more similar to each other after correction, and for K^{**}. While we have no ground-truth measurement with which to test our K estimations, we interpret the similarity between the distributions of K obtained by very different types of models as a sign that both are likely reproducing the major characteristics of the true K distribution.

In addition to checking the K values to determine whether they are below the threshold for CSS, we can also check for a dependence on MLT as an indication of whether CSS is the mechanism responsible for IB formation. EMIC scattering has been noted to been noted to contribute significantly to proton precipitation in the dusk sector (e.g. *Fuselier*, 2004, *Yahnin and Yahnina*, 2007, *Zhang et al.*, 2008). A number of previous studies have found a noon-midnight asymmetry in IB latitude (e.g. *Sergeev et al.*, 1993, *Ganushkina et al.*, 2005, *Asikainen et al.*, 2010, *Yue et al.*, 2014), along with a tendency for IB latitude to decrease as Sym-H becomes more negative (e.g. *Hauge and Söraas*, 1975, *Søraas et al.*, 2002, *Ganushkina et al.*, 2005, *Lvova et al.*, 2005, *Asikainen et al.*, 2010, *Dubyagin et al.*, 2018). In most cases the noon-

midnight asymmetry in latitude is accompanied by a weaker dawn-dusk asymmetry, with the minimum IB latitude occurring around 23 MLT. Figure 5.10a shows the latitude of our IB observations as a function of MLT, colored by Sym-H*. Both the noon-midnight and dawn-dusk asymmetries are visible, along with the correlation with Sym-H. Figure 5.10b shows K^* as a function of MLT, again colored according to Sym-H*. SWMF results are plotted with triangles and empirical models with squares. Figure 5.10 shows that the K^* correction exhibits none of the trends found in the IB latitude, which is consistent with CSS playing a significant role in IB formation since it suggests that K is controlling the IB latitude and not the other way around (as would be the case for EMIC scattering). Note however that the MLT dependence shown in Figure 5.10 is affected by the motions of the GOES and THEMIS satellites since we use only IB observations that are conjugate with those spacecraft.

Based on our K estimates, between roughly 31% (corresponding to $K^{**} < 8$) and 69% (corresponding to $K^{**} < 12$) of our HL IB observations could be the result of CSS, while between 20% and 39% of our LL IB observations could be the result of CSS. Of course, the true percentage of IB's meeting the threshold condition for CSS could be higher or lower depending on the accuracy of the K estimates. The lack of MLT or Sym-H dependence for K suggests that the CSS may be the responsible mechanism for a majority of the IB's, which implies that $K < 12$ (or perhaps a somewhat higher threshold) may be a sufficient condition for CSS to operate.

The conclusions of the chapter can be summarized as follows:

1. By correcting each K estimate using in situ observations from 2-3 conjugate satellites in the current sheet, we were able to produce highly consistent results, with nearly identical distributions of K obtained using two different classes of models.

2. Based on the assumption that CSS occurs when $K < 8 - 12$, between 31% and 69% of the upper poleward boundary IB observations and between 20% and

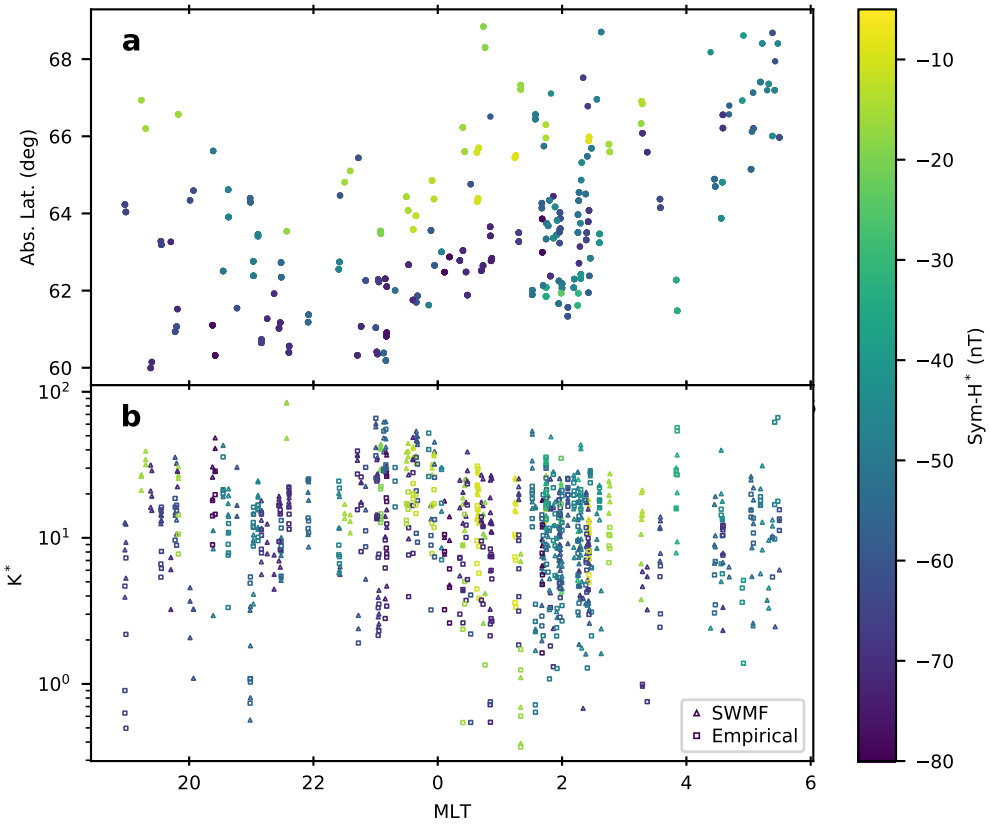

Figure 5.10: (a) IB latitude as a function of MLT, colored by Sym-H*, (b) K^* as a function of MLT, colored by Sym-H*.

39% of the equatorward boundary IB observations may be the result of CSS.

3. We find no correlation between K^* and Sym-H* or MLT, supporting the hypothesis that CSS played a significant role in forming the observed IB's.

This chapter and the preceding one both explored the degree of magnetotail stretching exhibited in SWMF, in empirical models, and in observations, during both quiet and storm conditions. Magnetotail stretching plays an important role in magnetospheric substorms. As was discussed in Chapter I, solar wind energy accumulates in the magnetotail prior to substorm onset, and this accumulated energy results in an overly stretched magnetic field geometry. This process can occur in MHD models as well, and this has led to the use of MHD models to explore many aspects of substorm dynamics. Chapter VI tests the ability of SWMF to reproduce observed substorm onset times during the 1-month period shown in Chapter III.

CHAPTER VI

Capability of model to predict substorms

6.1 Introduction

The preceding chapters explored many aspects of magnetospheric dynamics. Chapter III explored the behavior of geomagnetic indices during storm and quiet conditions, and Chapters IV and V explored the amount of magnetotail stretching during storm and quiet conditions. Throughout these, it was shown that the SWMF (Space Weather Modeling Framework) is able to reproduce many measures of magnetospheric behavior during both storm and quiet conditions. This chapter uses one of the simulations from Chapter III to test SWMF's ability to consistently reproduce the observed characteristics of substorms.

Geomagnetic substorms consist of an explosive release of stored solar wind energy from the magnetotail, much of which is deposited in the ionosphere. Originally they were observed as an auroral phenomenon (*Akasofu*, 1964), consisting of sudden brightening of auroral emissions accompanied by rapid changes in their spatial distribution. It is now recognized that a rapid reconfiguration of the night-side magnetic field, consisting of a plasmoid release and dipolarization, is a fundamental component of the substorm process. It is widely accepted that the plasmoid release coincides with the formation of field-aligned currents, termed the substorm current wedge, connecting the auroral zone to the magnetotail (e.g. *Kepko et al.*, 2015). When the concept

of the current wedge was first introduced, it was imagined as a pair of equal and opposite currents entering and exiting the ionosphere at the same latitude but different longitudes. More recent work has shown evidence that the upward and downward currents may overlap in longitude (*Clauer and Kamide*, 1985), and that the real structure may involve multiple filaments of upward and downward current (*Forsyth et al.*, 2014), possibly organized into localized regions of flow-driven current termed "wedgelets" (*Liu et al.*, 2013). However, some doubt has been cast on the wedgelet model (*Forsyth et al.*, 2014), and the manner in which wedgelets might contribute to filamentation remains an open question (*Kepko et al.*, 2015). Similarly, the behavior of the earthward flow upon arrival at the inner magnetosphere has not been clearly determined from observations (*Sergeev et al.*, 2012). A major factor limiting progress on these questions is a lack of sufficient observational data, due to the need for simultaneous observations in particular locations, or simply the need for more complete spatial coverage of the magnetosphere. Global magnetohydrodynamic (MHD) models have the potential to provide insights into the current and velocity distributions that would require an impractically large number of spacecraft to obtain using observations alone, as has been demonstrated already by a number of studies (e.g. *Ohtani and Raeder*, 2004, *Birn and Hesse*, 2013, *El-Alaoui et al.*, 2009). MHD models also have the potential to address a number of open questions about cause/effect relationships regarding substorms. For instance, the question of how substorm onset is influenced by solar wind conditions has not been fully resolved, with some holding that some or all substorms are "triggered" by changes in solar wind conditions (e.g. *Caan et al.*, 1977, *Lyons et al.*, 1997, *Russell*, 2000, *Hsu and McPherron*, 2003, 2004, *Newell and Liou*, 2011), and others claiming that the observed characteristics of substorms can be explained without invoking solar wind triggering (e.g. *Morley*, 2007, *Wild et al.*, 2009, *Freeman and Morley*, 2009). Similarly, the question of where a substorm originates in geospace (magnetotail, ionosphere, or somewhere else) has remained open

for a number of years (e.g. *Korth et al.*, 1991, *Angelopoulos et al.*, 2008, *Rae et al.*, 2009, *Henderson*, 2009). The capability of MHD models to provide a global, spatially resolved picture of the magnetosphere has been used in previous studies to shed light on such cause and effect relationships (e.g. *Zhu et al.*, 2004, *Raeder et al.*, 2010). However, such results have been limited to single event studies or idealized test cases, which leaves open questions about the degree to which MHD models can reproduce substorm dynamics consistently and reliably. Despite years of application of MHD models to substorms, no MHD model has been rigorously validated with regard to its ability to predict substorm onsets.

Validating any model (MHD or otherwise) for substorm prediction is complicated by the fact that substantial disagreement remains within the community about what constitutes a substorm. While a general consensus exists around some of the main features of substorms, the community has not developed a definition for the term "substorm" that is unambiguous, comprehensive, and widely agreed upon. This remains the case despite decades of attempts to clarify the salient characteristics of substorms (e.g. *Rostoker et al.*, 1980, *Rostoker*, 2002). As a result, different researchers studying the same time period often come to substantially different conclusions about what events should be considered substorms. A major factor contributing to the sometimes discordant results obtained is the fact that substorms produce numerous observational signatures, most of which have substantial limitations. Although a substorm widely is viewed as a global phenomenon, many of its effects are localized in a particular region. As a result, gaps in observational data can easily prevent detection of a substorm. The sparse distribution of ground-based magnetometers can result in negative bay onsets not being detected (*Newell and Gjerloev*, 2011a). Dipolarizations and plasmoids can only be detected when a satellite is on the night side of the Earth and in the right range of distance, MLT sector, and latitude. Moreover, a plasmoid that propagates too slowly relative to the observing spacecraft might go unnoticed

(*Nishida et al.*, 1986). At the same time, many observational features used to identify substorms can be caused by other phenomena. For instance, single-satellite observations may not be able to distinguish a plasmoid from other transient features in the current sheet (such as thickening, thinning, or bending) (*Eastwood et al.*, 2005). A storm sudden commencement can result in a negative bay at auroral magnetometers (*Heppner*, 1955, *Sugiura et al.*, 1968), as can a pseudobreakup (*Koskinen et al.*, 1993, *Ohtani et al.*, 1993, *Aikio et al.*, 1999) (although there is no clear threshold distinguishing a substorm from a pseudobreakup (*Aikio et al.*, 1999), and some researchers define a pseudobreakup as an expansion onset that lacks a negative bay enhancement (*Nakamura et al.*, 1994)). A discussion of the challenges faced by researchers in distinguishing different magnetospheric phenomena from each other can be found in *McPherron* (2015).

Differences in results obtained when different observational datasets are used can be substantial. An illustrative example is *Boakes et al.* (2009), which compared substorm onsets previously published by *Frey et al.* (2004) based on analysis of auroral images with energetic particle observations at geosynchronous orbit. *Boakes et al.* (2009) found that 26% of the auroral expansion onsets had no corresponding energetic particle injection even though a satellite was in position to detect such an injection, and suggested that such events might not be substorms.

The difficulty in positively identifying substorm onsets presents a problem for validation of substorm models. In the absence of a definitive substorm onset list against which to validate a model, those seeking to validate a substorm prediction model are left to choose among the published lists, or create a new one. Given the substantial differences between the existing onset lists, validation against any single onset list leaves open the question of whether the validation procedure is testing the model's ability to predict substorms, or merely the model's ability to reproduce a particular onset list, whose contents may or may not really be substorms.

One potential way to address the problems of onset list accuracy is to use multiple substorm signatures in combination, checking them against each other to prevent false positives or missed identifications. Comparing two or three substorm signatures by hand for individual events has been commonplace since the beginning of substorm research (e.g. *Akasofu*, 1960, *Cummings and Coleman*, 1968, *Lezniak et al.*, 1968), and a number of researchers have produced statistics comparing onset lists for two or more substorm signatures (e.g. *Moldwin and Hughes*, 1993, *Boakes et al.*, 2009, *Liou*, 2010, *Chu et al.*, 2015, *Forsyth et al.*, 2015, *Kauristie et al.*, 2017). *McPherron and Chu* (2017) demonstrated that a better onset list could be obtained using the midlatitude positive bay (MPB) index and the SML index together than by using either dataset alone.

Despite an awareness within the community that multiple observational signatures are required to positively identify a substorm, the work of *McPherron and Chu* (2017) has been the only one to date to use multiple signatures to create a combined onset list, and no attempt to create an onset list using more than two different signatures has been published. This may in part be due to the complexities involved in doing so. As was discussed earlier, the absence of a particular signature does not always indicate the absence of a substorm, while at the same time some identified signatures may not in fact be substorms. Ideally a combined list should somehow allow for these possibilities and correct for them. Further complicating matters is the fact that different signatures may be identified at different times for the same substorm.

In the present work we present a new procedure which uses multiple substorm signatures to identify substorm onsets. By using multiple datasets consisting of different classes of observations, we reduce the risk of missing substorms due to gaps in individual datasets. At the same time, the new procedure aims to reduce false identifications by only accepting substorm onsets that can be identified by multiple methods. Our procedure is generalizable to any combination of substorm onset

signatures, and allows for the possibility that the signatures may not be precisely simultaneous. We demonstrate the technique on observational data from January, 2005 and on output from an MHD simulation of the same the same time period. We present evidence that the procedure is successful at reducing false identifications while avoiding missed identifications due to observational data gaps, and that the resulting onset list is consistent with the known characteristics of substorms. Finally, we show preliminary evidence of predictive skill on the part of the MHD model.

6.2 Methodology

6.2.1 Identification of substorm events from combined signatures

Our procedure for combining multiple substorm onset lists consists of first convolving each onset list with a Gaussian kernel, then adding together the convolutions from all the onset lists to produce a nominal "substorm score." For a series of onset times τ_{ij} from a set of onset lists i, this score is given by

$$f(t) = \sum_{i=1}^{n_{sigs}} \sum_{j=1}^{n_{onset}} \exp\left(-\frac{(t-\tau_{ij})^2}{2\sigma^2}\right), \tag{6.1}$$

where σ is a tunable kernel width. The i's each represent a particular substorm onset list. The onset lists each represent a distinct substorm signature and are described in detail in Sections 6.2.4 and 6.2.5. The j's represent the onset times in each onset list. To obtain a list of onset times, we search for local maxima in this score, and keep any maxima that rise above a specified threshold. If the score remains above the threshold for the entire time between two maxima, the higher of the two is kept and the smaller one is discarded. If we choose a threshold greater than one, we effectively require that multiple substorm signatures occur within σ of each other in order to identify a substorm. We apply this procedure separately to the onset lists produced from the simulation and to the observational data.

The process is illustrated in Figure 6.1 for the 24-hour time period of January 12, 2005. The specifics of how the signatures were identified will be discussed in Section 6.2.4, but to illustrate the convolution procedures it sufficies to say that a list of candidate onset times was identified separately for each signature. Figures 6.1a-6.1e show the scores obtained from the onset list obtained from each signature using a kernel with $\sigma = 10$ minutes. Figure 6.1f shows the sum of the scores in Figures 6.1a-6.1e. The threshold value (in this case 1.5) is drawn in red, and vertical dashed lines mark the onset times identified from local maxima of the combined score that exceed the threshold. In order to exceed the threshold, at least three signatures must occur within a few minutes of each other, and this occurred only three times during the time period shown in Figure 6.1.

It is worth noting that the individual onset lists in Figure 6.1 are substantially different from each other, each identifying substorms at different times from the others, and several including candidate onset times that are not near those in any other list. Our procedure rejects those onsets, such as the MPB onset around 0600 UT, which appear only in one list. Near-simultaneous onsets are counted if two or more occur within a σ of each other, but nearby signatures that are too far apart may not result in a large enough increase, as is the case around 0900 UT when LANL, MPB, and AL onsets were identified but none were close enough to each other to increase the score above 1.5. Note that the kernel width $\sigma = 10$ and the threshold of 1.5 used in Figure 6.1 were chosen for illustrative purposes and not based on an optimization for best substorm identification. The threshold of 1.5 allows the identification of substorms based on nearby (within about 12 minutes) onsets from two lists, but the threshold could be increased to require two, three, or more simultaneous identifications. Reducing the threshold would increase the total number of substorm identifications, while increasing it would lower the number of substorm identifications. The implications of changing the threshold will be explored further in Section 6.3.2. Note also that the

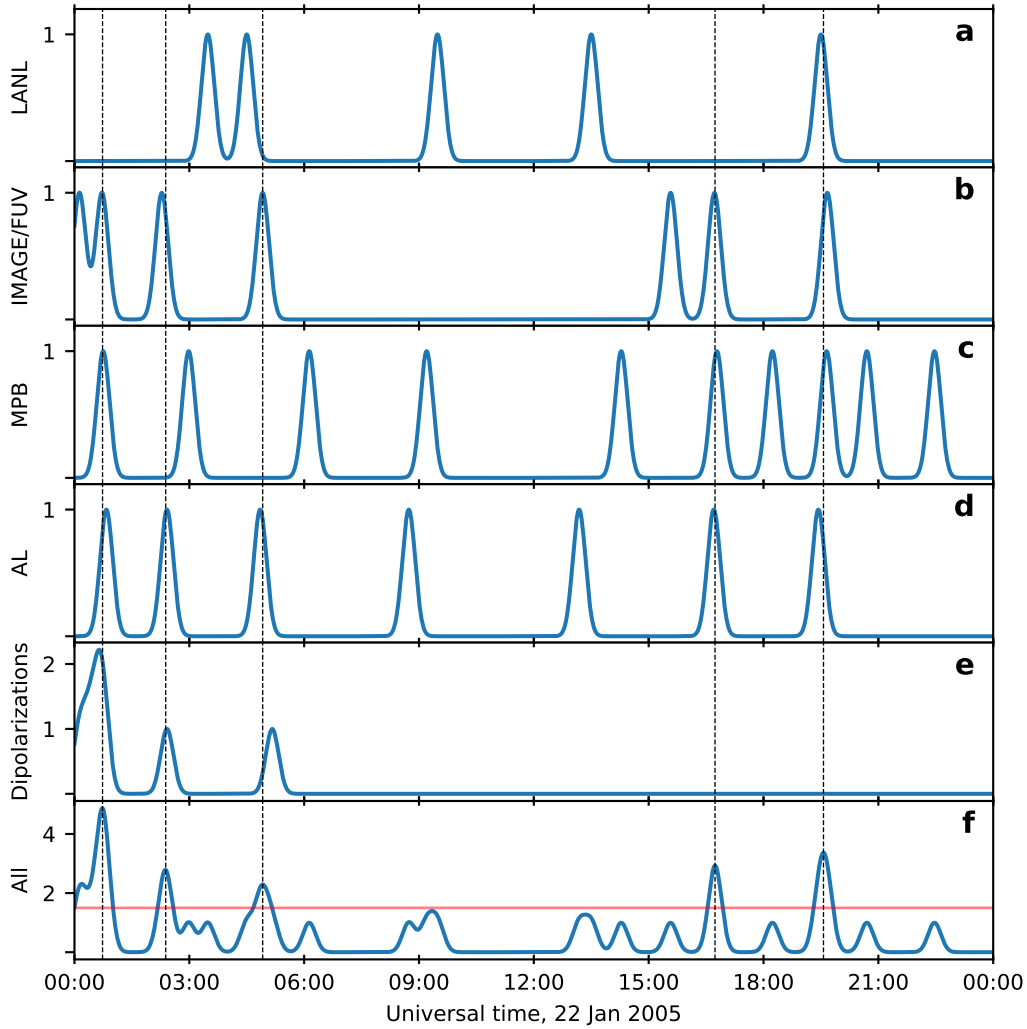

Figure 6.1: An illustration of the procedure used to combine multiple substorm onset lists into a single one. Panels (a-e) show scores obtained by convolving individual onset lists with a Gaussian kernel (using $\sigma = 10$ minutes), while (d) shows the combined score obtained by adding together the scores in panels (a-e). The threshold value of 1.5 is marked with a red horizontal line, and vertical dashed lines are drawn through local maxima of the combined score that exceed this threshold.

procedure requires the score to fall below the threshold in between maxima in order for them to be counted separately. As a result, a local maximum just past 0000 UT in Figure 6.1 is not counted as an onset, while a second, larger one about 20 minutes later is counted. Both would have been counted if the score had dropped below 1.5 between the two local maxima.

The convolution process effectively acts as a low-pass filter, with the choice of σ determining the minimum time between successive onsets. Previous research has shown that successive substorms rarely occur within 30 minutes of each other (e.g. *Borovsky et al.*, 1993), so we expect that appropriate values for σ will be on that order or smaller. Signatures from different onset lists can occur several minutes apart from each other for the same event, and setting $\sigma \leq 5$ minutes effectively treats these nearby but not simultaneous events as unrelated. Choosing $\sigma = 10$ minutes seems to be sufficient to combine these close-together onsets while still allowing for the possibility that a few substorms may occur within 30 minutes of each other. We used $\sigma = 10$ minutes for all the results shown in this chapter except where stated otherwise.

6.2.2 Event description

To test our technique we selected the month of January, 2005. *Morley* (2007) and *Morley et al.* (2009) had previously identified substorms from this time period, and it was identified as having a sufficient number to enable statistical analysis. The substorm database on the SuperMag website (`http://supermag.jhuapl.edu/substorms/`), which contains onsets identified from the SML index (*Newell and Gjerloev*, 2011b) using the *Newell and Gjerloev* (2011a) algorithm, lists 322 substorms during this period, placing it in the top 3% of 31-day periods included in that dataset. The substorm onset lists from *Borovsky and Yakymenko* (2017) include 124 AL onsets and 109 energetic particle injections during January, 2005, placing that month

in the top 3% in terms of AL onsets and in the top 7% in terms of energetic particle injections, compared with other 31-day periods from the same onset lists. *Frey et al.* (2004) (whose list has subsequently been updated to include 2003-2005 and published online at `http://sprg.ssl.berkeley.edu/image/`) lists 97 substorms in January 2005, placing the month in the top 13% of 31-day periods in that dataset.

Three geomagnetic storms occurred during this month: One on January 7 with a minimum Sym-H of -112 nT, one on January 16 with a minimum Sym-H of -107 nT, and one on January 21 with a minimum Sym-H of -101 nT. A table of the minima, maxima, and quartiles of various observed quantities over the course of the month can be found in *Haiducek et al.* (2017). Of particular note is the consistently high solar wind speed (median solar wind speed was 570 km/s), which may have contributed to the relatively high frequency of substorms during this period.

6.2.3 Model description

The simulations presented in this work were performed using the Block-Adaptive Tree Solar-Wind, Roe-Type Upwind Scheme (BATS-R-US) MHD solver (*Powell et al.*, 1999, *De Zeeuw et al.*, 2000). This was coupled to the Ridley Ionosphere Model (RIM, *Ridley et al.*, 2003, *Ridley et al.*, 2004) and the Rice Convection Model (RCM, *Wolf et al.*, 1982, *Sazykin*, 2000, *Toffoletto et al.*, 2003). The Space Weather Modeling Framework (SWMF, *Tóth et al.*, 2005, 2012) provided the interface between the different models. The inputs to the model are solar wind parameters (velocity, magnetic field, temperature, and pressure) and F10.7 radio flux. Results from the same simulation were previously reported in *Haiducek et al.* (2017) (and shown again in Chapter III), in which it was referred to as "Hi-res w/ RCM" to distinguish it from the other two simulations included in that paper. The model settings and grid configuration for the simulation are described in detail in *Haiducek et al.* (2017).

6.2.4 Identification of model signatures

The substorm process results in numerous observational signatures that can be levereged for identification. These include plasmoid releases, magnetic perturbations observable in the auroral zone and at mid latitudes, dipolarization of night-side magnetic fields observable from geosynchronous orbit, Earthward injection of energetic particles, and auroral brightenings. Several of these can be synthesized using MHD as well. Unfortunately, as was discussed in the Introduction, all of these signatures can be produced by other processes besides substorms, and this is true for both the observations and the model output. For instance, magnetospheric convection, pseudo-breakups and poleward boundary intensifications can cause a negative bay response in the northward magnetic field component at auroral-zone magnetometers, which could be interpreted as substorm onsets (*Pytte et al.*, 1978, *Koskinen et al.*, 1993, *Ohtani et al.*, 1993, *Aikio et al.*, 1999, *Kim et al.*, 2005). On the other hand, substorms could occur but not be identified because of the location of their activity, as was shown by *Newell and Gjerloev* (2011a) for auroral-zone magnetic field. Substorms could also be missed simply because they produce a response below the threshold selected for analysis. Even for analysis of model output, many of these factors remain relevant, and we aim to mitigate this by identifying multiple signatures for every substorm. Specifically, we identify dipolarization signatures at 6-7 R_E distances, negative bays in the AL index, positive bays in the midlatitude positive bay (MPB) index (*Chu et al.*, 2015), and plasmoid releases.

Figure 6.2 shows examples of substorm signatures from a substorm event on January 2, 2005. This substorm was selected for illustrative purposes because it can be identified by all four of the signatures used in the model output. Figures 6.2a-6.2c show time-series plots of B_z at $x = -7\ R_E$, in GSM (geocentric solar magnetospheric) coordinates, the AL index, and the MPB index. Apparent onset times identified from each curve are marked by triangles. Figures 6.2d-6.2f show the MHD solution within

the x-z (GSM) plane at 5-minute intervals during a plasmoid release. The backgrounds of Figures 6.2d-6.2f are colored according to the plasma pressure. Closed magnetic field lines are plotted in white, and open field lines in black. The Earth is shown as a pair of black and white semicircles, and surrounded by a grey circle denoting the inner boundary of the MHD domain. The approximate location of the reconnection region is denoted by a red triangle, and a blue dot marks where x=-7 R_E along the noon-midnight line (this is the location from which the data in Figure 6.2a was obtained).

A fundamental characteristic of a substorm is the tailward release of a plasmoid, and this is the first substorm signature we will describe. In observations, plasmoids are identified by a bipolar variation of B_z as observed by a spacecraft near the central plasma sheet (e.g. *Slavin et al.*, 1989, 1992, *Ieda et al.*, 2001, *Eastwood et al.*, 2005). MHD models provide data throughout the magnetosphere rather than being limited to a few point observations, and this enables several additional techniques for identifying plasmoids. One approach is to plot variables such as temperature, velocity, and magnetic field over time for different x coordinates along a line through the central plasma sheet at midnight. This produces a 2-D map showing the time evolution of the MHD solution in the plasma sheet, in much the same way that keograms are used to visualize the time evolution of auroral emissions (*Raeder et al.*, 2010). Plasmoids appear in such maps as tailward propagating magnetic field perturbations, with corresponding tailward flow velocity. Another approach for identifying plasmoids was proposed by *Honkonen et al.* (2011), who used the magnetic field topology derived from an MHD simulation to identify a plasmoid, which they define as a set of closed field lines that enclose a region of reconnecting open field lines. Probably the most common method is to plot magnetic field lines in the x-z plane, looking for evidence of a flux rope in the form of wrapped up or self-closed field lines, as in e.g. *Slinker et al.* (1995).

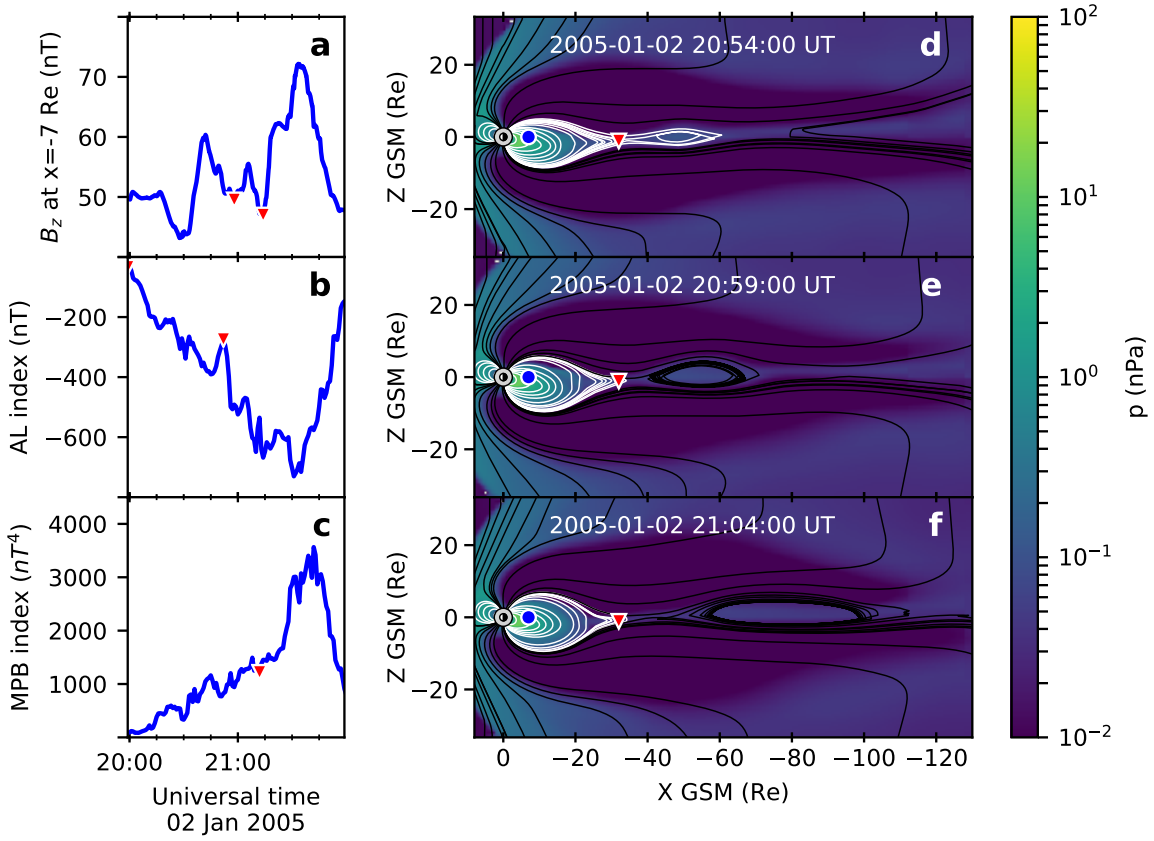

Figure 6.2: Model signatures for an example substorm. (a) B_z variations at $x = -7$ R_E along the GSM x axis. (b) AL index. (c) MPB index. Apparent substorm onset times are marked with triangles in (a-c). (d-f) $x - z$ (GSM) cut planes, at 5-minute intervals, colored by pressure. Closed magnetic field lines are drawn in white, and open field lines in black. Earth is drawn as a pair of black and white semicircles, surrounded by a grey circle denoting the inner boundary of the MHD domain. The location x = -7 R_E, from which the data in (a) was obtained, is marked a blue circle. The apparent X-line location is marked with a red triangle.

The method of visually identifying plasmoids by searching for regions of wrapped-up field lines is approach used in the present work. We require that such features be located in or near the central plasma sheet, and that they exhibit tailward motion. For each such plasmoid, we record the time of the first indication of tailward motion, and x and z coordinates of the apparent X-line at that time. Plasmoids for which the X-line is beyond 35 R_E down-tail are ignored. Figures 6.2d-6.2f show the kind of images that are used for this analysis. For the event in Figure 6.2, the first apparent tailward motion occurred at 2059 UT, and this time is shown in Figure 6.2d. The X-line occurs at around x=-32 R_E, and the plasmoid extends from there to -60 R_E. Figures 6.2e and 6.2f show the same plasmoid 5 and 10 minutes after release. Tailward motion is clearly apparent, with the center of the plasmoid moving from $x \approx -55$ to $x \approx -80$ R_E in 10 minutes.

While the plasmoid propagates tailward, the magnetic fields Earthward of the X-line undergo a dipolarization. Previous studies have identified dipolarizations by searching for sharp increases in B_z (e.g. *Lee and Lyons*, 2004, *Runov et al.*, 2009, *Birn et al.*, 2011, *Runov et al.*, 2012, *Liu et al.*, 2013, *Frühauff and Glassmeier*, 2017) or elevation angle

$$\theta = \tan^{-1}\left(\frac{B_z}{\sqrt{B_x^2 + B_y^2}}\right) \tag{6.2}$$

(e.g. *McPherron*, 1970, *Coroniti and Kennel*, 1972, *Noah and Burke*, 2013) within the night-side magnetotail. A number of studies have also used a decrease in

$$|B_r| = \left|\frac{xB_x + yB_y}{\sqrt{x^2 + y^2}}\right|, \tag{6.3}$$

coincident with the increase in B_z or θ, as criteria for identifying a dipolarization onset (e.g. *Nagai*, 1987, *Korth et al.*, 1991, *Schmid et al.*, 2011, *Liou et al.*, 2002). Automated procedures for identifying dipolarizations have been developed by *Fu et al.*

(2012) and *Liu et al.* (2013). We were unable to use the *Fu et al.* (2012) algorithm for this work because it uses flow velocity as part of its criteria, which is unavailable in the observational data for GOES. The *Liu et al.* (2013) algorithm was designed for THEMIS and uses B_z alone for event selection. Since our data was from 6-7 R_E from the Earth (where the fields differ substantially from those seen by THEMIS), and because we wished to use θ as an additional criterion, we developed a new algorithm to identify dipolarizations from the model output, which is described in detail in Appendix B.1. The algorithm was used to identify dipolarization signatures along the orbits of GOES 10 and 12, and at a fixed point located at $x = -7$ R_E in GSM coordinates on the sun-Earth line; this point is identified by a blue circle in Figures 6.2d-6.2f. A plot of B_z at $x = -7$ R_E is shown in Figure 6.2a, and two dipolarization onsets identified using our procedure are marked on the plot with triangles. The first of these is closely aligned with the plasmoid release time.

The dipolarization process can be interpeted as a partial redirection of cross-tail current into the ionosphere (e.g. *Bonnevier et al.*, 1970, *McPherron et al.*, 1973, *Kamide et al.*, 1974, *Lui*, 1978, *Kaufmann*, 1987). The closure of this current results in a negative bay in the northward component of the magnetic field on the ground in the auroral zone (*Davis and Sugiura*, 1966). As a result, substorm onsets can be identified by sharp negative diversions of the AL index. A number of algorithms have previously been developed for identifying substorm onsets from the AL index, including the *Newell and Gjerloev* (2011a) (SuperMag) algorithm and the Substorm Onsets and Phases from Indices of the Electrojet (SOPHIE) algorithm (*Forsyth et al.*, 2015).

In the present work we identify AL onsets using the algorithm presented in *Borovsky and Yakymenko* (2017). This algorithm was chosen for its simplicity and because it produces a distribution of inter-substorm timings that is consistent with that obtained from other signatures, as *Borovsky and Yakymenko* (2017) demon-

strated through comparison with timings of energetic particle injections. We apply the *Borovsky and Yakymenko* (2017) algorithm to a synthetic AL index computed from the model output using virtual magnetometers as described in *Haiducek et al.* (2017). An example AL onset is shown in Figure 6.2b. A negative bay onset, marked by a triangle, occurs just before 2100 UT, coincident with the plasmoid release at 2059 UT.

The integrated effect of the current closures into the auroral zone results in a northward diversion of the ground magnetic field in the mid latitudes, called a midlatitude positive bay (MPB, *McPherron et al.*, 1973). Often these are identified manually through examination of individual magnetometers (e.g. *McPherron*, 1972, *McPherron et al.*, 1973, *Caan et al.*, 1978, *Nagai et al.*, 1998, *Forsyth et al.*, 2015). However, the ASYM-H index may also be used (*Iyemori and Rao*, 1996, *Nosé et al.*, 2009). More recently, *Chu et al.* (2015) and *McPherron and Chu* (2017) have developed two versions of an index they call the MPB index, which is specifically designed to respond to a midlatitude positive bay, along with procedures for identifying substorm onsets using the MPB index. In the present work we use the MPB index implementation described in *Chu et al.* (2015) and its accompanying onset identification procedure. To evaluate the MPB index from the model output, we use a ring of 72 virtual magnetometers placed at a constant latitude of 48.86° and evenly spaced in MLT, and from these compute the MPB index and associated substorm onsets using the procedures described in *Chu et al.* (2015). An example of the MPB response is shown in Figure 6.2c. The MPB onset time occurs roughly 10 minutes after the plasmoid release time, but is well aligned with the second of the two dipolarizations in Figure 6.2a.

6.2.5 Identification of substorm events from observational data

When possible, we use the same procedures to identify substorm signatures in the observational data as we do with the model output. This includes the dipolariza-

tions, AL index, and MPB index. In some cases modifications are required due to limitations in the availability of observational data; for instance ground-based magnetometers are normally restricted to being placed on land with suitable terrain, and the locations of satellite observations are constrained by orbital mechanics. On the other hand, some observations rely on physical phenomena that cannot be modeled by the MHD code, such as energetic particle injections and auroral brightenings. In an effort to obtain the best possible identifications of observed substorms, we use as many observational datasets as possible, which for this time period included GOES magnetic field observations, the AL and MPB indices, energetic particle injections at geosynchronous orbit, and auroral brightenings.

We identify AL onsets by applying the procedure from *Borovsky and Yakymenko* (2017) to the SuperMag SML index (*Newell and Gjerloev*, 2011a). For simplicity, we will use the term AL throughout this chapter to refer to both the observed SML index and the synthetic AL computed from the model output. For the observed MPB index and MPB onsets, we use the values from the analysis previously reported in *Chu et al.* (2015). We identify dipolarizations by applying the procedure described in Appendix B.1 to measurements obtained with the magnetometers onboard GOES 10 and 12 (*Singer et al.*, 1996).

In addition to the dipolarization, another substorm signature that can be observed at geosynchronous orbit is the Earthward injection of energetic electrons and protons (e.g. *Lezniak et al.*, 1968, *DeForest and McIlwain*, 1971). Previous studies have identified a temporal association between such particle injections and auroral zone magnetic signatures (e.g. *Lezniak et al.*, 1968, *Kamide and McIlwain*, 1974, *Weygand et al.*, 2008), along with a connection between energetic particle injections and dipolarizations (e.g. *Sauvaud and Winckler*, 1980, *Birn et al.*, 1998). In the present work we use energetic particle injections identified by *Borovsky and Yakymenko* (2017) using the the Synchronous Orbit Particle Analyzer (SOPA) instrument

(*Cayton and Belian*, 2007) on the LANL-1990-095, LANL-1994-085, and LANL-97A satellites. The list of particle injections found in the supplemental data of *Borovsky and Yakymenko* (2017) is used as-is.

Some of the energetic particles produced by the substorm enter the ionosphere and cause a brightening and reconfiguration of the aurora. These can be observed from the ground using all-sky imagers, or from cameras onboard spacecraft. For the month of January, 2005, observations from the Imager for Magnetopause-to-Aurora Global Exploration (IMAGE) spacecraft are available for this purpose. The IMAGE spacecraft was in a highly elliptical polar orbit with an apogee of 45,600 km and an orbital period of 14 hours, providing 8-10 hours per orbit of good conditions for imaging the northern auroral oval (*Frey et al.*, 2004). *Frey et al.* (2004) examined images from the Far Ultraviolet Imager (FUV) instrument onboard IMAGE, and produced a list of northern hemisphere substorm onsets for the years 2000-2002, since updated to include 2003-2005. We use the January, 2005 portion of this list as part of our substorm identification.

6.3 Results

6.3.1 Substorm waiting times

The distribution of substorm waiting times (the amount of time that passes between successive substorms) gives an indication of the occurrence frequency for substorms. A number of previous papers have examined waiting times, including *Borovsky et al.* (1993) which identified substorm onsets from energetic particle injections and found the modal waiting time to be around 2.75 hours. *Chu et al.* (2015) and *McPherron and Chu* (2017) analyzed MPB onsets and reported modal waiting times of 80 and 43 minutes, respectively. *Kauristie et al.* (2017) reported modal waiting times of 32 minutes for AL onsets identified by *Juusola et al.* (2011) and

23 minutes for SML onsets identified by the *Newell and Gjerloev* (2011a) procedure. *Hsu and McPherron* (2012) obtained a modal waiting time of about 1.5 hours for AL onsets, about 2 hours for onsets identified from tail lobe fields, and about 2.5 hours for Pi 2 onsets. *Freeman and Morley* (2004) presented model results that reproduce the waiting time distribution from *Borovsky et al.* (1993).

To visualize the distributions of waiting times, we use kernel density estimates (KDEs) (*Parzen*, 1962), which approximate the probability density function of a distribution by convolving samples from the distribution with a Gaussian kernel. The resulting curve can be interpreted in the same way as a normalized histogram. For the observational data, we have estimated confidence intervals using a bootstrapping procedure as described in Appendix B.3. This provides a means to determine whether the waiting time distribution obtained from the model is significantly different from the observed distribution, in a statistical sense.

Figure 6.3 shows kernel density estimates of substorm waiting times. The observed onsets are shown in light blue, with the 95% confidence interval represented as a shaded region of lighter blue. The MHD results are shown in dark blue. Figure 6.3a shows the AL onsets, Figure 6.3b shows dipolarization onsets, Figure 6.3c shows MPB onsets, and Figure 6.3a shows all signatures in combination.

The observed distribution of waiting time between AL onsets (Figure 6.3a) shows a modal waiting time of around 3 hours, similar to the 2.75 hours reported by *Borovsky et al.* (1993), and significantly longer than those obtained by *Juusola et al.* (2011), *Newell and Gjerloev* (2011a), and *Hsu and McPherron* (2012). The model produces a slightly shorter waiting time, around 2 hours.

Dipolarizations produce a somewhat narrower waiting time distribution (Figure 6.3b), with the modes of both the model and observations occurring around 1.5 hours. This suggests that the dipolarizations are somewhat more frequent than AL onsets, consistent with the greater total number of dipolarizations compared with AL

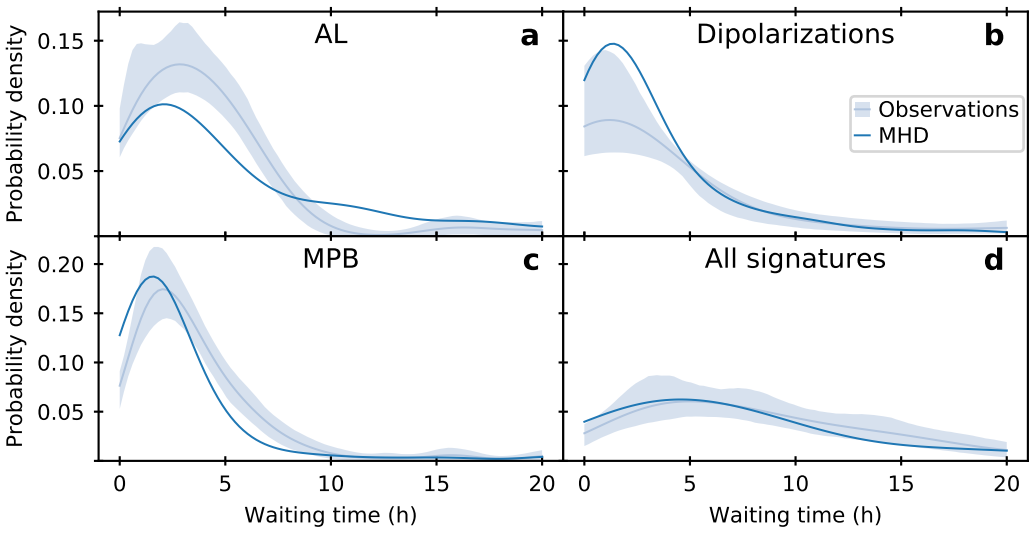

Figure 6.3: Substorm waiting times for MHD and observations. a) AL onsets only b) Dipolarizations only, and c) MPB onsets only d) All signatures combined.

onsets in the model (Table 6.3). The observations, on the other hand, have a smaller total number of dipolarizations than AL onsets, probably due largely to the fact that the observations were obtained from only two spacecraft, both in geosynchronous orbit over the western hemisphere, resulting in relatively poor temporal coverage. As a result, the observed waiting time distribution for dipolarizations has its mode in roughly the same place as that of the model, but with a significantly reduced height.

The observed waiting time distribution for MPB onsets (Figure 6.3c) has a mode around 2.5 hours, in between those of the dipolarizations and AL onsets. The waiting time distribution for model MPB onsets is largely similar to that of the observations, with the mode falling within the 95% confidence interval of the observations. However, the model distribution is somewhat narrower.

When all signatures are combined (Figure 6.3d), the resulting observed waiting time distributions have a mode around 5 hours, greater than any of the individual onsets. This reflects the fact that the Gaussian kernel used to combine scores serves as a low-pass filter. The rejection of signatures for which the score falls below the iden-

tification threshold due to lack of simultaneous signatures may also serve to increase the waiting time. The model waiting time distribution falls almost entirely within the confidence intervals of the observations, indicating that the model is largely successful at predicting the observed distribution.

To test the sensitivity of the waiting time distributions to the choice of kernel width and threshold, we plotted waiting time distributions for a range of each, as shown in Figure 6.4. Figure 6.4 shows the distribution of waiting times for the model and for the observations for three different choices of threshold and four different kernel widths, ranging from $\sigma = 5$ minutes to $\sigma = 20$ minutes. The y-axis of each panel shows the probability densities of waiting time, and the x axis shows the waiting times. Figures 6.4a, 6.4b, and 6.4c show waiting time distributions from the observations, while Figures 6.4d, 6.4e, and 6.4f show waiting time distributions obtained from the MHD simulation. Figures 6.4a and 6.4d show thresholds of 2.0, Figures 6.4b and 6.4e show thresholds of 2.5, and Figures 6.4c and 6.4f show thresholds of 3.0. Within each plot, the kernel width σ used in the substorm identification procedure is varied from $\sigma = 2$ minutes to $\sigma = 20$ minutes. $\sigma = 2$ minutes is depicted in purple with a dash-dot-dot pattern, $\sigma = 5$ minutes in red with a dash-dot pattern, $\sigma = 10$ minutes in green with dots, $\sigma = 15$ minutes in orange with dashes, and $\sigma = 15$ minutes in blue as a solid line.

From Figure 6.4, it is immediately apparent that the smallest kernel widths produce unrealistically long waiting time distributions. Related to this, the total number of substorms identified is also too small; in the case of $\sigma = 2$ and a threshold of 3.0, fewer than two substorms were identified in either the model or observations, and as a result no KDE is shown. As the kernel width is increased, the waiting time distributions become narrower and their modes shift toward smaller values. This indicates that larger kernel widths are tending to produce shorter waiting times as more substorms are identified by the procedure.

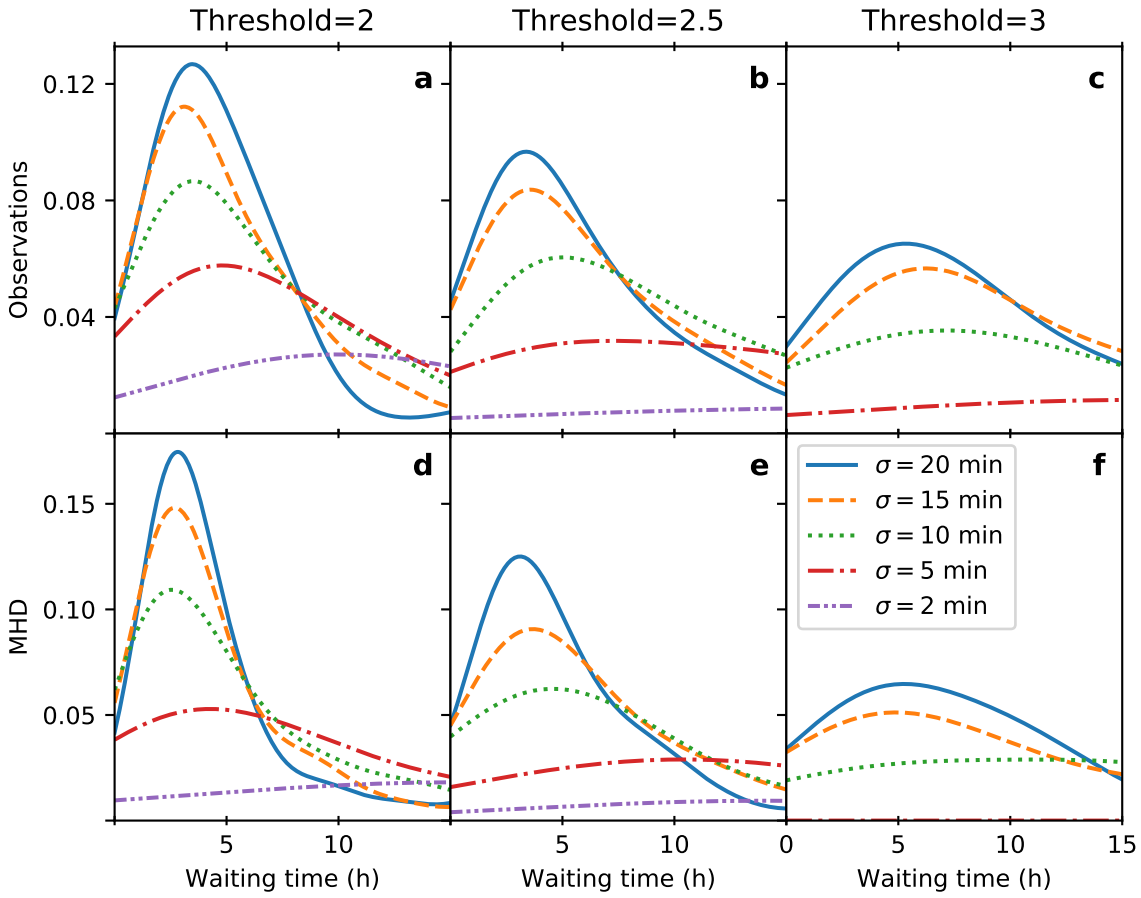

Figure 6.4: Distributions of substorm waiting times for a range of identification thresholds and kernel widths used in the identification procedure. a), b), and c): Observed waiting time distributions. d), e), and f): MHD waiting time distributions. a) and d): Threshold=2.0; b) and e): Threshold=2.5; c) and f): Threshold=3.0.

6.3.2 Forecast metrics

In order to evaluate the predictive capabilities of the model, we first apply the procedure described in Section 6.2.1 to the onset lists from the model and separately to the observed onset lists, in order to produce a combined onset list for each. We next divide the month into 30-minute bins, and determine whether an substorm onset from the each combined list was present in each bin. We then classify each bin according to whether a substorm was identified in the model, observations, neither, or both. The four categories are shown generically in Table 6.1: both the model and the observations (true positive, a in the table), in the observations only (false negative, b), in the model only (false positive, c), or in neither the model nor the observations (true negative, d). Table 6.2 shows actual values from the simulation, consisting of the total number of bins falling in each category for each of the three model runs. The counts in Table 6.2 were obtained using a threshold score of 2.5 for both the model and the observations. In total, 102 substorms were found in the observational data using this threshold. The MHD simulation under-predicts this total slightly, producing 97 substorms, of which 17 were true positives.

		Observations	
		Y	N
Predictions	Y	a	b
	N	c	d

Table 6.1: A generic contingency table.

		Observations	
		Y	N
SWMF	Y	17	80
	N	85	1306

Table 6.2: Contingency table for SWMF vs. observations

From the values in the contingency table we compute several metrics summarizing

the predictive abilities of the model. These include Probability of Detection (POD), Probability of False Detection (POFD), and the Heidke skill score (HSS), all of which are in common use in space weather applications (e.g. *Lopez et al.*, 2007, *Welling and Ridley*, 2010, *Pulkkinen et al.*, 2013, *Ganushkina et al.*, 2015, *Glocer et al.*, 2016, *Jordanova et al.*, 2017). The POD, given by

$$\mathrm{POD} = \frac{a}{a+c}, \tag{6.4}$$

(*Wilks*, 2011) indicates the relative number of times a substorm was forecast when one occurred in observations. A model that predicts all the observed events will have a POD of 1. POFD, given by

$$\mathrm{POFD} = \frac{b}{b+d} \tag{6.5}$$

indicates the relative number of times that a substorm was forecast when none occurred. Smaller values of POFD indicate better performance, and a model with no false predictions will have a POFD of 0.

Skill scores are a measure of relative accuracy (e.g. *Wilks*, 2011). The Heidke Skill Score (HSS) is based on the proportion correct (PC), defined as

$$\mathrm{PC} = \frac{a+d}{a+b+c+d}, \tag{6.6}$$

which measures the fraction of correct predictions relative to the total number of predictions. A perfect forecast would have a PC of 1. The HSS adjusts PC relative a reference value, PC_{ref}, which is the value of PC that would be obtained by a random forecast that is statistically independent of the observations, and is given by

$$\mathrm{PC}_{ref} = \frac{(a+b)(a+c)+(b+d)(c+d)}{(a+b+c+d)^2}. \tag{6.7}$$

The HSS is obtained from PC_{ref} as

$$\mathrm{HSS} = \frac{\mathrm{PC} - \mathrm{PC}_{ref}}{1 - \mathrm{PC}_{ref}} = \frac{2(ad - bc)}{(a + c)(c + d) + (a + b)(b + d)}. \tag{6.8}$$

The HSS ranges from -1 to 1, where 1 represents a perfect forecast, 0 is equivalent to a no-skill random forecast, and -1 represents the worst possible forecast.

All of the above metrics are subject to sampling uncertainties, meaning that any particular value could be obtained simply by chance, and might not be representative of the model's overall abilities. To address this, we estimate 95% confidence intervals for each metric. The 95% confidence interval is a range in which we estimate that each metric will fall for 95% of a given number of random samples of the dataset. Since no analytical formulas are known for computing confidence intervals for the HSS (*Stephenson*, 2000), we estimate the confidence interval using bootstrapping (e.g. *Conover*, 1999). The procedure is described in detail in Appendix B.3.

Figure 6.5 shows receiver operating characteristic (ROC) curves for the MHD model. An ROC curve, by definition, shows the probability of detection (POD) of a predictive model as a function of the probability of false detection (POFD), as the threshold for event identification is varied. To produce the curves in Figure 6.5, the threshold used to identify a substorm in the model output is varied along the length of each curve, while the threshold for identifying an observed substorm is held fixed. A curve for an observed threshold of 1.0 is shown in blue, an observed threshold of 2.0 is shown in orange, an observed threshold of 2.5 is shown in green, and an observed threshold of 3.0 is shown in red. The total number of observed substorms obtained with each threshold is shown in the legend. The green curve, corresponding to an observed threshold of 2.5, is drawn in bold since that is the threshold that was chosen for use throughout the remainder of the chapter. A black circle denotes the model threshold of 2.5. A diagonal grey line shows where POD equals POFD. For a good forecast, POD should exceed POFD, and this is the case along the entire length of

each curve (except at the extreme values of 0 and 1, where equality is expected).

The curve for an observed threshold of 3.0 shows higher POD than the lower thresholds. While higher POD is desirable, in this case it comes at the cost of an unrealistically low total number of substorms in the observations. The observed threshold of 3.0 means that we are only comparing with only those observed substorms that could be identified by more than 3 signatures, only 53 onsets in total. The lower threshold of 2.5 produces 102 substorms, which is in line with the totals obtained by *Borovsky and Yakymenko* (2017) and *Frey et al.* (2004) for the time period in question. Based on this, we decided to use the threshold of 2.5 for identifying an observed substorm throughout the remainder of the analysis.

Figure 6.6 shows the Heidke skill score (HSS) as a function of the ratio of the total number of model substorm bins to the total number of observed substorm bins. Figure 6.6 was produced by varying the modeled and observed thresholds in the same manner as was done to produce Figure 6.5. The x-axis value is obtained by dividing the total number of bins containing a substorm in the model output by the total number of bins containing a substorm in the observational data (i.e., $\frac{a+b}{a+c}$, referencing the labels in Table 6.1). Different observed thresholds are identified by color and shape in the same manner as Figure 6.5, with error bars denoting the 95% confidence interval for each skill score. Also like Figure 6.5, the case of the observed threshold equal to 2.5 is drawn with bold lines, and the case of both the model and observed threshold equal to 2.5 is marked with a black circle.

For a perfect forecast, the model should produce the same number of substorms as occur in the observations, in which case the count ratio on the x-axis of Figure 6.6 will equal one. The threshold of 2.5 for identifying a model substorm was chosen for the remainder of the analysis because it produces a ratio of model to observed substorms that is relatively close to 1.

For a skill score to represent a true predictive skill, it should be significantly

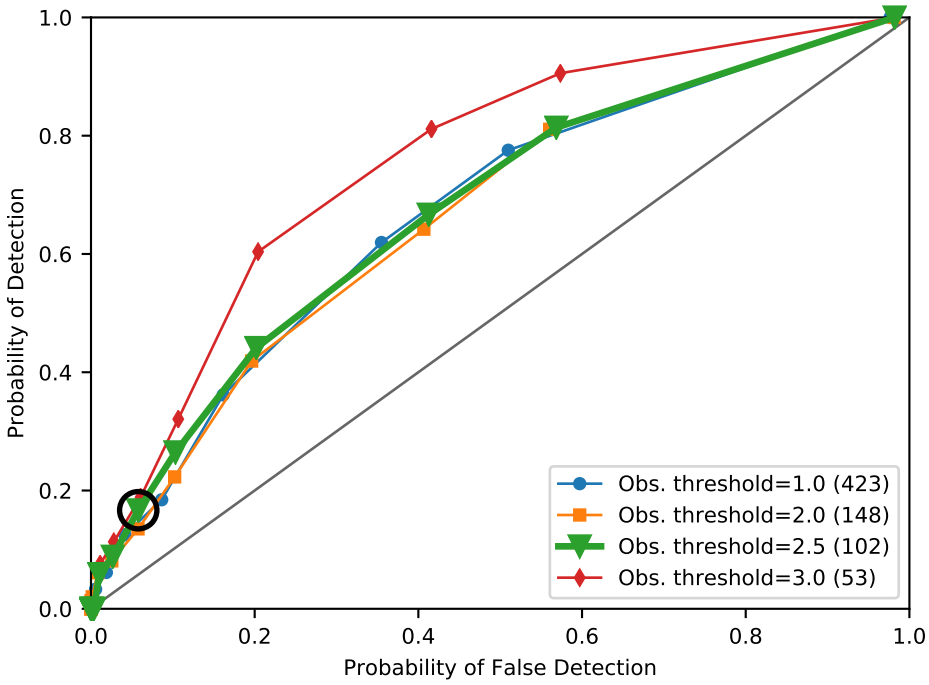

Figure 6.5: ROC curves for the MHD simulation. The threshold score for identifying substorms from the model output is varied to produce each curve, resulting in changes in the probability of detection (POD) and probability of false detection (POFD). Each curve is computed using a particular threshold score for identifying observed substorms; the thresholds and number of observed substorm identifications are listed in the legend. The case of the observed threshold equal to 2.5 is highlighted with a bold line, and the case of model threshold and the observed threshold both equal to 2.5 is highlighted with a black circle.

greater than zero, in a statistical sense. This is indicated by the lower end of the 95% confidence interval being greater than zero. A forecast satisfying this criterion is estimated to predict a value greater than zero 95% of the time. Figure 6.6 shows that the skill scores obtained from the MHD model are significantly greater than zero in the majority of cases. All of the skill scores obtained using model identification thresholds greater than zero and less than three were found to be statistically significant.

To test the sensitivity of these results to the kernel width, we tested a $\sigma = 20$ kernel width. Figure 6.7 shows the same analysis as Figure 6.6, but with the kernel width σ increased from 10 minutes to 20 minutes. The style and axes are the same as Figure 6.6, and the case of the modeled and observed threshold both set to 2.5 is identified with a black circle. Figure 6.7 shows that the skill scores are sensitive to the choice of kernel width, but not dramatically so. Doubling the kernel width appears to increase HSS by 10-30%, depending on the choice of threshold.

Table 6.3 shows the total number of events, POD, POFD, and HSS for each of the substorm identification procedures applied to the model output. The first row of the table, labeled "All," shows the metrics computed from all signatures, combined into a single onset list using the methodology in Section 6.2.1, and with 30-minute bins used to compute the metrics, as was done for Table 6.2, Figure 6.5, and Figure 6.6. The remaining rows show results for individual signatures, computed using 30-minute bins as for the "All" case, except that the individual onset lists are used directly to produce the contingency table (i.e., the convolution procedure described in Section 6.2.1 was not used). With the exception of the last column of the table, all quantities are obtained by testing each signature in the model output with observed signatures of the same category (for instance, model AL is compared with observed AL). These numbers are absent for the plasmoids since there was no observational plasmoid data with which to compare. The last column shows the HSS obtained using the single-signature onset list from each row and the observed onset list obtained using

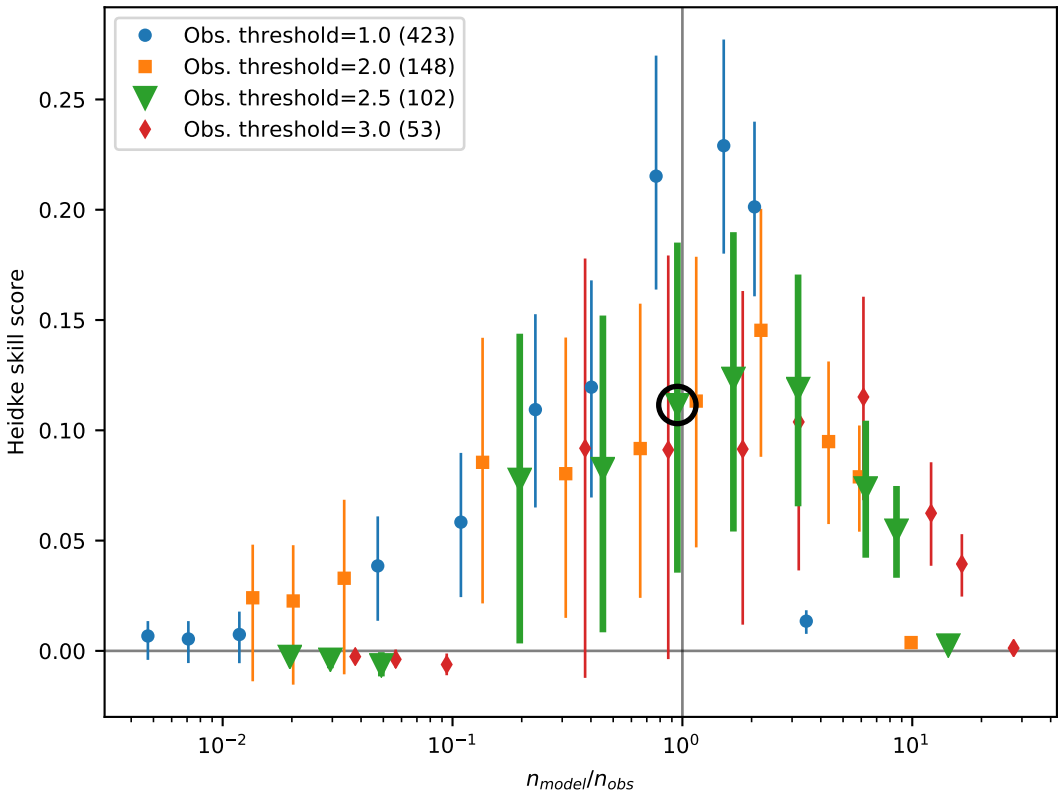

Figure 6.6: Heidke skill score as a function of the ratio of the number of model substorm bins to the number of observed substorm bins. The threshold score for identifying substorms is varied to produce a range of skill scores and ratios. Each color and shape corresponds to a particular threshold score for identifying observed substorms; the thresholds and number of observed substorm bins are listed in the legend. For a given observed threshold, different skill scores and ratios are obtained by varying the threshold for identifying a model substorm. Error bars represent the 95% confidence interval for each skill score. The case of observed threshold equal to 2.5 is drawn in bold, and the case of the model threshold and observed threshold both equal to 2.5 is marked with a black circle.

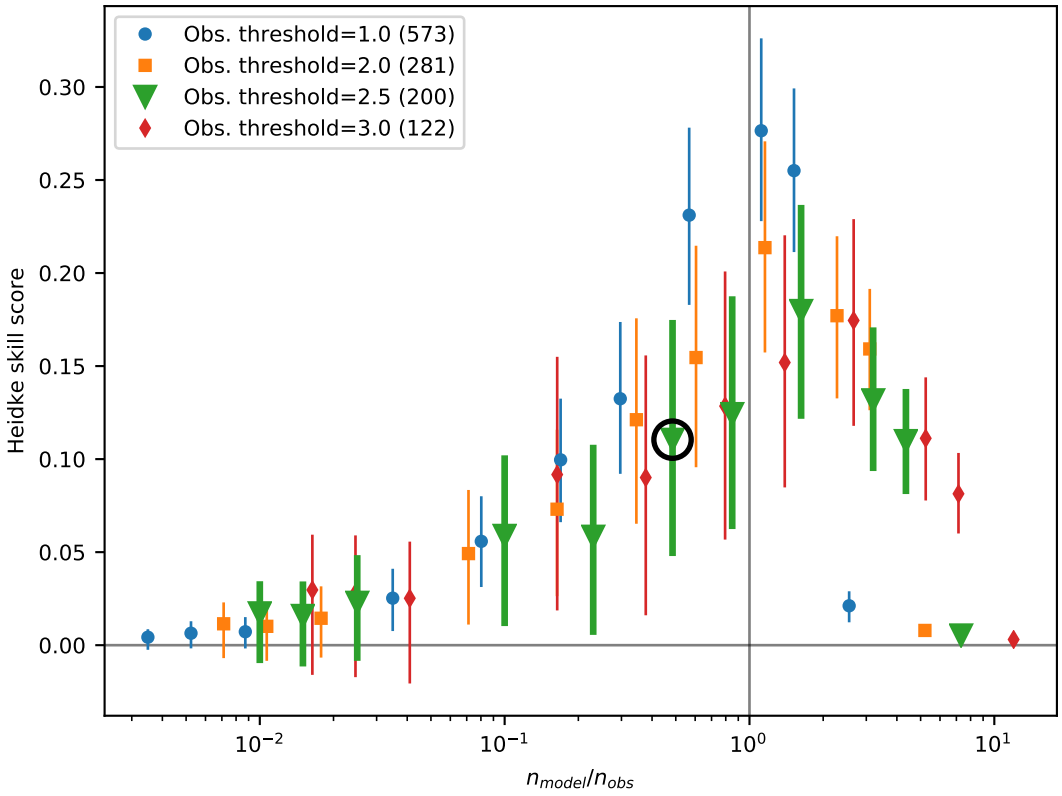

Figure 6.7: Heidke skill score as a function of the ratio of the number of model substorm bins to the number of observed substorm bins, using a kernel width $\sigma = 20$ minutes instead of the $\sigma = 10$ minutes width used elsewhere. The format is the same as Figure 6.6.

all signatures together. This gives an indication of how well the individual model signature predicts the combined (all signatures) observed substorm onsets. For the POD, POFD, and HSS, a bar over the number identifies the last significant digit, as determined by the size of the 95% confidence interval. For the skill scores, the limits of the confidence intervals are shown in brackets. The lower limits of the confidence intervals are positive for every case except the plasmoids, indicating that the skill scores are significantly greater than zero.

	SWMF events	Obs. events	POD	POFD	Heidke skill: Same signature	Heidke skill: All signatures
All	97	102	$0.1\overline{6}7$	$0.0\overline{5}8$	$0.1\overline{1}1$ [0.040, 0.19]	$0.1\overline{1}1$ [0.039, 0.18]
AL	100	156	$0.\overline{2}0$	$0.0\overline{5}2$	$0.1\overline{7}5$ [0.10, 0.25]	$0.1\overline{0}8$ [0.038, 0.18]
MPB	192	167	$0.\overline{2}7$	$0.1\overline{1}1$	$0.1\overline{4}8$ [0.086, 0.21]	$0.1\overline{3}3$ [0.068, 0.20]
dipolarizations	145	77	$0.\overline{2}6$	$0.0\overline{8}9$	$0.1\overline{2}1$ [0.053, 0.19]	$0.0\overline{8}9$ [0.03, 0.2]
plasmoids	397	–	–	–	–	$0.0\overline{2}6$ [−0.01, 0.07]

Table 6.3: Forecast metrics for each signature

Of all the signatures, the plasmoids releases do the least well at predicting the observed substorms. The AL and MPB produce higher skill scores than the dipolarizations, but the confidence intervals for all three overlap so the differences between them may not be statistically significant.

Far more plasmoid releases (397 in total) were identified than any other substorm signature, with the next most common signature being MPB onsets with only 192 occurrences. This strongly implies that the plasmoid release list contained a large number of false positives. While we have confidence that all the plasmoids were real (in the sense that they occurred within the simulation), the much smaller number of AL and MPB onsets (100 and 192, respectively) suggests that only a few of them were substorm related. The total number of events in the combined substorm list obtained from the simulation is only 97. This means that over 75% of the plasmoid releases were rejected by our substorm identification procedure, and indicates that it

is largely successful at eliminating false positive identifications.

6.3.3 Superposed epoch analysis

We now present superposed epoch analyses (SEAs) of parameters related to the solar wind driving during substorms and to the geomagnetic signatures of the substorms. SEA consists of shifting a set of time-series data $y(t)$ to a set of epoch times t_k, producing a group of time-series $y_k = y(t - t_k)$ from which properties common to the epoch times can be estimated (e.g. *Samson and Yeung*, 1986). Common properties of the SEA may be estimated and visualized in a variety of ways. Probably the most common approach is to use a measure of central tendency such as the mean or median to obtain a new time-series $\hat{s}(t)$ that estimates the typical behavior of $y(t)$ in the vicinity of the epoch times t_k. In the present work we will use the median of y_k to accomplish this. The epoch times t_k will come from one of two lists of substorm onset times (the from the MHD simulation and the other from the observations).

Computing an SEA using our substorm onset times serves as a diagnostic to determine whether the onset times identified by our selection procedure are consistent with previously reported behavior for substorms, in terms of both the solar wind driving and the geomagnetic response. With the model substorm onsets, the SEAs also provide a means to test how closely the model's behavior during substorms follows the observed behavior of the magnetosphere.

Figure 6.8 shows SEAs of the observational data and the model output, with the epoch times corresponding to substorm onset times obtained using each of the methods described in Sections 6.2.4-6.2.1. SEAs obtained using the combined onset list are shown as a thick blue cruve, along with all the individual signatures: MPB onsets (orange), IMAGE/FUV (green), plasmoids (red), AL (purple), LANL (brown), and dipolarizations (pink). The left column (Figures 6.8a-6.8d) shows observed results, while the right column (Figures 6.8e-6.8h) shows the MHD results. The variables

shown are IMF (interplanetary magnetic field) B_z (Figures 6.8a and 6.8e), solar wind ϵ (Figures 6.8b and 6.8f), the AL index (Figures 6.8c and 6.8g), and the MPB index (Figures 6.8d and 6.8h). IMF B_z is in GSM coordinates. ϵ provides an estimation of the rate at which solar wind energy is entering the magnetosphere (*Perreault and Akasofu*, 1978), and is given by

$$\epsilon = |u_x| \frac{B^2}{\mu_0} \sin\left(\frac{\theta_{clock}}{2}\right)^4. \tag{6.9}$$

Figures 6.8a and 6.8e shows SEAs for IMF B_z. It is apparent that the observed substorms are typically preceded by a decrease in IMF B_z, with the minimum B_z occurring just before the onset time and a recovery back to near-zero B_z following the onset. Similar behavior is present in both the model and the observations, but the decrease in B_z is somewhat sharper for the model onsets (with the exception of the plasmoids, which have a particularly weak decrease in B_z). The decrease is evident for all of the onset lists. In addition to the plasmoids, the AL onsets stand out significantly. When using AL onsets for the epoch times (both for observations and model) the minimum B_z occurs slightly later, which may be an indication that the AL onsets precede the other signatures on average. The model AL onsets are preceded by a 1-2 nT increase 1-2 hours prior to onset, and a particularly sharp decrease just prior to onset. The tendency of substorms to occur near a local minimum in IMF B_z has been previously reported, and our results are qualitatively similar to those obtained by SEA in previoius studies (e.g. *Caan et al.*, 1975, 1978, *Newell et al.*, 2001, *Freeman and Morley*, 2009, *Newell and Liou*, 2011, *Walach and Milan*, 2015).

Figures 6.8b and 6.8f show SEAs of ϵ. All onset lists correspond with an increase in ϵ prior to onset, with a maximum occurring just prior to onset, or in the case of AL, just after onset. A separate SEA of u_x (not shown) showed no appreciable trend, which indicates that the trend in ϵ is driven almost entirely by variation in B_z. However, despite a lack of change in u_x before and after onset, we found that

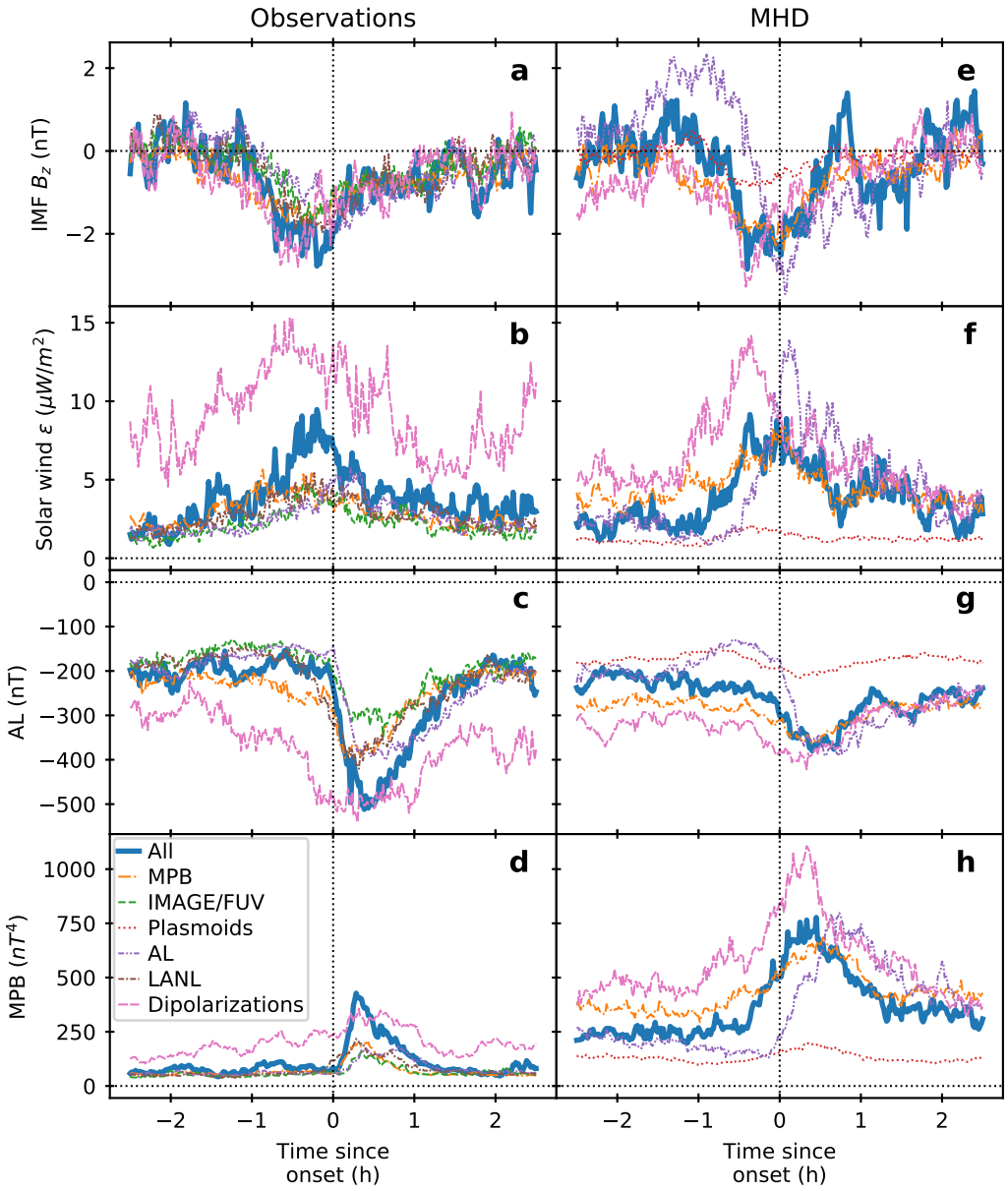

Figure 6.8: Superposed epoch analyses of IMF B_z, ϵ, AL, and MPB, comparing onsets identified from the model and from the observations. The left column shows SEAs computed using epoch times from the observations, while the right column shows SEAs computed using epoch times from the simulation. The AL and MPB data come from the respective datasets used to create the onsets (observations or model run), and the other values come from the solar wind data input to the model. The lines show the median value for each time offset. The thick blue line (labeled "All" in the legend) shows the SEA computed with epoch times from the combined onset list using all signatures, while thinner colored lines show SEAs obtained using epoch times from the individual signatures.

some classes of onsets seem to be associated with higher or lower u_x; most notably dipolarizations were associated with higher u_x than any other signature type, and this is responsible for the higher ϵ values associated with dipolarizations. Similar to the minima in B_z, the maxima in ϵ occur just prior to onset (except when AL is used to determine the onset; in that case the maxima occur just after onset). As with B_z, ϵ undergoes a sharp transition just prior to the model AL onsets, and the plasmoid release times are associated with only a very weak increase and decrease in ϵ.

Figures 6.8c and 6.8g show SEAs of AL. In the observations, a sharp decrease occurs at onset. This occurs for all of the individual signatures except for the dipolarizations. Dipolarizations are associated with a downward trend in AL but the decrease occurs gradually. When all signatures are combined, the associated decrease is stronger than even the decrease associated with the AL onsets themselves. The behavior of the observed AL index is qualitatively similar to what was obtained by previous authors. The approximately 2 hour recovery time is similar to the results of e.g. *Caan et al.* (1978), *Forsyth et al.* (2015), but the -500 nT minimum is lower than their results. In the model output, AL onsets are also associated with a sharp decrease at onset, but the the MPB onsets and dipolarizations are associated with gradual decreases in AL, while plasmoids are associated with a barely perceptible decrease. When AL onsets alone are used for the onset list, an increase occurs roughly one hour prior to onset, followed by a decrease similar to the observed one. When all the model signatures are combined, the increase prior to onset is absent, and the associated decrease in AL is weaker than occurs in observations.

The fact that the combined AL onsets are stronger on average in the observations than individual signatures implies that the process of combining signatures has eliminated some of the weaker AL onsets. On the other hand, the opposite occurs in the model output. This implies that combining signatures does not necessarily eliminate weak substorms, but rather those that are too far from the average. The fact that

the average in the model involves a weaker onset reflects the fact that the model produces weaker variations in AL in general, as was noted for the same simulation in *Haiducek et al.* (2017). The lack of association between dipolarizations and AL onsets in the observations may be due in part to the fact that only two satellites are used to identify dipolarizations (versus three for the LANL energetic particle injections). The model output uses dipolarizations identified from a third location (which is ideally positioned on the sun-Earth line), and in the model output the dipolarizations do not contrast as strongly from the other datasets in terms of their associated AL response.

Figures 6.8d and 6.8h show SEAs of the MPB index. All of the observed signatures are associated with an increase in MPB beginning at onset. Dipolarizations are associated with an additional gradual increase prior to onset, with the rate of increase becoming greater at the onset time. When all signatures are combined, the associated increase in MPB is noticeably stronger than for any single signature alone. In all cases, the shape is qualitatively similar to the superposed epoch analysis shown in *Chu et al.* (2015) for MPB onsets, which similar to our results showed peaks between 50 and 250 nT and recovery times on the order of 1 hour. With the model output, all of the signatures are also associated with an increase in MPB. However, the magnitude of this increase varies substantially from one signature to another. Plasmoid releases are associated with the weakest increase in MPB, while AL onsets are asssociated with the strongest increase. Combining all signatures together does not intensify the associated MPB response as it does for the observations, with the combined MPB curve falling in between that of the AL, dipolarization, and MPB onsets.

It is worth noting that plasmoid releases are only very weakly associated with changes in driving conditions (IMF and ϵ) or in response indicators (AL and MPB). This is related to the fact that many more plasmoid releases were identified than any other signature (see Table 6.3), which means that many plasmoid releases may have no associated auroral or geosynchronous response, or the response might be below

the threshold for selection. Such plasmoids may be too weak or too far down-tail to have a substantial effect close to the Earth. The state of the fields and plasmas in the inner magnetosphere may also influence how much energy from the plasmoid release is transported Earthward. Similarly, dipolarizations are also only weakly associated with changes in driving conditions and magnetospheric response, though they are more strongly associated than plasmoids are. Like the plasmoids, dipolarizations are observed in the magnetosphere and most likely some of them occur without a strong coupling to the ionosphere that would produce a typical substorm response.

6.4 Discussion

In the present work we have demonstrated a procedure to combine multiple substorm onset lists into a single list. We applied this procedure to observational data and to MHD output from the same one-month period. By performing superposed epoch analysis we demonstrated that the resulting onset list is consistent with previous results in terms of the solar wind driving and the geomagnetic response as measured by ground-based magnetometers. We showed that the total number of substorms and the waiting time distributions are also consistent with previous results. Finally, we showed preliminary evidence that our MHD model has statistically significant predictive skill and is able to reproduce the observed waiting time distribution, as well as some of the observed features in terms of driving and response.

The approach of combining onset lists obtained using different techniques into a single combined list appears to at least partially address the problems of false identifications and data gaps. More than twice as many plasmoid releases were identified from the model output than were obtained by analyzing any single observational signature, yet the total number of substorms identified in the model output is far smaller than the number of plasmoid releases, indicating that the vast majority of plasmoid releases were rejected for lack of an associated AL, MPB, or dipolarization signature.

Data gaps in the observations account for significant under-counting of dipolarization signatures, but the total number of observed substorms in the combined list is significantly higher. This suggests that the combined inputs from other observed signatures were able to compensate for the lack of continuous night-side magnetic field observations in geosynchronous orbit.

The total number of substorms, as well as our waiting time distribution, suggests that our method reduces the frequency and number of substorms compared to most individual identification strategies. We identified marginally fewer substorms than *Borovsky and Yakymenko* (2017), and far fewer than *Newell and Gjerloev* (2011a) for the same time period. We identified marginally more than *Frey et al.* (2004), but the *Frey et al.* (2004) method relied exclusively on the IMAGE/FUV spacecraft which only provided auroral observations 60-70% of the time, while our method provides much better temporal coverage owing to the use of multiple datasets. Related to this, our 5-hour modal waiting time is greater than most previously published results (e.g. *Borovsky et al.*, 1993, *Chu et al.*, 2015, *Kauristie et al.*, 2017, *Borovsky and Yakymenko*, 2017). This could be interpreted as an indication that our methodology misses substorms that should be included, or it could be interpreted as meaning that the previously published substorm lists contain events that should not be regarded as substorms.

Of course, the total number of substorms identified by our method can be increased or decreased by adjusting its tuning parameters: The detection threshold and the kernel width. Unfortunately neither of these has an obvious correct or best value, but it is possible to identify a range in which reasonable results can be expected. For instance, setting the kernel width too low can greatly reduce the number of events selected, in extreme cases selected no events at all. An overly large kernel width would cause unrelated onsets to be counted together, potentially inflating the total number of events. We have selected a kernel width of 10 minutes, but kernel widths

as small as 5 minutes and as large as 20 minutes might be considered reasonable. Similarly, the threshold condition can have a substantial effect on the total number of events selected, as was illustrated in Figures 6.5 and 6.6 in which the total number of observed events varies from 53 to 423 as the detection threshold is varied.

The relationship between the threshold and what events are selected depends on the number of signatures used as well as the distribution of waiting times in each. As a result, the threshold will need to be adjusted whenever signatures are added or removed. In the present work we selected the threshold intuitively based on an analysis of the ROC curves and the total number of events, but it may be possible to construct a heuristic based on the number of onset lists that are combined. A simple approach would be to scale the threshold linearly with the number of onset lists used. The threshold might be adjusted down for time periods in which one or more signatures is known to contain a data gap.

It is also worth noting that our procedure weights all signatures equally, convolving each with the same kernel function and adding them together. It would be possible to apply weight factors during summation if, for instance, one signature was considered more reliable than another. Lacking an objective means to determine appropriate weight factors, we have decided not to apply variable weights to the individual signatures in the present work. However, in the future it would be appropriate to apply weight factors to scale the scores obtained for each signature. One way to do this might be to compute weighting factors based on the average waiting time in each onset list. This would weight signatures such as plasmoids that occur very frequently (and probably are not always associated with substorms) less heavily than those that occur less frequently. Another approach might be to develop a reliability measure of some sort, which could be applied to each signature and used to compute its weighting factor. For some signatures, it might be appropriate to weight individual onsets according to a measure of event strength associated with that signature. For instance,

the amount of change in AL within a specified time after onset could be used as a measure of AL onset strength, and AL onsets with large changes could be weighted more strongly than those with small changes.

The use of a Gaussian kernel imposes a temporal symmetry, where onsets are treated as being related or not according to how close they occur in time relative to each other, without regard to which signature precedes the other. However, in reality a particular class of signature may tend to occur before or after onset, and the amount of time relative to onset may not be uniform. This could be accounted for by using a non-Gaussian kernel shape, which could be selected individually for each signature based on its tendency to lead or follow other signatures.

The tunability of our procedure, along with the possible modifications described in this section, give it a significant amount of flexibility. This enables it to be optimized to produce desired characteristics in terms of what events are identified. One approach might be to adjust the tuning parameters for best agreement with an established list. However, the lack of a community consensus on precise procedures, benchmarks, or tests for correct substorm identification precludes this approach. This lack of such a consensus has been an issue in the community for a while, and has been noted by a number of authors (e.g. *Rostoker et al.*, 1980, *McPherron and Chu*, 2017, 2018). While we can readily compare our list against existing ones, as has been done by a number of researchers (e.g. *Moldwin and Hughes*, 1993, *Boakes et al.*, 2009, *Liou*, 2010, *Chu et al.*, 2015, *Forsyth et al.*, 2015, *Kauristie et al.*, 2017), fundamentally such comparisons tell us about the similarities and differences between the lists and not which list is most correct. In the meantime, optimizing for known characteristics of substorms, rather than a specific list, is probably the best approach.

If our identification procedure is used applied for operational purposes, another important consideration is that the detection thresholds be adjusted based on the needs of forecast customers. In this case, factors such as the costs and risks associated

with false positive and false negative detections should be considered. Is the cost of responding to a false positive prediction greater or less than the cost incurred when a substorm arrives unannounced? Of course, this probably depends on the strength of an event, and ideally the procedure should be tuned in a manner that makes stronger events more likely to detect.

One of the possible operational applications for our identification procedure is the development of a substorm forecast product. This could be done using an MHD model as we demonstrated in the present work. The ability to simulate a substorm with an MHD model has been demonstrated previously (e.g. *Lyon et al.*, 1981, *Slinker et al.*, 1995, *Raeder et al.*, 2001b, *Wang et al.*, 2010). However, previous efforts simulating substorms with MHD have covered time periods lasting no more than a few days and at most several substorms, preventing a rigorous analysis of the model's predictive skill. In the present work we used a one-month simulation including around 100 substorms, which is sufficient to enable computation of forecast accuracy metrics such as POD, POFD, and HSS. This is the first attempt to rigorously evaluate an MHD model for its ability to predict substorms.

In our test, the MHD model demonstrated consistently positive predictive skill, with zero or negative skill scores occurring only in extreme cases of high or low detection thresholds. The skill scores achieved are closer to zero (no skill) than they are to one (perfect skill), however. This certainly leaves room for improvement, but it begs the question of whether scores on this level are sufficiently high to be useful. Some examples can be found in tropospheric modeling of operational models that produce skill scores on this level, particularly for long lead time forecasts of difficult to predict parameters such as precipitation (e.g. *Barnston et al.*, 1999). However, such comparisons are of limited utility not only because of the differences in the phenomenon being predicted, but also difference in the lead time and the temporal and spatial granularity of the forecast. Ultimately, an assessment of operational usefulness

depends on the manner in which the forecast is used by customers, including the operational impact and mitigation strategies available.

An obvious path forward with the MHD model is to explore whether this initial demonstration of predictive skill can be improved upon. The first step would be to conduct tests of different configurations of the model to determine the sensitivity of results to parameters such as grid resolution and boundary conditions. Another possible path for improvement is the incorporation of non-ideal MHD and other physical processes that were not incorporated in the simulation shown here. A likely candidate for this is the inclusion of additional resistive terms. It has long been recognized that resistivity plays an important role in controlling magnetotail dynamics such those associated with substorms. *Birn and Hones Jr.* (1981), for instance, demonstrated that an X-line formation and plasmoid release could be induced in an MHD simulation by abruptly increasing the amount of resistivity. In the present work, as with many efforts involving MHD simulation, we rely entirely on numerical resistivity to enable reconnection to occur. We showed that this produces substorms at a realistic rate, as evidenced by the fact that the total number of substorms is in line with other lists from the same time period, and the waiting time distribution obtained from the model falls within the 95% confidence interval of the observed distribution. This means that our numerical resistivity is realistic enough that the model can capture important aspects of the system dynamics. However, improving the prediction of substorms probably requires a more realistic resistivity model. One approach is to introduce Hall resistivity, which has been shown by observations to play a role in magnetotail reconnection (*Øieroset et al.*, 2001). Hall MHD has been implemented in SWMF (*Tóth et al.*, 2008), but has not been tested in the context of substorm prediction. Another approach that may improve substorm-related reconnection physics is the use of a particle-in-cell (PIC) model in place of MHD in and near the reconnection region. This has been demonstrated by *Tóth et al.* (2016), *Chen et al.* (2017) for magneto-

spheric simulations, but has not been tested for the magnetotail region of Earth nor for substorm prediction. On the other hand, the PIC approach, while promising for its ability to capture aspects of reconnection physics that are not incorporated in ideal MHD, is likely too computationally expensive for operational use in the near term.

Besides night-side reconnection, coupling between the magnetosphere and ionosphere plays an important role in the substorm process. For instance, ionospheric conductivity influences the strength and spatial distribution of field-aligned currents within the magnetosphere (e.g. *Ridley et al.*, 2004). However, there is considerable room for improvement in the models of this conductance, particularly in the auroral zone. SWMF currently estimates auroral-zone conductance using an empirical relationship based on the strength of field-aligned currents, since MHD does not directly estimate the precipitating fluxes that determine the conductivity in reality (*Ridley et al.*, 2004). An alternative might be to estimate the conductivity using the particle distributions in an inner magnetosphere model such as RCM, but this would the development of new empirical relationships between precipitating fluxes and conductivity. Other improvements to the MHD model that could influence magnetosphere-ionosphere coupling include the use of anisotropic pressure (*Meng et al.*, 2012a, 2013), polar outflow (*Glocer et al.*, 2009b), and multi-fluid MHD (*Glocer et al.*, 2009c), all of which have been implemented in BATS-R-US and demonstrated in magnetospheric simulations, but none of which have been tested for their effect on substorm prediction. The initial tests of anisotropic pressure and polar outflow in SWMF (*Meng et al.* (2012a) and *Glocer et al.* (2009b), respectively) both showed that simulations using those models have increased tail stretching compared with BATS-R-US simulations that do not use them, and this could have a significant influence on substorm dynamics since the substorm growth stage is associated with magnetotail stretching (e.g. *Kaufmann*, 1987, *Sergeev et al.*, 1990).

Of the enhancements mentioned above, ionospheric outflow may be particularly important because it has been shown to be associated with substorms. For instance *Øieroset et al.* (1999) and *Wilson et al.* (2004) both found that ionospheric outflow increases by a factor of two on average from quiet time to substorm onset, and that stronger substorms are associated with higher rates of ionospheric outflow. Modeling results have shown that ionospheric outflow can influence magnetospheric dynamics in general (e.g. *Winglee et al.*, 2002a, *Wiltberger et al.*, 2010) and substorm strength and onset times in particular (e.g. *Welling et al.*, 2016). Such results suggest that exploration of ionospheric outflow may be a fruitful path toward improved substorm prediction.

The conclusions of the chapter can be summarized as follows:

1. We have demonstrated a new technique for substorm identification that combines multiple observational signatures to reduce false positive identifications.

2. The total number of substorms identified using this technique is consistent with previously published results for the same time period.

3. The magnetospheric driving and response at the substorm onset times identified using our technique is consistent with expected behavior during substorms.

4. When our substorm identification technique is applied to output from an MHD simulation, we obtain a distribution of waiting times that is comparable to the observational data, driving conditions that are similar to those at the observed epoch times, and a magnetospheric response that is qualitatively similar (though quantitatively different) from the observed response.

5. The MHD simulation has weak, but statistically significant, skill in predicting substorms.

This chapter explored a particular magnetospheric process, the substorm, in which magnetotail dynamics play a particularly crucial role. An accurate representation of the substorm process in a model requires that the model incorporate many aspects of magnetotail structure and dynamics, including those explored in Chapters III-V. The next chapter summarizes the results of all four studies in the dissertation, and discusses possible paths for future study building on this work.

CHAPTER VII

Conclusions

This dissertation incorporates several projects aimed at furthering the validation of the SWMF (Space Weather Modeling Framework), and using SWMF to better understand magnetotail dynamics. The first of these, presented in Chapter III, was a validation effort aimed at testing SWMF's ability to reproduce the observed variations of geomagnetic indices and CPCP (cross-polar cap potential), all of which depend in part on the behavior of the magnetotail. The second, presented in Chapter IV, tested SWMF's ability to reproduce tail magnetic fields during quiet conditions, and provided new analysis helping to constrain the range of the K parameter for IB (isotropic boundary) observations during such conditions. This was extended to storm conditions in Chapter V, resulting in an estimate of the fraction of the time for which K is likely to be consistent with CSS (current sheet scattering) during storm conditions. Finally, Chapter VI presented a new technique for identifying substorm onsets, and the results of using the technique to identify substorm onsets in SWMF and in observational data. The SWMF onset times were compared with the observed values as a test of SWMF's ability to predict substorms.

The validation results in Chapter III show that SWMF performs extremely well in predicting the Sym-H index, with the model predictions falling only marginally outside the probable uncertainty for the observed values of Sym-H. The model also

does reasonably well in predicting Kp, AL, and CPCP, as indicated by their normalized RMSE (root mean squared error) values, but with conspicuous shortcomings in each case. The model persistently over-predicts Kp during quiet time, and persistently over-predicts CPCP on average. It predicts AL accurately on average, but under-predicts the magnitude of the most negative values of AL. This suggests an under-prediction of substorm strength and/or frequency, something that is addressed further in Chapter VI.

Because the conditions prior to substorm onset involve stretching of the tail-side magnetic fields, the model's ability to reproduce night-side fields can significantly affect its ability to produce realistic substorm dynamics. The work in Chapter IV tested the SWMF's accuracy in reproducing the night-side magnetic field by comparing SWMF magnetic fields with in situ observations. SWMF was then used to provide estimations of the K parameter associated with night-side IB observations. Using SWMF and several empirical models, it was shown that the IB observations were probably formed by CSS. Chapter V continued this work in a storm interval, showing that CSS operated for a significant fraction (at least 23% and possibly as high as 55%) of the IB observations. In Chapters IV and V, both the K estimates and the comparison with in situ satellite observations indicated that SWMF produced under-stretched magnetotail fields much of the time. These under-stretched fields may cause the simulated magnetosphere to have a reduced propensity to produce substorm onsets compared to the real magnetosphere, and may explain the under-prediction of strongly negative AL values noted in Chapter III.

The work in Chapter VI directly tested SWMF's ability to produce substorms. This began with the introduction of a new procedure for identifying substorms. This procedure utilizes lists of substorm onset times from multiple techniques and datasets. The new procedure combines the individual lists to produce a combined list, aiming to reduce false identifications by identifying points of correspondence between

the individual lists. This procedure was applied to both observational data and to simulation output, and the two were compared by computing metrics of prediction quality, along with confidence intervals for each metric. Of particular interest are the estimates of Heidke Skill Score (HSS). While the values were on the order of 0.1, indicating weak skill, the 95% confidence intervals indicate that the skill scores are statistically significant. This demonstrates that substorms can be predicted using MHD (magnetohydrodynamic) simulations.

All of the work in this chapter sheds light on magnetotail dynamics using SWMF. Magnetotail current systems such as the cross-tail current (and field-aligned currents connected to it) affect the geomagnetic indices studied in Chapter III. The IB studies presented in Chapters IV and V confirm the idea that the IB can be used to determine magnetotail geometry, and that this can also be done (some of the time) during storm conditions. These studies also showed a tendency of SWMF to produce under-stretched magnetic fields. Chapter VI demonstrated that, despite the tendency toward under-stretched fields, the SWMF does have statistically significant skill in predicting substorms.

7.1 Future Work

The work in this dissertation can be extended in a number of ways in order to better understand magnetotail and our ability to model it:

- **Exploration of seasonal dependencies** The one-month validation study presented in Chapter III covers a period of northern hemisphere winter during the declining phase of the solar cycle. Similarly, the isotropic boundaries studies presented in Chapters IV and V cover a northern hemisphere winter quiet-time period and southern hemisphere springtime storm interval. Similar studies covering a different time of year or different phase of the solar cycle would enable

an exploration of seasonal dependencies for the various metrics studied and SWMF's ability to reproduce them. Data from NOAA SWPC's operational applications of SWMF could be applied to this effort, but separate additional studies would enable these seasonal dependencies to be explored with other configurations of SWMF besides that used by SWPC.

- **Further validation with in situ magnetotail observations** The January, 2005 time period covered in Chapters III and VI provided little in terms of in situ observations of the magnetotail, with Geotail being the only spacecraft providing such observations. Conducting studies to those in Chapters III and VI during a different time period would enable in situ observations from the magnetotail to be used to further validate the model in terms of night-side magnetic fields and plasma moments, and observations of plasmoid releases and dipolarization fronts to be included in the substorm identifications.

- **Use IB observations to study the magnetotail fields in more detail** The work of Chapters IV and V could be extended to explore additional time periods. The inclusion of additional time periods could be used to help address the influence of satellite motion on the results, as well as to provide results that are more representative of magnetospheric behavior in general rather than the particular characteristics of the days-long time intervals included in those chapters. At the same time, the quality of individual K estimations could be estimated based on how well the different models agreed with each other in the K values, both before and after correction.

- **Compare IB observation results with EMIC wave observations** The results of Chapter V showed that many of the IB observations were associated with K low enough to be associated with IB observations, but no check was made for the presence of EMIC (electromagnetic ion-cyclotron) waves. Compar-

ing the K estimates with EMIC wave observations would provide an additional test for the scattering mechanism responsible for each IB observation, and such a comparison could be used to further constrain the appropriate threshold for K during storm conditions.

- **Test IB observations on the dayside** The studies in Chapters IV and V were both confined to the night side. However, the IB is found on the day side as well. Conducting similar studies on the day side would provide a means to explore the causes of IB formation on the day side. This could provide a means to further test the accuracy of the magnetospheric models, and to use them in exploring the causes of IB characteristics. For instance, as was mentioned earlier, previous studies have shown a day-night asymmetry in the IB latitude, with the IB forming at higher latitudes on the dayside than on the nightside. This could be due to a difference in the magnetic field geometry on the dayside (consistent with the compression of dayside field lines by the solar wind), or to a difference in the relative importance of the EMIC waves in formation of the IB on the day side versus the night side. Studies of dayside IB observations like those presented in Chapters IV and V for the nightside could help to better determine how the IB is formed on the dayside, while at the same time providing a new test of the accuracy of the dayside magnetic fields predicted by the models.

- **Implement uncertainty quantification for some or all of the quantities assessed** One limitation common to all the studies presented in this dissertation is that inputs to SWMF contribute significantly to the uncertainty of the model outputs. This is particularly true of the solar wind inputs, which are usually observed at the L1 point, approximately 1.48 million km from the Earth. Solar wind features observed at L1 may evolve significantly by the time they arrive at Earth. In addition, the L1 observations are only representative of what will

arrive at Earth if the solar wind is uniform or its flow direction is very close to being exactly radially outward from the sun. Recent work by *Morley et al.* (2018) addresses this using ensemble simulations with perturbed solar wind input, and similar techniques could be applied to obtain uncertainty estimates for the quantities studied in this dissertation. This would help inform efforts to develop better predictive capabilities, by showing which aspects of the prediction can be improved by upgrading the model, and which are limited by the model's inputs. Uncertainty quantification would also be very informative for helping to interpret the model output for other scientific applications and for operational forecasts, since it would provide a means to assess the significance of any features identified in the model output.

- **Apply data assimilation techniques to increase model accuracy** The work in this dissertation used MHD to estimate values for many quantities that can be obtained through observations, either on the ground or using satellites. The work in this dissertation used the available observations mainly for the purpose of validating the model, but such observations could also be used in a data assimilation scheme to update the model in order to provide a best estimate of the magnetospheric state. This was demonstrated by *Godinez et al.* (2016) with in situ observations of fluxes within the inner magnetosphere, but could in principle be applied to any observable quantity that can be predicted by the MHD simulation, including geomagnetic indices, IB latitudes, and magnetic fields observable by satellites.

- **Optimize the SWMF and its settings for better forecasting** The work presented here shows several weaknesses in SWMF, most notably a tendency to over-predict quiet-time Kp, a tendency to over-predict CPCP, and a tendency to produce under-stretched night-side magnetic fields. The model's skill

in predicting substorms can probably also be improved. Sensitivity studies and optimization studies could be conducted to identify paths for improving these by adjusting model settings. This could extend to replacement of various SWMF components, for instance the RCM (Rice Convection Model) could be substituted for one of the other inner magnetosphere models that have been coupled with the SWMF.

- **Test extended MHD models for their effect on tail stretching and other measures of magnetospheric state and dynamics** Several modifications to MHD including anisotropic MHD (*Meng et al.*, 2012b,a, 2013), multi-fluid MHD (*Glocer et al.*, 2009c), and Hall MHD (*Tóth et al.*, 2008) have been implemented in SWMF, but have not been validated for use in an operational context, nor tested for their ability to predict substorms. Preliminary tests with anisotropic MHD suggest that it has an affect on magnetotail stretching (*Meng et al.*, 2013), and the same may be true of multi-fluid or Hall MHD. Since tail stretching plays an important role in creating the conditions for substorm onset, the amount of tail stretching may affect substorm dynamics as well.

- **Explore alternatives for improving tail-side reconnection** Substorm dynamics depend crucially on the tail-side reconnection rate, which requires resistivity be present in the plasma. In an ideal MHD model, the only source of resistivity is numerical resistivity, which is the result of truncation errors introduced during discretization, and depends on the grid resolution. To more realistically model storms and substorms, this could be supplemented with a physical or empirical estimate of the resistivity. SWMF currently provides two such models. The first is a user-specified resistivity. The difficulty with this approach is a lack of observational data to determine the correct values to choose. The second is Hall MHD, which introduces a resistive term that depends on

the density, current, and magnetic field, which is more physically based but also quite computationally expensive in practice. Another option is to use a particle-in-cell (PIC) model in the reconnection region. This has been tested using SWMF (*Daldorff et al.*, 2014, *Tóth et al.*, 2016), but not for the magnetotail at Earth. PIC would likely provide the most detailed possible model of the reconnection process, but at an even higher computational cost than Hall MHD. However, tests with each may provide a path toward an alternative with a low enough computational cost to be feasible for forecasting applications.

APPENDICES

APPENDIX A

Model description

A.1 Model configuration details

A.1.0.1 MHD solver

For all of the runs in this paper we use BATS-R-US (Block Adaptive Tree Solar-Wind, Roe-type Upwind Scheme) (*Powell et al.*, 1999) to solve the ideal MHD (magnetohydrodynamic) equations. The flux scheme is Sokolov's Local Artificial Wind flux (see *Sokolov et al.*, 2002), and a Koren's third order limiter (*Koren*, 1993) with beta=1.2. Cross-sections of the two MHD grids are shown in Figure A.1. These cross-sections are in the X-Z plane through the origin; the grids are symmetric such that Y-Z cuts through the origin would look identical. Both are Cartesian grids in GSM (geocentric solar magnetospheric) coordinates, with the cell size varied using adaptive mesh refinement (AMR). The outer boundaries form a cube 256 Earth radii (R_e) in width. The grids are offset in the x direction so that they extends 32 R_e sunward of the Earth and 224 R_e tailward. In the y and z directions the grids are centered around the Earth, extending 128 R_e from the Earth along each of those axes. An inflow boundary condition populated with time-dependent solar wind data is used

on the boundary located at x=32 R_e, while the opposite face (at x=-224 R_e) uses an outflow boundary condition. The remaining outer boundaries use a zero-gradient boundary condition.

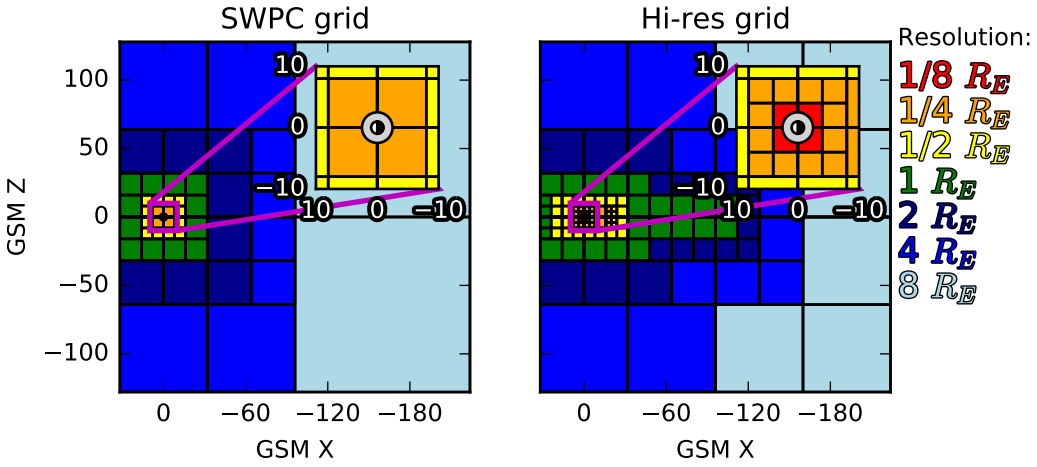

Figure A.1: X-Z cuts showing cell sizes in the two MHD grids. Left panel shows the grid used for the SWPC configuration (minimum cell size of 1/4 R_e, while the right panel shows the higher resolution grid used for the other two runs (minimum cell size of 1/8 R_e).

While the two grids are identical in their overall extent, their resolutions differ significantly. The SWPC grid (left panel of Figure A.1) has cell sizes ranging from 8 R_e at the outflow boundaries to 1/4 R_e within a 16 R_e diameter cube surrounding the Earth. The cell size of the high-resolution grid (right panel of Figure A.1) varies from 8 R_e at the outflow boundaries to 1/8 R_e near the Earth. The refined regions are the same as those used in *Welling and Ridley* (2010). A 1 R_e cell size is used in a region around the x axis extending from the inflow boundary to 112 R_e down-tail, while the near tail region from 8 to 20 R_e down-tail is resolved to 1/4 R_e. The minimum cell size occurs within an 8 R_e wide cube surrounding the Earth, from which a 2.5 R_e sphere is excluded from the MHD grid; this region is modeled through coupling to the ionospheric model described in the next section. The SWPC grid contains around 1 million cells, while the high-resolution grid contains 1.9 million cells.

A.1.0.2 Inner magnetosphere

In the inner magnetosphere, transport by gradient and curvature drift becomes more important to the plasma motion, making the ideal MHD approximation inaccurate there (*Heinemann and Wolf*, 2001). We model this region using the Rice Convection Model (RCM). By averaging out the gyro and bounce motion, this model treats the inner magnetosphere plasma as a fluid that drifts across field lines.

Unlike the MHD solver, the RCM breaks the plasma population into bins according to an energy invariant, and each energy invariant is treated as a separate fluid. In addition, oxygen, hydrogen, and electrons are treated as separate species. Since the MHD solver is being run in single-fluid mode, the coupling between the two codes must divide the MHD fluid into hydrogen and oxygen. The operational model used by SWPC accomplishes this by using a fixed ratio of 10% oxygen and 90% hydrogen by number density. However, we found that with the higher resolution grid this configuration resulted in poorer quality Sym-H predictions than with the lower-resolution grid. We were able to address this problem by replacing the fixed oxygen to hydrogen ratio with one computed using the empirical plasma sheet composition model from *Young et al.* (1982). The *Young et al.* (1982) model gives relative quantities of oxygen and hydrogen as a function of F10.7 and Kp. In our implementation, F10.7 values are provided through an input file, and Kp is obtained from the MHD solver. The results presented in this paper use the fixed ratios of 10% oxygen and 90% hydrogen for the SWPC configuration, and the *Young et al.* (1982) model for the high-resolution with RCM configuration.

A.1.0.3 Ionospheric electrodynamics

The Ridley Ionosphere Model (RIM) models calculates ionospheric parameters on a height-integrated basis. This model is described in *Ridley and Liemohn* (2002) and *Ridley et al.* (2004). It receives field-aligned current values from the MHD solver,

and from these calculates conductance and electric potential. The potential values are then passed back to the inner magnetosphere and MHD models, where they are used to determine the velocity tangent to the inner boundary (the velocity normal to the boundary is set to zero) (*Welling and Liemohn*, 2014). As discussed in *Welling and Liemohn* (2016), the ionospheric boundary is of crucial importance to the overall dynamics of the magnetospheric dynamics. While more sophisticated models exist to model the interaction through this boundary, most are either too computationally costly (such as the Polar Wind Outflow Model *Glocer et al.*, 2007), or lack a fully tested coupling to an MHD model.

APPENDIX B

Substorm identification details

B.1 Procedure for identifying dipolarizations

Our procedure aims to find points that satisfy the following criteria:

- Local minimum of θ
- Onset of a rapid increase in B_z and θ
- Near a local maximum of $|B_r|$

The procedure consists of first finding local minima in θ by searching for points that are less than both of their immediate neighbors (endpoints in the data are not considered). Neighboring points around each of these local minima are checked against a set of thresholds to determine whether they satisfy the criteria given above. Given a minimum in θ, denoted by the subscript i, we specify a set of ranges $m : n$ relative to i, and a threshold B_z or $|B_r|$ must satisfy within that range in order for i

to be considered a dipolarization candidate. The thresholds are defined as follows:

$$\begin{aligned} max(B_{z_{i:i+10}}) &> B_{z_i} + 2 \\ max(B_{z_{i:i+30}}) &> B_{z_i} + 10 \\ max(B_{z_{i:i+60}}) &> B_{z_i} + 16 \\ min(|B_r|_{i-10:i-2}) &< |B_r|_i - 0.25 \\ min(|B_r|_{i+2:i+20}) &< |B_r|_i - 0.5 \\ min(|B_r|_{i+10:i+40}) &< |B_r|_i - 2 \end{aligned} \tag{B.1}$$

The thresholds for B_z require an immediate increase in B_z (2 nT in 10 minutes), which proceeds to at least 10 nT within 30 minutes and 16 nT within 60 minutes. This is not a particularly fast increase; the thresholds are designed to identify all dipolarizations and not only the strong ones.

The thresholds for $|B_r|$ require an increase of at least 0.25 nT within the 10 minutes preceding the candidate onset, a decrease of 0.5 nT within the following 20 minutes, and a decrease of 2 nT within the following 40 minutes. These are fairly weak criteria, and are designed to select candidate onsets occurring near a local maximum, without requiring the maximum be particularly strong nor that the onset candidate occur exactly at the local maximum in $|B_r|$.

An additional procedure aims to prevent counting multiple onset times for a single dipolarization event. If an onsets j is followed by an onset k within the preceding 60 minutes, then we require

$$max(B_{z_{j:k}}) > 0.25 max(B_{z_{k:k+60}}); \tag{B.2}$$

that is, the maximum B_z between j and k must exceed 25% of the maximum B_z reached following onset k. If this threshold is not satisfied, the onset having the lowest value of θ is kept and the other is discarded. Finally, for a candidate dipolarization to be included in the final list, the satellite providing the observations must be located

on the night side; that is, MLT¡6 or MLT¿18.

The chosen thresholds are not particularly stringent individually, but in combination produce a set of dipolarizations that resembles what has been previously reported for ensembles of dipolarizations. To demonstrate this, we performed a superposed epoch analysis (SEA) of the magnetic fields for the two GOES satellites in the observations. This is shown in Figure B.1, which shows superposed epoch analyses of $|B_r|$, B_z, and θ for dipolarization onsets identified from the observational data and each of the three model runs. In this figure, and throughout the paper, plots comparing the model runs to each other and to observations use a common color scheme: Observations are shown in light blue, the Hi-res w/ RCM simulation in medium blue, the Hi-res w/o RCM simulation in orange, and the SWPC simulation in green. The lines in Figure B.1 represent the median of the SEA. The number of dipolarizations identified for each dataset is shown in parentheses in the legend. Although the thresholds specified allow for as little as a 16 nT increase in 60 minutes, the median increase is much faster, closer to 20 nT in 20 minutes. This is similar to what has been reported in previous studies such as *Liou et al.* (2002). The peaks in $|B_r|$ are less pronounced than what occurs in *Liou et al.* (2002). This could probably be addressed with more stringent criteria for $|B_r|$, at the cost of possibly missing some dipolarizations.

B.2 Comparison of inter-substorm intervals obtained using the Borovsky and Newell algorithms

Figure B.2 shows distributions of waiting times for AL onsets identified using the *Borovsky and Yakymenko* (2017) algorithm (blue curve), for AL onsets identified using the Supermag algorithm (*Newell and Gjerloev*, 2011a) (orange curve) and for energetic particle injections identified from LANL satellite data by *Borovsky and*

Yakymenko (2017) (green curve). The Supermag algorithm stands out with a modal 1-hour waiting time, while both the AL onsets and the LANL particle injections from *Borovsky and Yakymenko* (2017) produce a modal 3-hour waiting time. The fact that the *Borovsky and Yakymenko* (2017) algorithm produces an waiting time distribution that resembles that obtained using particle injections contributed to the decision to use the *Borovsky and Yakymenko* (2017) algorithm for substorm identification in the present work.

B.3 Bootstrapping procedure to estimate confidence intervals for forecast metrics and probability densities

The sampling distribution for the HSS is not known (*Stephenson*, 2000), and this means that no analytical formula is available to estimate the confidence interval. We instead employ a bootstrapping procedure (.e.g. *Conover*, 1999), which involves randomly sampling the binary event sequence in order to obtain an estimated distribution for the skill score. This is done as follows: Given a sequence of n observed bins o_i and n predicted bins p_i, we take a sequence of n random samples, with the same indices taken from both sequences. For instance, if $n = 9$, we might have

$$o = [0, 0, 1, 1, 0, 0, 1, 0, 1] \tag{B.3}$$

and

$$p = [0, 1, 0, 1, 0, 0, 0, 1, 1]. \tag{B.4}$$

We then generate a sequence of n random integers representing indices to be sampled from o and p, for instance we might randomly obtain the indices [8,1,4,4,2,6,5,0,3],

which would result in

$$o' = [1, 1, 1, 1, 1, 0, 0, 1, 0] \tag{B.5}$$

and

$$p' = [1, 0, 0, 1, 0, 1, 0, 1, 1], \tag{B.6}$$

from which we can compute a new HSS. We repeat this process N times (typically we use $N = 4000$). The 95% confidence interval for HSS is the 2.5th and 97.5th percentiles of the N skill scores obtained from the N sampled distributions. The same procedure is applied to estimate confidence intervals for hit rate and false positive rate.

To obtain a confidence interval for a kernel density estimate, a similar procedure is applied: Given a sequence of n values x_i for which a KDE is to be computed, n we generate a sequence of n random integers to be used as indices for x_i to produce a new sequence x'_j. A KDE $f_j(y)$ is computed from each sequence x'_j, and these points are evaluated at a series of points y_k. This process is repeated $N = 2000$ times, producing $n \times N$ probability density estimates $p_{jk} = f_j(y_k)$. For each y_k, the 95% confidence interval of the KDE is estimated as the 2.5th and 97.5th percentile of the p_j values obtained for that evaluation point y_k.

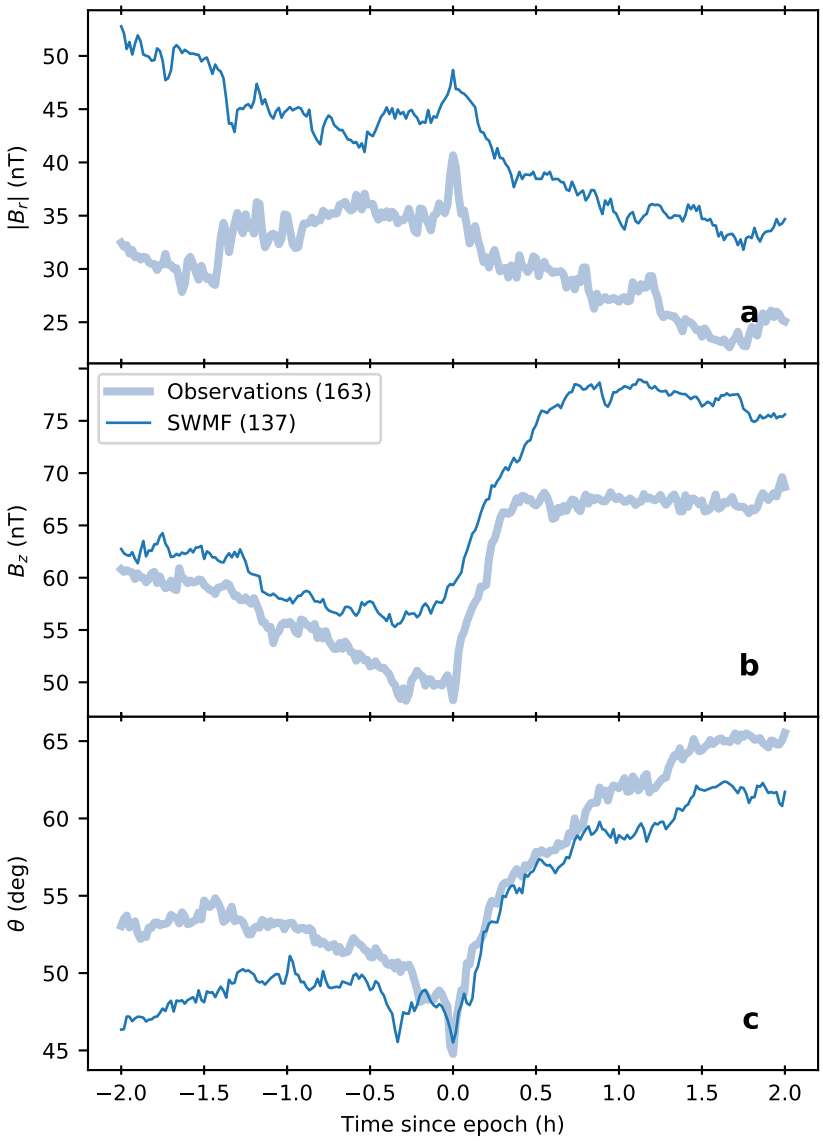

Figure B.1: Superposed epoch analysis of B_r, B_z, and inclination angle θ for all dipolarization onset times.

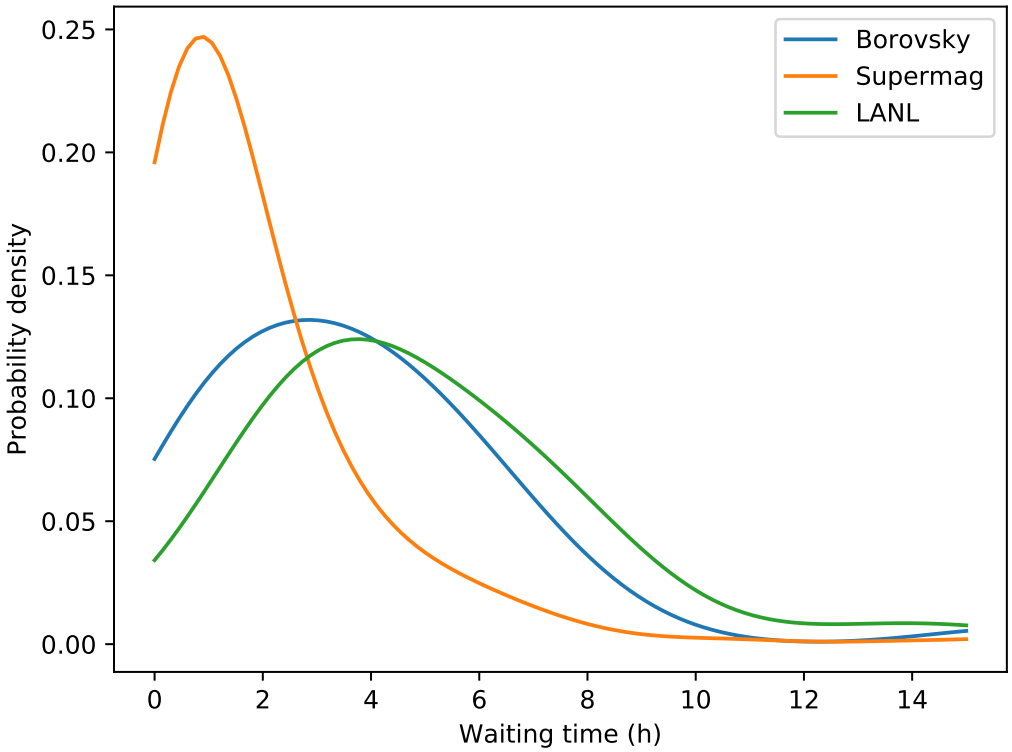

Figure B.2: Substorm waiting times for onsets obtained using the Borovsky (blue curve) and Supermag (orange curve)

BIBLIOGRAPHY

Aikio, A. T., V. A. Sergeev, M. A. Shukhtina, L. I. Vagina, V. Angelopoulos, and G. D. Reeves (1999), Characteristics of pseudobreakups and substorms observed in the ionosphere, at the geosynchronous orbit, and in the midtail, *Journal of Geophysical Research: Space Physics*, *104*(A6), 12,263–12,287, doi:10.1029/1999JA900118.

Akasofu, S.-I. (1960), Large-scale auroral motions and polar magnetic disturbancesI A polar disturbance at about 1100 hours on 23 september 1957, *Journal of Atmospheric and Terrestrial Physics*, *19*(1), 10–25, doi:10.1016/0021-9169(60)90103-3.

Akasofu, S.-I. (1964), The development of the auroral substorm, *Planetary and Space Science*, *101*(4), 273, doi:10.1016/0032-0633(64)90151-5.

Akasofu, S.-I. (2015), Auroral substorms as an electrical discharge phenomenon, *Progress in Earth and Planetary Science*, *2*(1), 20, doi:10.1186/s40645-015-0050-9.

Akasofu, S.-I., and S. Chapman (1963), The development of the main phase of magnetic storms, *Journal of Geophysical Research*, *68*(1), 125–129, doi:10.1029/JZ068i001p00125.

Akasofu, S. I., and C. I. Meng (1969), A study of polar magnetic substorms, *Journal of Geophysical Research*, *74*(1), 293–313, doi:10.1029/JA074i001p00293.

Akasofu, S.-I., and S. Yoshida (1966), Growth and decay of the ring current and the polar electrojets, *Journal of Geophysical Research*, *71*(1), 231–240, doi:10.1029/JZ071i001p00231.

Alfvén, H., and C. G. Fälthammar (1963), *Cosmical electrodynamics: Fundamental Principles (Volume 1)*, International series of monographs on physics, Clarendon Press.

Allen, J., H. Sauer, L. Frank, and P. Reiff (1989), Effects of the March 1989 solar activity, *Eos, Transactions American Geophysical Union*, *70*(46), 1479, doi:10.1029/89EO00409.

Anderson, B. J., et al. (2017), Comparison of predictive estimates of high-latitude electrodynamics with observations of global-scale birkeland currents, *Space Weather*, *15*(2), 352–373, doi:10.1002/2016SW001529, 2016SW001529.

Anderson, D., A. Anghel, J. Chau, and O. Veliz (2004), Daytime vertical $\mathbf{E} \times \mathbf{B}$ drift velocities inferred from ground-based magnetometer observations at low latitudes, *Space Weather*, *2*(11), S11,001, doi:10.1029/2004SW000095.

Angelopoulos, V., et al. (2008), Tail reconnection triggering substorm onset., *Science (New York, N.Y.)*, *321*(5891), 931–5, doi:10.1126/science.1160495.

Asikainen, T., V. Maliniemi, and K. Mursula (2010), Modeling the contributions of ring, tail, and magnetopause currents to the corrected Dst index, *Journal of Geophysical Research: Space Physics*, *115*(A12), doi:10.1029/2010JA015774.

Asikainen, T., K. Mursula, and V. Maliniemi (2012), Correction of detector noise and recalibration of NOAA/MEPED energetic proton fluxes, *Journal of Geophysical Research: Space Physics*, *117*(A9), A09,204, doi:10.1029/2012JA017593.

Auster, H. U., et al. (2008), The THEMIS Fluxgate Magnetometer, *Space Science Reviews*, *141*(1-4), 235–264, doi:10.1007/s11214-008-9365-9.

Axford, W. (1964), Viscous interaction between the solar wind and the earth's magnetosphere, *Planetary and Space Science*, *12*(1), 45–53, doi:10.1016/0032-0633(64)90067-4.

Axford, W. I., and C. O. Hines (1961), A UNIFYING THEORY OF HIGH-LATITUDE GEOPHYSICAL PHENOMENA AND GEOMAGNETIC STORMS, *Canadian Journal of Physics*, *39*(10), 1433–1464, doi:10.1139/p61-172.

Baker, D. N., R. L. McPherron, T. E. Cayton, and R. W. Klebesadel (1990), Linear prediction filter analysis of relativistic electron properties at 6.6 R _E , *Journal of Geophysical Research*, *95*(A9), 15,133, doi:10.1029/JA095iA09p15133.

Baker, K. B., and S. Wing (1989), A new magnetic coordinate system for conjugate studies at high latitudes, *Journal of Geophysical Research: Space Physics*, *94*(A7), 9139–9143, doi:10.1029/JA094IA07P09139.

Barnston, A. G., et al. (1999), NCEP Forecasts of the El Niño of 199798 and Its U.S. Impacts, *Bulletin of the American Meteorological Society*, *80*(9), 1829–1852, doi:10.1175/1520-0477(1999)080⟨1829:NFOTEN⟩2.0.CO;2.

Bartels, J. (1949), The standardized index, Ks, and the planetary index, Kp, *IATME Bull. 12b*, *97*(2010), 2021.

Bartels, J., N. H. Heck, and H. F. Johnston (1939), The three-hour-range index measuring geomagnetic activity, *Terrestrial Magnetism and Atmospheric Electricity*, *44*(4), 411–454, doi:10.1029/TE044i004p00411.

Berger, M., and P. Colella (1989), Local adaptive mesh refinement for shock hydrodynamics, *Journal of Computational Physics*, *82*(1), 64–84, doi:10.1016/0021-9991(89)90035-1.

Berger, M. J. (1987), Adaptive finite difference methods in fluid dynamics, *In Von Karman Inst. for Fluid Dynamics, Computational Fluid Dynamics 50 p (SEE N88-15951 08-34)*.

Berger, M. J., and A. Jameson (1985), Automatic adaptive grid refinement for the Euler equations, *AIAA Journal*, *32*(4), 561–568, doi:10.2514/3.8951.

Birn, J., and M. Hesse (2013), The substorm current wedge in MHD simulations, *Journal of Geophysical Research: Space Physics*, *118*(6), 3364–3376, doi:10.1002/jgra.50187.

Birn, J., and E. W. Hones Jr. (1981), Three-Dimensional Computer Modeling of Dynamic Reconnection in the Geomagnetic Tail, *J. Geophys. Res.*, *86*(A8), 6802–6808, doi:10.1029/JA086iA08p06802.

Birn, J., M. F. Thomsen, J. E. Borovsky, G. D. Reeves, D. J. McComas, R. D. Belian, and M. Hesse (1998), Substorm electron injections: Geosynchronous observations and test particle simulations, *Journal of Geophysical Research: Space Physics*, *103*(A5), 9235–9248, doi:10.1029/97JA02635.

Birn, J., R. Nakamura, E. V. Panov, and M. Hesse (2011), Bursty bulk flows and dipolarization in MHD simulations of magnetotail reconnection, *Journal of Geophysical Research: Space Physics*, *116*(A1), doi:10.1029/2010JA016083.

Blagoveshchensky, D. V., and T. D. Borisova (2000), Substorm effects of ionosphere and HF propagation, *Radio Science*, *35*(5), 1165–1171, doi:10.1029/1998RS001776.

Boakes, P. D., S. E. Milan, G. A. Abel, M. P. Freeman, G. Chisham, and B. Hubert (2009), A statistical study of the open magnetic flux content of the magnetosphere at the time of substorm onset, *Geophysical Research Letters*, *36*(4), doi:10.1029/2008GL037059, l04105.

Bolduc, L. (2002), GIC observations and studies in the Hydro-Québec power system, *Journal of Atmospheric and Solar-Terrestrial Physics*, *64*(16), 1793–1802, doi:10.1016/S1364-6826(02)00128-1.

Bonnevier, B., R. Boström, and G. Rostoker (1970), A three-dimensional model current system for polar magnetic substorms, *Journal of Geophysical Research*, *75*(1), 107–122, doi:10.1029/JA075i001p00107.

Borovsky, J. E. (2012), The effect of sudden wind shear on the Earth's magnetosphere: Statistics of wind shear events and CCMC simulations of magnetotail disconnections, *Journal of Geophysical Research: Space Physics*, *117*(A6), doi:10.1029/2012JA017623.

Borovsky, J. E., and M. Hesse (2007), The reconnection of magnetic fields between plasmas with different densities: Scaling relations, *Physics of Plasmas*, *14*(10), 102,309, doi:10.1063/1.2772619.

Borovsky, J. E., and K. Yakymenko (2017), Substorm occurrence rates, substorm recurrence times, and solar wind structure, *Journal of Geophysical Research: Space Physics*, *122*(3), 2973–2998, doi:10.1002/2016JA023625.

Borovsky, J. E., R. J. Nemzek, and R. D. Belian (1993), The occurrence rate of magnetospheric-substorm onsets: Random and periodic substorms, *Journal of Geophysical Research: Space Physics*, *98*(A3), 3807–3813, doi:10.1029/92JA02556.

Boteler, D. H. (2001), Space Weather Effects on Power Systems, in *Space Weather*, edited by P. P. Song, H. J. Singer, and G. L. Siscoe, pp. 347–352, American Geophysical Union, doi:10.1029/GM125p0347.

Boynton, R. J., M. A. Balikhin, S. A. Billings, H. L. Wei, and N. Ganushkina (2011), Using the NARMAX OLS-ERR algorithm to obtain the most influential coupling functions that affect the evolution of the magnetosphere, *Journal of Geophysical Research: Space Physics*, *116*(A5), A05,218, doi:10.1029/2010JA015505.

Brambles, O. J., W. Lotko, B. Zhang, M. Wiltberger, J. Lyon, and R. J. Strangeway (2011), Magnetosphere Sawtooth Oscillations Induced by Ionospheric Outflow, *Science*, *332*(6034), 1183–1186, doi:10.1126/science.1202869.

Brambles, O. J., W. Lotko, B. Zhang, J. Ouellette, J. Lyon, and M. Wiltberger (2013), The effects of ionospheric outflow on ICME and SIR driven sawtoothevents, *Journal of Geophysical Research: Space Physics*, *118*(10), 6026–6041, doi:10.1002/JGRA.50522.

Bräysy, T., K. Mursula, and G. Marklund (1998), Ion cyclotron waves during a great magnetic storm observed by Freja double-probe electric field instrument, *Journal of Geophysical Research: Space Physics*, *103*(A3), 4145–4155, doi:10.1029/97JA02820.

Brio, M., and C. Wu (1988), An upwind differencing scheme for the equations of ideal magnetohydrodynamics, *Journal of Computational Physics*, *75*(2), 400–422, doi:10.1016/0021-9991(88)90120-9.

Bristow, W. A., R. A. Greenwald, S. G. Shepherd, and J. M. Hughes (2004), On the observed variability of the cross-polar cap potential, *Journal of Geophysical Research: Space Physics*, *109*(A2), doi:10.1029/2003JA010206.

Büchner, J., and L. M. Zelenyi (1987), Chaotization of the electron motion as the cause of an internal magnetotail instability and substorm onset, *Journal of Geophysical Research*, *92*(A12), 13,456–13,466, doi:10.1029/JA092iA12p13456.

Burlaga, L., E. Sittler, F. Mariani, and R. Schwenn (1981), Magnetic loop behind an interplanetary shock: Voyager, Helios, and IMP 8 observations, *Journal of Geophysical Research*, *86*(A8), 6673, doi:10.1029/JA086iA08p06673.

Burlaga, L. F., and K. W. Ogilvie (1969), Causes of sudden commencements and sudden impulses, *Journal of Geophysical Research*, *74*(11), 2815–2825, doi:10.1029/JA074i011p02815.

Burton, R. K., R. L. McPherron, and C. T. Russell (1975), An empirical relationship between interplanetary conditions and Dst, *Journal of Geophysical Research*, *80*(31), 4204–4214, doi:10.1029/JA080i031p04204.

Caan, M. N., R. L. McPherron, and C. T. Russell (1975), Substorm and interplanetary magnetic field effects on the geomagnetic tail lobes, *Journal of Geophysical Research*, *80*(1), 191–194, doi:10.1029/JA080i001p00191.

Caan, M. N., R. L. McPherron, and C. T. Russell (1977), Characteristics of the association between the interplanetary magnetic field and substorms, *Journal of Geophysical Research*, *82*(29), 4837–4842, doi:10.1029/JA082i029p04837.

Caan, M. N., R. L. McPherron, and C. T. Russell (1978), The statistical magnetic signature of magnetospheric substorms, *Planetary and Space Science*, *26*(3), 269–279, doi:10.1016/0032-0633(78)90092-2.

Campbell, W. H. (1980), Observation of electric currents in the Alaska oil pipeline resulting from auroral electrojet current sources, *Geophysical Journal International*, *61*(2), 437–449, doi:10.1111/j.1365-246X.1980.tb04325.x.

Cash, M. D., S. Witters Hicks, D. A. Biesecker, A. A. Reinard, C. A. de Koning, and D. R. Weimer (2016), Validation of an operational product to determine l1 to earth propagation time delays, *Space Weather*, *14*(2), 93–112, doi:10.1002/2015SW001321, 2015SW001321.

Cassak, P. A., and M. A. Shay (2007), Scaling of asymmetric magnetic reconnection: General theory and collisional simulations, *Physics of Plasmas*, *14*(10), doi:10.1063/1.2795630.

Cayton, T., and R. D. Belian (2007), Numerical modeling of the Synchronous Orbit Particle Analyzer (SOPA, Version 2) that flew on S/C 1990-095, *Tech. rep.*, Los Alamos National Laboratory, Los Alamos, NM.

Cayton, T. E., R. D. Belian, S. P. Gary, T. A. Fritz, and D. N. Baker (1989), Energetic electron components at geosynchronous orbit, *Geophysical Research Letters*, *16*(2), 147–150, doi:10.1029/GL016i002p00147.

Chao, J. K., J. R. Kan, A. T. Lui, and S. I. Akasofu (1977), A model for thinning of the plasma sheet, *Planetary and Space Science*, *25*(8), 703–710, doi:10.1016/0032-0633(77)90122-2.

Chapman, S., and V. C. A. Ferraro (1929), The Electrical State of Solar Streams of Corpuscles, *Monthly Notices of the Royal Astronomical Society*, *89*(5), 470–479, doi:10.1093/mnras/89.5.470.

Chapman, S., and V. C. A. Ferraro (1931), A new theory of magnetic storms, *Journal of Geophysical Research*, *36*(2), 77, doi:10.1029/TE036i002p00077.

Chapman, S., and V. C. A. Ferraro (1940), The theory of the first phase of a geomagnetic storm, *Journal of Geophysical Research*, *45*(3), 245, doi:10.1029/TE045i003p00245.

Chen, J., and P. J. Palmadesso (1986), Chaos and Nonlinear Dynamics of Single-Particle Orbits in a Magnetotaillike Magnetic Field, *Journal of Geophysical Research*, *91*(1), 1499–1508, doi:10.1029/JA091iA02p01499.

Chen, Y., et al. (2017), Global Three-Dimensional Simulation of Earth's Dayside Reconnection Using a Two-Way Coupled Magnetohydrodynamics With Embedded Particle-in-Cell Model: Initial Results, *Journal of Geophysical Research: Space Physics*, *122*(10), 10,318–10,335, doi:10.1002/2017JA024186.

Chu, X., R. L. McPherron, T. S. Hsu, and V. Angelopoulos (2015), Solar cycle dependence of substorm occurrence and duration: Implications for onset, *Journal of Geophysical Research A: Space Physics*, *120*(4), 2808–2818, doi:10.1002/2015JA021104.

Clauer, C. R., and Y. Kamide (1985), DP 1 and DP 2 current systems for the March 22, 1979 substorms, *Journal of Geophysical Research*, *90*(A2), 1343, doi:10.1029/JA090iA02p01343.

Conover, W. J. (1999), *Practical nonparametric statistics*, 3rd ed., Wiley.

Cornwall, J. M. (1965), Cyclotron instabilities and electromagnetic emission in the ultra low frequency and very low frequency ranges, *Journal of Geophysical Research*, *70*(1), 61–69, doi:10.1029/JZ070i001p00061.

Coroniti, F. V. (1980), On the tearing mode in quasi-neutral sheets, *Journal of Geophysical Research*, *85*(A12), 6719, doi:10.1029/JA085iA12p06719.

Coroniti, F. V., and C. F. Kennel (1972), Changes in magnetospheric configuration during the substorm growth phase, *Journal of Geophysical Research*, *77*(19), 3361–3370, doi:10.1029/JA077i019p03361.

Cortie, A. L. (1912), Sun-spots and Terrestrial Magnetic Phenomena, 1898-1911: the Cause of the Annual Variation in Magnetic Disturbances, *Monthly Notices of the Royal Astronomical Society*, *73*(1), 52–60, doi:10.1093/mnras/73.1.52.

Cummings, W. D., and P. J. Coleman (1968), Simultaneous Magnetic Field Variations at the Earth's Surface and at Synchronous, Equatorial Distance. Part I. Bay-Associated Events, *Radio Science*, *3*(7), 758–761, doi:10.1002/rds196837758.

Daglis, I. A. (1997), The role of magnetosphere-ionosphere coupling in magnetic storm dynamics, in *Magnetic Storms*, pp. 107–116, American Geophysical Union (AGU), doi:10.1029/GM098p0107.

Daldorff, L. K. S., G. Tóth, T. I. Gombosi, G. Lapenta, J. Amaya, S. Markidis, and J. U. Brackbill (2014), Two-way coupling of a global Hall magnetohydrodynamics model with a local implicit particle-in-cell model, *Journal of Computational Physics*, *268*(0), 236–254, doi:http://dx.doi.org/10.1016/j.jcp.2014.03.009.

Daly, P. (2002), Users guide to the Cluster science data system, *Tech. rep.*, European Space Agency.

Davis, T. N., and M. Sugiura (1966), Auroral electrojet activity index AE and its universal time variations, *Journal of Geophysical Research*, *71*(3), 785–801, doi:10.1029/JZ071i003p00785.

De Zeeuw, D., T. Gombosi, C. Groth, K. Powell, and Q. Stout (2000), An adaptive MHD method for global space weather simulations, *IEEE Transactions on Plasma Science*, *28*(6), 1956–1965, doi:10.1109/27.902224.

De Zeeuw, D. L., S. Sazykin, R. A. Wolf, T. I. Gombosi, A. J. Ridley, and G. Tóth (2004), Coupling of a global MHD code and an inner magnetospheric model: Initial results, *Journal of Geophysical Research*, *109*(A12), A12,219, doi:10.1029/2003JA010366.

DeForest, S. E. (1972), Spacecraft charging at synchronous orbit, *Journal of Geophysical Research*, *77*(4), 651–659, doi:10.1029/JA077i004p00651.

DeForest, S. E., and C. E. McIlwain (1971), Plasma clouds in the magnetosphere, *Journal of Geophysical Research*, *76*(16), 3587–3611, doi:10.1029/JA076i016p03587.

Delcourt, D. C., J.-A. Sauvaud, R. F. Martin, and T. E. Moore (1996), On the nonadiabatic precipitation of ions from the near-Earth plasma sheet, *Journal of Geophysical Research: Space Physics*, *101*(A8), 17,409–17,418, doi:10.1029/96JA01006.

Delcourt, D. C., T. E. Moore, B. L. Giles, and M.-C. Fok (2000), Quantitative modeling of modulated ion injections observed by Polar-Thermal Ion Dynamics Experiment in the cusp region, *Journal of Geophysical Research: Space Physics*, *105*(A11), 25,191–25,203, doi:10.1029/2000JA000034.

Delcourt, D. C., H. V. Malova, and L. M. Zelenyi (2006), Quasi-adiabaticity in bifurcated current sheets, *Geophysical Research Letters*, *33*(6), L06,106, doi:10.1029/2005GL025463.

Dessler, A. J., W. E. Francis, and E. N. Parker (1960), Geomagnetic storm sudden-commencement rise times, *Journal of Geophysical Research*, *65*(9), 2715–2719, doi:10.1029/JZ065i009p02715.

Dickinson, R. E., E. C. Ridley, and R. G. Roble (1981), A three-dimensional general circulation model of the thermosphere, *Journal of Geophysical Research*, *86*(A3), 1499, doi:10.1029/JA086iA03p01499.

Dubyagin, S., N. Ganushkina, S. Apatenkov, M. Kubyshkina, H. Singer, and M. Liemohn (2013), Geometry of duskside equatorial current during magnetic storm main phase as deduced from magnetospheric and low-altitude observations, *Annales Geophysicae*, *31*(3), 395–408, doi:10.5194/angeo-31-395-2013.

Dubyagin, S., N. Ganushkina, M. Kubyshkina, and M. Liemohn (2014), Contribution from different current systems to SYM and ASY midlatitude indices, *Journal of Geophysical Research: Space Physics*, *119*(9), 7243–7263, doi:10.1002/2014JA020122.

Dubyagin, S., N. Y. Ganushkina, and V. Sergeev (2018), Formation of 30 KeV Proton Isotropic Boundaries During Geomagnetic Storms, *Journal of Geophysical Research: Space Physics*, doi:10.1002/2017JA024587.

Dungey, J. W. (1961), Interplanetary Magnetic Field and the Auroral Zones, *Physical Review Letters*, *6*(2), 47–48, doi:10.1103/PhysRevLett.6.47.

Eastwood, J. P., et al. (2005), Observations of multiple X-line structure in the Earth's magnetotail current sheet: A Cluster case study, *Geophysical Research Letters*, *32*(11), L11,105, doi:10.1029/2005GL022509.

El-Alaoui, M., M. Ashour-Abdalla, R. J. Walker, V. Peroomian, R. L. Richard, V. Angelopoulos, and A. Runov (2009), Substorm evolution as revealed by THEMIS satellites and a global MHD simulation, *Journal of Geophysical Research*, *114*(A8), A08,221, doi:10.1029/2009JA014133.

Evans, D. S., and M. S. Greer (2000), Polar Orbiting Environmental Satellite Space Environment Monitor -2 Instrument Descriptions and Archive Data Documentation, *Tech. rep.*, National Oceanic and Atmospheric Administration, Boulder, Colorado.

Facskó, G., I. Honkonen, T. Živković, L. Palin, E. Kallio, K. Ågren, H. Opgenoorth, E. I. Tanskanen, and S. Milan (2016), One year in the Earth's magnetosphere: A global MHD simulation and spacecraft measurements, *Space Weather*, *14*(5), 351–367, doi:10.1002/2015SW001355.

Fairfield, D. H., and L. J. Cahill (1966), Transition region magnetic field and polar magnetic disturbances, *Journal of Geophysical Research*, *71*(1), 155–169, doi:10.1029/JZ071i001p00155.

Fairfield, D. H., A. Otto, T. Mukai, S. Kokubun, R. P. Lepping, J. T. Steinberg, A. J. Lazarus, and T. Yamamoto (2000), Geotail observations of the Kelvin-Helmholtz instability at the equatorial magnetotail boundary for parallel northward fields, *Journal of Geophysical Research: Space Physics*, *105*(A9), 21,159–21,173, doi:10.1029/1999JA000316.

Fedorenko, R. (1962), A relaxation method for solving elliptic difference equations, *USSR Computational Mathematics and Mathematical Physics*, *1*(4), 1092–1096, doi:10.1016/0041-5553(62)90031-9.

Ferraro, V. C. A. (1952), On the theory of the first phase of a geomagnetic storm: A new illustrative calculation based on an idealised (plane not cylindrical) model field distribution, *Journal of Geophysical Research*, *57*(1), 15–49, doi:10.1029/JZ057i001p00015.

Fok, M.-C., R. a. Wolf, R. W. Spiro, and T. E. Moore (2001), Comprehensive computational model of Earth's ring current, *Journal of Geophysical Research: Space Physics*, *106*(A5), 8417–8424, doi:10.1029/2000JA000235.

Forsyth, C., I. J. Rae, J. C. Coxon, M. P. Freeman, C. M. Jackman, J. Gjerloev, and A. N. Fazakerley (2015), A new technique for determining Substorm Onsets and Phases from Indices of the Electrojet (SOPHIE), *Journal of Geophysical Research: Space Physics*, *120*(12), 10,592–10,606, doi:10.1002/2015JA021343.

Forsyth, C., et al. (2014), In situ spatiotemporal measurements of the detailed azimuthal substructure of the substorm current wedge, *Journal of Geophysical Research: Space Physics*, *119*(2), 927–946, doi:10.1002/2013JA019302.

Foster, J. C. (1983), An empirical electric field model derived from Chatanika radar data, *Journal of Geophysical Research*, *88*(A2), 981, doi:10.1029/JA088iA02p00981.

Freeman, M. P., and S. K. Morley (2004), A minimal substorm model that explains the observed statistical distribution of times between substorms, *Geophysical Research Letters*, *31*(12), doi:10.1029/2004GL019989.

Freeman, M. P., and S. K. Morley (2009), No evidence for externally triggered substorms based on superposed epoch analysis of IMF B z, *Geophysical Research Letters*, *36*(21), L21,101, doi:10.1029/2009GL040621.

Frey, H. U., S. B. Mende, V. Angelopoulos, and E. F. Donovan (2004), Substorm onset observations by IMAGE-FUV, *Journal of Geophysical Research*, *109*(A10), A10,304, doi:10.1029/2004JA010607.

Friis-Christensen, E., Y. Kamide, A. D. Richmond, and S. Matsushita (1985), Interplanetary magnetic field control of high-latitude electric fields and currents determined from Greenland Magnetometer Data, *Journal of Geophysical Research*, *90*(A2), 1325, doi:10.1029/JA090iA02p01325.

Frühauff, D., and K.-H. Glassmeier (2017), The Plasma Sheet as Natural Symmetry Plane for Dipolarization Fronts in the Earth's Magnetotail, *Journal of Geophysical Research: Space Physics*, *122*(11), 11,373–11,388, doi:10.1002/2017JA024682.

Fu, H. S., Y. V. Khotyaintsev, A. Vaivads, M. André, and S. Y. Huang (2012), Occurrence rate of earthward-propagating dipolarization fronts, *Geophysical Research Letters*, *39*(10), doi:10.1029/2012GL051784.

Fuselier, S. A. (2004), Generation of transient dayside subauroral proton precipitation, *Journal of Geophysical Research*, *109*(A12), A12,227, doi:10.1029/2004JA010393.

Gannon, J., and J. Love (2011), USGS 1-min Dst index, *Journal of Atmospheric and Solar-Terrestrial Physics*, *73*(2-3), 323–334, doi:10.1016/j.jastp.2010.02.013.

Ganushkina, N. Y., T. I. Pulkkinen, M. V. Kubyshkina, H. J. Singer, and C. T. Russell (2002), Modeling the ring current magnetic field during storms, *Journal of Geophysical Research*, *107*(A7), 1092, doi:10.1029/2001JA900101.

Ganushkina, N. Y., T. I. Pulkkinen, M. V. Kubyshkina, H. J. Singer, and C. T. Russell (2004), Long-term evolution of magnetospheric current systems during storms, *Annales Geophysicae European Geosciences Union*, *22*(4), 1317–1334.

Ganushkina, N. Y., M. W. Liemohn, M. V. Kubyshkina, R. Ilie, and H. J. Singer (2010), Distortions of the magnetic field by storm-time current systems in Earth's magnetosphere, *Annales Geophysicae*, *28*(1), 123–140, doi:10.5194/angeo-28-123-2010.

Ganushkina, N. Y., O. A. Amariutei, D. Welling, and D. Heynderickx (2015), Nowcast model for low-energy electrons in the inner magnetosphere, *Space Weather*, *13*(1), 16–34, doi:10.1002/2014SW001098.

Ganushkina, N. Y., et al. (2005), Proton isotropy boundaries as measured on mid- and low-altitude satellites, *Annales Geophysicae*, *23*(5), 1839–1847, doi:10.5194/angeo-23-1839-2005.

Gilson, M. L., J. Raeder, E. Donovan, Y. S. Ge, and L. Kepko (2012), Global simulation of proton precipitation due to field line curvature during substorms, *Journal of Geophysical Research: Space Physics*, *117*(A5), A05,216, doi:10.1029/2012JA017562.

Gjerloev, J. W. (2009), A Global Ground-Based Magnetometer Initiative, *Eos, Transactions American Geophysical Union*, *90*(27), 230, doi:10.1029/2009EO270002.

Gjerloev, J. W. (2012), The SuperMAG data processing technique, *Journal of Geophysical Research: Space Physics*, *117*(A9), doi:10.1029/2012JA017683, a09213.

Glocer, A., T. I. Gombosi, G. Tóth, K. C. Hansen, A. J. Ridley, and A. Nagy (2007), Polar wind outflow model: Saturn results, *J. Geophys. Res.*, *112*, doi:10.1029/2006JA011755.

Glocer, A., G. Tóth, M. Fok, and T. Gombosi (2009a), Integration of the radiation belt environment model into the space weather modeling framework, *J. Atmos. Solar-Terr. Phys.*, *71*, 1653–1663, doi:10.1016/j.jastp.2009.01.003.

Glocer, A., G. Tóth, T. Gombosi, and D. Welling (2009b), Modeling ionospheric outflows and their impact on the magnetosphere, initial results, *Journal of Geophysical Research: Space Physics*, *114*(A5), A05,216, doi:10.1029/2009JA014053.

Glocer, A., G. Tóth, Y. Ma, T. Gombosi, J.-C. Zhang, and L. M. Kistler (2009c), Multifluid Block-Adaptive-Tree Solar wind Roe-type Upwind Scheme: Magnetospheric composition and dynamics during geomagnetic storms-Initial results, *Journal of Geophysical Research: Space Physics*, *114*(A12), doi:10.1029/2009JA014418.

Glocer, A., et al. (2016), Community-wide validation of geospace model local K-index predictions to support model transition to operations, *Space Weather*, *14*(7), 469–480, doi:10.1002/2016SW001387.

Godinez, H. C., Y. Yu, E. Lawrence, M. G. Henderson, B. Larsen, and V. K. Jordanova (2016), Ring current pressure estimation with RAM-SCB using data assimilation and Van Allen Probe flux data, *Geophysical Research Letters*, *43*(23), 11,948–11,956, doi:10.1002/2016GL071646.

Gombosi, T. (1998), *Physics of the Space Environment*, Cambridge University Press.

Gonzalez, W. D., B. T. Tsurutani, and A. L. Clúa de Gonzalez (1999), Interplanetary origin of geomagnetic storms, *Space Science Reviews*, *88*(3/4), 529–562, doi:10.1023/A:1005160129098.

Gosling, J. T., D. J. McComas, J. L. Phillips, and S. J. Bame (1991), Geomagnetic activity associated with earth passage of interplanetary shock disturbances and coronal mass ejections, *Journal of Geophysical Research*, *96*(A5), 7831, doi:10.1029/91JA00316.

Groth, C. P. T., D. L. De Zeeuw, T. I. Gombosi, and K. G. Powell (2000), Global three-dimensional MHD simulation of a space weather event: CME formation, interplanetary propagation, and interaction with the magnetosphere, *Journal of Geophysical Research: Space Physics*, *105*(A11), 25,053–25,078, doi:10.1029/2000JA900093.

Guild, T. B., H. E. Spence, E. L. Kepko, V. Merkin, J. G. Lyon, M. Wiltberger, and C. C. Goodrich (2008), Geotail and LFM comparisons of plasma sheet climatology: 1. Average values, *Journal of Geophysical Research: Space Physics*, *113*(A4), doi:10.1029/2007JA012611.

Gvozdevsky, B. B., V. A. Sergeev, and K. Mursula (1997), Long lasting energetic proton precipitation in the inner magnetosphere after substorms, *Journal of Geophysical Research: Space Physics*, *102*(A11), 24,333–24,338, doi:10.1029/97JA02062.

Haiducek, J. D., D. T. Welling, N. Y. Ganushkina, S. K. Morley, and D. S. Ozturk (2017), SWMF Global Magnetosphere Simulations of January 2005: Geomagnetic Indices and Cross-Polar Cap Potential, *Space Weather*, *15*(12), 1567–1587, doi:10.1002/2017SW001695.

Hajj, G. A., B. D. Wilson, C. Wang, X. Pi, and I. G. Rosen (2004), Data assimilation of ground GPS total electron content into a physics-based ionospheric model by use of the Kalman filter, *Radio Science*, *39*(1), doi:10.1029/2002RS002859.

Halford, A. J., B. J. Fraser, and S. K. Morley (2010), EMIC wave activity during geomagnetic storm and nonstorm periods: CRRES results, *Journal of Geophysical Research: Space Physics*, *115*(A12), A12,248, doi:10.1029/2010JA015716.

Hauge, R., and F. Söraas (1975), Precipitation of $>$ 115 kev protons in the evening and forenoon sectors in relation to the magnetic activity, *Planetary and Space Science*, *23*(8), 1141–1154, doi:10.1016/0032-0633(75)90164-6.

Heinemann, M., and R. A. Wolf (2001), Relationships of models of the inner magnetosphere to the rice convection model, *J. Geophys. Res.*, *106*(A8), 15,545 – 15,554.

Henderson, M. G. (2009), Observational evidence for an inside-out substorm onset scenario, *Annales Geophysicae*, *27*(5), 2129–2140, doi:10.5194/angeo-27-2129-2009.

Hendricks, S., and M. Sugiura (1967), Provisional hourly values of equatorial Dst for 1961, 1962, and 1963.

Heppner, J. P. (1955), Note on the occurrence of world-wide S.S.C.'s during the onset of negative bays at College, Alaska, *Journal of Geophysical Research*, *60*(1), 29–32, doi:10.1029/JZ060i001p00029.

Hirsch, C. (2007), *Numerical Computation of Internal and External Flows: The Fundamentals of Computational Fluid Dynamics*, Elsevier Science.

Honkonen, I., M. Palmroth, T. I. Pulkkinen, P. Janhunen, and A. Aikio (2011), On large plasmoid formation in a global magnetohydrodynamic simulation, *Annales Geophysicae*, *29*(1), 167–179, doi:10.5194/angeo-29-167-2011.

Hsu, T.-S., and R. L. McPherron (2003), Occurrence frequencies of IMF triggered and nontriggered substorms, *Journal of Geophysical Research*, *108*(A7), 1307, doi: 10.1029/2002JA009442.

Hsu, T.-S., and R. L. McPherron (2004), Average characteristics of triggered and nontriggered substorms, *Journal of Geophysical Research*, *109*(A7), A07,208, doi: 10.1029/2003JA009933.

Hsu, T.-S., and R. L. McPherron (2012), A statistical analysis of substorm associated tail activity, *Advances in Space Research*, *50*(10), 1317–1343, doi:10.1016/J.ASR. 2012.06.034.

Huang, C.-L., H. E. Spence, H. J. Singer, and N. A. Tsyganenko (2008), A quantitative assessment of empirical magnetic field models at geosynchronous orbit during magnetic storms, *Journal of Geophysical Research: Space Physics*, *113*(A4), doi: 10.1029/2007JA012623.

Huang, C.-L., H. E. Spence, H. J. Singer, and W. J. Hughes (2010), Modeling radiation belt radial diffusion in ULF wave fields: 1. Quantifying ULF wave power at geosynchronous orbit in observations and in global MHD model, *Journal of Geophysical Research: Space Physics*, *115*(A6), doi:10.1029/2009JA014917.

Huba, J. D., G. Joyce, and J. A. Fedder (2000), Sami2 is Another Model of the Ionosphere (SAMI2): A new low-latitude ionosphere model, *Journal of Geophysical Research: Space Physics*, *105*(A10), 23,035–23,053, doi:10.1029/2000JA000035.

Hultqvist, B. (1979), The hot ion component of the magnetospheric plasma and some relations to the electron component-observations and physical implications, *Space Science Reviews*, *23*(4), 581–675, doi:10.1007/BF00212357.

Ieda, A., D. H. Fairfield, T. Mukai, Y. Saito, S. Kokubun, K. Liou, C. I. Meng, G. K. Parks, and M. J. Brittnacher (2001), Plasmoid ejection and auroral brightenings, *Journal of Geophysical Research: Space Physics*, *106*(A3), 3845–3857, doi:10.1029/1999JA000451.

Ilie, R., M. W. Liemohn, G. Toth, and R. M. Skoug (2012), Kinetic model of the inner magnetosphere with arbitrary magnetic field, *Journal of Geophysical Research: Space Physics*, *117*(A4), doi:10.1029/2011JA017189.

Ilie, R., N. Ganushkina, G. Toth, S. Dubyagin, and M. W. Liemohn (2015), Testing the magnetotail configuration based on observations of low-altitude isotropic boundaries during quiet times, *Journal of Geophysical Research: Space Physics*, *120*(12), 10,557–10,573, doi:10.1002/2015JA021858.

Imhof, W. L., J. B. Reagan, and E. E. Gaines (1977), Fine-scale spatial structure in the pitch angle distributions of energetic particles near the midnight trapping boundary, *Journal of Geophysical Research*, *82*(32), 5215–5221, doi:10.1029/JA082i032p05215.

Iyemori, T. (1990), Storm-time magnetospheric currents inferred from mid-latitude geomagnetic field variations., *Journal of geomagnetism and geoelectricity*, *42*(11), 1249–1265, doi:10.5636/jgg.42.1249.

Iyemori, T., and D. R. K. Rao (1996), Decay of the Dst field of geomagnetic disturbance after substorm onset and its implication to storm-substorm relation, *Annales Geophysicae*, *14*(6), 608–618, doi:10.1007/s00585-996-0608-3.

Jaggi, R. K., and R. A. Wolf (1973), Self-consistent calculation of the motion of a sheet of ions in the magnetosphere, *Journal of Geophysical Research*, *78*(16), 2852–2866, doi:10.1029/JA078i016p02852.

Janhunen, P. (1996), GUMICS-3 A Global Ionosphere-Magnetosphere Coupling Simulation with High Ionospheric Resolution, in *Environment Modeling for Space-Based Applications*, *ESA Special Publication*, vol. 392, edited by T.-D. Guyenne and A. Hilgers, p. 233.

Janhunen, P., M. Palmroth, T. Laitinen, I. Honkonen, L. Juusola, G. Facskó, and T. I. Pulkkinen (2012), The GUMICS-4 global MHD magnetosphere-ionosphere coupling simulation, *Journal of Atmospheric and Solar-Terrestrial Physics*, *80*(0), 48–59, doi:http://dx.doi.org/10.1016/j.jastp.2012.03.006.

Johnson, J. R., and S. Wing (2014), External versus internal triggering of substorms: An information-theoretical approach, *Geophysical Research Letters*, doi:10.1002/2014GL060928.

Jones, E., T. Oliphant, P. Peterson, et al. (2001, updated frequently), SciPy: Open source scientific tools for Python, [Online; accessed 2017-03-06].

Jordanova, V., et al. (2017), Specification of the near-Earth space environment with SHIELDS, *Journal of Atmospheric and Solar-Terrestrial Physics*, doi:10.1016/j.jastp.2017.11.006.

Jordanova, V. K., L. M. Kistler, J. U. Kozyra, G. V. Khazanov, and A. F. Nagy (1996), Collisional losses of ring current ions, *Journal of Geophysical Research: Space Physics*, *101*(A1), 111, doi:10.1029/95JA02000.

Juusola, L., N. Østgaard, E. Tanskanen, N. Partamies, and K. Snekvik (2011), Earthward plasma sheet flows during substorm phases, *Journal of Geophysical Research: Space Physics*, *116*(A10), A10,228, doi:10.1029/2011JA016852.

Juusola, L., et al. (2014), Statistical comparison of seasonal variations in the GUMICS-4 global MHD model ionosphere and measurements, *Space Weather*, *12*(10), 582–600, doi:10.1002/2014SW001082.

Kalegaev, V. V., N. Y. Ganushkina, T. I. Pulkkinen, M. V. Kubyshkina, H. J. Singer, and C. T. Russell (2005), Relation between the ring current and the tail current during magnetic storms, *Annales Geophysicae*, *23*(2), 523–533.

Kamide, Y., and S. Matsushita (1979), Simulation studies of ionospheric electric fields and currents in relation to field-aligned currents 1. Quiet periods, *J. Geophys. Res.*, *84*, 4083, doi:10.1029/JA084iA08p04083.

Kamide, Y., and C. E. McIlwain (1974), The onset time of magnetospheric substorms determined from ground and synchronous satellite records, *Journal of Geophysical Research*, *79*(31), 4787–4790, doi:10.1029/JA079i031p04787.

Kamide, Y., F. Yasuhara, and S.-I. Akasofu (1974), On the cause of northward magnetic field along the negative X axis during magnetospheric substorms, *Planetary and Space Science*, *22*(8), 1219–1229, doi:10.1016/0032-0633(74)90006-3.

Katus, R. M., and M. W. Liemohn (2013), Similarities and differences in low- to middle-latitude geomagnetic indices, *Journal of Geophysical Research: Space Physics*, *118*(8), 5149–5156, doi:10.1002/jgra.50501.

Kaufmann, R. L. (1987), Substorm currents: Growth phase and onset, *Journal of Geophysical Research*, *92*(A7), 7471, doi:10.1029/JA092iA07p07471.

Kauristie, K., A. Morschhauser, N. Olsen, C. C. Finlay, R. L. McPherron, J. W. Gjerloev, and H. J. Opgenoorth (2017), On the Usage of Geomagnetic Indices for Data Selection in Internal Field Modelling, *Space Science Reviews*, *206*(1-4), 61–90, doi:10.1007/s11214-016-0301-0.

Kennel, C. F., and H. E. Petschek (1966), Limit on stably trapped particle fluxes, *Journal of Geophysical Research*, *71*(1), 1–28, doi:10.1029/JZ071i001p00001.

Kepko, L., et al. (2015), Substorm Current Wedge Revisited, *Space Science Reviews*, *190*(1-4), 1–46, doi:10.1007/s11214-014-0124-9.

Kertz, W. (1958), *Ein neues Mass für die Feldstärke des erdmagnetischen äquatorialen Ringstroms: von Walter Kertz*, Vandenhoeck und Ruprecht.

Kim, K.-H., K. Takahashi, D. Lee, P. R. Sutcliffe, and K. Yumoto (2005), Pi2 pulsations associated with poleward boundary intensifications during the absence of substorms, *Journal of Geophysical Research*, *110*(A1), A01,217, doi: 10.1029/2004JA010780.

Koons, J. F., and H. C. Fennell (2006), Space weather effects on communications satellites, *The Radio Science Bulletin*, *2006*(316), 27–41, doi:10.1007/978-3-540-34578-7_9.

Koren, B. (1993), A robust upwind discretisation method for advection, diffusion and source terms, in *Numerical Methods for Advection-Diffusion Problems*, edited by C. Vreugdenhil and B.Koren, p. 117, Vieweg, Braunschweig.

Korth, A., Z. Y. Pu, G. Kremser, and A. Roux (1991), A Statistical Study of Substorm Onset Conditions at Geostationary Orbit, in *Magnetospheric Substorms, Volume 64*, edited by J. R. Kan, T. A. Potemra, S. Kokubun, and T. Iijima, pp. 343–351, American Geophysical Union (AGU), Washington, D. C., doi: 10.1029/GM064p0343.

Koskinen, H. E. J., R. E. Lopez, R. J. Pellinen, T. I. Pulkkinen, D. N. Baker, and T. Bösinger (1993), Pseudobreakup and substorm growth phase in the ionosphere and magnetosphere, *Journal of Geophysical Research: Space Physics*, *98*(A4), 5801–5813, doi:10.1029/92JA02482.

Kress, B. T., M. K. Hudson, M. D. Looper, J. Albert, J. G. Lyon, and C. C. Goodrich (2007), Global mhd test particle simulations of ¿10 mev radiation belt electrons during storm sudden commencement, *Journal of Geophysical Research: Space Physics*, *112*(A9), doi:10.1029/2006JA012218, a09215.

Kronberg, E. A., et al. (2014), Circulation of Heavy Ions and Their Dynamical Effects in the Magnetosphere : Recent Observations and Models Charge Energy Mass experiment Extreme Ultraviolet radiation, *Space Science Reviews*, *184*, 173–235, doi:10.1007/s11214-014-0104-0.

Leach, R., and M. Alexander (1995), Failures and Anomalies Attributed to Spacecraft Charging, *Tech. rep.*, NASA, Huntsville, AL.

Ledvina, B. M., J. J. Makela, and P. M. Kintner (2002), First observations of intense GPS L1 amplitude scintillations at midlatitude, *Geophysical Research Letters*, *29*(14), 4–1–4–4, doi:10.1029/2002GL014770.

Lee, D.-Y., and L. R. Lyons (2004), Geosynchronous magnetic field response to solar wind dynamic pressure pulse, *Journal of Geophysical Research*, *109*(A4), A04,201, doi:10.1029/2003JA010076.

Lezniak, T. W., R. L. Arnoldy, G. K. Parks, and J. R. Winckler (1968), Measurement and Intensity of Energetic Electrons at the Equator at 6.6 Re, *Radio Science*, *3*(7), 710–714, doi:10.1002/rds196837710.

Liang, J., E. Donovan, B. Ni, C. Yue, F. Jiang, and V. Angelopoulos (2014), On an energy-latitude dispersion pattern of ion precipitation potentially associated with magnetospheric EMIC waves, *Journal of Geophysical Research: Space Physics*, *119*(10), 8137–8160, doi:10.1002/2014JA020226.

Liemohn, M. W., J. U. Kozyra, V. K. Jordanova, G. V. Khazanov, M. F. Thomsen, and T. E. Cayton (1999), Analysis of early phase ring current recovery mechanisms during geomagnetic storms, *Geophysical Research Letters*, *26*(18), 2845–2848, doi:10.1029/1999GL900611.

Liemohn, M. W., J. U. Kozyra, M. F. Thomsen, J. L. Roeder, G. Lu, J. E. Borovsky, and T. E. Cayton (2001), Dominant role of the asymmetric ring current in producing the stormtime Dst*, *Journal of Geophysical Research: Space Physics*, *106*(A6), 10,883–10,904, doi:10.1029/2000JA000326.

Liemohn, M. W., A. J. Ridley, D. L. Gallagher, D. M. Ober, and J. U. Kozyra (2004), Dependence of plasmaspheric morphology on the electric field description during the recovery phase of the 17 April 2002 magnetic storm, *Journal of Geophysical Research*, *109*(A3), A03,209, doi:10.1029/2003JA010304.

Liemohn, M. W., D. L. De Zeeuw, N. Y. Ganushkina, J. U. Kozyra, and D. T. Welling (2013), Magnetospheric cross-field currents during the January 6-7, 2011 high-speed stream-driven interval, *Journal of Atmospheric and Solar-Terrestrial Physics*, *99*, 78–84, doi:10.1016/j.jastp.2012.09.007.

Lincoln, J. V. (1967), I-3 - geomagnetic indices, in *Physics of Geomagnetic Phenomena*, *International Geophysics*, vol. 11, Part 1, edited by S. MATSUSHITA and W. H. CAMPBELL, pp. 67 – 100, Academic Press, doi:http://dx.doi.org/10.1016/B978-0-12-480301-5.50009-4.

Liou, K. (2010), Polar Ultraviolet Imager observation of auroral breakup, *Journal of Geophysical Research: Space Physics*, *115*(A12), doi:10.1029/2010JA015578.

Liou, K., P. T. Newell, C.-I. Meng, A. T. Y. Lui, M. Brittnacher, and G. Parks (1997), Dayside auroral activity as a possible precursor of substorm onsets: A survey using Polar ultraviolet imagery, *Journal of Geophysical Research: Space Physics*, *102*(A9), 19,835–19,843, doi:10.1029/97JA01741.

Liou, K., C.-I. Meng, A. T. Y. Lui, P. T. Newell, and S. Wing (2002), Magnetic dipolarization with substorm expansion onset, *Magnetospheric Physics: Magnetosphereinner*, doi:10.1029/2001JA000179.

Liu, J., V. Angelopoulos, A. Runov, and X.-Z. Zhou (2013), On the current sheets surrounding dipolarizing flux bundles in the magnetotail: The case for wedgelets,

Journal of Geophysical Research: Space Physics, *118*(5), 2000–2020, doi:10.1002/jgra.50092.

Lockwood, M., and S. K. Morley (2004), A numerical model of the ionospheric signatures of time-varying magneticreconnection: I. ionospheric convection, *Annales Geophysicae*, *22*(1), 73–91.

Lopez, R., J. Lyon, M. Wiltberger, and C. Goodrich (2001), Comparison of global mhd simulation results with actual storm and substorm events, *Advances in Space Research*, *28*(12), 1701 – 1706, doi:http://dx.doi.org/10.1016/S0273-1177(01)00535-X.

Lopez, R. E., S. Hernandez, M. Wiltberger, C. L. Huang, E. L. Kepko, H. Spence, C. C. Goodrich, and J. G. Lyon (2007), Predicting magnetopause crossings at geosynchronous orbit during the Halloween storms, *Sp. Weather*, *5*(1), doi:10.1029/2006SW000222.

Lui, A. T. Y. (1978), Estimates of current changes in the geomagnetotail associated with a substorm, *Geophysical Research Letters*, *5*(10), 853–856, doi:10.1029/GL005i010p00853.

Lvova, E. A., V. A. Sergeev, and G. R. Bagautdinova (2005), Statistical study of the proton isotropy boundary, *Annales Geophysicae*, *23*, 1311–1316.

Lyon, J. G., S. H. Brecht, J. D. Huba, J. A. Fedder, and P. J. Palmadesso (1981), Computer Simulation of a Geomagnetic Substorm, *Physical Review Letters*, *46*(15), 1038–1041, doi:10.1103/PhysRevLett.46.1038.

Lyons, L. R., G. T. Blanchard, J. C. Samson, R. P. Lepping, T. Yamamoto, and T. Moretto (1997), Coordinated observations demonstrating external substorm triggering, *Journal of Geophysical Research: Space Physics*, *102*(A12), 27,039–27,051, doi:10.1029/97JA02639.

Maltsev, Y. (2004), Points of controversy in the study of magnetic storms, *Space Science Reviews*, *110*(3/4), 227–277, doi:10.1023/B:SPAC.0000023410.77752.30.

Mann, I. R., et al. (2008), The Upgraded CARISMA Magnetometer Array intheTHEMIS Era, *Space Science Reviews*, *141*(1-4), 413–451, doi:10.1007/s11214-008-9457-6.

Mayaud, P. N. (1980), *Derivation, Meaning, and Use of Geomagnetic Indices*, American Geophysical Union, Washington, DC, doi:10.1002/9781118663837.

McComas, D. J., S. J. Bame, P. Barker, W. C. Feldman, J. L. Phillips, P. Riley, and J. W. Griffee (1998), Solar wind electron proton alpha monitor (swepam) for the advanced composition explorer, in *The Advanced Composition Explorer Mission*, edited by C. T. Russell, R. A. Mewaldt, and T. T. Von Rosenvinge, pp. 563–612, Springer Netherlands, Dordrecht, doi:10.1007/978-94-011-4762-0_20.

McFadden, J. P., C. W. Carlson, D. Larson, J. Bonnell, F. Mozer, V. Angelopoulos, K.-H. Glassmeier, and U. Auster (2008a), THEMIS ESA First Science Results and Performance Issues, *Space Science Reviews*, *141*(1-4), 477–508, doi:10.1007/s11214-008-9433-1.

McFadden, J. P., C. W. Carlson, D. Larson, M. Ludlam, R. Abiad, B. Elliott, P. Turin, M. Marckwordt, and V. Angelopoulos (2008b), The THEMIS ESA Plasma Instrument and In-flight Calibration, *Space Science Reviews*, *141*(1-4), 277–302, doi:10.1007/s11214-008-9440-2.

McPherron, R. (1972), Substorm related changes in the geomagnetic tail: the growth phase, *Planetary and Space Science*, *20*(9), 1521–1539, doi:10.1016/0032-0633(72)90054-2.

McPherron, R. L. (1970), Growth phase of magnetospheric substorms, *Journal of Geophysical Research*, *75*(28), 5592–5599, doi:10.1029/JA075i028p05592.

McPherron, R. L. (2015), Earth's Magnetotail, in *Magnetotails in the Solar System*, edited by A. Keiling, C. M. Jackman, and P. A. Delamere, pp. 61–84, American Geophysical Union (AGU), Hoboken, NJ, doi:10.1002/9781118842324.ch4.

McPherron, R. L., and X. Chu (2017), The Mid-Latitude Positive Bay and the MPB Index of Substorm Activity, *Space Science Reviews*, *206*(1-4), 91–122, doi:10.1007/s11214-016-0316-6.

McPherron, R. L., and X. Chu (2018), The Midlatitude Positive Bay Index and the Statistics of Substorm Occurrence, *Journal of Geophysical Research: Space Physics*, doi:10.1002/2017JA024766.

McPherron, R. L., C. T. Russell, and M. P. Aubry (1973), Satellite studies of magnetospheric substorms on August 15, 1968: 9. Phenomenological model for substorms, *Journal of Geophysical Research*, *78*(16), 3131–3149, doi:10.1029/JA078i016p03131.

Meng, C. I., and S. I. Akasofu (1969), A study of polar magnetic substorms: 2. Three-dimensional current system, *Journal of Geophysical Research*, *74*(16), 4035–4053, doi:10.1029/JA074i016p04035.

Meng, X., G. Tóth, M. W. Liemohn, T. I. Gombosi, and A. Runov (2012a), Pressure anisotropy in global magnetospheric simulations: A magnetohydrodynamics model, *Journal of Geophysical Research: Space Physics*, *117*(A8), doi:10.1029/2012JA017791.

Meng, X., G. Tóth, I. V. Sokolov, and T. I. Gombosi (2012b), Classical and semirelativistic magnetohydrodynamics with anisotropic ion pressure, *J. Comput. Phys.*, *231*, 3610–3622, doi:10.1016/j.jcp.2011.12.042.

Meng, X., G. Tóth, A. Glocer, M.-C. Fok, and T. I. Gombosi (2013), Pressure anisotropy in global magnetospheric simulations: Coupling with ring current models, *Journal of Geophysical Research: Space Physics*, *118*(9), 5639–5658, doi: 10.1002/jgra.50539.

Mertens, C. J., B. T. Kress, M. Wiltberger, S. R. Blattnig, T. S. Slaba, S. C. Solomon, and M. Engel (2010), Geomagnetic influence on aircraft radiation exposure during a solar energetic particle event in October 2003, *Space Weather*, *8*(3), S03,006, doi:10.1029/2009SW000487.

Meurant, M., J.-C. Gérard, C. Blockx, E. Spanswick, E. F. Donovan, B. Hubert, V. Coumans, and M. Connors (2007), EL - a possible indicator to monitor the magnetic field stretching at global scale during substorm expansive phase: Statistical study, *Journal of Geophysical Research: Space Physics*, *112*(A5), A05,222, doi:10.1029/2006JA012126.

Milan, S. E. (2004), Dayside and nightside contributions to the cross polar cap potential: placing an upper limit on a viscous-like interaction, *Annales Geophysicae*, *22*(10), 3771–3777, doi:10.5194/angeo-22-3771-2004.

Miura, A., and P. L. Pritchett (1982), Nonlocal stability analysis of the MHD Kelvin-Helmholtz instability in a compressible plasma, *Journal of Geophysical Research*, *87*(A9), 7431, doi:10.1029/JA087iA09p07431.

Moen, J., and A. Brekke (1993), The solar flux influence of quiet-time conductances in the auroral ionosphere, *Geophys. Res. Lett.*, *20*, 971.

Moldwin, M. B., and W. J. Hughes (1993), Geomagnetic substorm association of plasmoids, *Journal of Geophysical Research: Space Physics*, *98*(A1), 81–88, doi: 10.1029/92JA02153.

Montgomery, D. C., E. A. Peck, and G. G. Vining (2012), *Introduction to linear regression analysis*, 645 pp., Wiley.

Morley, S. (2007), 7th Australian Space Science Conference Proceedings.

Morley, S., A. Rouillard, and M. Freeman (2009), Recurrent substorm activity during the passage of a corotating interaction region, *Journal of Atmospheric and Solar-Terrestrial Physics*, *71*(10), 1073–1081, doi:10.1016/j.jastp.2008.11.009.

Morley, S., J. Koller, D. Welling, B. Larsen, and J. Niehof (2014), SpacePy: Python-Based Tools for the Space Science Community, Astrophysics Source Code Library.

Morley, S. K., D. T. Welling, J. Koller, B. A. Larsen, M. G. Henderson, and J. Niehof (2011), SpacePy - A Python-based Library of Tools for the Space Sciences, *Proceedings of the 9th Python in Science Conference*, pp. 39–45.

Morley, S. K., D. T. Welling, and J. R. Woodroffe (2018), Perturbed Input Ensemble Modeling with the Space Weather Modeling Framework, *Space Weather*, pp. 1–24, doi:10.1029/2018SW002000.

Mursula, K., and B. Zieger (1996), The 13.5-day periodicity in the Sun, solar wind, and geomagnetic activity: The last three solar cycles, *Journal of Geophysical Research: Space Physics*, *101*(A12), 27,077–27,090, doi:10.1029/96JA02470.

Nagai, T. (1987), Field-aligned currents associated with substorms in the vicinity of synchronous orbit: 2. GOES 2 and GOES 3 observations, *Journal of Geophysical Research*, *92*(A3), 2432, doi:10.1029/JA092iA03p02432.

Nagai, T., et al. (1998), Structure and dynamics of magnetic reconnection for substorm onsets with Geotail observations, *Journal of Geophysical Research: Space Physics*, *103*(A3), 4419–4440, doi:10.1029/97JA02190.

Nakamura, R., D. N. Baker, T. Yamamoto, R. D. Belian, E. A. Bering, J. R. Benbrook, and J. R. Theall (1994), Particle and field signatures during pseudobreakup and major expansion onset, *Journal of Geophysical Research*, *99*(A1), 207, doi:10.1029/93JA02207.

Newell, P. T., and J. W. Gjerloev (2011a), Evaluation of SuperMAG auroral electrojet indices as indicators of substorms and auroral power, *Journal of Geophysical Research: Space Physics*, *116*(A12), A12,211, doi:10.1029/2011JA016779.

Newell, P. T., and J. W. Gjerloev (2011b), Substorm and magnetosphere characteristic scales inferred from the SuperMAG auroral electrojet indices, *Journal of Geophysical Research: Space Physics*, *116*(A12), A12,232, doi:10.1029/2011JA016936.

Newell, P. T., and K. Liou (2011), Solar wind driving and substorm triggering, *Journal of Geophysical Research: Space Physics*, *116*(A3), doi:10.1029/2010JA016139.

Newell, P. T., and C.-I. Meng (1992), Mapping the dayside ionosphere to the magnetosphere according to particle precipitation characteristics, *Geophysical Research Letters*, *19*(6), 609–612, doi:10.1029/92GL00404.

Newell, P. T., V. A. Sergeev, G. R. Bikkuzina, and S. Wing (1998), Characterizing the state of the magnetosphere: Testing the ion precipitation maxima latitude (b2i) and the ion isotropy boundary, *Journal of Geophysical Research: Space Physics*, *103*(A3), 4739–4745, doi:10.1029/97JA03622.

Newell, P. T., K. Liou, T. Sotirelis, and C.-I. Meng (2001), Auroral precipitation power during substorms: A Polar UV Imager-based superposed epoch analysis, *Journal of Geophysical Research: Space Physics*, *106*(A12), 28,885–28,896, doi:10.1029/2000JA000428.

Newell, P. T., T. Sotirelis, K. Liou, C.-I. Meng, and F. J. Rich (2007), A nearly universal solar wind-magnetosphere coupling function inferred from 10 magnetospheric state variables, *Journal of Geophysical Research: Space Physics*, *112*(A1), doi:10.1029/2006JA012015.

Ngwira, C. M., A. Pulkkinen, L.-A. McKinnell, and P. J. Cilliers (2008), Improved modeling of geomagnetically induced currents in the South African power network, *Space Weather*, *6*(11), doi:10.1029/2008SW000408.

Ngwira, C. M., A. Pulkkinen, M. M. Kuznetsova, and A. Glocer (2014), Modeling extreme "carrington-type" space weather events using three-dimensional global mhd simulations, *Journal of Geophysical Research: Space Physics*, *119*(6), 4456–4474, doi:10.1002/2013JA019661.

Ngwira, C. M., et al. (2013), Simulation of the 23 july 2012 extreme space weather event: What if this extremely rare cme was earth directed?, *Space Weather*, *11*(12), 671–679, doi:10.1002/2013SW000990.

Nishida, A., M. Scholer, T. Terasawa, S. J. Bame, G. Gloeckler, E. J. Smith, and R. D. Zwickl (1986), Quasi-stagnant plasmoid in the middle tail: A new preexpansion phase phenomenon, *Journal of Geophysical Research*, *91*(A4), 4245, doi:10.1029/JA091iA04p04245.

Noah, M. A., and W. J. Burke (2013), Sawtooth-substorm connections: A closer look, *Journal of Geophysical Research: Space Physics*, *118*(8), 5136–5148, doi:10.1002/jgra.50440.

Nosé, M., et al. (2009), New substorm index derived from high-resolution geomagnetic field data at low latitude and its comparison with AE and ASY indices, in *Proc. XIII IAGA Workshop*, edited by J. Love, pp. 202–207, Golden, CO.

O'Brien, T. P. (2009), SEAES-GEO: A spacecraft environmental anomalies expert system for geosynchronous orbit, *Space Weather*, *7*(9), doi:10.1029/2009SW000473.

Ogino, T., R. J. Walker, and M. Ashour-Abdalla (1992), A global magnetohydrodynamic simulation of the magnetosheath and magnetosphere when the interplanetary magnetic field is northward, *IEEE Transactions on Plasma Science*, *20*(6), 817–828, doi:10.1109/27.199534.

Ohtani, S., M. Nosé, G. Rostoker, H. Singer, and A. Lui (2001), Storm-substorm relationship: Contribution of the tail current, *J. Geophys.*

Ohtani, S., et al. (1993), A multisatellite study of a pseudo-substorm onset in the near-Earth magnetotail, *Journal of Geophysical Research: Space Physics*, *98*(A11), 19,355–19,367, doi:10.1029/93JA01421.

Ohtani, S.-i., and J. Raeder (2004), Tail current surge: New insights from a global MHD simulation and comparison with satellite observations, *Journal of Geophysical Research*, *109*(A1), A01,207, doi:10.1029/2002JA009750.

Øieroset, M., M. Yamauchi, L. Liszka, S. P. Christon, and B. Hultqvist (1999), A statistical study of ion beams and conics from the dayside ionosphere during different phases of a substorm, *Journal of Geophysical Research: Space Physics*, *104*(A4), 6987–6998, doi:10.1029/1998JA900177.

Øieroset, M., T. D. Phan, M. Fujimoto, R. P. Lin, and R. P. Lepping (2001), In situ detection of reconnection in the Earth's magnetotail, *Letters to Nature*, *412*(July), 414–416, doi:10.1038/35086520.

Palmroth, M., T. I. Pulkkinen, P. Janhunen, and C.-C. Wu (2003), Stormtime energy transfer in global mhd simulation, *Journal of Geophysical Research: Space Physics*, *108*(A1), doi:10.1029/2002JA009446, 1048.

Parker, E. N. (1957), Sweet's mechanism for merging magnetic fields in conducting fluids, *Journal of Geophysical Research*, *62*(4), 509–520, doi:10.1029/JZ062i004p00509.

Parker, E. N. (1958), Dynamics of the Interplanetary Gas and Magnetic Fields, *The Astrophysical Journal*, *128*(3), 664–676, doi:10.1086/146579.

Parzen, E. (1962), On Estimation of a Probability Density Function and Mode, *The Annals of Mathematical Statistics*, *33*(3), 1065–1076, doi:10.1214/aoms/1177704472.

Pembroke, A., F. Toffoletto, S. Sazykin, M. Wiltberger, J. Lyon, V. Merkin, and P. Schmitt (2012), Initial results from a dynamic coupled magnetosphere-ionosphere-ring current model, *Journal of Geophysical Research: Space Physics*, *117*(A2), doi:10.1029/2011JA016979, a02211.

Peredo, M., D. P. Stern, and N. A. Tsyganenko (1993), Are existing magnetospheric models excessively stretched?, *Journal of Geophysical Research*, *98*(A9), 15,343, doi:10.1029/93JA01150.

Perreault, P., and S.-I. Akasofu (1978), A study of geomagnetic storms, *Geophysical Journal International*, *54*(3), 547–573, doi:10.1111/j.1365-246X.1978.tb05494.x.

Petschek, H. E. (1964), Magnetic Field Annihilation, *The Physics of Solar Flares, Proceedings of the AAS-NASA Symposium*, p. 425, doi:10.1007/s13398-014-0173-7.2.

Pirjola, R., D. Boteler, A. Viljanen, and O. Amm (2000), Prediction of geomagnetically induced currents in power transmission systems, *Advances in Space Research*, *26*(1), 5–14, doi:10.1016/S0273-1177(99)01019-4.

Powell, K. G., P. L. Roe, T. J. Linde, T. I. Gombosi, and D. L. De Zeeuw (1999), A Solution-Adaptive Upwind Scheme for Ideal Magnetohydrodynamics, *Journal of Computational Physics*, *154*(2), 284–309, doi:10.1006/jcph.1999.6299.

Pu, Z.-Y., and M. G. Kivelson (1983), Kelvin:Helmholtz Instability at the magnetopause: Solution for compressible plasmas, *Journal of Geophysical Research*, *88*(A2), 841, doi:10.1029/JA088iA02p00841.

Pulkkinen, A., L. Rastätter, M. Kuznetsova, M. Hesse, A. Ridley, J. Raeder, H. J. Singer, and A. Chulaki (2010), Systematic evaluation of ground and geostationary magnetic field predictions generated by global magnetohydrodynamic models, *Journal of Geophysical Research: Space Physics*, *115*(A3), doi:10.1029/2009JA014537, a03206.

Pulkkinen, A., et al. (2013), Community-wide validation of geospace model ground magnetic field perturbation predictions to support model transition to operations, *Space Weather*, *11*(6), 369–385, doi:10.1002/swe.20056.

Pulkkinen, A., et al. (2017), Geomagnetically induced currents: Science, engineering, and applications readiness, *Space Weather*, *15*(7), 828–856, doi:10.1002/2016SW001501.

Pytte, T., R. L. McPherron, E. W. Hones, and H. I. West (1978), Multiple-satellite studies of magnetospheric substorms: Distinction between polar magnetic substorms and convection-driven negative bays, *Journal of Geophysical Research*, *83*(A2), 663, doi:10.1029/JA083iA02p00663.

Rae, I. J., et al. (2009), Timing and localization of ionospheric signatures associated with substorm expansion phase onset, *Journal of Geophysical Research: Space Physics*, *114*(A1), doi:10.1029/2008JA013559.

Raeder, J., J. Berchem, and M. Ashour-Abdalla (1998a), The Geospace Environment Modeling Grand Challenge: Results from a Global Geospace Circulation Model, *Journal of Geophysical Research: Space Physics*, *103*(A7), 14,787–14,797, doi:10.1029/98JA00014.

Raeder, J., J. Berchem, and M. Ashour-Abdalla (1998b), The geospace environment modeling grand challenge: Results from a global geospace circulation model, *Journal of Geophysical Research: Space Physics*, *103*(A7), 14,787–14,797, doi:10.1029/98JA00014.

Raeder, J., Y. Wang, T. Fuller-Rowell, and H. Singer (2001a), Global simulation of magnetospheric space weather effects of the bastille day storm, *Solar Physics*, *204*(1), 323–337, doi:10.1023/A:1014228230714.

Raeder, J., P. Zhu, Y. Ge, and G. Siscoe (2010), Open Geospace General Circulation Model simulation of a substorm: Axial tail instability and ballooning mode preceding substorm onset, *Journal of Geophysical Research*, *115*, A00I16, doi:10.1029/2010JA015876.

Raeder, J., et al. (2001b), Global simulation of the Geospace Environment Modeling substorm challenge event, *Journal of Geophysical Research*, *106*(A1), 381–395, doi:10.1029/2000JA000605.

Rajaram, R., G. L. Kalra, and J. N. Tandon (1973), Viscous interaction at the solar wind-magnetosphere boundary, *Journal of Atmospheric and Terrestrial Physics*, *35*(11), 2069–2079, doi:10.1016/0021-9169(73)90120-7.

Rastätter, L., M. M. Kuznetsova, A. Vapirev, A. Ridley, M. Wiltberger, A. Pulkkinen, M. Hesse, and H. J. Singer (2011), Geospace environment modeling 2008-2009 challenge: Geosynchronous magnetic field, *Space Weather*, *9*(4), doi:10.1029/2010SW000617, s04005.

Rastätter, L., et al. (2013), Geospace environment modeling 2008-2009 challenge: Dst index, *Space Weather*, *11*(4), 187–205, doi:10.1002/swe.20036.

Reiff, P. H., R. W. Spiro, and T. W. Hill (1981), Dependence of polar cap potential drop on interplanetary parameters, *Journal of Geophysical Research: Space Physics*, *86*(A9), 7639–7648, doi:10.1029/JA086iA09p07639.

Rème, H., et al. (2001), First multispacecraft ion measurements in and near the Earth's magnetosphere with the identical Cluster ion spectrometry (CIS) experiment, *Annales Geophysicae*, *19*(10/12), 1303–1354, doi:10.5194/angeo-19-1303-2001.

Richmond, A. D. (1992), Assimilative mapping of ionospheric electrodynamics, *Adv. Space Res.*, *12*, 59.

Richmond, A. D., and Y. Kamide (1988), Mapping electrodynamic features of the high-latitude ionosphere from localized observations: Technique, *Journal of Geophysical Research*, *93*(A6), 5741, doi:10.1029/JA093iA06p05741.

Richmond, A. D., et al. (1980), An empirical model of quiet-day ionospheric electric fields at middle and low latitudes, *Journal of Geophysical Research: Space Physics*, *85*(A9), 4658–4664, doi:10.1029/JA085iA09p04658.

Ridley, A., T. Gombosi, and D. Dezeeuw (2004), Ionospheric control of the magnetosphere: conductance, *Annales Geophysicae*, *22*, 567–584, doi:10.5194/angeo-22-567-2004.

Ridley, A. J., and M. W. Liemohn (2002), A model-derived storm time asymmetric ring current driven electric field description, *Journal of Geophysical Research: Space Physics*, *107*(A8), SMP 2–1–SMP 2–12, doi:10.1029/2001JA000051.

Ridley, A. J., T. I. Gombosi, D. L. De Zeeuw, C. R. Clauer, and A. D. Richmond (2003), Ionospheric control of the magnetosphere: Thermospheric neutral winds, *J. Geophys. Res.*, *108*(A8), 1328, doi:10.1029/2002JA009464.

Roe, P. L., and D. S. Balsara (1996), Notes on the eigensystem of magnetohydrodynamics, *SIAM Journal on Applied Mathematics*, *56*(1), 57–67, doi:10.1137/S003613999427084X.

Rostoker, G. (1972), Geomagnetic indices, *Reviews of Geophysics*, *10*(4), 935, doi:10.1029/RG010i004p00935.

Rostoker, G. (1983), Triggering of expansive phase intensifications of magnetospheric substorms by northward turnings of the interplanetary magnetic field, *Journal of Geophysical Research*, *88*(A9), 6981, doi:10.1029/JA088iA09p06981.

Rostoker, G. (2002), Identification of substorm expansive phase onsets, *Journal of Geophysical Research*, *107*(A7), 1137, doi:10.1029/2001JA003504.

Rostoker, G., S.-I. Akasofu, J. Foster, R. Greenwald, Y. Kamide, K. Kawasaki, A. Lui, R. McPherron, and C. Russell (1980), Magnetospheric substormsdefinition and signatures, *Journal of Geophysical Research*, *85*(A4), 1663, doi:10.1029/JA085iA04p01663.

Runov, A., V. Angelopoulos, M. I. Sitnov, V. A. Sergeev, J. Bonnell, J. P. McFadden, D. Larson, K.-H. Glassmeier, and U. Auster (2009), THEMIS observations of an earthward-propagating dipolarization front, *Geophysical Research Letters*, *36*(14), L14,106, doi:10.1029/2009GL038980.

Runov, A., V. Angelopoulos, and X.-Z. Zhou (2012), Multipoint observations of dipolarization front formation by magnetotail reconnection, *Journal of Geophysical Research: Space Physics*, *117*(A5), A05,230, doi:10.1029/2011JA017361.

Russell, C. T. (2000), How northward turnings of the IMF can lead to substorm expansion onsets, *Geophysical Research Letters*, *27*(20), 3257–3259, doi:10.1029/2000GL011910.

Russell, C. T., P. J. Chi, D. J. Dearborn, Y. S. Ge, B. Kuo-Tiong, J. D. Means, D. R. Pierce, K. M. Rowe, and R. C. Snare (2008), THEMIS Ground-Based Magnetometers, *Space Science Reviews*, *141*(1-4), 389–412, doi:10.1007/s11214-008-9337-0.

Samson, J., and K. Yeung (1986), Some generalizations on the method of superposed epoch analysis, *Planetary and Space Science*, *34*(11), 1133–1142, doi:10.1016/0032-0633(86)90025-5.

Sauvaud, J.-A., and J. Winckler (1980), Dynamics of plasma, energetic particles, and fields near synchronous orbit in the nighttime sector during magnetospheric substorms, *Journal of Geophysical Research*, *85*(A5), 2043, doi:10.1029/JA085iA05p02043.

Sazykin, S. Y. (2000), Theoretical Studies of Penetration of Magnetospheric Electric Fields to the Ionosphere, Ph.D. thesis, Utah State University, Logan, Utah.

Schmid, D., M. Volwerk, R. Nakamura, W. Baumjohann, and M. Heyn (2011), A statistical and event study of magnetotail dipolarization fronts, *Annales Geophysicae*, *29*(9), 1537–1547, doi:10.5194/angeo-29-1537-2011.

Schunk, R. W., and A. F. Nagy (2000), *Ionospheres*, Cambridge University Press, Cambridge University.

Scott, D. W. (2015), Multivariate density estimation: theory, practice, and visualization.

Sergeev, V., and N. Tsyganenko (1982), Energetic particle losses and trapping boundaries as deduced from calculations with a realistic magnetic field model, *Planetary and Space Science*, *30*(10), 999–1006, doi:10.1016/0032-0633(82)90149-0.

Sergeev, V., E. Sazhina, N. Tsyganenko, J. Lundblad, and F. Søraas (1983), Pitch-angle scattering of energetic protons in the magnetotail current sheet as the dominant source of their isotropic precipitation into the nightside ionosphere, *Planetary and Space Science*, *31*(10), 1147–1155, doi:10.1016/0032-0633(83)90103-4.

Sergeev, V. A., and B. B. Gvozdevsky (1995), MT-index – a possible new index to characterize the magnetic configuration of magnetotail, *Annales Geophysicae*, *13*(10), 1093–1103, doi:10.1007/s00585-995-1093-9.

Sergeev, V. A., P. Tanskanen, K. Mursula, A. Korth, and R. C. Elphic (1990), Current sheet thickness in the near-Earth plasma sheet during substorm growth phase, *Journal of Geophysical Research*, *95*(A4), 3819, doi:10.1029/JA095iA04p03819.

Sergeev, V. A., M. Malkov, and K. Mursula (1993), Testing the isotropic boundary algorithm method to evaluate the magnetic field configuration in the tail, *Journal of Geophysical Research: Space Physics*, *98*(A5), 7609–7620, doi:10.1029/92JA02587.

Sergeev, V. A., T. A. Kornilova, I. A. Kornilov, V. Angelopoulos, M. V. Kubyshkina, M. Fillingim, R. Nakamura, J. P. McFadden, and D. Larson (2010), Auroral signatures of the plasma injection and dipolarization in the inner magnetosphere, *Journal of Geophysical Research: Space Physics*, *115*(A2), doi:10.1029/2009JA014522.

Sergeev, V. A., V. Angelopoulos, and R. Nakamura (2012), Recent advances in understanding substorm dynamics, *Geophysical Research Letters*, *39*(5), doi:10.1029/2012GL050859.

Sergeev, V. A., I. A. Chernyaev, V. Angelopoulos, and N. Y. Ganushkina (2015a), Magnetospheric conditions near the equatorial footpoints of proton isotropy boundaries, *Annales Geophysicae*, *33*(12), 1485–1493, doi:10.5194/angeo-33-1485-2015.

Sergeev, V. A., S. A. Chernyaeva, S. V. Apatenkov, N. Y. Ganushkina, and S. V. Dubyagin (2015b), Energy-latitude dispersion patterns near the isotropy boundaries of energetic protons, *Annales Geophysicae*, *33*(8), 1059–1070, doi:10.5194/angeo-33-1059-2015.

Sidgreaves, W., and B. Stewart (1868), Results of a Preliminary Comparison of Certain Curves of the Kew and Stonyhurst Declination Magnetographs, *Proceedings of the Royal Society of London*, *17*(0), 236–238, doi:10.1098/rspl.1868.0035.

Singer, H., L. Matheson, R. Grubb, A. Newman, and D. Bouwer (1996), Monitoring space weather with the GOES magnetometers, in *Proceedings of SPIE*, vol. 2812, edited by E. R. Washwell, pp. 299–308, International Society for Optics and Photonics, doi:10.1117/12.254077.

Skone, S., and M. de Jong (2000), The impact of geomagnetic substorms on GPS receiver performance, *Earth, Planets and Space*, *52*(11), 1067–1071, doi:10.1186/BF03352332.

Slapak, R., H. Nilsson, L. G. Westerberg, and R. Larsson (2015), O+ transport in the dayside magnetosheath and its dependence on the IMF direction, *Annales Geophysicae*, *33*(3), 301–307, doi:10.5194/angeo-33-301-2015.

Slavin, J. A., M. F. Smith, E. L. Mazur, D. N. Baker, T. Iyemori, H. J. Singer, and E. W. Greenstadt (1992), ISEE 3 plasmoid and TCR observations during an extended interval of substorm activity, *Geophysical Research Letters*, *19*(8), 825–828, doi:10.1029/92GL00394.

Slavin, J. A., et al. (1989), CDAW 8 observations of plasmoid signatures in the geomagnetic tail: An assessment, *Journal of Geophysical Research*, *94*(A11), 15,153, doi:10.1029/JA094iA11p15153.

Slinker, S. P., J. A. Fedder, and J. G. Lyon (1995), Plasmoid formation and evolution in a numerical simulation of a substorm, *Geophysical Research Letters*, *22*(7), 859–862, doi:10.1029/95GL00300.

Smith, E. J., and J. H. Wolfe (1976), Observations of interaction regions and corotating shocks between one and five AU: Pioneers 10 and 11, *Geophysical Research Letters*, *3*(3), 137–140, doi:10.1029/GL003i003p00137.

Sokolov, I., E. V. Timofeev, J. Sakai, and K. Takayama (2002), Artificial wind – a new framework to construct simple and efficient upwind shock-capturing schemes, *J. Comp. Phys.*, *181*, 354–393, doi:10.1006/jcph.2002.7130.

Sonett, C. P. (1960), Coupling of the Solar Wind and the Exosphere, *Physical Review Letters*, *5*(2), 46–48, doi:10.1103/PhysRevLett.5.46.

Sonnerup, B. U. Ö. (1974), Magnetopause reconnection rate, *Journal of Geophysical Research*, *79*(10), 1546–1549, doi:10.1029/JA079i010p01546.

Søraas, F. (1972), ESRO IA/B Observations at High Latitudes of Trapped and Precipitating Protons with Energies above 100 keV, in *Earth's Magnetospheric Processes*, pp. 120–132, Springer, Dordrecht, doi:10.1007/978-94-010-2896-7_12.

Søraas, F., J. Lundblad, N. Maltseva, V. Troitskaya, and V. Selivanov (1980), A comparison between simultaneous I.P.D.P. groundbased observations and observations of energetic protons obtained by satellites, *Planetary and Space Science*, *28*(4), 387–405, doi:10.1016/0032-0633(80)90043-4.

Søraas, F., K. Aarsnes, K. Oksavik, and D. S. Evans (2002), Ring current intensity estimated from low-altitude proton observations, *Journal of Geophysical Research*, *107*(A7), 1149, doi:10.1029/2001JA000123.

Spiro, R. W., P. H. Reiff, and L. J. Maher (1982), Precipitating electron energy flux and auroral zone conductances-An empirical model, *Journal of Geophysical Research*, *87*(A10), 8215, doi:10.1029/JA087iA10p08215.

Stephenson, D. B. (2000), Use of the Odds Ratio for Diagnosing Forecast Skill, *Weather and Forecasting*, *15*(2), 221–232, doi:10.1175/1520-0434(2000)015⟨0221:UOTORF⟩2.0.CO;2.

Stout, Q. F., D. L. De Zeeuw, T. I. Gombosi, C. P. T. Groth, H. G. Marshall, and K. G. Powell (1997), Adaptive blocks, in *Proceedings of the 1997 ACM/IEEE conference on Supercomputing (CDROM) - Supercomputing '97*, pp. 1–10, ACM Press, New York, New York, USA, doi:10.1145/509593.509650.

Sugiura, M., and D. J. Poros (1972), Provisional hourly values of equatorial Dst for 1971.

Sugiura, M., T. L. Skillman, B. G. Ledley, and J. P. Heppner (1968), Propagation of the sudden commencement of July 8, 1966, to the magnetotail, *Journal of Geophysical Research*, *73*(21), 6699–6709, doi:10.1029/JA073i021p06699.

Sweet, P. A. (1958), The Neutral Point Theory of Solar Flares, in *Proceedings of the International Astronomical Union*, vol. 6, edited by B. Lehnert, pp. 123–134, Cambridge University Press.

Tanskanen, E. I. (2009), A comprehensive high-throughput analysis of substorms observed by IMAGE magnetometer network: Years 1993-2003 examined, *Journal of Geophysical Research: Space Physics*, *114*(A5), A05,204, doi:10.1029/2008JA013682.

Tapping, K. F. (2013), The 10.7 cm solar radio flux (F 10.7), *Space Weather*, *11*(7), 394–406, doi:10.1002/swe.20064.

Taylor, J. (1997), *An introduction to error analysis : the study of uncertainties in physical measurements*, University Science Books, Sausalito, Calif.

Thomsen, M. F. (2004), Why Kp is such a good measure of magnetospheric convection, *Space Weather*, *2*(11), doi:10.1029/2004SW000089.

Tikhonov, A., and A. Samarskii (1962), Homogeneous difference schemes, *USSR Computational Mathematics and Mathematical Physics*, *1*(1), 5–67, doi:10.1016/0041-5553(62)90005-8.

Toffoletto, F., S. Sazykin, R. Spiro, and R. Wolf (2003), Inner magnetospheric modeling with the Rice Convection Model, *Space Science Reviews*, *107*(1-2), 175–196, doi:10.1023/A:1025532008047.

Tóth, G., Y. Ma, and T. I. Gombosi (2008), Hall magnetohydrodynamics on block-adaptive grids, *Journal of Computational Physics*, *227*(14), 6967–6984, doi:10.1016/j.jcp.2008.04.010.

Tóth, G., et al. (2005), Space Weather Modeling Framework: A new tool for the space science community, *Journal of Geophysical Research: Space Physics*, *110*(A12), doi:10.1029/2005JA011126.

Tóth, G., et al. (2012), Adaptive Numerical Algorithms in Space Weather Modeling, *J. Comput. Phys.*, *231*(3), 870–903, doi:10.1016/j.jcp.2011.02.006.

Tóth, G., et al. (2016), Extended magnetohydrodynamics with embedded particle-in-cell simulation of Ganymede's magnetosphere, *Journal of Geophysical Research: Space Physics*, *121*(2), 1273–1293, doi:10.1002/2015JA021997.

Tsyganenko, N. A. (1982), Pitch-angle scattering of energetic particles in the current sheet of the magnetospheric tail and stationary distribution functions, *Planetary and Space Science*, *30*(5), 433–437, doi:10.1016/0032-0633(82)90052-6.

Tsyganenko, N. A. (1989), A magnetospheric magnetic field model with a warped tail current sheet, *Planetary and Space Science*, *37*(1), 5–20, doi:10.1016/0032-0633(89)90066-4.

Tsyganenko, N. A. (1995), Modeling the Earth's Magnetospheric Magnetic Field Confined Within a Realistic Magnetopause, *J. Geophys. Res.*, *100*(A4), 5599–5612, doi:10.1029/94JA03193.

Tsyganenko, N. A. (2001), Empirical Magnetic Field Models for the Space Weather Program, in *Space Weather*, edited by P. P. Song, H. J. Singer, and G. L. Siscoe, pp. 273–280, American Geophysical Union (AGU), doi:10.1029/GM125p0273.

Tsyganenko, N. A. (2002), A model of the near magnetosphere with a dawn-dusk asymmetry 1. Mathematical structure, *Journal of Geophysical Research: Space Physics*, *107*(A8), SMP 12–1–SMP 12–15, doi:10.1029/2001JA000219.

Tsyganenko, N. A., and V. A. Andreeva (2015), A forecasting model of the magnetosphere driven by an optimal solar wind coupling function, *Journal of Geophysical Research: Space Physics*, *120*(10), 8401–8425, doi:10.1002/2015JA021641.

Tsyganenko, N. A., and V. A. Andreeva (2016), An empirical RBF model of the magnetosphere parameterized by interplanetary and ground-based drivers, *Journal of Geophysical Research: Space Physics*, *121*(11), 10,786–10,802, doi:10.1002/2016JA023217.

Tsyganenko, N. A., and M. I. Sitnov (2005), Modeling the dynamics of the inner magnetosphere during strong geomagnetic storms, *Journal of Geophysical Research*, *110*(A3), A03,208, doi:10.1029/2004JA010798.

Usanova, M. E., I. R. Mann, J. Bortnik, L. Shao, and V. Angelopoulos (2012), THEMIS observations of electromagnetic ion cyclotron wave occurrence: Dependence on AE, SYMH, and solar wind dynamic pressure, *Journal of Geophysical Research: Space Physics*, *117*(A10), A10,218, doi:10.1029/2012JA018049.

Vasyliunas, V. M. (1970), Mathematical models of magnetospheric convection and its coupling to the ionosphere, in *Particles and Fields in the Magnetosphere*, edited by B. M. McCormac, pp. 60–71, D. Reidel Publishing, Dordrecht, Holland, doi: 10.1007/978-94-010-3284-1_6.

Voronkov, I. O., E. F. Donovan, and J. C. Samson (2003), Observations of the phases of the substorm, *Journal of Geophysical Research: Space Physics*, *108*(A2), doi: 10.1029/2002JA009314.

Walach, M.-T., and S. E. Milan (2015), Are steady magnetospheric convection events prolonged substorms?, *Journal of Geophysical Research: Space Physics*, *120*(3), 1751–1758, doi:10.1002/2014JA020631.

Wang, H., S. Ma, and A. J. Ridley (2010), Comparative study of a substorm event by satellite observation and model simulation, *Chinese Science Bulletin*, *55*(9), 857–864, doi:10.1007/s11434-009-0282-4.

Wanliss, J. A., and K. M. Showalter (2006), High-resolution global storm index: Dst versus sym-h, *Journal of Geophysical Research: Space Physics*, *111*(A2), doi: 10.1029/2005JA011034, a02202.

Weimer, D. R. (1995), Models of high-latitude electric potentials derived with a least error fit of spherical harmonic coefficients, *Journal of Geophysical Research*, *100*(A10), 19,595, doi:10.1029/95JA01755.

Weimer, D. R. (2004), Correction to "Predicting interplanetary magnetic field (IMF) propagation delay times using the minimum variance technique", *Journal of Geophysical Research*, *109*(A12), A12,104, doi:10.1029/2004JA010691.

Weimer, D. R. (2005), Improved ionospheric electrodynamic models and application to calculating joule heating rates, *Journal of Geophysical Research: Space Physics*, *110*(A5), doi:10.1029/2004JA010884, a05306.

Weimer, D. R., and J. H. King (2008), Improved calculations of interplanetary magnetic field phase front angles and propagation time delays, *Journal of Geophysical Research: Space Physics*, *113*(A1), doi:10.1029/2007JA012452.

Weimer, D. R., D. M. Ober, N. C. Maynard, M. R. Collier, D. J. McComas, N. F. Ness, C. W. Smith, and J. Watermann (2003), Predicting interplanetary magnetic field (imf) propagation delay times using the minimum variance technique, *Journal of Geophysical Research: Space Physics*, *108*(A1), doi:10.1029/2002JA009405, 1026.

Welling, D. T., and M. W. Liemohn (2014), Outflow in global magnetohydrodynamics as a function of a passive inner boundary source, *Journal of Geophysical Research: Space Physics*, *119*(4), 2691–2705, doi:10.1002/2013JA019374.

Welling, D. T., and M. W. Liemohn (2016), The ionospheric source of magnetospheric plasma is not a black box input for global models, *Journal of Geophysical Research: Space Physics*, *121*(6), 5559–5565, doi:10.1002/2016JA022646, 2016JA022646.

Welling, D. T., and A. J. Ridley (2010), Validation of SWMF magnetic field and plasma, *Space Weather*, *8*(3), doi:10.1029/2009SW000494.

Welling, D. T., and S. G. Zaharia (2012), Ionospheric outflow and cross polar cap potential: What is the role of magnetospheric inflation?, *Geophysical Research Letters*, *39*(23), doi:10.1029/2012GL054228.

Welling, D. T., V. K. Jordanova, A. Glocer, G. Toth, M. W. Liemohn, and D. R. Weimer (2015), The two-way relationship between ionospheric outflow and the ring current, *Journal of Geophysical Research: Space Physics*, *120*(6), 4338–4353, doi:10.1002/2015JA021231.

Welling, D. T., A. R. Barakat, J. V. Eccles, R. W. Schunk, and C. R. Chappell (2016), Coupling the Generalized Polar Wind Model to Global Magnetohydrodynamics: Initial Results, in *MagnetosphereIonosphere Coupling in the Solar System*, vol. 222, pp. 179–194, Washington, DC, doi:10.15142/T3C88J.

Welling, D. T., B. J. Anderson, G. Crowley, A. A. Pulkkinen, and L. Rastätter (2017), Exploring predictive performance: A reanalysis of the geospace model transition challenge, *Space Weather*, *15*(1), 192–203, doi:10.1002/2016SW001505, 2016SW001505.

West, H. I., R. M. Buck, and M. G. Kivelson (1978), On the configuration of the magnetotail near midnight during quiet and weakly disturbed periods: Magnetic field modeling, *Journal of Geophysical Research*, *83*(A8), 3819, doi:10.1029/JA083iA08p03819.

Weygand, J. M., R. McPherron, K. Kauristie, H. Frey, and T.-S. Hsu (2008), Relation of auroral substorm onset to local AL index and dispersionless particle injections, *Journal of Atmospheric and Solar-Terrestrial Physics*, *70*(18), 2336–2345, doi:10.1016/J.JASTP.2008.09.030.

Wild, J. A., E. E. Woodfield, and S. K. Morley (2009), On the triggering of auroral substorms by northward turnings of the interplanetary magnetic field, *Annales Geophysicae*, *27*(9), 3559–3570, doi:10.5194/angeo-27-3559-2009.

Wilkinson, D. C. (1994), National Oceanic and Atmospheric Administration's spacecraft anomaly data base and examples of solar activity affecting spacecraft, *Journal of Spacecraft and Rockets*, *31*(2), 160–165, doi:10.2514/3.26417.

Wilks, D. S. (2011), *Statistical methods in the atmospheric sciences*, 676 pp., Elsevier/Academic Press.

Williams, D. J., and L. R. Lyons (1974), The proton ring current and its interaction with the plasmapause: Storm recovery phase, *Journal of Geophysical Research*, *79*(28), 4195–4207, doi:10.1029/JA079i028p04195.

Wilson, G. R., D. M. Ober, G. A. Germany, and E. J. Lund (2004), Nightside auroral zone and polar cap ion outflow as a function of substorm size and phase, *Journal of Geophysical Research: Space Physics*, *109*(A2), doi:10.1029/2003JA009835.

Wiltberger, M., W. Wang, A. Burns, S. Solomon, J. Lyon, and C. Goodrich (2004), Initial results from the coupled magnetosphere ionosphere thermosphere model: magnetospheric and ionospheric responses, *Journal of Atmospheric and Solar-Terrestrial Physics*, *66*(15-16), 1411–1423, doi:10.1016/j.jastp.2004.03.026.

Wiltberger, M., W. Lotko, J. G. Lyon, P. Damiano, and V. Merkin (2010), Influence of cusp O ⁺ outflow on magnetotail dynamics in a multifluid MHD model of the magnetosphere, *Journal of Geophysical Research: Space Physics*, *115*(A10), A00J05, doi:10.1029/2010JA015579.

Wiltberger, M., E. Rigler, V. Merkin, J. Lyon, B. M. Wiltberger, V. Merkin SlavaMerkin, and j. J. Lyon JohnLyon (2017), Structure of High Latitude Currents in Magnetosphere-Ionosphere Models, *Space Sci Rev*, *206*, 575–598, doi:10.1007/s11214-016-0271-2.

Winglee, R. (2000), Mapping of ionospheric outflows into the magnetosphere for varying IMF conditions., *J. Atmos. and Terr. Phys.*, *62*, 527.

Winglee, R. M., D. Chua, M. Brittnacher, G. K. Parks, and G. Lu (2002a), Global impact of ionospheric outflows on the dynamics of the magnetosphere and cross-polar cap potential, *Journal of Geophysical Research*, *107*(A9), 1237, doi:10.1029/2001JA000214.

Winglee, R. M., D. Chua, M. Brittnacher, G. K. Parks, and G. Lu (2002b), Global impact of ionospheric outflows on the dynamics of the magnetosphere and cross-polar cap potential, *Journal of Geophysical Research: Space Physics*, *107*(A9), SMP 11–1–SMP 11–12, doi:10.1029/2001JA000214, 1237.

Wolf, R. A., M. Harel, R. W. Spiro, G.-H. Voigt, P. H. Reiff, and C.-K. K. Chen (1982), Computer simulation of inner magnetospheric dynamics for the magnetic storm of July 29, 1977, *Journal of Geophysical Research*, *87*(A8), 5949–5962, doi:10.1029/JA087iA08p05949.

Wu, C. C., R. J. Walker, and J. M. Dawson (1981), A three dimensional mhd model of the earth's magnetosphere, *Geophysical Research Letters*, *8*(5), 523–526, doi:10.1029/GL008i005p00523.

Yahnin, A. G., and T. A. Yahnina (2007), Energetic proton precipitation related to ion-cyclotron waves, *Journal of Atmospheric and Solar-Terrestrial Physics*, *69*(14), 1690–1706, doi:10.1016/j.jastp.2007.02.010.

Yokoyama, N., and Y. Kamide (1997), Statistical nature of geomagnetic storms, *Journal of Geophysical Research: Space Physics*, *102*(A7), 14,215–14,222, doi:10.1029/97JA00903.

Young, D. T., H. Balsiger, and J. Geiss (1982), Correlations of magnetospheric ion composition with geomagnetic and solar activity, *Journal of Geophysical Research*, *87*(A11), 9077, doi:10.1029/JA087iA11p09077.

Yu, Y., and A. J. Ridley (2008), Validation of the space weather modeling framework using ground-based magnetometers, *Space Weather*, *6*(5), doi:10.1029/2007SW000345.

Yu, Y., A. J. Ridley, D. T. Welling, and G. Tóth (2010), Including gap region field-aligned currents and magnetospheric currents in the MHD calculation of ground-based magnetic field perturbations, *Journal of Geophysical Research: Space Physics*, *115*(A8), doi:10.1029/2009JA014869.

Yue, C., C.-P. Wang, L. Lyons, J. Liang, E. F. Donovan, S. G. Zaharia, and M. Henderson (2014), Current sheet scattering and ion isotropic boundary under 3-D empirical force-balanced magnetic field, *Journal of Geophysical Research: Space Physics*, *119*(10), 8202–8211, doi:10.1002/2014JA020172.

Zaharia, S., V. K. Jordanova, M. F. Thomsen, and G. D. Reeves (2006), Self-consistent modeling of magnetic fields and plasmas in the inner magnetosphere: Application to a geomagnetic storm, *Journal of Geophysical Research*, *111*(A11), A11S14, doi:10.1029/2006JA011619.

Zhang, B., W. Lotko, M. Wiltberger, O. Brambles, and P. Damiano (2011), A statistical study of magnetosphere-ionosphere coupling in the Lyon-Fedder-Mobarry global MHD model, *Journal of Atmospheric and Solar-Terrestrial Physics*, *73*(5-6), 686–702, doi:10.1016/j.jastp.2010.09.027.

Zhang, Y., L. J. Paxton, and Y. Zheng (2008), Interplanetary shock induced ring current auroras, *Journal of Geophysical Research: Space Physics*, *113*(A1), A01,212, doi:10.1029/2007JA012554.

Zheng, Y., A. T. Y. Lui, M.-C. Fok, B. J. Anderson, P. C. Brandt, T. J. Immel, and D. G. Mitchell (2006), Relationship between Region 2 field-aligned current and the ring current: Model results, *Journal of Geophysical Research*, *111*(A11), A11S06, doi:10.1029/2006JA011603.

Zheng, Y., A. T. Lui, M.-C. Fok, B. J. Anderson, P. C. Brandt, and D. G. Mitchell (2008), Controlling factors of Region 2 field-aligned current and its relationship to the ring current: Model results, *Advances in Space Research*, *41*(8), 1234–1242, doi:10.1016/j.asr.2007.05.084.

Zhu, P., A. Bhattacharjee, and Z. W. Ma (2004), Finite k y ballooning instability in the near-Earth magnetotail, *Journal of Geophysical Research*, *109*(A11), A11,211, doi:10.1029/2004JA010505.